Search for third-generation squarks in all-hadronic final states at the LHC with the ATLAS detector 1

Silvia Fracchia

Search for third-generation squarks in all-hadronic final states at the LHC with the ATLAS detector [1]

Silvia Fracchia

Institut de Física d'Altes Energies
Universitat Autònoma de Barcelona
Departament de Física
Facultat de Ciències
Edifici Cn E-08193 Bellaterra (Barcelona)

Programa de doctorat en Física

Thursday 20th October, 2016

supervised by
Mario Martínez Pérez
ICREA / Institut de Física d'Altes Energies
Universitat Autònoma de Barcelona
Edifici Cn E-08193 Bellaterra (Barcelona)

[1] Tesis doctoral

Contents

Chapter 1

Introduction

The Large Hadron Collider (LHC) at CERN offers the unique opportunity to explore the energy frontier in particle physics.

In 2012, the ATLAS and CMS Experiments at the LHC established the presence of a resonant signal with mass around 125 GeV which is attributed to the Standard Model (SM) Higgs boson. The SM can now be regarded as a consistent theory that, over the last decades, provided very accurate predictions of many physics phenomena. However, the SM is regarded as incomplete since it does not answer a series of fundamental questions like, for example, the nature of Dark Matter or the hierarchy problem, among others.

Supersymmetry (SUSY) is considered one of the favored theories beyond the SM and this has motivated a lot of effort from the experimental point of view, over the last decades, to prove its existence. SUSY provides elegant solutions to many of the SM open questions. For example, it protects the Higgs boson mass from receiving large quadratic corrections and contains a valid candidate for Dark Matter.

Of particular interest are the searches for the supersymmetric partners of the quarks of the third generation, the stop and the sbottom. This kind of searches represents one of the pillars of the LHC program. Naturalness arguments require the stop and the sbottom to be light, with their masses not exceeding the TeV-scale. This results into the possibility of producing them at the LHC. An extensive program of searches was carried out during the Run-1 of the LHC, and strong constrains on the masses of the stop and the sbottom were set by both the ATLAS and the CMS Collaborations.

The increase in center-of-mass energy at the start of the LHC Run-2, from $\sqrt{s}$ =8 TeV to $\sqrt{s}$ =13 TeV, has translated into a significant increase in the cross section for the pair production of third-generation squarks.

In this thesis, the search for the direct pair production of the sbottom quark with the first data collected by the ATLAS Experiment at $\sqrt{s}$ =13 TeV is presented. The search is based on the data collected in 2015 and is performed in a full hadronic final state, characterized by the presence of two b-jets and large missing transverse momentum.

The thesis is organized as follows: an overview of the theoretical and phenomenological concepts at the basis of a search for new phenomena at hadron colliders is given in Chapter 2, where SUSY will be also introduced, mostly focusing on the minimal supersymmetric extension of the SM and R-parity conserving scenarios. The ATLAS detector and its components are briefly described in Chapter 3, followed by a description of the techniques used for reconstructing the physics objects used in the search, such as jets and missing transverse momentum, in Chapter 4. Chapter 5 is devoted to the presentation of a sensitivity study for the sbottom search, which was performed before the start of Run-2. The search for the sbottom with the Run-2 data are presented in Chapter 6, including the full exploration of the strategy used to estimate the dominant SM backgrounds. The results of this search are interpreted in terms of direct sbottom pair production and prospects for future searches are given at the end of the Chapter. Finally, the conclusions are collected in Chapter 7.

The results presented in this thesis led to the following publications by the ATLAS Collaboration:

- *Search for bottom squark pair production in proton-proton collisions at $\sqrt{s}$ =13 TeV with the ATLAS detector* (Eur. Phys. J. C, (2016) 76:547).
- *Search for Bottom Squark Pair Production with the ATLAS Detector in proton-proton Collisions at $\sqrt{s}$ =13 TeV* (ATLAS-CONF-2015-066, December 2015).
- *Sensitivity studies for squarks and gluinos with 1-10 fb^{-1} of 13 TeV data* (ATL-PHYS-PUB-2015-005, March 2015).

The thesis is complemented by a number of appendixes. In particular, Appendix B discusses the detector work carried out in the Tile Calorimeter. Appendix C summarizes the work, performed at the early stages of the development of this thesis, on the search for the SM Higgs boson decaying to b-quarks and produced in association with a vector boson. The search was performed using the full Run-1 dataset collected at $\sqrt{s}$ =7 and 8 TeV and was documented in the following publication by the ATLAS Collaboration: *Search for the $b\bar{b}$ decay of the Standard Model Higgs boson in associated (W/Z)H production with the ATLAS detector* (ATLAS-CONF-2013-079, July 2013).

Finally, some work was recently performed, together with the rest of the IFAE team, in the search for the supersymmetric partner of the top quark, in all hadronic final states with large jet multiplicity, at least two b-jets and large missing transverse momentum. This search led to a publication by the ATLAS Collaboration, using the data collected in 2015 and the first part of 2016 at $\sqrt{s}$ =13 TeV and corresponding to 13.3 fb^{-1} of integrated luminosity: *Search for a Scalar Partner of the Top Quark in the Jets+$E_{\mathrm{T}}^{\mathrm{miss}}$ Final State at $\sqrt{s}$ =13 TeV with the ATLAS detector* (ATLAS-CONF-2016-077, August 2016).

Chapter 2

Theory and Phenomenology

This chapter is aimed to give an overview of the theoretical concepts which are at the basis of the searches presented in this thesis. First of all, the Standard Model (SM) of particle physics, i.e. the theory describing the elementary particles and their fundamental interactions, will be introduced in Section 2.1.

The SM is a very successful theory which gives accurate predictions of experimental observations. Nevertheless, it leaves some fundamental questions unanswered. A possible extension of the SM is Supersymmetry, an appealing theoretical framework which is able to find answers to some of the main open questions. Supersymmetry will be introduced in Section 2.2, focusing on R-parity conserving scenarios and on the properties of the supersymmetric partners of the third-generation quarks. The latter, and specifically the supersymmetric partner of the bottom quark, are the protagonists of the search presented in Chapters 5 and 6.

Finally, an overview of the phenomenology of high-energy hadron collisions, as well as the techniques used to model them with Monte Carlo simulations, will be given in Section 2.3.

2.1 The Standard Model

The SM of particle physics is a quantum field theory which describes the properties of the elementary particles and of three of their fundamental interactions, namely the electromagnetic (EM), the weak and the strong forces. The development of the model dates back to the 1960s and the 1970s and its success has been proven since then with the discovery of the predicted particles and the measurement of their properties.

The SM is based on the $\mathrm{SU(3)_C} \otimes \mathrm{SU(2)_L} \otimes \mathrm{U(1)_Y}$ symmetry group, where $\mathrm{SU(3)_C}$ represents the color symmetry of the strong interaction and $\mathrm{SU(2)_L} \otimes \mathrm{U(1)_Y}$ is the symmetry group of the local gauge transformations of the weak isospin T_3 and the weak ypercharge Y. The SM Lagrangian is invariant under the transformations of this symmetry group

and can be separated into the sum of a term responsible for the strong interaction, $\mathcal{L}_{QCD}$, and an electroweak term $\mathcal{L}_{EW}$.

In the following sections, the particle content of the Standard Model will be presented, followed by a brief description of the different interactions and, finally, of the Higgs mechanism. A detailed description of the topics covered in this section can be found in Refs. [1–5].

2.1.1 The particle content

The SM predicts the existence of elementary particles with half integer spin (in units of $\hbar$), called *fermions* and organized in three families, and of additional particles with integer spin, called *bosons*. Fermions represent the building blocks of matter, while bosons are identified as the mediators of the fundamental forces.

There are two different classes of fermions, characterized by different quantum numbers: six leptons (and their antiparticles) and six quarks (and their antiparticles). Each class of fermions is divided in three families or generations. The fermionic sector is summarized in Table 2.1, showing their masses [1], electric charges and interactions.

The lepton generations are composed by neutrinos with zero electric charge and electrically charged leptons. The quantum number associated to leptons is the lepton flavor, which corresponds to 1 for leptons and -1 for anti-leptons. The lepton flavor is conserved separately for the three generations in electroweak interactions. The neutrinos are considered as massless in the SM, although there is experimental evidence that they have a non-zero mass, even if very small, following the observation of neutrino oscillations [8]. For the purpose of this thesis, the small mass of neutrinos can be safely ignored.

The quarks interact via the electromagnetic, weak and strong forces. Unlike the leptons, the quarks are confined within the hadrons and are not observed as physical particles. There are two different types of hadrons, baryons and mesons. The former are made of a combination of three quarks while the latter are made of a quark-antiquark pair. The baryon number is a conserved multiplicative quantum number which was originally introduced to explain the stability of the proton. The baryon number is 1 for baryons, -1 for anti-baryons and 0 for mesons. Because of the confinement of the quarks into hadrons, their masses cannot be measured directly, but they are determined indirectly from their influence on the properties of the hadrons. When talking about quark masses, one should keep in mind that they are defined in a specific theoretical model and, in particular, they depend on the renormalization scheme used to define the theory.

[1] As it is said later in this section, in the case of the quarks the mass values depend on the chosen renormalization scheme. The quark masses in Table 2.1 are obtained using perturbative QCD with the so-called $\overline{MS}$ renormalization scheme [6, 7].

Fermion type	1st gen. (mass)	2nd gen. (mass)	3rd gen. (mass)	Electric charge (Q/e)	Interactions
Leptons	ν_e (< 2 eV)	ν_μ (< 0.19 MeV)	ν_τ (< 18.2 MeV)	0	Weak
	e (0.5109989461(31) MeV)	μ (105.6583745(24) MeV)	τ (776.86 ± 0.12 MeV)	-1	EM and weak
Quarks	*Up* u ($2.2^{+0.6}_{-0.4}$ MeV)	*Charm* c (1.27 ± 0.03 GeV)	*Top* t ($173.21 \pm 0.51 \pm 0.71$ GeV)	+2/3	EM, weak and strong
	Down d ($4.7^{+0.5}_{-0.4}$ MeV)	*Strange* s (96^{+8}_{-4} MeV)	*Bottom* b ($4.18^{+0.04}_{-0.03}$ GeV)	-1/3	

Table 2.1: Classification of the fermionic content of the SM. For each lepton and quark there is a corresponding anti-particle. All the mass values are taken from Ref. [9]. The u-, d-, and s-quark masses are estimates of the so-called current-quark masses, in a mass-independent subtraction scheme such as $\overline{MS}$ at a scale $\mu \approx 2$ GeV. The c- and b-quark masses are the running masses in the $\overline{MS}$ scheme [6, 7]. The t-quark mass comes from direct measurements.

The top quark is the elementary particle with the highest mass and has a very short lifetime of about $5{\times}10^{-25}$ s. No top bound state can be observed, as it immediately decays in a W boson and a b quark through weak interaction, with a branching ratio of about 100%.

In addition to the fermions, the SM predict the existence of vector bosons, mediating the interactions, and a scalar Higgs boson. The bosonic sector of the SM is summarized in Table 2.2, showing the interaction they mediate, their mass, their electric charge and their spin. The photon is the mediator of the electromagnetic interaction, is electrically neutral (therefore is its own antiparticle) and is massless. Three massive vector bosons, the electrically neutral Z^0 and the charged $W^\pm$, are responsible for the weak interaction. The gluons, g, are massless and they are the mediators of the strong interaction. Gluons carry the color charge themselves and can therefore interact with each other. Finally, the scalar Higgs boson is the last particle which found a place in the SM, as it will be described in Section 2.1.4.

Mediator	Mass [GeV]	Interaction	Electric charge (Q/e)	Spin
Gluon ($\times 8$) (g)	0	Strong	0	1
Photon (γ)	0	EM	0	1
Z	91.1876 ± 0.0021	Weak (neutral)	0	1
$W^\pm$	80.385 ± 0.015	Weak (charged)	± 1	1
Higgs (H)	125.09 ± 0.24	-	0	0

Table 2.2: Classification of the bosonic sector in the Standard Model. All the mass values are taken from Ref. [9].

2.1.2 Quantum electrodynamics

Quantum electrodynamics (QED) is the quantum field theory of the electromagnetic interaction and was developed at the turn of the 1940s and the 1950s by Feynman, Schwinger and Tomonaga. It can be obtained from classical electrodynamics by quantizing the Maxwell equations for the electrical and magnetic fields.

The starting point of this gauge theory is the Dirac equation of motion for fermions. Denoting with Ψ a spinor representing a matter field, with $\bar{\Psi}$ its adjoint, with γ_μ (μ =1,2,3,4) the Dirac matrices and with m the mass of the fermion, one can write the Lagrangian for a free fermion as

$$\mathcal{L}_{free} = \bar{\Psi}(i\gamma_\mu \partial^\mu - m)\Psi. \tag{2.1}$$

The QED Lagrangian can be obtained by promoting the invariance of the free Lagrangian under global gauge transformations of the Dirac field, $\Psi \rightarrow e^{i\alpha}\Psi$, to the invariance under local gauge transformations, $\Psi \rightarrow e^{i\alpha(x)}\Psi$. In order to do this, one has to introduce a gauge field, A_μ, and transforming the partial derivative in a covariant derivative including the new field A_μ and the coupling constant e:

$$\partial^\mu \rightarrow D_\mu = \partial^\mu - ieA_\mu. \tag{2.2}$$

A kinetic term has to be added for the new field A_μ, which has the the form of $F_{\mu\nu}F^{\mu\nu}$, where $F_{\mu\nu} \equiv \partial_\mu A_\nu - \partial_\nu A_\mu$. The QED Lagrangian can finally be written as:

$$\mathcal{L}_{QED} = \mathcal{L}_{free} + e\bar{\Psi}\gamma_\mu A^\mu \Psi - \frac{1}{4}F_{\mu\nu}F^{\mu\nu}, \tag{2.3}$$

where the second term describes the interaction between the Dirac field and A_μ. The coupling constant e has the interpretation of the electric charge of the field Ψ, which in QED represents the electron. The spin-1 field A_μ can be associated with the photon, which appears as a consequence of the requirement of the local gauge invariance.

QED represents the prototype gauge field theory, with an internal gauge symmetry, $U(1)$, which results into local gauge invariance with the electric charge e as the quantity conserved, according to Noether's theorem [10].

The electric charge is usually written in terms of the dimensionless ratio α, known as the fine structure constant:

$$\alpha = \frac{e^2}{4\pi\hbar c} \approx \frac{1}{137}. \tag{2.4}$$

Setting $\hbar = c = 1$, one has $e = \sqrt{4\pi\alpha} \approx 0.3$. For this reason, α can be regarded as the QED coupling constant.

2.1.3 Electroweak theory

Quantum electrodynamics and the theory of weak interactions, the latter developed from Fermi's effective field theory of the β-decay [11], are included into a more general framework, the electroweak theory, which describes simultaneously the electromagnetic and weak interactions, seen as two manifestations of the same fundamental interaction. In particular, QED and the weak theory can be seen as the low energy limits of the unified theory.

The starting point which lead to the formulation of the electroweak theory can be seen in the impossibility of calculating reliably loop diagrams in Fermi's theory, due to the fact that it was not renormalizable. A solution to this problem was found by Glashow, Salam and Weinberg in the 1960s by unifying the two interactions.

The symmetry group of the electroweak theory is $\mathrm{SU(2)_L} \otimes \mathrm{U(1)_Y}$. $\mathrm{SU(2)_L}$ is the symmetry group of the charged current processes, mediated by the $W^{\pm}$ bosons. In this type of processes, the interaction only affects the left-handed fermions (right-handed anti-fermions), where the left and right chiral components of a spinor field $\Psi = \Psi_L + \Psi_R$ can be defined as $\Psi_{L/R} = {}^1\!/_2(1 \mp \gamma^5\Psi)$, with $\gamma^5 = i\gamma^0\gamma^1\gamma^2\gamma^3$. A new quantum number called weak isospin, T_3, is introduced. This number is associated to the different spin-like multiplets and is conserved in weak interactions. Charged current interactions transform the left-handed fermions as doublets and right-handed fermions as singlets:

$$\begin{aligned} f_L^i &= \begin{pmatrix} \nu_L^i \\ \ell_L^i \end{pmatrix}, \begin{pmatrix} u_L^i \\ d_L^i \end{pmatrix} \\ f_R^i &= \ell_R^i,\ u_R^i,\ d_R^i \end{aligned} \tag{2.5}$$

where $i = 1, 2, 3$ is the family (generation) index. The same scheme can be applied to the quark families, so that an up-type quark can be transformed into a down-type quark violating the quark flavour quantum number.

The $\mathrm{U(1)_Y}$ part of the symmetry group is based on the concept of hypercharge, defined from the electric charge of the fermion and its weak isospin as $Q = T_3 + Y/2$.

Similarly to the case of QED, it is possible to obtain the SM electroweak Lagrangian by requiring invariance under local gauge group transformations and introducing the covariant derivative:

$$\nabla_\mu \equiv \partial_\mu - ig\vec{T} \cdot \vec{W}_\mu - ig'\frac{Y}{2}B_\mu, \tag{2.6}$$

where g and g' are the coupling constant of the $\mathrm{SU(2)_L}$ and $\mathrm{U(1)_Y}$ gauge groups, respectively, and new vector boson fields (the Yang-Mills fields) are introduced. The fields $\vec{W}_\mu \equiv (W_\mu^1, W_\mu^2, W_\mu^3)$ are the gauge vector bosons of the $\mathrm{SU(2)_L}$ group and belong to an isospin vector, while B_μ is the gauge boson of the $\mathrm{U(1)_Y}$ group and is an isospin scalar. The new gauge bosons are massless, in order to keep the theory invariant under gauge transformations, in contrast with experimental observations which point to massive vector

bosons. A mechanism needs to be introduced in order to generate non-zero masses while preserving the consistency of the theory at high energies, as it will be described in the following section.

The $W^{\pm}$ bosons can be obtained from a linear combination of W^1_μ and W^2_μ, with $T_3 = \pm 1$ as

$$W^{\pm}_\mu = \frac{1}{\sqrt{2}}(W^1_\mu \mp iW^2_\mu). \tag{2.7}$$

From the combination of the neutral fields W^0_μ and B_μ, both with $T_3 = 0$, one can obtain the real fields propagators A_μ and Z^0_μ, after introducing the weak mixing angle, also known as the Weinberg angle:

$$\begin{pmatrix} Z^0_\mu \\ A^0_\mu \end{pmatrix} = \begin{pmatrix} cos\theta_W & -sin\theta_W \\ sin\theta_W & cos\theta_W \end{pmatrix} \begin{pmatrix} W^3_\mu \\ B^0_\mu \end{pmatrix} \tag{2.8}$$

The Weinberg angle is a free parameter of the theory and has to be determined experimentally. The most recent value, obtained by electroweak processes near the Z-pole, is $\sin^2\theta = 0.23155 \pm 0.0005$ [9].

From Eq. 2.8, it follows that that the Z boson, being a mixture of W^3_μ and B^0_μ, interacts with both the left- and right-handed components of the fermions.

The following relation between the couplings g, g', the Weinberg angle and the electron charge e holds:

$$\frac{g}{sin\theta_W} = \frac{g'}{cos\theta_W} = e. \tag{2.9}$$

2.1.4 The Higgs mechanism

The electroweak theory, based on the $\mathrm{SU(2)_L} \otimes \mathrm{U(1)_Y}$ symmetry group, is successful in creating the four mediators of the electroweak interaction, but both the mediators and the matter fields remain massless. The particle masses need to be introduced in a way that preserves the gauge invariance of the Lagrangian, in order to keep the theory renormalizable. A way to achieve this is provided by the so called Higgs mechanism, which was proposed in 1964 by Higgs and Englert. The goal can be achieved with the spontaneous symmetry breaking from $\mathrm{SU(3)_C} \otimes \mathrm{SU(2)_L} \otimes \mathrm{U(1)_Y}$ to $\mathrm{SU(3)_C} \otimes \mathrm{U(1)_Q}$, which results in the introduction of a massive scalar boson in the theory, the Higgs boson. The latter has been for several years the missing piece of the SM required to complete the theory and make it consistent with the experimental observations of the bosons and fermions masses.

On July 4^{th} 2012, the ATLAS and CMS Collaborations announced the discovery of a particle consistent with the SM Higgs boson, with a mass of about 125 GeV [12, 13] and, more recently, provided a precise measurement of its mass [14].

In order to realize the spontaneous symmetry breaking, an isospin doublet of complex

scalar fields, called the Higgs field Φ, has to be introduced:

$$\Phi = \begin{pmatrix} \phi^+ \\ \phi^0 \end{pmatrix}, \tag{2.10}$$

where "+" and "0" indicate the electric charge of the field. Imposing gauge invariance, the Higgs field can be described by the a Lagrangian of this kind:

$$\mathcal{L}_{Higgs} = D^\mu \Phi^\dagger D_\mu \Phi - V(\Phi), \tag{2.11}$$

where

$$V(\Phi) = \mu^2 \Phi^\dagger \Phi - \lambda (\Phi^\dagger \Phi)^2, \ \lambda \in \Re \tag{2.12}$$

The covariant derivative is defined in Eq. 2.2. Assuming $\lambda > 0$ and $\mu^2 < 0$, the potential $V(\Phi)$ has a minimum along the circumference $(-\mu^2/2\lambda)^{1/2} e^{i\theta}$ ($\theta \in [0, 2\pi]$). Therefore the state of minimum energy, the vacuum state, is degenerate and the spontaneous symmetry breaking occurs when one of these minimum states is explicitly chosen. In order to keep the photon massless, the symmetry is chosen to be broken in a way that the Higgs component with zero electric charge is the one acquiring a non-zero vacuum expectation value (VEV):

$$\Phi_0 \equiv \langle 0|\Phi|0\rangle = \begin{pmatrix} 0 \\ \frac{v}{\sqrt{2}} \end{pmatrix}, \tag{2.13}$$

where

$$v = \left(-\frac{\mu^2}{2\lambda}\right)^{1/2} > 0 \tag{2.14}$$

After this choice of the VEV, the Higgs field can be redefined as a small oscillation around the minimum, because of local gauge invariance:

$$\Phi(x) = \frac{1}{\sqrt{2}} \begin{pmatrix} 0 \\ v + h(x) \end{pmatrix}, \tag{2.15}$$

By replacing this field in the Lagrangian, one can compute the interaction terms between the Higgs field and the vector bosons and extract the tree level predictions for their masses, which turn out to be:

$$m_W = \frac{vg}{2} \tag{2.16}$$

$$m_Z = v\frac{\sqrt{g^2 + g'^2}}{2}, \tag{2.17}$$

where the Z boson is identified as

$$Z_\mu = \frac{gW_\mu^3 - g'B_\mu}{\sqrt{g^2 + g'^2}} \tag{2.18}$$

by combining Eq. 2.8 and Eq. 2.9. The mass of the Higgs boson is found to be $m_H = \sqrt{2}\mu = \sqrt{2\lambda}v$.

Finally, the mass of the fermions has to be introduced in the theory. In order to do this, a new term is added to the Lagrangian, which describes the interactions between the Higgs field and the fermion fields via the matrices λ_f:

$$\mathcal{L}_{Yukawa} = \sum_{f=l,q} \lambda_f \left[\bar{f}_L \Phi f_R + \bar{f}_R \bar{\Phi} f_L\right]. \tag{2.19}$$

The gauge invariance of the Yukawa Lagrangian is guaranteed from the fact that the combinations $\bar{f}_L \Phi f_R$ and $\bar{f}_R \bar{\Phi} f_L$ are $SU(2)_L$ singlets. The tree level predictions for the mass of the fermions f can be obtained by introducing the expansion from Equation 2.15 in the Yukawa Lagrangian:

$$m_f = \lambda_f \frac{v}{\sqrt{2}}. \tag{2.20}$$

The strength of the coupling with the Higgs boson is proportional to the mass of the interacting particle.

2.1.5 Quantum chromodynamics

Quantum chromodynamics (QCD) is the quantum field theory describing the strong interaction and responsible to confine the quarks in the hadrons. The gauge symmetry group of QCD is $\mathrm{SU(3)_C}$ where color is introduced as a new quantum number. Color refers to three different possible states of the quark, by convention indicated with blue, red and green. The eight generators of the group are the Gell-Mann matrices λ^α ($\alpha = 1, ..., 8$), corresponding to eight mediator vector bosons, the gluons, which are massless and carry a color charge themselves, thus allowing self-couplings.

Once again, the QCD Lagrangian can be obtained by promoting the global gauge symmetry to a local one and introducing the covariant derivative:

$$\nabla_\mu \equiv \partial_\mu - i g_s \left(\frac{\lambda_\alpha}{2}\right) A^\alpha_\mu \tag{2.21}$$

where g_s is the strong coupling constant and A^α_μ are the gluon fields.

The QCD Lagrangian can be written as

$$\mathcal{L}_{\mathrm{QCD}} = \sum_f \bar{q}_f(x) \left(i\gamma^\mu \nabla_\mu - m_{q_f}\right) q_f(x) - \frac{1}{4} F^\alpha_{\mu\nu} F^{\alpha\,\mu\nu}, \tag{2.22}$$

where q_f is a color triplet of quarks with flavour f and the field tensor $F^\alpha_{\mu\nu}$ is given by

$$F^\alpha_{\mu\nu} = \partial_\mu A^\alpha_\nu - \partial_\nu A^\alpha_\mu - g_s f_{\alpha\beta\delta} A^\beta_\mu A^\delta_\nu. \tag{2.23}$$

In Eq. 2.23, $f_{\alpha\beta\delta}$ are the structure constants of the $SU(3)_C$ group and the third term represents the self-interaction of the gluon.

The QCD coupling strength, usually referred as $\alpha_s \equiv g_s^2/4\pi$, varies with the energy scale of the interaction. In particular, it is small at high energies (or equivalently at short distances) and increases at low energies (large distances), as it can be seen in Figure 2.1. This behavior has been verified in deep inelastic scattering experiments. As a consequence of this, one finds the two most remarkable properties of QCD: asymptotic freedom and color confinement, meaning that isolated free quarks cannot exist in nature. At high energies, in the asymptotic freedom regime, QCD can be described with perturbative theory.

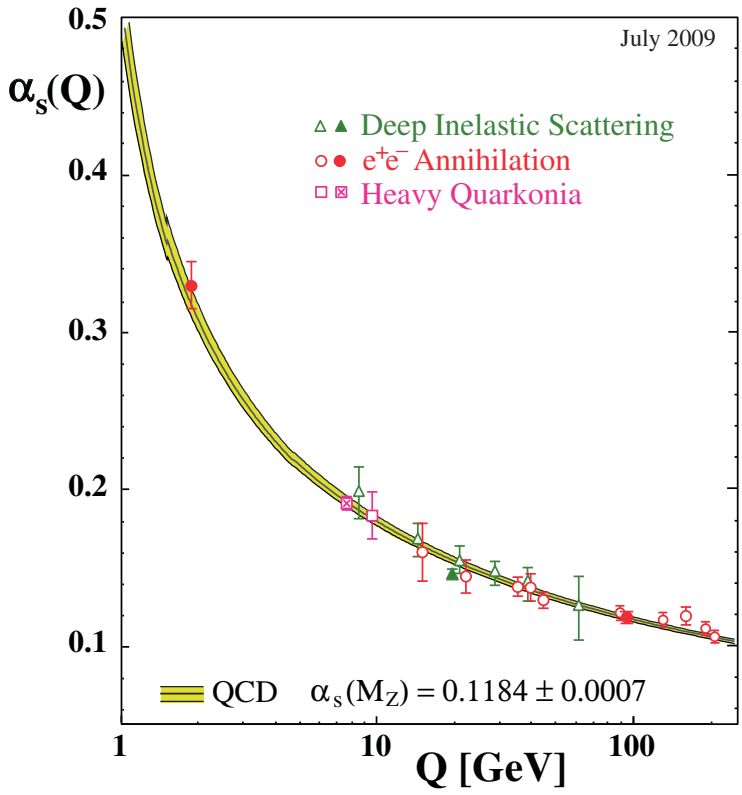

Figure 2.1: Measurement of $\alpha_s(Q)$ taken from Ref. [15].

When perturbative QCD (pQCD) can be used, the QCD running coupling strength can be expressed as:

$$\alpha_s(Q^2) = \frac{\alpha_s(\mu^2)}{1 + \left(\frac{\alpha_s(\mu^2)}{12\pi}\right)(11n_c - 2n_f)\left(ln\frac{Q^2}{\mu 2}\right)}, \tag{2.24}$$

where Q is the momentum scale at which the coupling strength is computed, n_c is the number of colors, n_f is the number of flavors taking part in the interaction (which can be up to six in the SM) and μ^2 is a reference scale at which the value of α_s is known and is often taken as the Z boson mass ($\alpha_s(M_Z^2) = 0.1185 \pm 0.0006$). The QCD coupling strength is a renormalizable quantity which depends on the energy scale used for the renormalization. This is an unphysical energy scale which is generally chosen to be close to the momentum scale of the studied interaction.

Instead of μ^2, a new parameter, Λ_{QCD}, can be defined as an intrinsic QCD scale where the strong coupling constant diverges. The experimental value for Λ_{QCD} corresponds to 100 MeV$< \Lambda_{QCD} <$500 MeV. Then $\alpha_s(Q^2)$ can be written as

$$\alpha_s(Q^2) = \frac{12\pi}{\big(11n_c - 2n_f\big)ln\left(\frac{Q^2}{\Lambda_{QCD}^2}\right)}. \tag{2.25}$$

From this expression, one can easily see that that α_s becomes large for energy scales of the order of Λ_{QCD}^2, while the asymptotic freedom is reached when $Q^2 \gg \Lambda_{QCD}^2$ and α_s becomes small.

The dependence of the coupling strength from the energy scale of the interaction is not exclusive of QCD, but holds also for the other interactions of the SM. What is peculiar of QCD, is the way the coupling constant evolves with the energy scale. For example, the evolution of the coupling strength of QED with the energy scale Q can be written as:

$$\alpha(Q^2) = \frac{\alpha(\mu^2)}{1 - \alpha(\mu^2)\frac{z_f}{3\pi}ln(-Q^2/\mu^2)}, \tag{2.26}$$

where $z_f = \sum_f Q_f^2$ is the sum over the active fermions and anti-fermions charges (in units of e) and μ is a reference scale. It can be seen that, contrarily to the QCD case, the QED coupling constant increases with the energy scale. Typical choices of μ in QED are $\mu \approx 1$ MeV, resulting in $\alpha \approx 1/137$, or $\mu = M_Z$, resulting in $\alpha(M_Z) \approx 1/129$. It turns out that the effect of the running QED coupling constant is very small and can safely be neglected at atomic or nuclear scales (at relatively low p_T).

2.2 Beyond the Standard Model: Supersymmetry

This section will start with a brief description of the reasons which motivate the existence of an extension of the Standard Model at high energies. An overview of Supersymmetry will then be given, mostly focusing on the Minimal Supersymmetric Standard Model, which represents the SM extension considered for the searches presented in this thesis, and its phenomenology at hadron colliders. A more complete presentation of SUSY, including its algebra and the derivation of its Lagrangian, can be found in Refs. [16–18].

2.2.1 Reasons for going beyond the Standard Model

The Standard Model represents so far the most successful theory of particle physics, providing very accurate predictions of the particles properties, confirmed by a large amount of experimental evidence. There is however a series of physical arguments which motivate the existence of a theory which extends the SM at higher energies.

First of all, gravity does not find a description within the Standard Model. A new theory would therefore be required at the reduced Planck scale, $M_P = (8\pi G_{Newton})^{-1} = 2.4 \times 10^{18}$ GeV, where gravitational effects become non negligible. Moreover, following the success of the electroweak unification, it would be desirable to achieve also an unification of the electroweak and strong interactions in the framework of a Grand Unified Theory (GUT) [19]. In the SM it is not possible to achieve the unification of the gauge coupling constants, as it can be seen in Figure 2.2 (left). Here the running of the inverse of the coupling constants is shown, as a function of the energy of the interaction, for the $\mathrm{U(1)_Y}$ symmetry group (α_1), for the $\mathrm{SU(2)_L}$ symmetry group (α_2) and for the $\mathrm{SU(3)_C}$ symmetry group (α_3). If one considers a minimal supersymmetric extension of the SM, which will be illustrated in the following section, the gauge coupling unification can be obtained at an energy scale of about 10^{16} GeV, as it can be seen in Figure 2.2 (right).

Another indication pointing to new physics is represented by the so called *hierarchy problem*, which can be regarded as a consequence of the very large ratio M_P/M_W. As it was seen in Section 2.1.4, the tree level prediction for the Higgs boson is found to be $m_H = \sqrt{2}\mu = \sqrt{2\lambda}v$. However, in the SM the mass of a scalar particle can get large radiative corrections. Differently from fermions and vector bosons, in fact, spin-0 fields are not protected by any chiral or gauge symmetries against acquiring large masses through radiative corrections.

The first order loop corrections diagrams to the μ^2 parameter are shown in Figure 2.3 for a fermionic and a scalar particle loop.

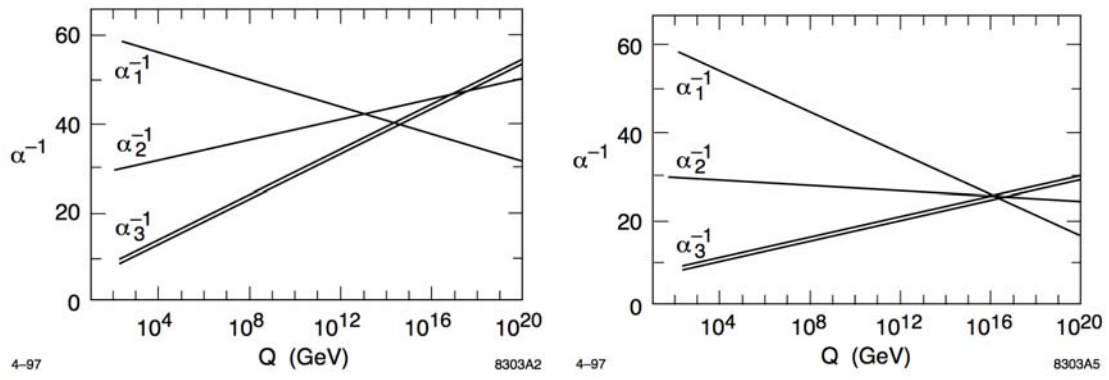

Figure 2.2: The running of the inverse of the coupling constants in the SM and in a minimal supersymmetric extension of the SM. The coupling constant α_1 corresponds to the $U(1)_Y$ symmetry group, α_2 to $SU(2)_L$ and α_3 to $SU(3)_C$ [20].

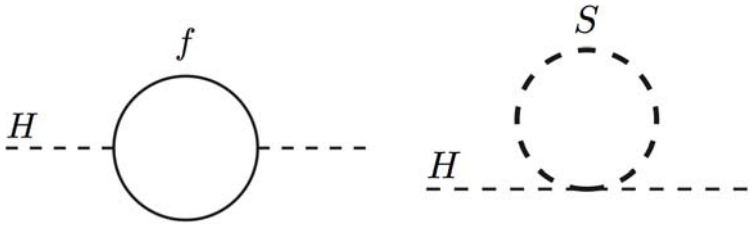

Figure 2.3: One-loop quantum corrections to the Higgs squared mass parameter due to a fermion (left) and to a scalar particle (right).

By denoting the tree level contribution to the squared mass parameter as μ_0^2 and including the first order quantum corrections from the fermionic and the scalar loop one has:

$$\mu^2 = \mu_0^2 - \frac{\lambda_s}{16\pi^2}\Lambda_{cutoff}^2 + \frac{k y_f^2}{8\pi^2}\Lambda_{cutoff}^2, \tag{2.27}$$

where λ_s represents the coupling of the Higgs boson with the scalar particle, y_f is the Yukawa coupling of the Higgs boson with the fermion, k is a color factor (1 for leptons and 3 for quarks), and Λ_{cutoff} is a cutoff scale which is introduced in order to regularize the otherwise divergent corrections. The latter can be interpreted as the energy scale at which new physics enters and the SM ceases to be valid and an upper bound to Λ_{cutoff} is represented by the Planck mass.

The Higgs boson mass is known to be $m_H \cong 125$ GeV. This small value of the Higgs boson mass represents a problem, because it implies that the quantum corrections to the squared mass parameter could be as big as 30 order of magnitudes. An enormous, unnatural fine tuning would be required to recover the value of the measured Higgs boson mass. Moreover, this problem also affects all the particles that acquire their masses through spontaneous electroweak symmetry breaking, such as the W and Z bosons, the

quarks and the charged leptons.

This problem could be elegantly solved if, for each SM particle, another particle with spin differing by half a unit would exist. In this case, the corrections from fermion loops could be roughly canceled by the ones from scalar loops. This is exactly what happens in supersymmetric extensions of the SM, where the problem of the unnatural fine tuning is solved, as it will be explained in the next section.

As a final remark, it has become very clear, thanks to astronomical and cosmological observations, that ordinary matter only accounts for about the 5% of the observable universe. Studies on the Cosmic Microwave Background, as well as measurements of the rotational curves of the galaxies, hint to the presence of the so called Dark Matter [21], which does not found any candidate in the SM particle spectrum, and for which SUSY predicts a suitable candidate.

2.2.2 Overview of Supersymmetry

Among the various theories elaborated as potential extensions of the SM in the last 50 years, Supersymmetry (SUSY) is the one that gained the major attention from the experimental point of view. The reason for this is that SUSY provides elegant solutions to problems of the SM mentioned in the previous section.

The basic idea behind a Supersymmetric theory is a correspondence between fermions and bosons. The generator of SUSY transformations is the fermionic operator Q, which is an anti-commuting spinor with spin $1/2$ which transforms SM fermions into bosons and vice versa:

$$Q|\text{Boson}\rangle \propto |\text{Fermion}\rangle \quad \text{and} \quad Q|\text{Fermion}\rangle \propto |\text{Boson}\rangle \tag{2.28}$$

The hermitian conjugate of the Q operator, $Q^\dagger$, is also a symmetry generator, as spinors are intrinsically complex objects. These two operators satisfy the following commutation and anti-commutation rules, which relate them to the the four-momentum generator of spacetime translations P^μ:

$$\begin{aligned} &\{Q, Q^\dagger\} = P^\mu, \\ &\{Q, Q\} = \{Q^\dagger, Q^\dagger\} = 0, \\ &[P^\mu, Q] = [P^\mu, Q^\dagger] = 0 \end{aligned} \tag{2.29}$$

Supersymmetric particles are organized into supermultiplets, which are irreducible representations of the supersymmetry algebra. Each supermultiplet contains an equal number of fermion and boson degrees of freedom:

$$n_B = n_F \tag{2.30}$$

Fermions and bosons in a supermultiplet are transformed into one another by a combination of the Q and $Q^\dagger$ operators. From the first of Eq. 2.29 it follows that the Q and $Q^\dagger$ operators commute with the squared-mass operator P^2 and, therefore, particles belonging to the same supermultiplet must be mass degenerate. Moreover, Q and $Q^\dagger$ also commute with the generators of gauge transformations, thus resulting that particles in the same supermultiplet must share the same quantum numbers (electric charge, weak isospin, and color).
As it was said previously, supermultiplets must satisfy Eq. 2.30, which results in a set of possible irreducible combinations.

- *Chiral supermultiplets*, containing one Weyl fermion [2] with two helicity states and two real scalars, assembled in a complex scalar field.
- *Gauge supermultiplets*, containing one spin-1 vector boson, which has to be massless before the spontaneous symmetry breaking in order to keep the theory renormalizable and has two helicity states, and a massless spin-$1/2$ Weyl fermion with the same gauge transformation properties for left-handed and for right-handed components.
- In the case gravity is included and the spin-2 graviton is the gauge boson, with two helicity states, this would have a spin-$3/2$ superpartner called *gravitino*.

Each of the SM fundamental particles belong to either a chiral or gauge supermultiplet, and must have a superpartner with spin differing by half a unit. In particular, SM fermions belong to chiral supermultiplets, since only this type of supermultiplets can contain fermions whose left-handed helicity states transform differently than their right-handed states.

By convention, the spin-0 superpartners of the SM fermions are indicated by adding a s (for scalar) before their name and they are generically called squarks and sleptons. Both the left- and the right-handed components of the fermions have their own complex scalar partner. The spin-$1/2$ super partners of the SM bosons are called with their SM name followed by the suffix $-ino$ and are generally indicated as gauginos and higgsinos. Superpartners are indicated by superimposing a tilde to the SM particle symbol: for example, the superpartner of a left-handed SM fermion f_L is indicated with $\tilde{f}_L$ and analogously for the right handed part. In the case of sfermions, the helicity state simply indicates the helicity state of the fermion partner.

A supersymmetric theory requires the existence of two Higgs chiral supermultiplets. This is due to the fact that, with only one Higgs chiral supermultiplet, the electroweak gauge symmetry would suffer a triangular gauge anomaly [18]. Moreover, two different Higgs chiral supermultiplets with Y=$1/2$ and Y=-$1/2$ are needed to give mass to the up-type quarks and to the down-type quarks and to the charged leptons, respectively. Therefore,

[2] Weyl fermions are two-component spinors. They can be seen as the solutions of the Weyl equation, which represents a particular case of the Dirac equation for massless fields.

in SUSY one has two $SU(2)_L$-doublet complex scalar fields with $Y=\pm 1/2$, indicated with H_u and H_d, respectively.

Since none of the superpartners of the SM particles has been observed so far, SUSY must be a broken symmetry. Moreover, the symmetry breaking must be soft, meaning that it does not introduce quadratic divergent radiative corrections and their energy scales remain at the electroweak scale [22]. This requirement can be understood by thinking to the hierarchy problem introduced in Section 2.2.1. In Supersymmetry, two complex scalar fields are introduced for each SM fermion and this is exactly what is needed to cancel the quadratic divergent terms in Eq. 2.27, but only if a relation holds between the associated dimensionless couplings, of the type $\lambda_s = \mid \lambda_f \mid^2$. This is true if the symmetry is unbroken or in the case of a soft symmetry breaking.

2.2.3 The Minimal Supersymmetric Standard Model

The Minimal Supersymmetric Standard Model (MSSM) is the framework where the analysis described in Chapter 6 is carried out. In the MSSM a minimum number of additional particles are added and there are no additional gauge interactions. The MSSM Lagrangian is constructed by including all possible interaction terms that satisfy the $SU(3)_C \otimes SU(2)_L \otimes U(1)_Y$ gauge invariance. It can be written as the sum of a SUSY invariant term which contain all the gauge and Yukawa interactions terms, as well as interaction terms between SM particles and their superpartners, plus additional SUSY breaking terms:

$$\mathcal{L} = \mathcal{L}_{SUSY} + \mathcal{L}_{soft} \tag{2.31}$$

The particle content of the MSSM is summarized in Table 2.3 and Table 2.4, for the chiral and gauge supermultiplets, respectively. Similarly to the SM, no right-handed neutrinos are predicted in the MSSM, As already mentioned, two complex scalar Higgs doublets are required in SUSY, H_u and H_d, where the first couples only to up-type quarks and the second only to down-type quarks and charge leptons.

As for the SM, the Higgs scalar potential is introduced with the form:

$$\begin{aligned} V =& (|\mu|^2 + m_{H_u}^2)(|H_u^0|^2 + |H_u^+|^2) \\ &+ (|\mu|^2 + m_{H_d}^2)(|H_d^0|^2 + |H_d^-|^2) \\ &+ \left[b(H_u^+ H_d^- - H_u^0 H_d^0) + c.c.\right] \\ &+ \frac{1}{8}(g^2 + g'^2)(|H_u^0|^2 + |H_u^+|^2 - |H_d^0|^2 - |H_d^-|^2)^2 \\ &+ \frac{1}{2} g^2 \left|H_u^+ H_d^{0*} - H_u^0 H_d^{-*}\right|^2 \end{aligned} \tag{2.32}$$

Supermultiplet symbol	Spin-1/2	Spin-0	Name
Q_i	$(u_L,\ d_L)$	$(\tilde{u}_L,\ \tilde{d}_L)$	Squark
$\bar{u}_i$	$u_R^\dagger$	u_R^*	Squark
$\bar{d}_i$	$d_R^\dagger$	d_R^*	Squark
L_i	$(\nu_L,\ e_L)$	$(\tilde{\nu}_L,\ \tilde{e}_L)$	Slepton
$\bar{e}_i$	$e_R^\dagger$	e_R^*	Slepton
H_u	$(\tilde{H}_u^+,\ \tilde{H}_u^0)$	$(H_u^+,\ H_u^0)$	Higgsino
H_d	$(\tilde{H}_d^0,\ \tilde{H}_d^-)$	$(H_d^0,\ H_d^-)$	Higgsino

Table 2.3: List of chiral supermultiplets, represented by their gauge eigenstates. The index i, with i =1,2,3 represents the quark or lepton generation.

Gauge symmetry group	Spin-1	Spin-1/2	Name
$\mathrm{SU(3)_C}$	g	$\tilde{g}$	Gluinos
$\mathrm{SU(2)_L}$	$W^\pm$, W^3	$\tilde{W}^\pm$, $\tilde{W}^3$	Winos
$\mathrm{U(1)_Y}$	B^0	$\tilde{B}^0$	Bino

Table 2.4: List of SUSY gauge supermultiplets.

By requiring the potential to break the electroweak symmetry, both the Higgs doublets acquiring a non-zero VEV, v_u and v_d, which can be related to the Z boson mass and to the electroweak gauge couplings as

$$v_u^2 + v_d^2 \equiv v = \frac{2M_Z^2}{g^2 + g'^2} \approx (174\ \mathrm{GeV})^2, \tag{2.33}$$

where v is the VEV of the SM Higgs boson. The latter, together with the ratio between v_u and v_d, defined as

$$\tan\beta = \frac{v_u}{v_d}, \tag{2.34}$$

are generally used, instead of v_u and v_d.

The two Higgs doublets contain eight independent components: three of them are absorbed to give masses to the electroweak vector bosons through the electroweak symmetry breaking, while the other five are left as physical mass eigenstates and are denoted as h^0, H^0, A^0 and $H^\pm$. The first two, h^0 and H^0, are neutral CP-even scalars, A^0 is a neutral CP-odd scalar and $H^\pm$ are charged scalars. Their masses are computed at tree level by rotating the fields in the scalar potential so that the mass terms are diagonal, leading to:

$$\begin{aligned} m_{A_0}^2 &= \frac{2b}{\sin(2\beta)}, \\ m_{h_0,H_0}^2 &= \frac{1}{2}\left(m_{A_0}^2 + m_Z^2 \mp \sqrt{(m_{A_0}^2 - m_Z^2)^2 + 4m_Z^2 m_{A_0}^2 \sin^2(2\beta)}\right), \\ m_{H^\pm}^2 &= m_{A_0}^2 + m_W. \end{aligned} \tag{2.35}$$

While the masses of A^0, H^0 and $H^\pm$ can be arbitrarily large, it turns out that the mass of h^0 is bounded from above ($m_{h^0} < m_Z|\cos(2\beta)|$). The tree level formula has however to be modified by adding the radiative corrections (mostly from from top and stop loops), which can be very large [23].

After the electroweak symmetry breaking, the Higgsinos and electroweak gauginos mix with each other forming physical mass eigenstates. The neutral Higgsinos ($\tilde{H}_u^0$ and $\tilde{H}_u^0$) mix with neutral gauginos ($\tilde{B}^0$ and $\tilde{W}^3$) and form four mass eigenstates called neutralinos and indicated with $\tilde{\chi}_i^0$, with i=1, 2, 3, 4. By convention, the lightest neutralino is denoted as $\tilde{\chi}_1^0$. The charged Higgsinos ($\tilde{H}_u^+$ and $\tilde{H}_d^-$) mix with the winos ($\tilde{W}^\pm$) and form two mass eigenstates with electric charge ±1 called charginos and indicated as $\tilde{\chi}_i^\pm$, with i=1, 2. Gluinos do not mix, as they are an octet with color charge, differently from any of the other gauginos.

The mass expressions for the neutralinos, charginos and the gluinos at tree level can be obtained by diagonalizing the correspondent gauginos mass matrix in the gauge eigenstate basis and turn out to be:

$$\begin{aligned}
m_{\tilde{\chi}_1^0} &= M_1 - \frac{m_Z^2 s_W^2 (M_1 + \mu \sin 2\beta)}{\mu^2 - M_1^2} \\
m_{\tilde{\chi}_2^0} &= M_2 - \frac{m_W^2 (M_2 + \mu \sin 2\beta)}{\mu^2 - M_2^2} \\
m_{\tilde{\chi}_3^0}, m_{\tilde{\chi}_4^0} &= |\mu| + \frac{m_W^2 (I - \sin 2\beta(\mu + M_1 c_W^2 + M_2 s_W^2))}{2(\mu + M_1)(\mu + M_2)}, \\
& |\mu| + \frac{m_W^2 (I + \sin 2\beta(\mu - M_1 c_W^2 - M_2 s_W^2))}{2(\mu - M_1)(\mu - M_2)}
\end{aligned} \tag{2.36}$$

$$\begin{aligned}
m_{\tilde{\chi}_1^\pm}, m_{\tilde{\chi}_2^\pm} = \frac{1}{2}\Big(& |M_2|^2 + |\mu|^2 + 2m_W^2 \\
& \mp \sqrt{(|M_2|^2 + |\mu| + 2m_W^2)^2 - 4|\mu M_2 - m_W^2 \sin 2\beta|^2} \Big)
\end{aligned} \tag{2.37}$$

$$m_{\tilde{g}} = M_3, \tag{2.38}$$

where M_1, M_2 and M_3 are the gaugino mass terms coming from the MSSM soft Lagrangian and $I = \pm1$ is the sign of μ.

Squark gauge eigenstates also mix to form mass eigenstates. Ignoring inter-generational mixing, squark mass eigenstates are obtained by diagonalizing a series of 2×2 squark mass-squared matrices (one for each quark flavour) in the basis ($\tilde{q}_L$, $\tilde{q}_R$). These matrices have the form (as in Ref. [24]):

$$M_{\tilde{q}} = \begin{pmatrix} m_{\tilde{q}_L}^2 & A_q m_q \\ A_q m_q & m_{\tilde{q}_R}^2 \end{pmatrix}, \tag{2.39}$$

with

$$\begin{aligned} m^2_{\tilde{q}_L} &= M^2_{\tilde{Q}} + m^2_Z \cos 2\beta (T^q_{3L} - e_q \sin^2 \theta_W) + m^2_q, \\ m^2_{\tilde{q}_R} &= M^2_{\{\tilde{u},\tilde{d}\}} + e_q \sin^2 \theta_W + m^2_q, \\ A_q &= a_q - \{\cot\beta, \tan\beta\}, \end{aligned} \tag{2.40}$$

In these equations, e_q and T^q_3 are the electric charge and the third component of the weak isospin of the squark $\tilde{q}$, and m_q is the mass of the partner quark. $M_{\tilde{Q}}$, $M_{\tilde{u}}$ and $M_{\tilde{d}}$ are the soft SUSY breaking masses, and a_q are the trilinear couplings of the interaction terms between scalar particles, which are matrices with dimension of mass and come from the SUSY breaking part of the Lagrangian. An equivalent description holds for sleptons, in analogy to down-type squarks.

As one can see in Eq. 2.39, the off-diagonal terms of $M_{\tilde{q}}$ are proportional to the quark (slepton) mass. While these terms can be neglected for the squarks of the first two generations (and for all the sleptons with the exception of the stau), which can therefore be considered as mass degenerates, this cannot be done in the case of the squarks of the third generation (and for the stau). The left- and right-handed components of the top squark can be highly mixed due to the large value of its mass and the same can happen for the bottom squark (and the stau) for large values of $\tan\beta$. By diagonalizing $M_{\tilde{Q}}$ for stops and sbottoms one obtains the following mass eigenstates (and analogously for the stau):

$$m^2_{\tilde{q}_{1,2}} = \frac{1}{2}\left(m^2_{\tilde{q}_L} + m^2_{\tilde{q}_R} \mp \sqrt{\left(m^2_{\tilde{q}_L} - m^2_{\tilde{q}_R}\right)^2 + 4A^2_q m_q} \right). \tag{2.41}$$

for $\tilde{q}_1 = \tilde{t}_1, \tilde{b}_1$ and $\tilde{q}_2 = \tilde{t}_2, \tilde{b}_2$.

The properties of the squarks of the third generation are particularly interesting for SUSY, as it will be explained in Section 2.2.3.2, as well as for the context of this thesis.

In the SM there are strong experimental limits for processes violating the conservation of the lepton and baryon quantum numbers (L and B, respectively). One example is given by the stability of the proton. In the MSSM Lagrangian one could introduce gauge interaction terms, representing interactions between SM and SUSY particles, which would violate the B and L conservation. In order to overcome this problem a new symmetry, called R-parity, is introduced. The new symmetry provides a multiplicative conserved quantum number, which is defined from B and L and the spin s of the particle as:

$$P_R = (-1)^{3(B-L)-2s} \tag{2.42}$$

This new symmetry results in eliminating possible B and L violating terms from the MSSM Lagrangian. With this definition, all SM particles have $P_R = +1$, while SUSY particles have $P_R = -1$.

Assuming R-parity conservation translates into a series of important phenomenological consequences.

- SUSY particles can only be produced pair-wise at colliders.
- The lightest supersymmetric particle (LSP) must be stable and, if it is electrically neutral and only weakly interacting, it provides a good dark matter candidate. In the MSSM the LSP is often identified with the lightest neutralino χ_1^0.
- Each SUSY particle must decay in an odd number of SUSY particles. Following the previous point, this means that an odd number of LSPs will be produced at the end of a decay chain.

In the minimal supersymmetric extension the SM, assuming R-parity conservation, 105 new free parameters are added to the 19 free parameters of the SM [3], most of them coming from the soft SUSY breaking, for a total of 124 parameters to be determined. The free parameters of the MSSM are represented by the gaugino mass terms (M_1, M_2, M_3), the Higgs mass terms, the squared mass matrices of the chiral supermultiplets and the trilinear couplings a_q. The latter can be assumed to have non-negligible diagonal terms only for third-generation squarks, as it was seen in Section 2.2.3.

A possibility to reduce the number of free parameters of the MSSM is to assume some kind of mass unification at a high energy scale. This assumption is motivated by the fact that with SUSY the gauge coupling unification is achieved at an energy scale of $\sim 10^{16}$ GeV. Typically, all the scalar particles and the gauginos are required to be unified and have common mass values of m_0 and $m_{1/2}$, respectively. This can be seen in Figure 2.4, where the evolution of the scalar and gaugino mass parameters is shown as a function of the logarithm of the energy scale for a mSUGRA model (see next section). In this Figure, the solid lines labeled M_1, M_2 and M_3 are the running gaugino masses which unify at $m_{1/2}$. The dot-dashed lines labeled H_u and H_d are the running values of $(\mu^2 + H_u^2)^{1/2}$ and $(\mu^2 + H_d^2)^{1/2}$, which unify at $\mu^2 + m_0^2$. The other solid lines represent the running masses of the squarks and the sleptons of the first two generations, while the remaining dashed line represent the square roots of the third-generation parameters $m^2_{\bar{d}_3}$, $m^2_{Q_3}$, $m^2_{\bar{u}_3}$, $m^2_{L_3}$ and $m^2_{\bar{e}_3}$.

[3] The 19 free parameters of the Standard Model are the fermions and Higgs boson masses, the gauge coupling constants of the three fundamental interactions, the CKM mixing angle and the CP violating phase and the VEV of the Higgs field.

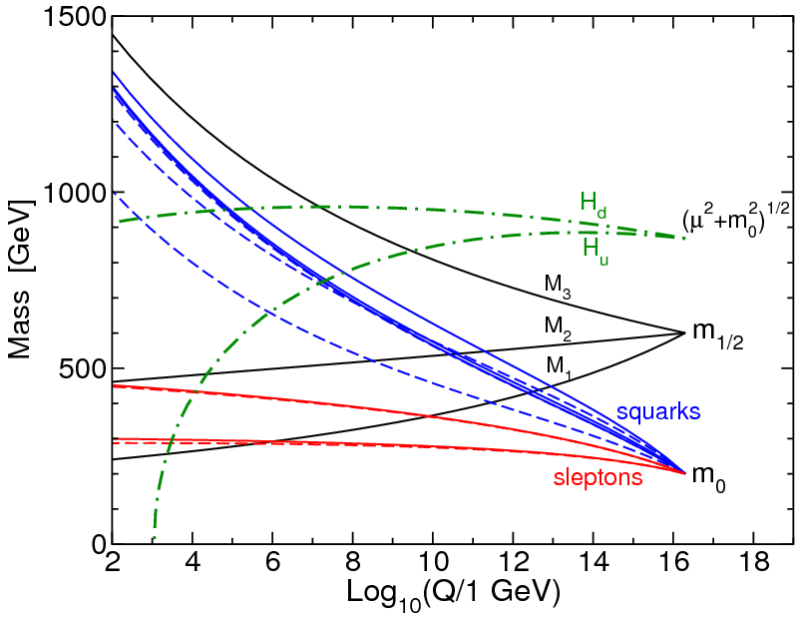

Figure 2.4: Evolution of the scalar and gaugino mass parameters as a function of the logarithm of the energy scale for a mSUGRA model [16]. More details are in the text.

2.2.3.1 Supersymmetry breaking

As it was already pointed out previously, the SUSY breaking must be soft [22], in order to be applicable to TeV-scale phenomena. However, there is no obvious way to break SUSY spontaneously. Generally it is assumed that SUSY breaking happens in a hidden sector, which consists of particles that are neutral with respect to the SM gauge group, and its effects are then transmitted to the MSSM particles by some messengers.

The two most popular theoretical models for the SUSY breaking are listed below.

- In the constrained MSSM, traditionally known as *minimum supergravity* (mSUGRA), it is assumed that the SUSY breaking in the hidden sector is transmitted to the visible sector by the gravitational interaction. In mSUGRA, one is left with only 5 free parameters, which are m_0, $m_{1/2}$, A_0, $\tan\beta$ and the sign of μ. A gravitino with mass $m_{3/2} \sim m_{Soft}$, where m_{Soft} is the scale of soft SUSY breaking, is also included in the model.

- In *gauge mediated symmetry breaking* (GMSB) models, the SUSY breaking is transmitted to the MSSM particles via ordinary gauge interactions. In these models the mass of the gravitino is not related to the soft breaking scale and is expected to be very light and is usually identified with the LSP.

Another possibility, which does not make any specific assumption on the SUSY breaking model, is that of using a phenomenological approach to study a more comprehensive subset of the MSSM. This approach is referred to as phenomenological MSSM (pMSSM)

and makes use of constrains derived from experimental data to reduce the number of free parameters.

A variety of simplified models [25] are considered in searches for Supersymmetry at the LHC. These models are very popular because they allow to focus on a given final state which has sensitivity at the LHC, without having to explore the full parameter space. Simplified models are generally used to test specific processes, where the particles of interest are decoupled from the rest of the MSSM spectrum, which is set to higher energy scales not accessible by the experiment. A large number of searches involving simplified models are performed at the LHC, and in particular at the ATLAS Experiment. In the context of this thesis, searches for squarks of the third generation are the most interesting and more details about these particles will be given in the following section.

2.2.3.2 Third-generation squarks

The naturalness principle [26] allows to set stringent constrains on the masses of the top and bottom squarks. Considering once more the first order radiative corrections to the Higgs squared mass parameter in Eq. 2.27, in SUSY the scalar partners of the SM fermions contribute to the corrections proportionally to the Yukawa couplings of the SM fermions. This contribution will be larger for the stop and the sbottom with respect to rest of the squarks. Therefore, by requiring these corrections to be at most of the same order of magnitude of m_h^2, one can set strong theoretical upper limits on the mass of the stop, which must be at the TeV-scale. The left-handed sbottom must also be light since it shares the same chiral supermultiplet with the left-handed stop. Therefore, searches for the squarks of the third generation represent an important instrument to probe natural SUSY.

Pairs of stop and sbottom particles can be produced at hadron colliders at lowest order in pQCD in quark-antiquark annihilation and gluon-gluon fusion. The leading order cross sections for these processes can be written as:

$$\begin{aligned}\sigma_{q\bar{q}\to\tilde{q}_k\bar{\tilde{q}}_k} &= \frac{\alpha_s^2\pi}{s}\frac{2}{27}\beta_k^3 \\ \sigma_{gg\to\tilde{q}_k\bar{\tilde{q}}_k} &= \frac{\alpha_s^2\pi}{s}\left\{\beta_k\left(\frac{5}{48}+\frac{31m_{\tilde{q}_k}^2}{24s}\right)+\left(\frac{2m_{\tilde{q}_k}^2}{3s}+\frac{m_{\tilde{q}_k}^4}{6s^2}\right)\log\left(\frac{1-\beta_k}{1+\beta_k}\right)\right\},\end{aligned} \tag{2.43}$$

where $k = 1, 2$, $\tilde{q} = \tilde{t}, \tilde{b}$ and $\beta_k = \sqrt{1 - 4m_{\tilde{q}_k/s}}$.

For the analysis described in Chapter 5 and Chapter 6, a simplified model for sbottom pair production with the sbottom decaying into a b-quark and a $\tilde{\chi}_1^0$ with a branching ratio of 100% will be considered. In this simplified model, the gluino as well as the first and second generations of squarks are considered very heavy and are decoupled from the model.

2.3 QCD phenomenology at hadron colliders

This section is devoted to give an overview of some relevant aspects of QCD phenomenology at hadron colliders, where it plays a crucial role. A comprehensive overview of QCD at colliders can be found in Refs. [27, 28].

2.3.1 QCD factorization

At the LHC, hadron interactions take place between colliding proton beams. Protons are composite objects and their dynamics, at energy scales close to their mass, is strongly non-perturbative. In most of the cases, the beam collisions result into soft elastic or inelastic proton scattering with small momentum transfer and perturbative QCD cannot be used to describe the processes. However, the interactions of interest happen at high momentum transfer scales Q^2. As it will be seen later, in such cases the interaction can be separated into a hard scattering process, which occurs between the constituents of the proton and can be computed with perturbative QCD, and a low energy process, which includes the non-perturbative contributions.

The partonic cross section $\hat{\sigma}_{a,b\to c}$ for the hard scattering is process dependent and can be computed with pQCD, where a and b represent the interacting partons (either quarks or gluons) and c is the final state resulting from the interaction. Due to the renormalization of α_s, the partonic cross section also depends the renormalization scale μ_R.

The parton distribution functions (PDFs) are used to relate the partons and the original protons. If A is the original incoming proton, the PDFs $f_{a/A}(x_a)$ represent the probability that a parton a with momentum fraction x_a is extracted from the original proton A.

The hadronic cross section for two objects A and B interacting to give the decay product X can be expressed as a convolution of the PDFs with the partonic cross section:

$$\sigma(A,B\to X) = \sum_{a,b}\int_0^1 dx_a \int_0^1 dx_b f_{a/A}(x_a,\mu_F^2) f_{b/B}(x_b,\mu_F^2) d\sigma_{a,b\to c}(x_a,x_b,\alpha_s(\mu_F^2,\mu_R^2,Q^2/\mu_F^2)) \tag{2.44}$$

As it can be seen in Eq. 2.44, the PDFs depend also on the factorization scale μ_F, which comes from the factorization theorem [29]. The latter holds for inclusive QCD processes and allows to factorize the hadronic cross section into short- and long-distance effects, where the factorization is delimited by μ_F. This means that, in Eq. 2.44, all high scale contributions are described by the partonic cross section, while all the contributions at lower scales, including non-perturbative ones, are absorbed into the PDFs.

Both the renormalization and the factorization scales are typically chosen to be of the

order energy scale Q^2 of the interaction under study.

Because of the non-perturbative contributions, the functional form of the PDFs for quarks and gluons need to be measured experimentally in lepton-hadron deep inelastic scattering experiments and in hadron-hadron collisions and for different values of Q^2. Previous high energy physics experiments, like those at the Tevatron and HERA, provided a lot of information about PDFs.

It is possible to predict the PDF evolution with Q^2 can be predicted using the DGLAP (Dokshitzer-Gribov-Lipatov-Altarelli-Parisi) equations [30]. At leading order, these equations can be derived from QCD vertices and can be expanded in powers of $\alpha_S(Q^2)$ and can be written as:

$$\frac{df_i(x,Q^2)}{dQ^2} = \sum_j \frac{\alpha_s(Q^2)}{2\pi} \int_x^1 \frac{dz}{z} P_{j\to i}(z) f_j(x/z, Q^2), \tag{2.45}$$

where $P_{j\to i}(z)$ are the so called splitting functions and represent the probability that a parton j radiates a parton i, carrying a fraction z of its longitudinal momentum.

The PDFs for the valence quarks of the proton, the gluon and the sea quarks can be seen in Figure 2.5 for two different values of Q^2. Several groups provide PDFs parametrizations from the results of experiments and measurements, such as CTEQ [31], CT10 [32], MSTW [33] and NNPDF [34]. The PDFs in Figure 2.5 were extracted by the NNPDF collaboration. From the same figure, one can see that the valence quarks dominate at large x, while the gluons and the sea quarks dominate at low x.

The calculation of the partonic cross section occurs through a perturbation expansion in the coupling constants and therefore it never leads to an exact values. Higher order corrections can be computed and, at the LHC, QCD corrections represent in general the most relevant ones. Examples of diagrams contributing to next-to-leading-order (NLO) QCD corrections to the vector boson quark-antiquark vertex are shown in Figure 2.6, with additional real or virtual radiation.

2.3.2 Monte Carlo simulation

Monte Carlo (MC) generators [36] are very important tools in high energy physics and are needed to simulate the complexity of hadron-hadron collisions. The description of the QCD phenomenology represents the biggest challenge of MC simulation at hadron colliders. The scheme of a MC simulated proton-proton collision event is shown in Figure 2.7. Here, the dotted circle H separates the contributions which can be described with perturbative QCD (hard process, initial and final state radiation) from non-perturbative contributions (parton shower, hadronization and underlying event). A brief overview of the main concepts behind MC simulation will be given in this section, together with a description of the main features of the MC generators that are used in the analysis presented in the thesis.

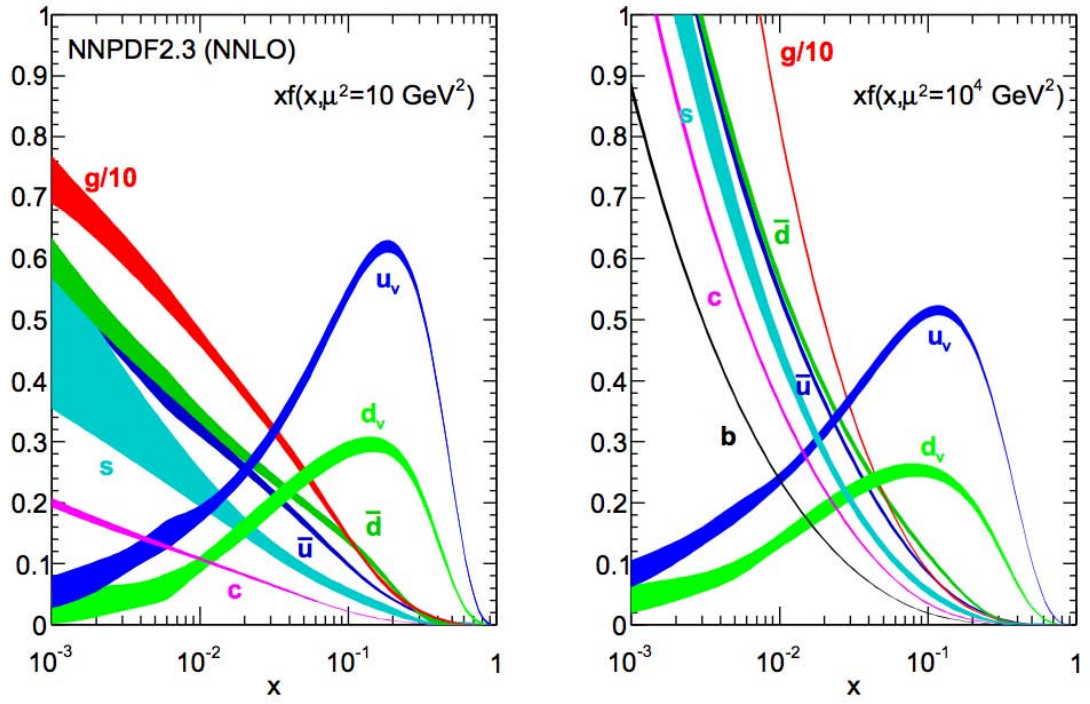

Figure 2.5: Distributions of the parton distribution functions $xf(x)$ obtained in NNLO `NNPDF2.3` global analysis at scales $\mu^2 = 10\,\mathrm{GeV}^2$ and $\mu^2 = 10^4\,\mathrm{GeV}^2$, with $\alpha_s(M_Z) = 0.118$. [35]

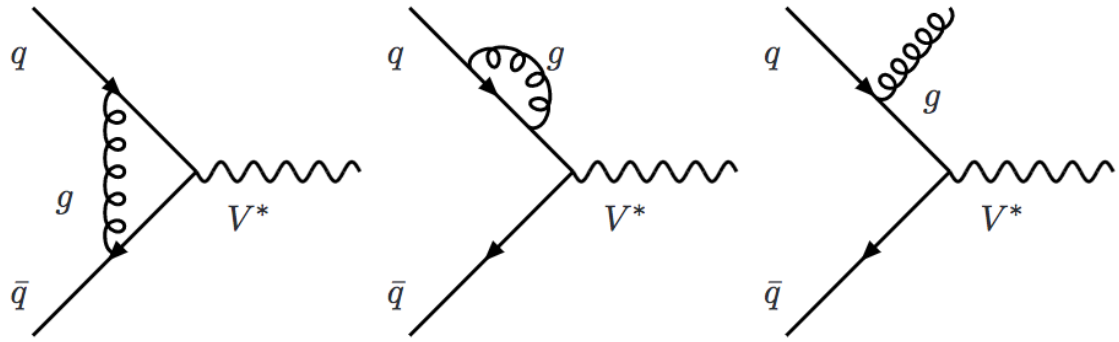

Figure 2.6: Diagrams contributing to NLO QCD corrections for the production of a vector boson from the interaction of two quarks.

2.3.2.1 Hard scattering process

The starting point of the MC generation for hadronic collisions is the theoretical calculation of the cross section of the hard scattering process, which can be done from Eq. 2.44. MC generators provide calculations of the cross section using pQCD for a fixed order in α_S. For most of the generators this calculation is only possible at LO for all $2\to N$ processes with $N \leq 6$. Calculations beyond LO exist only for a limited number of

generators and only for specific processes. Higher order corrections can be added to the pQCD calculation from the LO generator with the parton showering process.

It is a common procedure to define the k-factor as

$$k_{NLO} = \frac{\sigma_{NLO}}{\sigma_{LO}} \tag{2.46}$$

The k-factor is used as a multiplicative factor to the LO cross section, in cases where the generator can only provide the cross section at LO, but the theoretical calculation at NLO exists. This is typically a good approximation except in case of large real emission contributions. In analogy, NNLO k-factors can be defined.

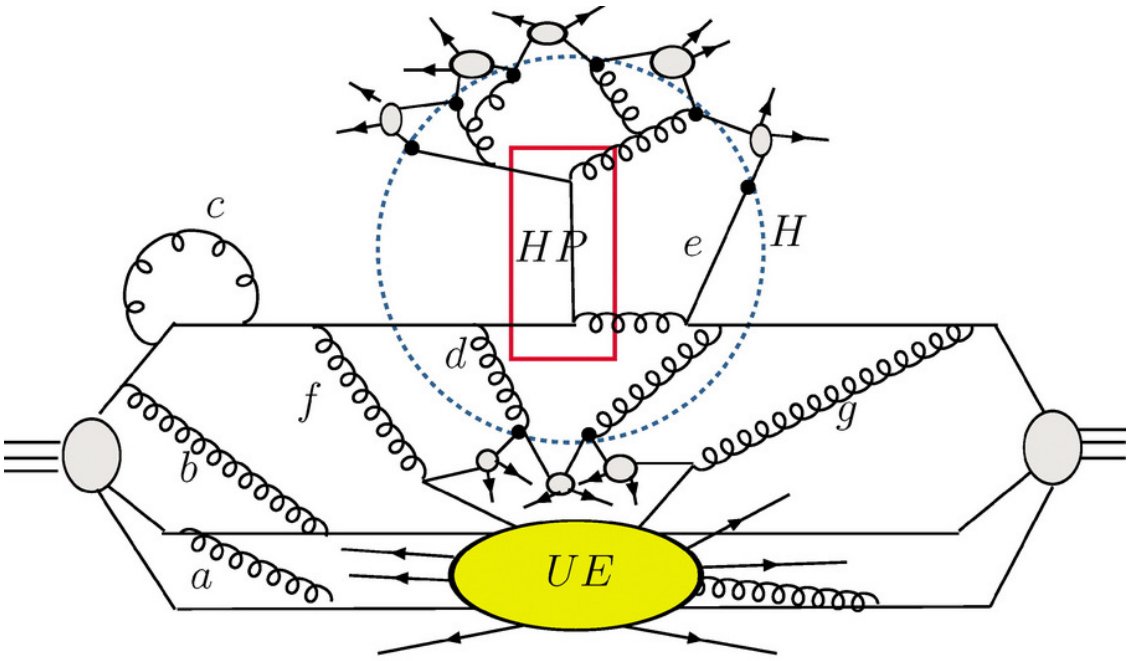

Figure 2.7: Scheme of the MC description of a hard proton-proton collision. HP denotes the hard process and UE is the underlying event [37].

2.3.2.2 Parton shower and hadronization

Final (or initial) state partons from the hard process can go through successive emission of quarks and gluons. This process is simulated using parton shower generators and is regulated by the DGLAP splitting functions calculated at LO, in the limit of small angle emission.

The probability for a parton to evolve from an initial scale Q_{start} to a splitting scale Q_{split} without radiating or branching is assessed using Sudakov form factors, which are weighted by the PDFs. The parton showering continues until the parton cascade reaches the Λ_{QCD} scale, below which the perturbative regime is not valid anymore. In the case of initial-state radiation the algorithm is applied backwards in time. As a consequence

of the parton showering process, the parton emitted in the hard scattering gives rise to several partons which are usually collimated in a cone around the direction of the original parton.

As it was already mentioned, in many cases the simulation of the hard process is at LO and additional radiation jets are added with the parton shower mechanism. However, such a procedure is generally non reliable if one requires a very hard and well separated jet, in which case the additional parton must be described by the matrix element itself. If the hard scattering is described with matrix elements, then a procedure is needed to remove the double-counting of events in some region of the phase-space when the hard scattering is matched to the parton shower. In order to remove this overlap, the phase space is separated into a region dominated by hard emission, where the matrix element provides a better description, and one dominated by soft emission, better described by the parton shower. This is done by introducing resolution parameters that distinguish between resolved and non-resolved jets. Different matching schemes exist, such as the Catani-Krauss-Kuhn-Webber (CKKW) [38] and the Michelangelo L. Mangano (MLM) [39] methods.

Once the Λ_{QCD} is reached, the partons recombine into color-singlet hadrons in a process called hadronization. The final hadrons can be used to define jets, with the aim of reproducing the kinematics of the original hard parton. These jets are called "particle level" jets. At the energy scale of hadronization, pQCD cannot be used anymore and different phenomenological models exist to describe this process, which are tuned with experimental data. The string model is based on string dynamics to describe the color flux between quarks. The strings breaks, producing a $q\bar{q}$ pair, when the string energy exceeds the mass of the $q\bar{q}$ pair. In the cluster model, first the gluons remaining from the parton shower are split in $q\bar{q}$ pairs. Color-singlet $q\bar{q}$ pairs then form clusters with the neighboring quarks and antiquarks, which then decay into pairs of hadrons, according to the available phase-space. A sketch of the strong and cluster hadronization models is shown in Figure 2.8.

After the hadronization, the resulting hadrons can decay according to standard branching ratios if unstable.

2.3.2.3 Underlying event and pileup

In a hadron-hadron collision additional interactions can occur among partons which are not involved in the hard scattering process. This type of interactions, called underlying event, happen at low transferred momentum, therefore perturbative theory cannot be used, and can also give contributions to the final state. There are several phenomenological models which describe the underlying event and rely massively on data. These models are used in combination with the matrix element and parton shower generators and are to large extent independent from the hard scattering description.

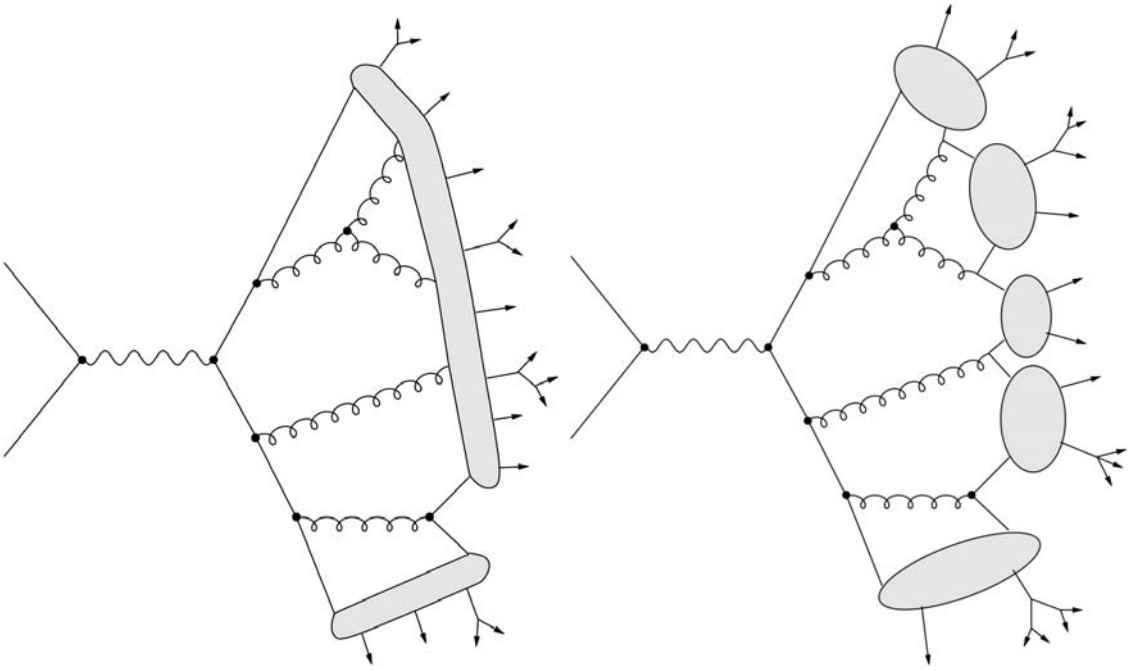

Figure 2.8: Parton shower followed by hadronization from the string (left) or cluster (right) models [27].

In order to give a full description of the MC event, one has to also take into account contributions due to the soft scattering of protons contained in the same bunches as the ones producing the hard scattering (in-time pileup) or belonging to different bunches (out-of-time pileup). The pileup is independent from the hard scattering process, is dominated by soft contributions, and is simulated using minimum bias event samples in MC overlaid with the main interaction. The pileup interactions are completely independent from the hard scattering process and are parametrized using the number of hadrons in each colliding bunch and the time separation between bunches.

2.3.2.4 Monte Carlo generators

Several MC event generators are available on the market and were used in the work documented in this thesis.

Pythia [40], Herwig [41, 42] and Sherpa [43] are general purpose MC event generators, which simulate a broad range of physics processes. They use leading order matrix elements and are able to simulate the full event chain, from the description of hard scattering to the addition of the underlying event. These generators can be used standalone or in combination with hard scattering generators which do not have parton showering or hadronization implemented. In this thesis, the Sherpa generator is used to simulate Z+jets and W+jets production.

Madgraph [44] is a multi-purpose event generator which only generates the LO ma-

trix element of the hard interaction for several processes. It is generally interfaced with PYTHIA for the parton showering, the hadronization and the underlying event. In this thesis, MADGRAPH was used to simulate the SUSY signals (see Section 6.1.5) and the associated production of a top quark pair with a W or Z boson.

POWHEG [45] is an event generator that use matrix elements at NLO in pQCD. In this thesis, it is used to simulate processes involving the production of a top quark, interfaced with PYTHIA for the modeling of the parton shower, hadronization and underlying event.

Chapter 3

The ATLAS detector at the LHC

Located at CERN, at the border between Switzerland and France, the Large Hadron Collider (LHC) is currently the world's largest proton-proton (pp) collider. It started its activity in 2010 and, after three years of operations at the unprecedented center-of-mass energies of 7 and 8 TeV, since 2015 it's colliding protons at $\sqrt{s}$ =13 TeV.
The results which will be presented in this thesis are obtained using data from pp collisions collected and reconstructed by the ATLAS (A Toroidal LHC ApparatuS) detector, one of the multipurpose experiments operating at the LHC and designed to investigate a broad range of physics scenarios from the study of pp collisions. The work performed for one of the ATLAS subdetectors, the Tile hadronic calorimeter, is described in Appendix B.

After a brief overview of the LHC complex, this chapter will describe the ATLAS detector.

3.1 The Large Hadron Collider

The LHC [46] is a two-ring superconducting hadron accelerator and collider situated in a 27.6 km long tunnel, originally built for the Large Electron-Positron (LEP) machine. The latter was an electron-positron collider operating between 1989 and 2000 at CERN and later dismantled to allow the preparation of the hadron collider.

The LHC has been designed to achieve a center-of-mass energy of $\sqrt{s} = 14$ TeV for pp collisions and a luminosity of 10^{34} cm^{-2}s^{-1}. Heavy ions (Pb-Pb) collisions with a center-of-mass energy of $\sqrt{s}_{NN} = 2.76$ TeV per nucleon can also occur, as well as proton-ion (p-Pb) collisions with $\sqrt{s}_{NN} = 5.02$ TeV.

An injection chain formed of different pre-accelerators (each of them existing before the LHC construction) supplies the LHC with protons, as illustrated in Figure 3.1. Protons are produced from a hydrogen gas source and pre-accelerated to an energy of 50 MeV with the LINAC 2. The proton beams are then injected in a series of pre-accelerators, before being transferred to the two beam pipes of the LHC, where they reach the final energy of 6.5 TeV: the Proton Synchrotron Booster (PSB) (where they reach 1.4 GeV),

the Proton Synchrotron (25 GeV) and the Super Proton Synchrotron (450 GeV). Details about the injection chain can be found in Ref. [47].

Operating since 2010, the LHC has delivered pp collisions at $\sqrt{s}$ =7 and 8 TeV in 2010-2011 and 2012, respectively, being this period referred as "Run-1". After two years of technical shutdown, the accelerator resumed the operations, delivering collisions at $\sqrt{s}$ =13 TeV in 2015. On the accelerator ring, proton beams collide in four interaction points.

Four main detectors have been built around the interaction points (ALICE [48], ATLAS [49], CMS [50] and LHCb [51]), each with a specific physics program. They are illustrated in Figure 3.1. The ATLAS detector will be described in the following sections.

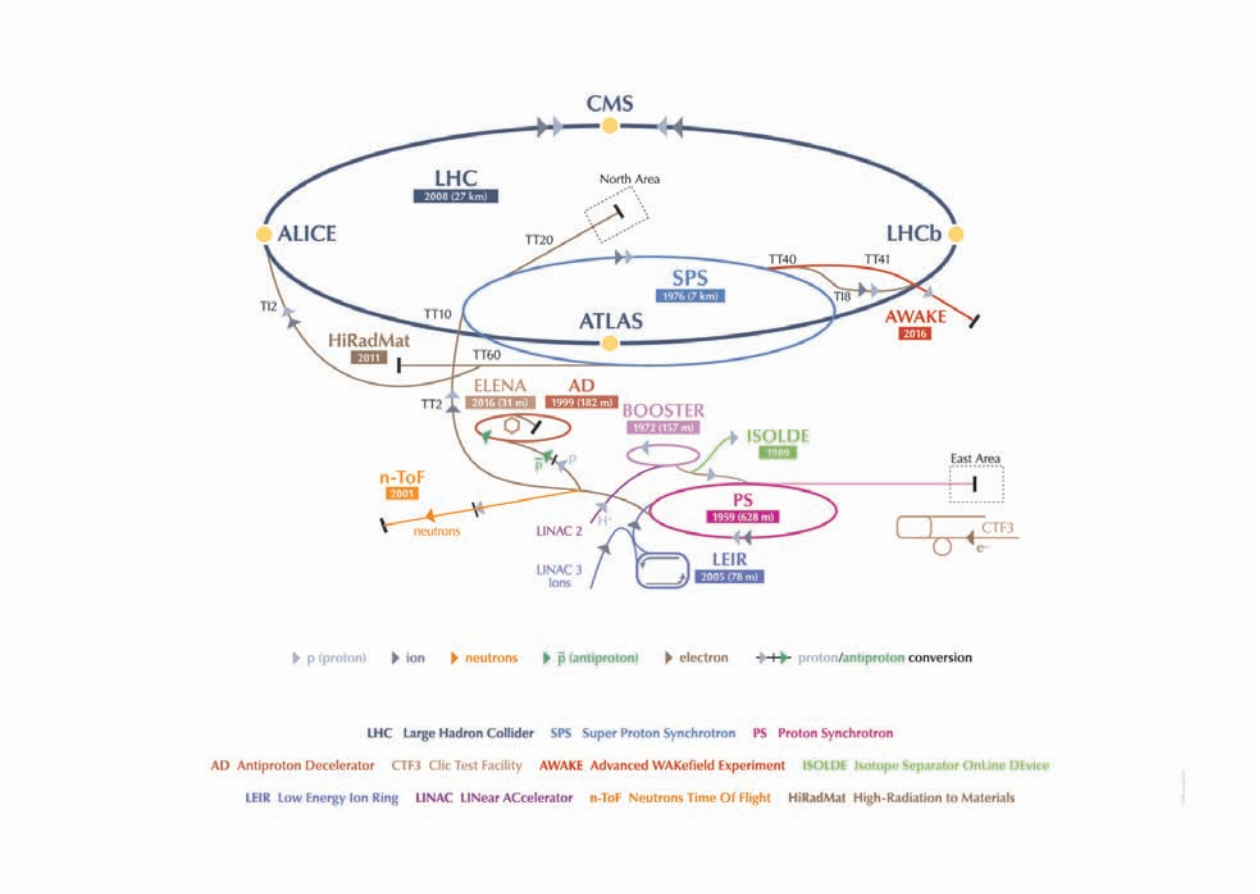

Figure 3.1: Representation of the CERN accelerator complex [52], necessary to inject protons in the LHC (dark blue). The four main experiments, ATLAS, CMS, ALICE and LHCb are indicated. Pre-accelerators (LINAC 2, BOOSTER, PS and SPS) together with heavy ions facilities and minor experiments are also shown.

3.2 The ATLAS detector

ATLAS (A Toroidal LHC ApparatuS) is one of the four multipurpose detectors operating at the LHC. It is 46 m long, 25 m in diameter, and weighs about 7000 t. The ATLAS detector is constituted of several subdetectors arranged concentrically around the beam axis, each of them playing a specific role in the reconstruction and identification of the decay products from pp collisions, namely electrons, muons, taus, photons, jets and missing transverse momentum. A detailed description of the ATLAS detector can be find in Ref. [49]. The structure of the ATLAS detector is shown in Figure 3.2.

Closest to the collision point, the Inner Detector (ID) is used for the reconstruction of the tracks coming from charged particles. The ID is included in a solenoidal magnetic field which is used for bending the particle trajectories. The calorimeter systems surround the ID and provide the containment of the electromagnetic and hadronic showers. Finally, muons are identified and reconstructed in the outermost muon spectrometer (MS), thanks to a toroidal magnetic field. The different components of ATLAS will be briefly described in the following paragraphs.

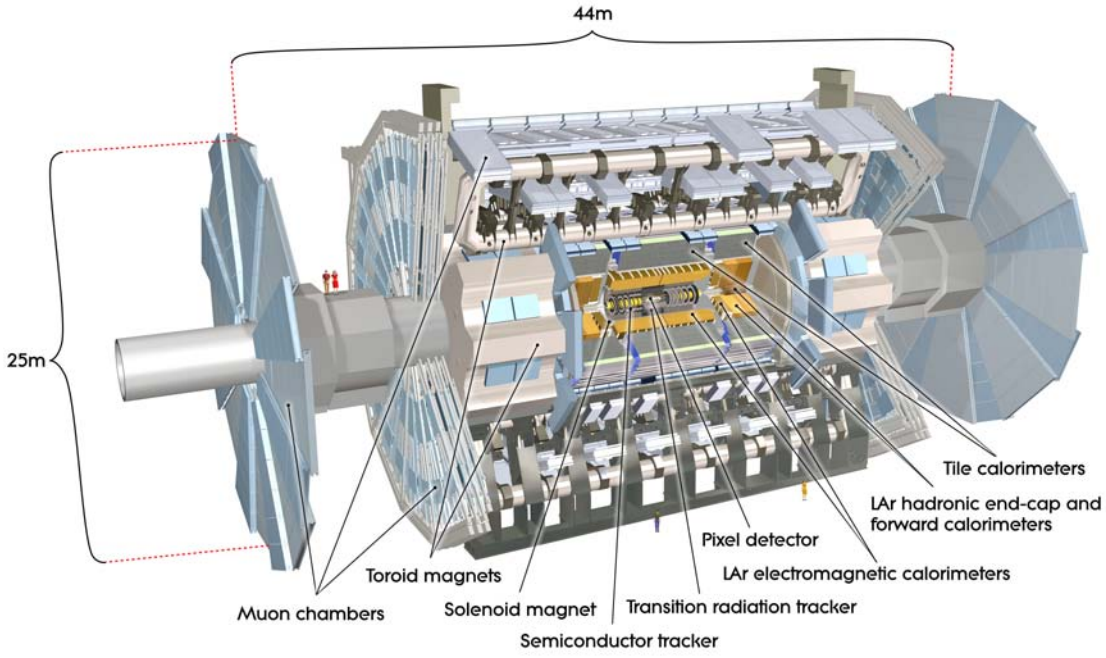

Figure 3.2: View of the ATLAS detector [49].

ATLAS reference system The ATLAS reference system is a Cartesian right-handed coordinate system with *origin* in the nominal point of interaction (IP), x *axis* pointing from the IP to the center of the LHC ring, y *axis* pointing upwards and positive z *axis* defined along the anti-clockwise beam direction.

The azimuthal angle ϕ is measured around the beam axis, and the polar angle θ is measured with respect to the z-axis. The pseudo-rapidity definition is:

$$\eta = -\ln\left(\tan\frac{\theta}{2}\right). \tag{3.1}$$

The transverse momentum, p_{T} and the transverse energy, E_{T}, and the missing transverse momentum, $\vec{p}_{\mathrm{T}}^{\,\mathrm{miss}}$, are defined in the x-y plane.

The angular distance ΔR is defined as:

$$\Delta R = \sqrt{(\Delta\eta)^2 + (\Delta\phi)^2}, \tag{3.2}$$

where $\Delta\eta$ and $\Delta\phi$ are the difference in η and ϕ, respectively. This reference system will be used in the following.

A summary of the η coverage and the expected transverse momentum and energy resolution of the different ATLAS subdetectors can be found in Table 3.1.

Detector component	Required resolution	$\lvert\eta\rvert$ coverage Measurement	Trigger
Tracking (ID)	$\sigma_{p_{\mathrm{T}}}/p_{\mathrm{T}} = 0.05\%\ p_{\mathrm{T}} \oplus 1\%$	< 2.5	
EM calorimetry	$\sigma_E/E = 10\%/\sqrt{E} \oplus 0.7\%$	< 3.2	< 2.5
Hadronic calorimetry			
barrel and end-cap	$\sigma_E/E = 50\%/\sqrt{E} \oplus 3\%$	< 3.2	< 3.2
forward	$\sigma_E/E = 100\%/\sqrt{E} \oplus 10\%$	$3.1 - 4.9$	$3.1 - 4.9$
Muon spectrometer	$\sigma_{p_{\mathrm{T}}}/p_{\mathrm{T}} = 100\%$ at $p_{\mathrm{T}} = 1$ TeV	< 2.7	< 2.4

Table 3.1: Summary of the ATLAS subdetectors $|\eta|$ coverage, and expected performance [49].

3.2.1 The magnet system

Four large superconducting magnets are used in ATLAS, one solenoid and three toroids (one barrel and two end-caps), which provide the magnetic field over a volume of approximately 12,000 m^3. The layout of the ATLAS magnets can be seen in Figure 3.2. The system of magnets has a diameter of 22 m and length of 26 m, with a stored energy of 1.6 GJ.

The solenoid is aligned to the beam axis and placed between the Inner Detector and the electromagnetic calorimeter, providing a 2 T axial magnetic field for the Inner Detec-

tor. It is 5.8 m long, with an inner diameter of 2.46 m and a thickness of 5 cm.

The barrel toroid and the two end-cap toroids produce a toroidal magnetic field of approximately 0.5 T and 1 T for the muon detectors in the central and end-cap regions, respectively. Each toroid magnet consists of eight coils assembled in radial symmetry around the beam axis. The barrel toroid system is 25 m long, has an inner radius of 4.7 m and an outer radius of 10.05 m. A view of the barrel toroid is shown in Figure 3.3. The endcap toroids are rotated by 22.5 with respect to the barrel toroid, in order to optimize the bending power in the transition region between them.

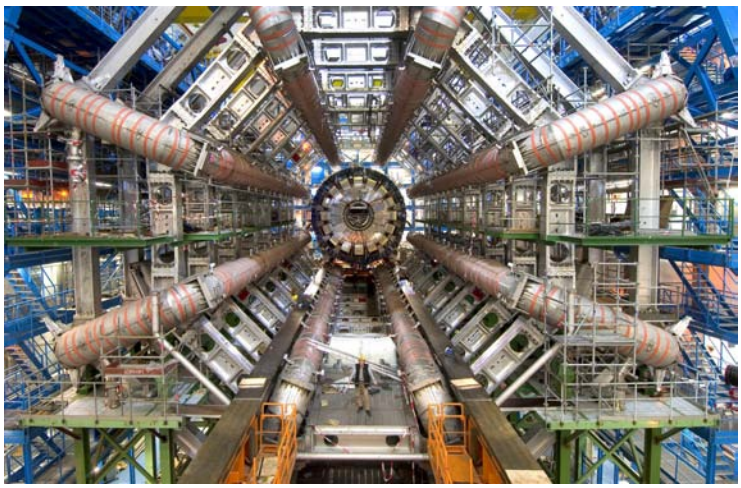

Figure 3.3: View of the barrel toroid magnet system of the ATLAS detector ©CERN

3.2.2 The Inner Detector

In order to cope with the very large track density in the ATLAS detector and to achieve the high momentum and vertex resolutions required by the benchmark physics processes, the ATLAS tracking detectors must be characterized by very fine granularity, fast response and good radiation resistance. The Inner Detector (ID), whose geometrical layout is illustrated in Figure 3.4, is the most inner part of ATLAS and is designed to reconstruct charged particle tracks and vertexes and to measure the momentum of charged particles within the pseudorapidity range $|\eta|<2.5$. It is constituted of three subdetectors, both silicon and gas based: the Pixel and silicon microstrip trackers and the Transition Radiation Tracker. The three subdetectors are contained within a cylindrical envelope of length 3512 mm and of radius 1150 mm, surrounded by a solenoid providing a magnetic field of 2 T.

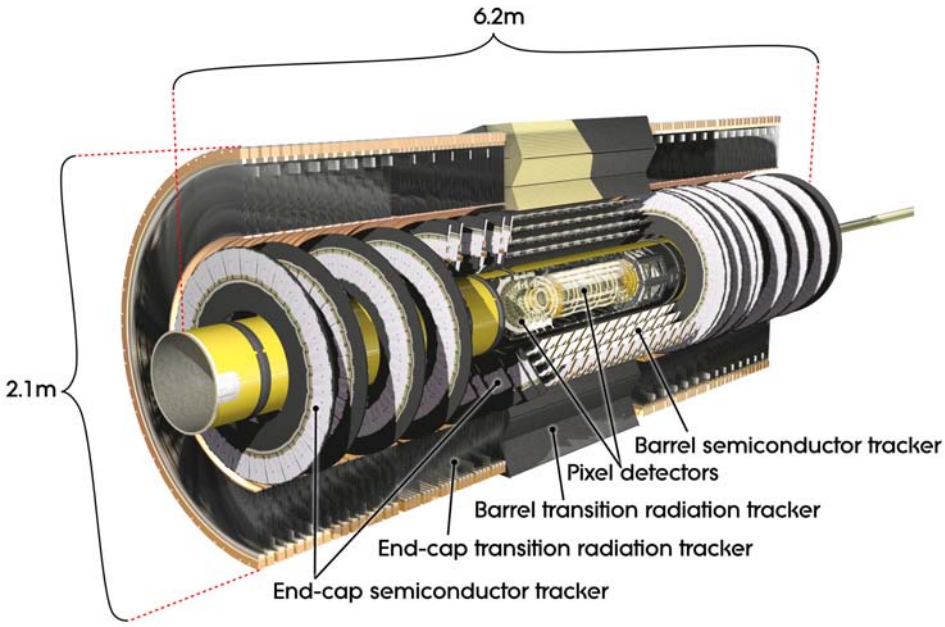

Figure 3.4: Geometrical layout of the ATLAS Inner Detector [49].

The three ID subdetectors are:

- The **Pixel detector**, made of radiation hard silicon sensors (pixels) and used to reconstruct charged particle tracks around the vertex region, where the highest granularity is achieved. It is crucial in the reconstruction of primary and secondary vertexes and consists of 4 layers of barrel pixel detector and two end caps of three pixel disks each, for a total of 80.4 million readout channels. The fourth layer, called Insertable B-Layer (IBL), was installed during Long Shutdown 1 (from February 2013 until May 2015) between the existing Pixel Detector and a new smaller beam pipe at a radius of 3.3 cm [53]. The minimum size of a pixel sensor is 50 x 400 μm^2 and the resolution is 10 μm in the R-ϕ plane and 115 μm in z.

- The **Semi-Conductor Tracker** (**SCT**), used in the intermediate radial range and consisting of silicon microstrip detectors arranged in layers of stereo strips. Approximately eight strips are crossed by each track and, since the position is determined from hits in overlapping strips, four space-points per track are usually available. Each silicon detector is 6.36 x 6.40 cm^2 with 780 readout strips of 80 μm pitch. The SCT is equipped with 6.2 million readout channels and its sensors provide a resolution of 17 μm in the R-ϕ plane. It is especially relevant for the momentum reconstruction.

- **The Transition radiation tracker** (**TRT**), the outermost of the three tracking

subsystems of the ID. It is a straw-tube tracker which consists of drift tubes with a diameter of 4 mm interleaved with transition radiation material, covering the pseudorapidity range of $|\eta|<2$. Each tube acts as a small proportional counter and is made of Kapton with a conducting coating. In the center of each tube there is a 31 μm diameter gold-plated tungsten wire. The TRT provides track information only in the R-ϕ plane, with an intrinsic single point resolution of 130 μm per straw. It has 351.000 readout channels. The very large number of straw hits (about 35 per track) is significantly important for the momentum measurement, and compensates for the worse resolution with respect to the silicon trackers.

Combining the information from the three subdetectors the ID transverse momentum resolution measured with cosmic muons is:

$$\frac{\sigma_{p_T}}{p_T} = P_1 \oplus P_2 \times p_T, \tag{3.3}$$

where $P_1 = 1.6 \pm 0.1\%$ and $P_2 = (53 \pm 2) \times 10^{-5}$ GeV^{-1}. This results into a resolution of 1.6% for tracks with p_T ~1 GeV and of ~50% for tracks with p_T ~1 TeV.

3.2.3 The Calorimeter systems

The ATLAS calorimeters, illustrated in Figure 3.5, surround the Inner Detector and cover the range $|\eta|<4.9$. Two types of calorimeters with different sampling materials are used, providing good containment for electromagnetic and hadronic showers. The hadronic central part is constituted of a lead and plastic tiles sampling calorimeter (TileCal), while a liquid Argon (LAr) calorimeter is used for the electromagnetic and the hadronic end-cap and forward sections.

The electromagnetic (EM) calorimeter is characterized by a fine granularity for precision measurements of electrons and photons, while the hadronic (HAD) calorimeter has a coarser granularity and is devoted to jet reconstruction and missing transverse momentum measurements.

The calorimeter systems have in total 187648 cells, organized in different layers in depth, and roughly 375000 read-out channels. The cell granularity in ϕ and η ranges from 0.025 in the central part of the EM calorimeter, to 0.1 for most of the HAD calorimeter sections, up to 0.4 for the most forward part of the HAD calorimeter ($3.2<|\eta|<4.9$).

The thickness of the EM calorimeter is greater than 22 radiation lengths (X_0) for the barrel, while it is greater than 24 X_0 in the end-caps. There are approximately 9.7 interaction lengths (λ) of active hadronic calorimeter in the barrel (10 in the end-caps), providing good resolution for high-energy jets. This thickness, together with the large η coverage, ensures good E_T^{miss} measurements.

The **electromagnetic LAr calorimeter** uses liquid argon as active medium and lead absorber plates. The electrodes are made of Kapton with an accordion geometry, which was chosen in order to provide a continuous calorimeter coverage in ϕ. The liquid Argon is kept at a temperature of 88K with a cryogenic system, whose major components are housed between the LAr and the Tile calorimeters. Figure 3.6 (left) shows the structure of one slice of the EM LAr calorimeter.

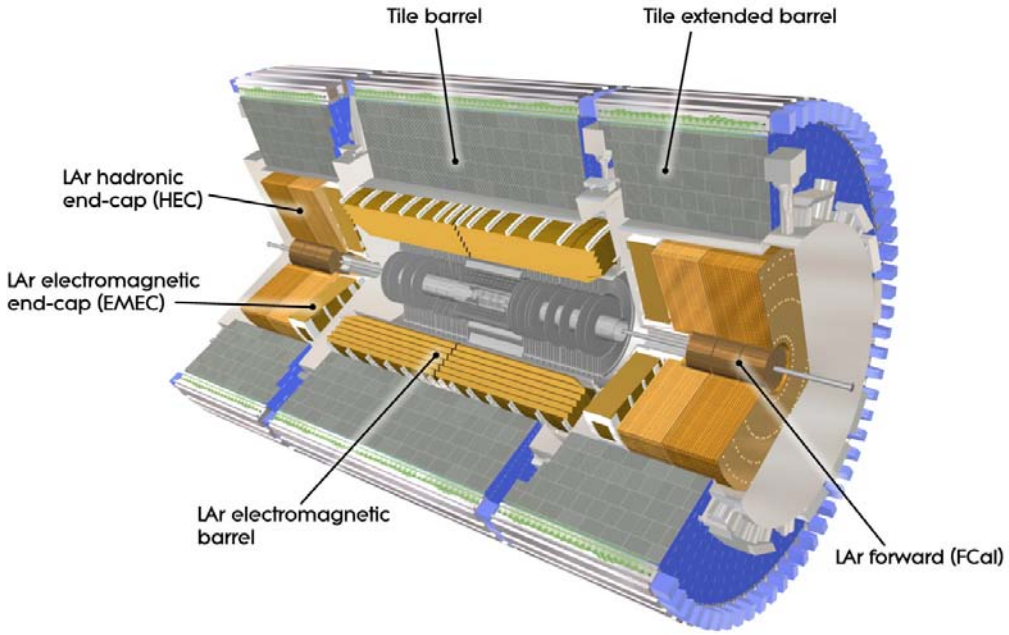

Figure 3.5: View of the ATLAS calorimeter systems [49].

Charged particles going through the active material create pairs of ions and electrons which drift in opposite directions due to the presence of an electric field and are collected by the electrodes.

The EM LAr calorimeter is divided into a barrel part (EMB, $|\eta|<1.475$) and two end-caps (EMEC, $1.5<|\eta|<3.2$). Each part has its own cryostat. All LAr detectors are segmented transversely and divided in four layers in depth (a presampler and three layers), for a total of 182,468 cells. The granularity of the different layers versus their η coverage is shown in Table 5.2.

As it was mentioned previously, the central part of the calorimeter uses a scintillating tiles technology, while the end-cap and forward hadronic calorimeter use the same LAr technology as the electromagnetic calorimeter.

	EM calorimeter			
	Barrel		**End-cap**	
X_0 (total)	>22		>24	
	$\Delta\eta \times \Delta\phi$	$\|\eta\|$	$\Delta\eta \times \Delta\phi$	$\|\eta\|$
Presampler	0.025×0.1	< 1.52	0.025×0.1	1.5-1.8
First layer	$0.025/8 \times 0.1$	< 1.40	0.050×0.1	1.375-1.425
	0.025×0.025	$1.40 - 1.475$	0.025×0.1	1.425-1.5
			$0.025/8 \times 0.1$	1.5-1.8
			$0.025/6 \times 0.1$	1.8-2.0
			$0.025/4 \times 0.1$	2.0-2.4
			0.025×0.1	2.4-2.5
			0.1×0.1	2.5-3.2
Second layer	0.025×0.025	< 1.40	0.050×0.025	1.375-1.425
	0.075×0.025	$1.40 - 1.475$	0.025×0.025	1.425-2.5
			0.1×0.1	2.5-3.2
Third layer	0.050×0.025	< 1.35	0.050×0.025	1.5-2.5

Table 3.2: Granularity versus η coverage of the different layers of the electromagnetic LAr calorimeter.

The **Tile Calorimeter (TileCal)** uses plastic scintillator as the active medium and low-carbon steel as the absorber. It surrounds the electromagnetic calorimeter and is divided into a long barrel (LB, $|\eta|<1.0$) and two extended barrels (EB, $0.8<|\eta|<1.7$). Both the LB and the EB are segmented into 64 modules in ϕ and each module is further segmented radially into three layers which are approximately 1.5, 4.1 and 1.8 λ thick for the LB and 1.5, 2.6 and 3.3 for the EB. The structure of a TileCal module can be seen in Figure 3.6.

The summary of the granularity versus η coverage of the different layers of the Tile calorimeter and the other hadronic calorimeters is given in Table 3.3.

	Hadronic calorimeter			
	Scintillator tile		**LAr hadronic**	
	Barrel	Extended barrel	End-cap	
$\|\eta\|$ coverage	< 1.0	0.8-1.7	1.5-2.5	2.5-3.2
Number of layers	3	3	4	
Granularity ($\Delta\eta \times \Delta\phi$)	0.1×0.1	0.1×0.1	0.1×0.1	0.2×0.2
(last layer)	0.2×0.1	0.2×0.1		
λ (total)	7.4 (9.7 with EM)	7.4 (10 with EM)		

Table 3.3: Granularity versus η coverage of the different layers of the hadronic calorimeter.

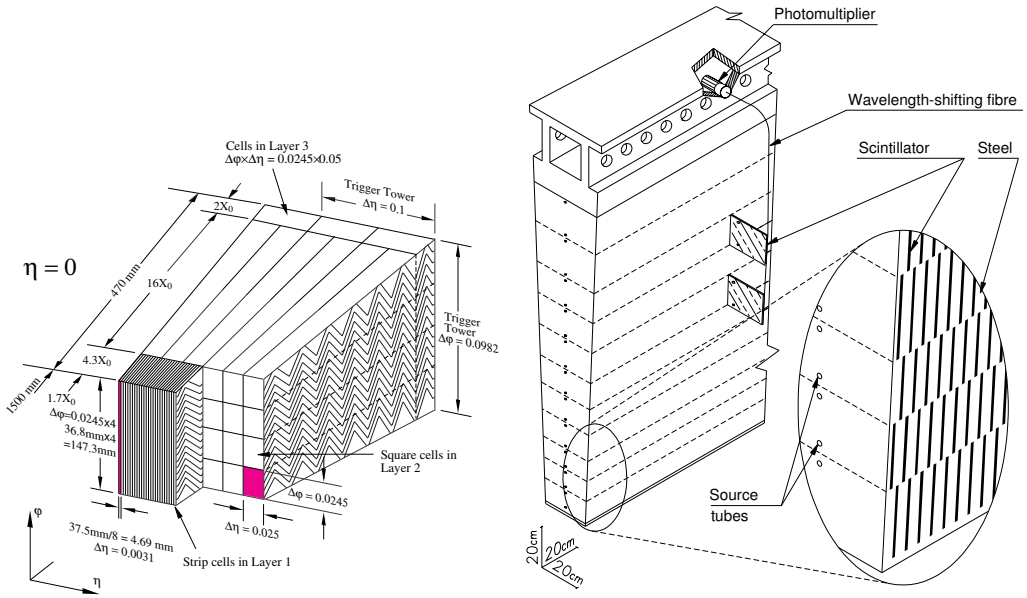

Figure 3.6: Structure of LAr and TileCal modules [54, 55].

The scintillation light from the tiles is collected by wavelength-shifting fibers coupled to the tiles and connected to photomultiplier tubes, for a total of 9836 readout channels. 480 of these channels belong to the special gap-crack scintillators, located on the inner radius surface of the extended barrel modules, in the region $1.0<|\eta|<1.6$. Other 32 belong to the Minimum Bias Trigger Scintillators (MBTS), which are located on the front face of the LAr end-cap cryostat in the range $2.12<|\eta|<3.85$.

As already mentioned in the introduction, the work developed in the Tile calorimeter during the course of this thesis will be described in Appendix B.

The **Hadronic End-cap Calorimeter (HEC)** is a copper/liquid-argon detector located directly behind the end-cap EM calorimeter. It consists of two independent wheels per end-cap made of parallel copper plates as absorber and LAr gaps as active medium. Each wheel is divided into two segments in depth. The HEC covers the region $1.5<|\eta|<3.2$.

The **Forward Calorimeter (FCal)** consists of three modules per end-cap: the first is made of copper absorber, and is optimized for electromagnetic measurements, while the other two are made of tungsten and measure mainly the energy from hadronic interactions. All modules use liquid Argon as active medium. The FCal covers the region $3.1<|\eta|<4.9$.

3.2.4 The Muon Spectrometer

The Muon Spectrometer (MS) is the outermost part of the ATLAS detector. Its layout is illustrated in Figure 3.7. The MS has been designed to identify and measure high momentum muons and is composed of four subdetectors that make use of different

technologies: Monitored Drift Tubes (MDT), Cathode Strip Chambers (CSC), Resistive Plate Chambers (RPC) and Thin Gap Chambers (TGC). The MS is based on the magnetic deflection of muon tracks in the large superconducting air-core toroid magnets described in section 3.2.1. The magnetic field is almost orthogonal to the muon trajectories and bends them along the θ angle. The properties of the muon spectrometer systems and their η coverage are summarized in Table 3.4.

	Muon spectrometer			
	MDT	**CSC**	**RPC**	**TGC**
$\|\eta\|$ coverage	< 2.7 (innermost layer < 2.0)	2.0-2.7	< 1.05	1.05-2.7 (1.05-2.4 trigger)
Number of chambers	1150	32	606	3588
Number of channels	354000	310000	373000	318000
Function	Precision tracking	Precision tracking	Triggering, ϕ-coordinate	Triggering, ϕ-coordinate

Table 3.4: Properties and η coverage of the different Muon spectrometer subsystems.

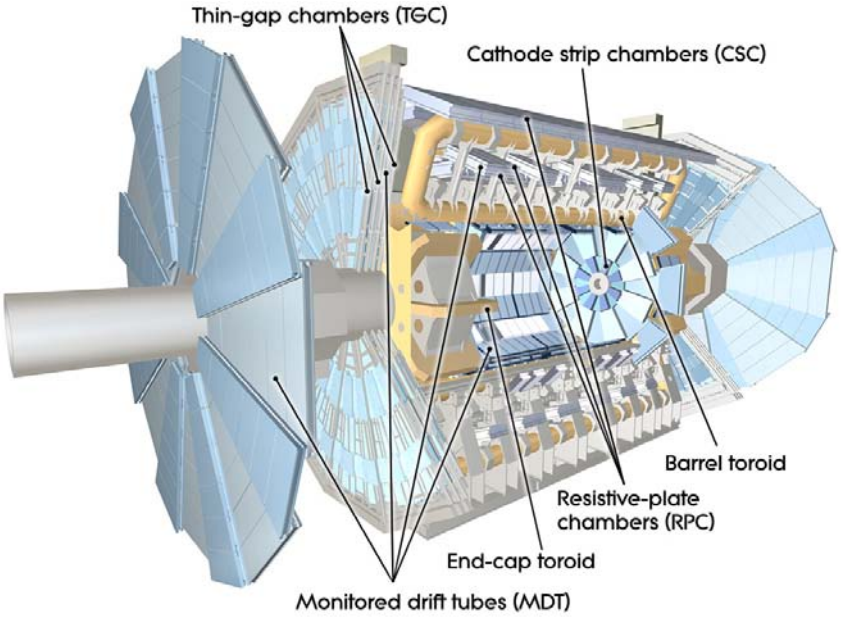

Figure 3.7: Layout of the ATLAS muon spectrometer [46].

The **Monitor Drifted Tubes** provide the muon momentum measurement for $|\eta| < 2.7$, thanks to a precision coordinate measurement in the bending direction of the air-core toroidal magnet. A cylindrical aluminum drift tube filled with gas and a central wire at a high potential represents the basic element of the detector. The gas in the tubes is ionized by the passage of the muons and the charges produced are collected on the wire.

The **Cathode Strip Chambers** are multiwire proportional chambers with cathodes

segmented into strips and are used at high pseudo-rapidity (2.0<| η |<2.7) in order to cope with the higher muon rate and background conditions.

The **Resistive Plate Chambers** (in the barrel) and the **Thin Gap Chambers** (in the end-caps) are used for the trigger (see below) and can provide bunch-crossing identification and well-defined p_{T} thresholds. They can also measure the muon coordinate in the ϕ direction.

3.2.5 The trigger system

In Run-2, the ATLAS trigger system consists of a hardware-based Level1 (L1) system, which uses a limited amount of detector information, and a single software-based high level trigger (HLT), which uses the information from all the subdetectors.

For each bunch crossing, the trigger system verifies if at least one of hundreds of conditions (triggers) is satisfied. These conditions are based on the identification of combinations of candidate physics objects (signatures) such as electrons, photons, muons and jets. In addition, there are triggers for inelastic *pp* collisions (minimum bias) and triggers based on global event properties such as missing transverse energy and summed transverse energy.

The scheme of the Run-2 ATLAS trigger system is shown in Figure 3.8.

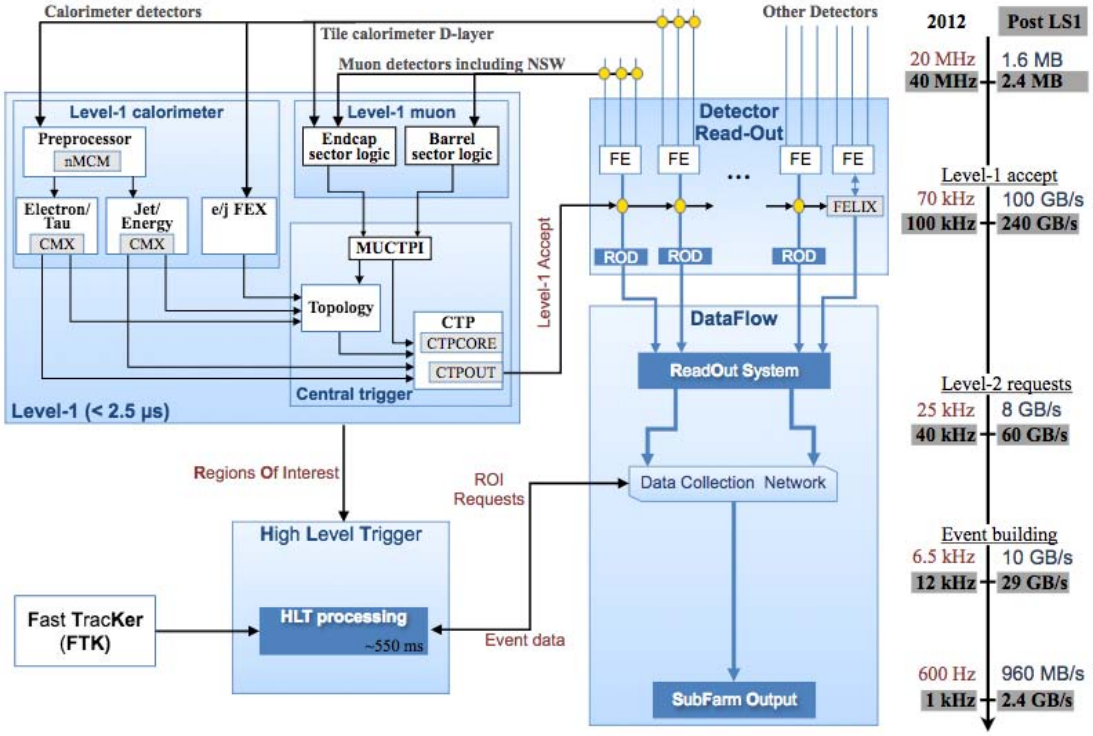

Figure 3.8: Schematic overview of the ATLAS trigger and data acquisition system (TDAQ) in Run-2 [56].

The L1 trigger is implemented in fast electronics in order to minimize the latency time and uses the information from calorimeters and muon trigger chambers to determine Regions of Interest (RoI), using criteria as energy thresholds. The L1 trigger is designed to reduce the rate from about 40 MHz to a maximum of 100 kHz with an average processing time per event of 2.5 μs. It consists of the L1 calorimeter trigger system (L1Calo), the L1 muon trigger system (L1Muon), new L1 topological trigger modules (L1Topo) and the Central Trigger Processors (CTP).

At the HLT, fast algorithms accessing data from a RoI or online algorithms similar to offline analysis procedures run on a unique PC farm within a processing time of 0.2 s on average. The rate is finally reduced to approximately 1 kHz and these selected events are saved permanently.

Details about the ATLAS trigger and data acquisition system (TDAQ) in Run-2 are given in Ref. [56].

3.2.6 Luminosity

Several subdetectors contribute to the measurement of the ATLAS luminosity, using different methods and algorithms [57]. In searches for new physics, the accurate information about the delivered luminosity is crucial to evaluate background levels and determine the sensitivity to the signatures of new phenomena.

The instantaneous luminosity, $\mathcal{L}$, can be expressed in terms of accelerator parameters, as:

$$\mathcal{L} = \frac{n_b f_r n_1 n_2}{2\pi \Sigma_x \Sigma_y}, \tag{3.4}$$

where n_1 and n_2 are the bunch populations (protons per bunch) in beams 1 and 2 respectively, f_r is the revolution frequency of the LHC, n_b are the bunch pairs colliding in each revolution and Σ_x and Σ_y characterize the horizontal and vertical convolved beam widths. The latter information is extracted in a van der Meer (VdM) scan. During a VdM scan, the two LHC beams are moved in steps of known distance, on both the horizontal and vertical direction. The total absolute luminosity can then be computed with Equation 3.4.

The luminosity can be re-written as:

$$\mathcal{L} = \frac{R_{\text{inel}}}{\sigma_{\text{inel}}} = \frac{\langle\mu\rangle n_b f_r}{\sigma_{\text{inel}}} = \frac{\langle\mu\rangle_{\text{vis}} n_b f_r}{\sigma_{\text{vis}}}, \tag{3.5}$$

where R_{inel} is the rate of inelastic collisions, σ_{inel} is the pp inelastic cross section, $\langle\mu\rangle$ is the average number of interactions per bunch crossing (BC), $\langle\mu\rangle_{\text{vis}} = \epsilon\langle\mu\rangle$ and $\sigma_{\text{vis}} = \epsilon\sigma_{\text{inel}}$, where ϵ is the efficiency of a particular detector and algorithm. Therefore the ATLAS luminosity can be determined for a given measure of $\langle\mu\rangle_{\text{vis}}$ through equation 3.5. In order to measure $\langle\mu\rangle_{\text{vis}}$ with a subdetector, ATLAS primarily uses event counting algorithms,

for which the number of events that satisfy a given criteria (typically a number of hits above a certain threshold) is compared with the total number of bunch crossings. In a vdM scan $\langle\mu\rangle_{\text{vis}} \ll 1$, and the average number of visible inelastic interactions per BC is given by the expression:

$$\langle\mu\rangle_{\text{vis}} = \frac{N}{N_{\text{BC}}}, \tag{3.6}$$

where N is the number of events that satisfies the event selection criteria during a given time interval and N_{BC} is the total number of bunch crossings during the same interval. Figure 3.9 (left) shows the peak instantaneous luminosity delivered to ATLAS during pp collisions at $\sqrt{s}$ =13 TeV (in stable beams periods only) for each LHC fill. The peak instantaneous luminosity is shown as a function of the time in 2015. The maximum peak instantaneous luminosity reached in 2015 was 5.0×10^{33} cm^{-2}s^{-1}. The luminosity-weighted distribution of the mean number of interactions per crossing for the 2015 pp collision data is shown in Figure 3.9 (right).

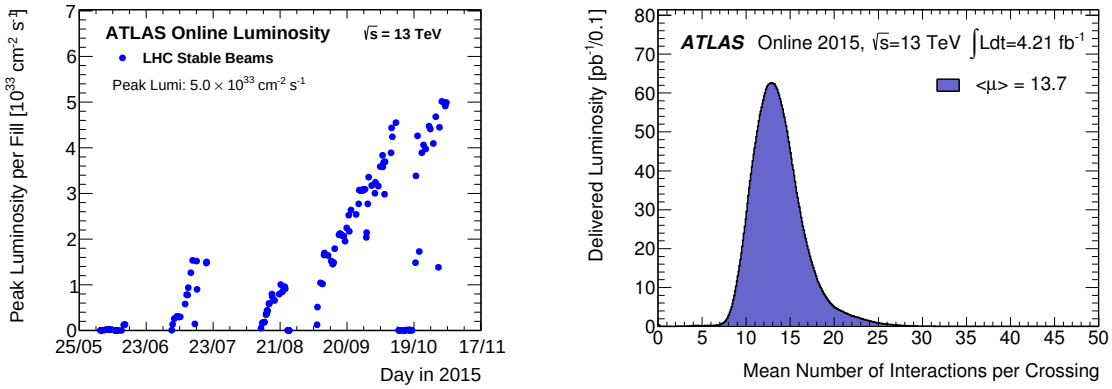

Figure 3.9: The peak instantaneous luminosity delivered to ATLAS during stable beams for pp collisions at 13 TeV center-of-mass energy is shown for each LHC fill as a function of time in 2015 (left). The luminosity-weighted distribution of the mean number of interactions per crossing for the 2015 pp collision data (right).

The integrated luminosity, defined as

$$\mathcal{L}_{int} = \int \mathcal{L} \mathrm{d}t [\mathrm{cm}^{-2}], \tag{3.7}$$

represents the recorded data integrated over a given amount of time, typically the so-called luminosity block, corresponding to about one minute of data taking, in which the instantaneous luminosity can be considered constant. In 2015 ATLAS recorded 3.9 fb^{-1} of luminosity (4.2 fb^{-1} delivered) at $\sqrt{s} = 13$ TeV.

3.2.7 Data quality

During the data taking, the status of the ATLAS detector is monitored and recorded by several online applications, including the trigger and data acquisition system (see Section 3.2.5), the detector control system (DCS) [58] and the online data quality monitoring framework (DQMF) [59]. A specific set of triggers is used to select events which are used for detector monitoring and are saved in the so-called "express stream". This stream is promptly reconstructed in the ATLAS Tier-0 farm.

Monitoring plots are produced and checked both automatically by the offline DQMF and by detector experts [60]. These checks are important to provide feedback on the quality of the collected data.

Data taken with similar LHC and ATLAS conditions are grouped in periods and sub-periods. After a sub-period is closed, the correspondent data are additionally inspected by detector experts, making sure that possible problems are identified, and finally signed off. Once this certification procedure is concluded, the data are released for analysis.

The main result of the ATLAS data quality infrastructure is the so-called "good run list" (GRL) file, which contains the list of luminosity blocks approved for the analysis. More than one GRLs are produced, for different needs of the corresponding physics studies, by requiring different subdetectors to be good, and are finally delivered to the analyzers.

Chapter 4

Reconstruction of physics objects

In this section, the reconstruction of physics objects in the ATLAS detector, relevant for the analysis presented later in this thesis, is described. This includes the reconstruction of the interaction vertex, as well as the reconstruction of electrons, muons, jets of hadrons and the missing transverse energy, and the technique used for identifying jets originating from B-hadrons (b-jets). More details related to specific selections adopted in the analysis will be given in the relevant chapters.

4.1 Reconstruction of charged tracks and the interaction vertex

Tracks of charged particles, reconstructed in the Inner Detector, are not used as standalone objects but constitute inputs to most of the physics objects described in the following sections. They are reconstructed with a sequence of algorithms using ID information [61]:

- The **inside-out algorithm** is the baseline algorithm, used to reconstruct the tracks of primary particles, i.e. particles with a mean lifetime higher than 3×10^{-11} s. It starts from 3-point seeds in the silicon detectors, then other hits are added and the track is finally extended to the TRT. The track is required to have p_T >0.4 GeV in order to be retained.

- The **back-tracking algorithm** is used to identify secondary particles, coming from the decay of primary particles. It starts from segments reconstructed in the TRT and extends them inwards by adding silicon hits.

- Finally tracks with a TRT segment but no association to the Pixel or SCT detectors are referred to as **TRT-standalone tracks**.

Tracks with p_T >400 MeV are used to identify the primary vertex of the hard interaction. The vertex with highest $\sum p_T^2$, summed over all the tracks associated with it, is defined

as the primary vertex (PV) and generally corresponds to the hard-scatter vertex.

As it will be described later in this chapter, tracks play also a crucial role in algorithms for identifying jets coming from B-hadrons, in providing lepton p_T measurements, as well as in the E_T^{miss} calculation.

4.2 Electrons

The reconstruction and identification of electrons will be briefly described in the following. The reconstruction step allows to identify the electron candidates, while different identification selections result in electron samples with different purities.

Reconstruction. Different algorithms are used for the reconstruction of electrons [62] depending on whether they are central or forward.

Central electrons, i.e. those in the region $|\eta|<2.5$, where the Inner Detector is operative, are reconstructed by matching the energy deposits (clusters) [63] in the EM calorimeter with reconstructed tracks in the ID. The EM clusters are seeded by towers of size $\Delta\eta \times \Delta\phi = 0.025 \times 0.025$ in the EM calorimeter with total transverse energy above 2.5 GeV. The reconstruction of the clusters is based on a fixed-size sliding window algorithm [63].

Tracks are extrapolated from their last measured point to the middle layer of the EM calorimeter and their coordinates are compared to a corresponding seed cluster position in that layer. The electron is reconstructed if at least one track is matched to the seed cluster. If more than one track is matched to a cluster, the preference is given to tracks with hits in the Pixel or the SCT detectors, and the distance ΔR to the seed cluster is minimized in order to select the track.

For the Run-2 analyses, the track associated with the electron is required to be compatible with the primary vertex, in order to reduce the background from conversions and secondary particles.

Once the cluster and the track are matched, the electron candidate ϕ and η coordinates are taken from the corresponding track parameters at the vertex. The energy is taken from the cluster and is adjusted by correcting for energy deposits outside the EM calorimeter according to that predicted by MC simulations. The correction is evaluated in benchmark processes such as $W \to e\nu$ and $Z \to ee$.

Forward electrons, in the region $2.5<|\eta|<4.9$, are reconstructed only from energy deposits in the calorimeters, given the absence of tracking detectors in that region. The reconstruction happens by grouping neighboring 3-dimensional cells, taking into account the significance of their energy content with respect to the expected noise (topological clusters). For reconstructing an electron candidate in the forward region, the transverse energy is required to be above 5 GeV and the hadronic energy content to be small.

Identification. The identification criteria are required to provide good separation between signal electrons and background electrons coming from hadrons misidentification, non-isolated electrons (e.g. from semi-leptonic decays of heavy-flavor particles) and electrons from photon conversions. These criteria are based on sequential cuts on calorimeter, tracking and combined track/cluster variables.

Three sets of selection criteria for central electrons are defined [64], to be used in the analyses, with increasing background rejection power: loose, medium and tight. Shower-shape variables in the first two layers of the EM calorimeter, as well as hadronic leakage information and requirements on the associated track quality and track-cluster matching are used for defining the loose reference criteria. In the medium selection, the loose requirements are tightened and new constraints are added, namely a loose selection on the transverse impact parameter (d_0) and on the number of hits in the TRT associated with the track. Also, a measured hit in the innermost layer of the pixel detector is required, in order to discriminate against photon conversions. Finally, for the tight selection, one imposes additional requirements on the ratio of the candidate's reconstructed energy to its track momentum (E/p), together with stricter requirements on the discriminating variables and on TRT information, and a veto on reconstructed photon conversion vertices associated with the cluster.

In the analysis described in this thesis, loose electrons with low p_T requirements (p_T >10 GeV) are used to veto events when the absence of leptons is required. The tight criteria is instead used for selecting events with electrons in the final state. Calorimeter or track based isolation requirements can be applied in addition to further discriminate between signal and background electrons. The absolute electron energy scale is determined using the $Z \to ee$ resonance, while the electron energy resolution its related uncertainties are derived by studying the Z resonance width, as described in Refs. [65, 66].

Efficiency. The performance of the electron reconstruction and identification is quantified with the total efficiency:

$$\varepsilon_{total} = \varepsilon_{reconstruction} \times \varepsilon_{identification} \times \varepsilon_{isolation} \times \varepsilon_{trigger}, \tag{4.1}$$

with the various efficiency components measured with respect to the previous step. In Eq. 4.1, $\varepsilon_{isolation}$ is the efficiency of the isolation selection, which can be either constant or can depend on the transverse energy of the electron, and $\varepsilon_{trigger}$ is defined as the fraction of events selected by the electron trigger (see Section 3.2.5) in a sample of events with electrons reconstructed by the offline algorithm. The trigger efficiency is defined for a given offline identification algorithm and isolation operating point. Simulated samples are corrected in order to reproduce the measured data efficiencies as closely as possible. A multiplicative correction factor is applied to MC, based on the ratio between data and

MC efficiencies. These data-to-MC correction factors are usually close to unity.

The efficiency corrections are parametrized as a function of the electron E_T and η. The different efficiency components are measured in events containing well-known resonance decays to electrons, such as $Z \to ee$ and $J/\Psi \to ee$ using a tag-and-probe method [64].

Averaging over η, the reconstruction efficiency varies from 97% to 99% between the endcap and barrel regions, for electrons with $E_T > 15$ GeV. Lower efficiencies (95%) are obtained in the calorimeter transition region. For energetic electrons with $E_T > 80$ GeV, the reconstruction efficiency is about 99% over the whole η range. The identification efficiency depends strongly on the energy of the electron and ranges, on average, between 80%, for the tight working point, to ∼95% for the loose working point.

4.3 Muons

In this section, the muon reconstruction and identification procedures will be briefly described.

Reconstruction. The muon reconstruction in ATLAS is based on the information from different subdetectors: the Inner Detector, the Muon Spectrometer, and the Calorimeters. Four "types" of muons are defined, depending on the subdetectors used in the reconstruction [67].

- *Combined (CB) muons*: tracks are reconstructed independently in the ID and the MS and then combined. CB muon candidates represent the main type of reconstructed muons and have the highest muon purity.
- *Extrapolated (ME) muons*: tracks are only reconstructed in the MS. This type of muons is used mainly in the range $2.5 < |\eta| < 2.7$ where there is no coverage from the ID. The track is extrapolated back to the point of closest approach to the beam line, considering the estimated energy loss of muons in the calorimeters.
- *Segment-tagged (ST) muons*: tracks reconstructed in the ID are extrapolated to the MS if the muon candidate has at least one local track segment in the MDT or CSC chambers.
- *Calorimeter-tagged (CT) muons*: a track in the ID is associated to an energy deposit in the calorimeters compatible with a minimum ionizing particle. Tagged muons are mostly used in regions with reduced MS acceptance.

Identification. Four muon identification selections (medium, loose, tight and high-p_T) are used in the physics analyses to select prompt muons and to reduce the background, mostly coming from pion and kaon decays. These identifications categories are based on

variables like the q/p significance and ρ'. The former is defined as the absolute value of the difference between the ratio of the charge and momentum of the muons measured in the ID and MS divided by the sum in quadrature of the corresponding uncertainties. The latter is defined as the absolute value of the difference between the transverse momentum measurements in the ID and MS divided by the p_T of the combined track, and the normalized χ^2 of the combined track fit. In addition, there are also requirements on the number of hits in the MS layers and the transverse momentum of the tracks. Details of each selection are illustrated in Ref [67]. In this thesis, only combined muons will be considered, identified with the medium selection. As for the electrons, further rejection of background muons can be achieved by applying calorimeter or track based isolation requirements.

Studies of the muon momentum scale and resolution were performed using $> Z \to \mu\mu$ and $J/\Psi \to \mu\mu$ decays and are used to correct the MC simulation and to improve the agreement with data. The dimuon mass resolution varies between 1.2% (1.6%) to 1.6% (1.9%) for J/Ψ (Z) decays from small to large pseudorapidity values.

Efficiency. The combination of all the muon reconstruction types gives a uniform muon reconstruction efficiency of about 99% over most the detector regions.

The efficiency of the muon identification selections within the acceptance of the ID ($|\eta|<2.5$) is obtained with a tag-and-probe method, based on the selection of an almost pure muon sample from $J/\Psi \to \mu\mu$ or $Z \to \mu\mu$ [67]. On average, the efficiencies of the loose and medium selections are very similar throughout most of the pseudo-rapidity coverage and above 98%, while they vary between 90 and 98% for the tight selection. The efficiency of the high-p_T selection is significantly lower, because of the strict requirements on momentum resolution. The correction scale factors applied to MC are, also in the case of muons, very close to unity.

4.4 Jets

Jets are key ingredients at high energy hadron colliders. In this thesis, jets are reconstructed using the anti-k_t jet algorithm [68], based on input positive-energy topological clusters (topo-clusters) and are calibrated using MC simulation.

4.4.1 Cluster formation

The topological clustering algorithm [63] is designed to follow the shower development of a single particle interacting with the calorimeters, profiting of their fine granularity. Figure 4.1 (left) shows a schema of a topological cluster formation.

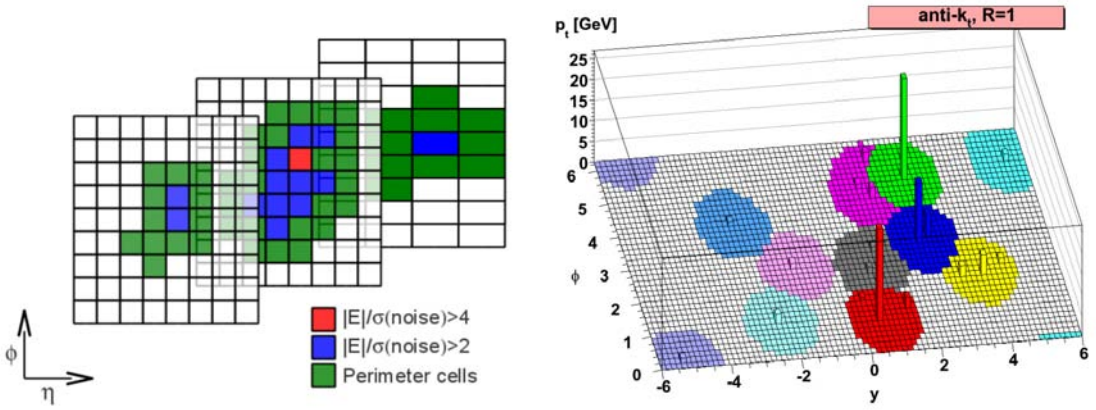

Figure 4.1: Topo-cluster formation in the three hadronic layers in the barrel, the grid represents calorimeter cells (left). Illustration of the jets clustering with the anti-k_t algorithm [68] (right).

Topo-clusters are built from topologically connected calorimeter cells that contain a significant energy deposit above the noise. The signal significance is measured independently in each cell using the signal to noise (S/N) ratio. The cell noise includes a component from the electronic noise and a component from pileup which are summed in quadrature.

The formation of a topo-cluster starts by taking all cells with a signal to noise ratio $|S/N| \geq 4$ as seed cells, considered in descending order of S/N. All neighboring cells with $|S/N| \geq 2$ are then added to the topo-cluster. These requirements allow to effectively suppress noise. To ensure that the tails of the shower are not removed, cells with $|S/N| \geq 0$ are finally added to the cluster.

In order to prevent low-energy pileup energy depositions from creating large clusters dominated by pileup noise, clusters are forbidden from growing from the PS layers of the calorimeter using neighbors in those same layers.

Topo-clusters are treated as massless and are calibrated at the electromagnetic scale, which correctly measures the energy deposited in the calorimeter by particles produced in electromagnetic showers. Their energy is given by the sum of the energies of the cells belonging to the topo-cluster.

Topo-clusters can be additionally calibrated in a way to correctly reconstruct the calorimeter response to hadrons. This is obtained with the local cell signal weighting (LCW) method [69], which first classifies topo-clusters as either electromagnetic or hadronic, depending on their measured energy density and the longitudinal shower depth. According to this classification, in order to correct the signals from hadronic deposits, energy corrections are derived from single charged and neutral pion in MC simulations.

4.4.2 Jet finding algorithm

The requirement of infrared and collinear (IRC) safety, meaning that the jet measurements should not change in case of soft or collinear parton emission, discourages the choice of cone-type algorithms for the reconstruction of jets. Sequential clustering algorithms are preferred in LHC experiments, although they require larger computational time.

The anti-k_t algorithm [68] for the reconstruction of jets fulfills the requirement of IRC safety. It is a "soft-resilient" jet algorithm, meaning that the shape of reconstructed jets is not influenced by soft radiation and the resulting jets have a well-defined conical shape, allowing robust pileup corrections.

The clustering of hard and soft particles into jets with the anti-k_t algorithm is illustrated in Figure 4.1 (right). The inputs to the jet algorithm are stable simulated particles, reconstructed tracks in the Inner Detector or topo-clusters in the calorimeter.

For all the input constituents, the algorithm computes the following quantities:

$$d_{ij} = \min\left(\frac{1}{k_{ti}^2}, \frac{1}{k_{tj}^2}\right)\frac{\Delta R_{ij}^2}{R^2} \tag{4.2a}$$

$$d_{iB} = \frac{1}{k_{ti}^2}, \tag{4.2b}$$

where $\Delta R_{ij}^2 = (\eta_i - \eta_j)^2 + (\phi_i - \phi_j)^2$, R is a parameter of the algorithm that approximately controls the size of the jet and k_{ti} is the transverse momentum of the constituent i. Jets in ATLAS are reconstructed with radius parameters R=0.4 or R=0.6.

The variable d_{iB} is the distance between the constituent i and the beam and it is introduced to separate constituents coming from the interactions from proton remnants. Similarly, d_{ij} is the distance between the constituents i and j. The smallest distance is found by the jet clustering algorithm. If the smallest distance is d_{ij}, i and j are combined into a single object, while if the smallest distance is d_{iB}, the constituent i is considered as a jet and is removed from the list for successive iterations. For defining the four-momentum of the recombined object the four-momenta of its constituents are summed vectorially. After recombination, the distances are recalculated with the remaining objects, and the procedure repeated until no entities are left in the list. Finally, jets are defined with a minimum transverse momentum threshold p_T, that is used as a scale to separate soft and hard interactions.

In the case of the reconstruction of very boosted objects decaying hadronically (for example a boosted $t\bar{t}$ system), it could happen that jets reconstructed with the anti-k_t algorithm with R=0.4 partially overlap. A possible way to reconstruct such objects is the use of large R values (in the range between 0.8 and 1.2) and then resolve subjets multiplicities inside this large jet.

4.4.3 Jet calibration

A jet calibration procedure is adopted, in order to restore the jet energy scale to that corresponding to particle-level jets before detector effects [70]. The jet direction is first corrected to point back to the identified hard scatter vertex. Figure 4.2 shows an overview of the ATLAS calibration scheme for calorimeter jets, consisting of different steps which will be explained in the following paragraphs.

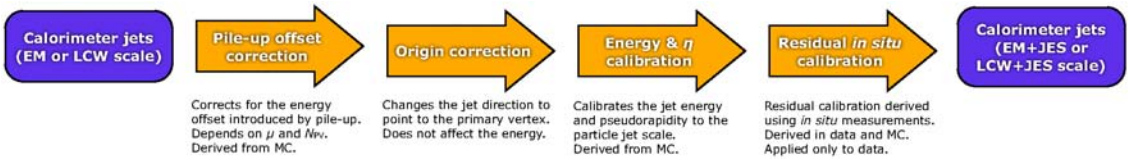

Figure 4.2: Overview of the ATLAS jet calibration [69].

The final calibrated jet p_T in data is given by the following expression:

$$p_T^{corr} = f(p_T, \eta) \times C(p_T^{EM}, \eta, N_{PV}, \mu, \{g_i\}) \times p_T^{EM}, \tag{4.3}$$

where p_T^{EM} is the p_T of the jet reconstructed from topo-clusters at the EM energy scale (but the same methodology could be applied to jets from topo-clusters calibrated with the LCW method). The term $C(p_T^{EM}, \eta, N_{PV}, \mu, \{g_i\})$ includes:

- the removal of pileup effects using an area-based subtraction procedure and residual corrections depending on the number of primary vertexes N_{PV} and the average number of interactions per bunch crossing $\langle\mu\rangle$;
- jet energy scale and η corrections derived from MC simulation;
- global sequential corrections exploiting the topology of the energy deposits in the calorimeter and tracking information and based on a series of variables here indicated as $\{g_i\}$.

Finally, $f(p_T, \eta)$ is a term related to the final *in situ* corrections accounting for differences between data and MC simulation.

Pile-up corrections The several interactions per bunch crossing in ATLAS introduce an energy offset which must be corrected in the jet calibration. Besides the *in-time pileup*, which is due to *pp* collisions within a single bunch crossing, further signal modulation in the calorimeters can be introduced by the *out-of-time pileup*, due to collisions in other bunch crossings. Corrections to the jet transverse momentum are applied to take into account these effects [71]. In order to derive the corrections, an area-based subtraction

method is used, which utilizes the average energy density in the $\eta \times \phi$ plane (ρ) and the area of the jet (A). The energy density is defined for each jet as p_T/A and the ρ per event is obtained from the average energy density of central jets with $|\eta|<2.0$.

A residual correction is parametrized from MC simulations as a function of the number of reconstructed primary vertices in the event (N_{PV}), which measures the number of collisions in the event, and on the expected average number of bunch crossings ($\langle\mu\rangle$), which is sensitive to out-of-time pileup.
The jet p_T after the area-based correction and the residual correction is given by the following expression:

$$p_T^{corr} = p_T^{EM} - \rho \times A - \alpha \times (N_{PV} - 1) - \beta \times \langle\mu\rangle, \tag{4.4}$$

where α and β are obtained from the residual dependence in the MC simulation and are parametrized as a function of the jet η. Figure 4.3 shows the dependence of the reconstructed jet p_T on pileup and the linear fit used to derive the residual correction, as well as the application of this correction which results in removing the residual pileup effects.

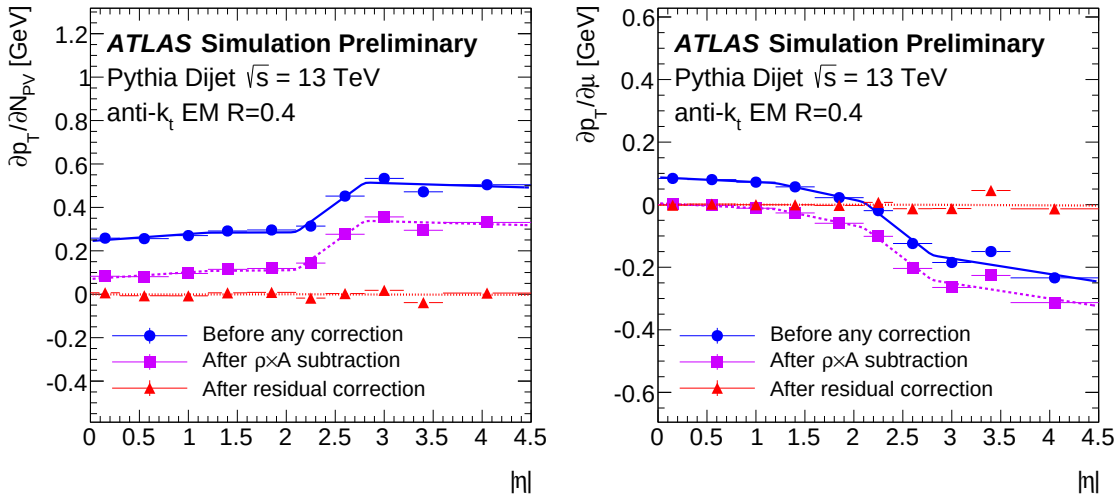

Figure 4.3: Dependence of the reconstructed jet p_T on in-time pileup (left) and out-of-time pileup (right) at various correction stages in bins of jet $|\eta|$ and the linear fit used to define the residual correction. The red curve shows the application of the residual corrections α (left) and β (right) [70].

An additional requirement is imposed to reduce the effect of pileup, based on a multivariate discriminant variable called Jet Vertex Tagger (JVT), described in Ref. [72], with the aim of identifying the vertex from which a jet is originated. The JVT is used to suppress jets coming from pileup interactions instead of the primary vertex and constitutes an improvement of the Jet Vertex Fraction (JVF) variable used in Run-1. The

latter is calculated as the ratio of the sum of transverse momentum of matched tracks that originate from a chosen primary vertex to the sum of transverse momentum of all matched tracks in the jet, independently of their origin. The JVT requirement is applied for jets with 20 GeV<p_T <60 GeV and | η |<2.4.

Jet energy scale and η corrections The jet energy scale (JES) calibration is derived from an inclusive dijet MC simulated sample [69], by relating the reconstructed jet energy to the energy of the jet before the detector simulation is applied ("truth" jet). To derive the jet energy scale factors, isolated jets are matched in ΔR with truth jets, also built with the anti-k_t algorithm and reconstructed from stable particles in the final state. The correction factors, dependent on η and p_T, are derived from the ratio of energies of the two matched jets E_{calo}/E_{truth}. Figure 4.4 (left) shows this ratio as a function of the pseudo-rapidity of the reconstructed jet, for different calibrated jet energies. The inverse of the response shown in each bin corresponds to the average JES correction. Regions with lower energy response correspond to gaps and transitions between calorimeter subdetectors. The reconstructed pseudo-rapidity direction can be biased due to the calorimeter response in different η regions. This effect is also corrected with MC-based correction factors, as shown in Figure 4.4 (right) as a function of η.

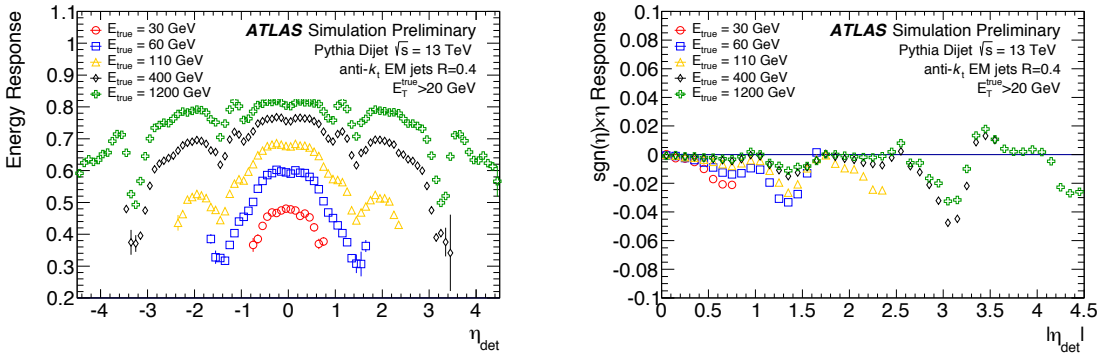

Figure 4.4: The energy response (left) and bias in the η reconstruction (right) as a function of η for EM scale anti-k_t jets with R=0.4, after the pileup corrections have been applied [70].

Global sequential corrections At the end of the calibration scheme described above, a set of sequential corrections are applied to correct for the jet energy dependence from longitudinal and transverse features of the jet, as described in Ref. [73], thus improving the jet energy resolution. Corrections are applied taking into account the dependence from: the fraction of energy deposited in the first layer of the Tile calorimeter, the fraction

of energy deposited in the third layer of the electromagnetic calorimeter, the number of tracks associated to a jet, the p_T-weighted width of the tracks associated to the jet and the number of muon segments associated to the jet. All these variables are indicated as $\{g_i\}$ in Equation 4.3.

Jet residual corrections Finally, differences between data and MC simulation in the jet p_T measurement are taken into account via dedicated corrections derived using *in situ* techniques. These techniques exploit the transverse momentum balance between the jet to be calibrated and a well-measured photon, Z boson or system of low p_T jets, which is used as the reference object against which the jet recoils [74]. The corrections are only applied to data and are computed using γ/Z+jet and multijet processes in data and MC simulation. In each case, the ratio between the jet p_T and the reconstructed reference object (e.g. the γ or Z boson) is built, p_T^{jet}/p_T^{ref}. The ratio is compared in data and MC and finally the *in situ* correction is applied to data.

Figure 4.5 shows the p_T balance, $\langle p_T^{jet}/p_T^{ref} \rangle$ for anti-kt R=0.4 jets calibrated with the EM+JES scheme as a function of p_T^{ref}, for jets selected in the central region of the hadronic calorimeter ($\mid \eta^{lead\ jet} \mid$<0.8) (left), as well as a function of the calibrated jet η (right). In order to derive this ratio, data and simulated γ+jets events have been used, requiring the photon and the leading jet to be back-to-back by applying selection criteria to the azimuthal angle between them. In this case, p_T^{ref} corresponds to the projection of the photon transverse momentum on the leading jet axis. The p_T balance ranges between 0.9 and 1 both in data and in the simulation, and it is higher for larger values of p_T^{ref} and for central values in η. A good agreement between the measurements in data and in two different MC simulations is observed. The difference of response in data and MC is shown against the jet p_T for the 2015 dataset in Figure 4.6, obtained using different *in situ* techniques. A general offset of about 3-4% is observed in the data-to-MC response ratios for jet transverse momenta below 100 GeV. The offset decreases to ∼2% at higher p_T (p_T >200 GeV).

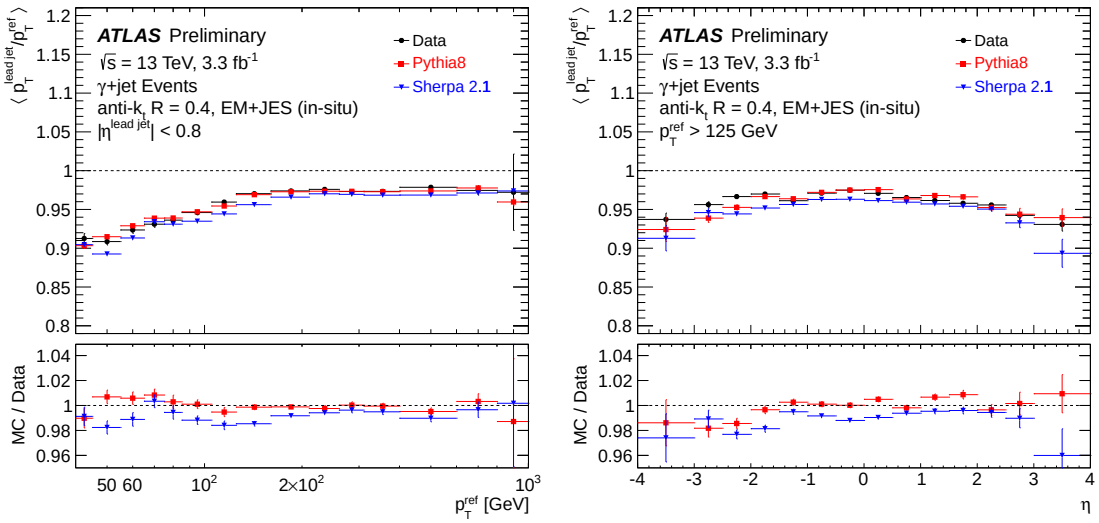

Figure 4.5: The ratio p_T^{jet}/p_T^{ref} for anti-kt R=0.4 jets calibrated with the EM+JES (in-situ) scheme as a function of p_T^{ref}, for jets selected in the central region of the hadronic calorimeter (| $\eta^{lead\ jet}$ |<0.8) (left) and of the calibrated jet η (right). The ratio is shown for both data and two different MC simulations for γ+jets. Only statistical uncertainties are shown [75].

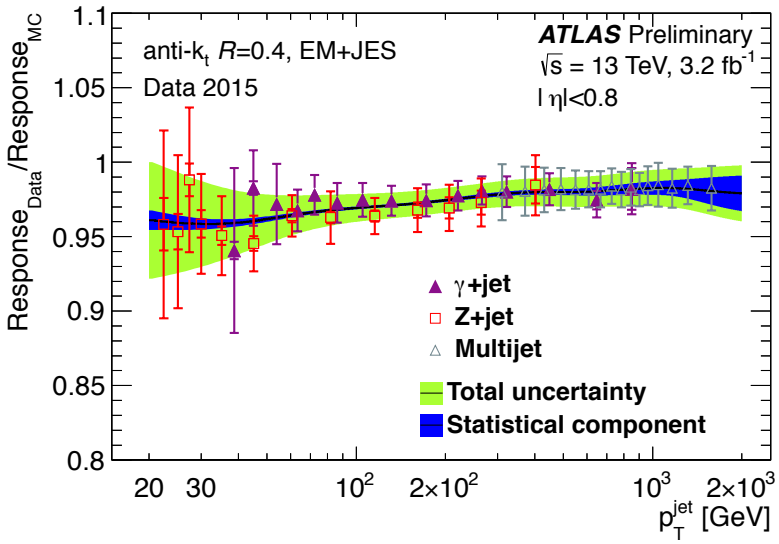

Figure 4.6: Jet response ratio of the data to the Monte Carlo simulation, for anti-k_t R=0.4 jets calibrated with the EM+JES scheme, as a function of p_T for three *in situ* techniques combined to determine the *in situ* energy scale correction: Z+jet (squares), γ+jet (full triangles) and multijet (empty triangles). The error bars indicate the statistical and the total uncertainties [76].

4.5 Identification of *b*-jets

Jets originating from B-hadrons (b-jets), i.e. containing a b-quark, are key objects for many searches and measurements in the LHC physics program and, in particular, for the analysis which will be described in this thesis.

In order to distinguish this type of jets from those originating from gluons, light and c-quarks, several algorithms have been developed, exploiting the long lifetime, high mass and decay multiplicity of B-hadrons. They are commonly referred as "b-tagging" algorithms. B-hadrons have a relatively long lifetime, around 1.6 (1.5) $\times$ 10^{-12} s for $B^{\pm}$ (B^0) mesons, which leads to a measurable flight length of a few millimeters before their subsequent decay. This results in the presence of a displaced secondary vertex (SV).

There are different means for identifying the B-hadrons decay at a SV. One way is to measure the impact parameters (IP) of tracks coming from the decay, i.e. the distance from the point of closest approach of the track to the interaction vertex. The sign of the IP is positive if the point of closest approach lies upstream with respect to the jet direction and negative otherwise. One can also attempt to reconstruct the secondary vertex explicitly. Another way is based on the topological structure of weak B-hadrons decays inside the jet, assuming they occur on the B-hadron flight direction, and tries to reconstruct the full B-hadron decay chain.

In the ATLAS experiment, three different basic b-tagging algorithms, based on the B-hadrons decay features described above, are used:

- Impact parameter based algorithms (IP2D, IP3D) [77]:
- Secondary vertex reconstruction based algorithms (SV) [77].
- Decay chain multi-vertex reconstruction algorithms (JetFitter) [78].

The final b-tagging algorithm used in Run-2 is the so-called MV2c20 discriminant [79] and is defined as the output of a Boosted Decision Tree (BDT) using, as input variables, the outputs of the basic b-tagging algorithms mentioned above. The training of the BDT is performed on a set of about 5 million $t\bar{t}$ events and assigning b-jets as signal and a mixture of 80% light-flavor jets and 20% c-jets as background. The flavor label for simulated jets is assigned by matching to truth-level weakly decaying b and c hadrons. If no match is found, in order, for b, c hadrons or τ leptons, the jet is labeled as a light-flavor jet. Other background mixtures of light and c-flavor jets were considered for the BDT training, including a background sample formed by only light-flavor jets. In this case, the outcome of the BDT training is called MV2c00 discriminant. The mixture used for the MV2c20 discriminant was found to be a good compromise between light and $c-$jets rejection. The output distribution of the MV2c20 algorithm is shown in Figure 4.7.

Four operating points are defined by a single cut value on the MV2c20 distribution. Each point provides a specific b-jet efficiency with which a jet containing a B-hadron is

tagged by the b-tagging algorithm for a $t\bar{t}$ sample, summarized in Table 4.1. For the analysis described in the thesis the 77% b-jet efficiency working point will be used.

Figure 4.8 shows the performance of the b-tagging algorithms MV2c20 and MV2c00, in terms of the b-jet efficiency versus both the light and c-jets rejection. One can see that, at the cost of a slightly lower light-flavor jets rejection with respect to MV2c00, MV2c20 has a significant larger rejection for c-jets.

The MV2 algorithm represents a significant improvement and also a simplification of the main b-tagging algorithm used in Run-1, called MV1. The latter was based on a neural network rather than on a BDT. In the Run-2 analysis, the MV2c20 discriminant will be used for selecting $b-$jets, while the MV1 was used for the preliminary sensitivity studies presented in Chapter 5.

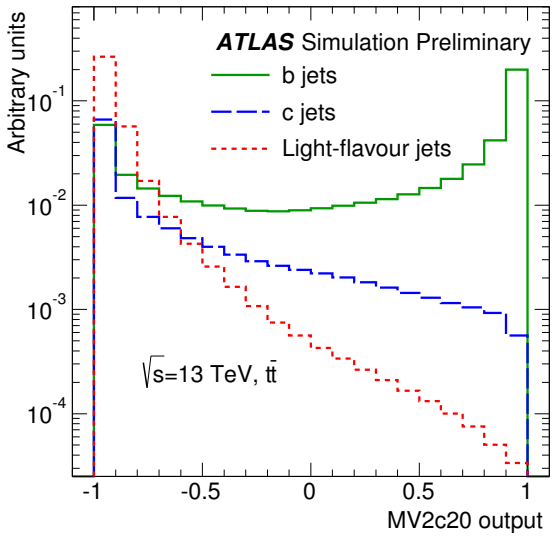

Figure 4.7: The output distribution of the MV2c20 b-tagging algorithm for b- (solid green), c-(dashed blue) and light-flavor (dotted red) jets in $t\bar{t}$ events [79].

Cut on MV2c20 output	b-jet efficiency [%]	c-jet rejection	τ-jet rejection	Light-jet rejection
0.4496	60	21	93	1900
-0.0436	70	8.1	26	440
-0.4434	77	4.5	10	140
-0.7887	85	2.6	3.8	28

Table 4.1: Operating points for the MV2c20 b-tagging algorithm shown with the reference numbers for the efficiency and rejection rates [79].

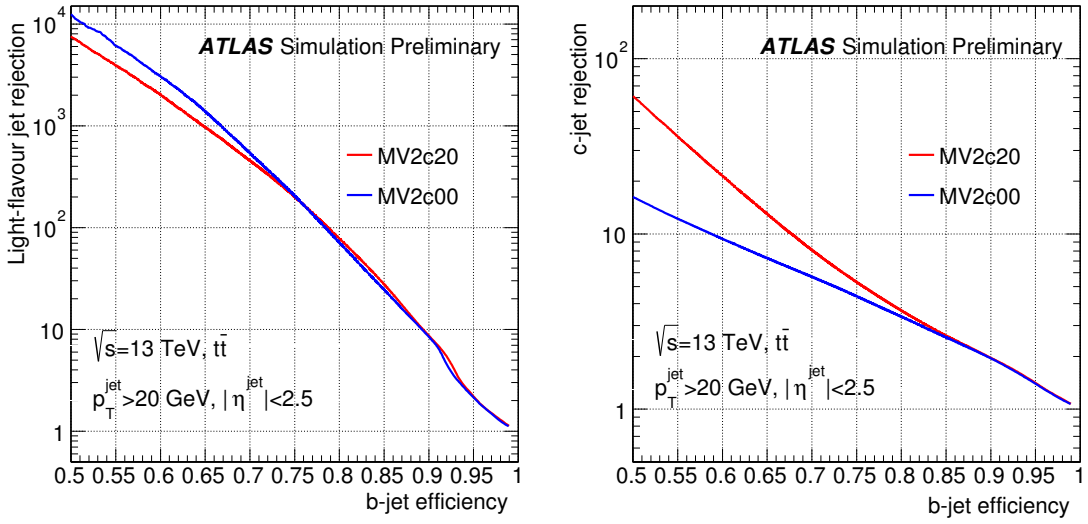

Figure 4.8: The light-flavor (left) and c-jet (right) rejection versus b-jet efficiency for the MV2c20 (red) and the MV2c00 (blue) b-tagging algorithms in $t\bar{t}$ events [79].

4.6 Missing transverse momentum

An imbalance in the sum of visible momenta in the plane transverse to the beam axis is known as missing transverse momentum, $\vec{p}_{\mathrm{T}}^{\,\mathrm{miss}}$. The magnitude of this vector is the so-called missing transverse energy, denoted as $E_{\mathrm{T}}^{\mathrm{miss}}$. The $\vec{p}_{\mathrm{T}}^{\,\mathrm{miss}}$ is another fundamental ingredient of the analysis presented in this thesis and, in general, of many physics searches at the LHC, such as R-parity conserving SUSY searches.

The $\vec{p}_{\mathrm{T}}^{\,\mathrm{miss}}$ is obtained from the negative vector sum of the momenta of all particles detected in a pp collision [80]. Reconstructed and calibrated objects are used to calculate the two components of the $\vec{p}_{\mathrm{T}}^{\,\mathrm{miss}}$ in an event as:

$$p_{x(y)}^{miss} = p_{x(y)}^{miss,e} + p_{x(y)}^{miss,\gamma} + p_{x(y)}^{miss,\tau} + p_{x(y)}^{miss,jets} + p_{x(y)}^{miss,\mu} + p_{x(y)}^{miss,soft}, \tag{4.5}$$

where the terms for jets, charged leptons and photons are the negative sum of the momenta for the respective calibrated objects. Energy deposits in the calorimeters are associated to these reconstructed objects in the following order: electrons (e), photons (γ), hadronically decaying τ-leptons, jets and muons (μ). To suppress contributions from jets originating from pileup interactions, a requirement on the JVT variable may be applied to select jets.

Contributions in the detector which are not associated with any object constitute the soft term. This can be reconstructed from ID tracks (track-based soft term) or calorimeter deposits (calorimeter-based soft term) and is included in the $\vec{p}_{\mathrm{T}}^{\,\mathrm{miss}}$ calculation in order to recover the contribution from low low p_T particles.

The values of $E_{\mathrm{T}}^{\mathrm{miss}}$ and its azimutal coordinate ϕ^{miss} are defined as:

$$E_{\mathrm{T}}^{\mathrm{miss}} = \sqrt{(p_x^{\mathrm{miss}})^2 + (p_y^{\mathrm{miss}})^2}, \qquad \phi^{\mathrm{miss}} = \arctan\,(p_y^{\mathrm{miss}}/p_x^{\mathrm{miss}}). \tag{4.6}$$

The distributions of the E_T^{miss} and of its track soft term for the 2015 dataset are presented in Figure 4.9 for a $Z \to \mu\mu$ selection, where the MC has been normalized to the cross section and the recorded luminosity. A good description of the E_T^{miss} by the MC samples is observed.

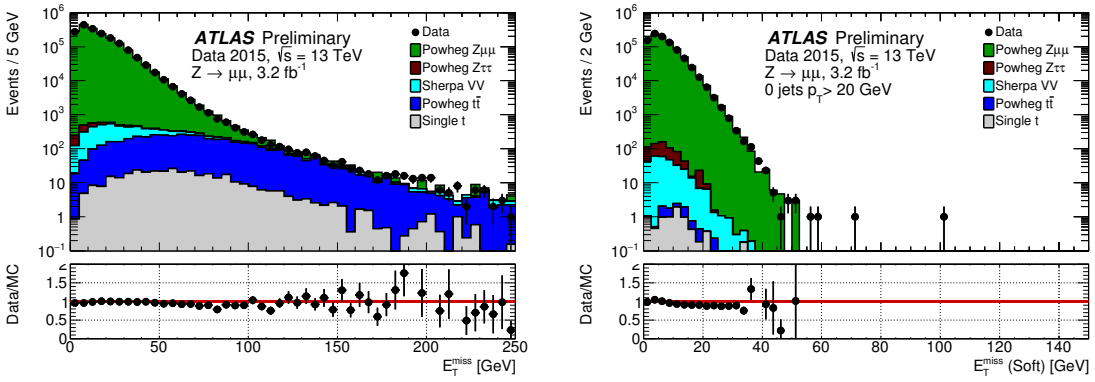

Figure 4.9: E_T^{miss} distribution (left) and track-based soft term E_T^{miss} distribution requiring 0 jets (right) for a final state of Z decay to a pair of muons for the 2015 dataset, corresponding to 3.2 fb^{-1} [81]. The expectation from MC simulation is superimposed after each MC sample is weighted with its corresponding cross section.

The performance of the E_T^{miss} depends significantly on the amount of in-time and out-of-time pileup of the event and is studied in $Z \to \ell\ell$ and $W \to e\nu$ processes [80]. The first process has a very clean signature without genuine E_T^{miss}, so the measured missing momentum comes from the mismeasurement of objects due to non perfect reconstruction or detector response. The second process has real E_T^{miss}.

The total transverse energy $\sum E_T$, which is defined as the scalar sum of transverse momenta of the hard objects and soft term contributions, is another important quantity to estimate the event activity.

The E_T^{miss} resolution can be evaluated in bins of $\sum E_T$ (or of number of primary vertices) for $Z \to \ell\ell$ data and MC events by estimating the width of E_x^{miss} and E_y^{miss} for each bin. The resolution curves obtained with the 2015 dataset are shown in Figure 4.10 as a function of the $\sum E_T$ in the event (left) and as a function of N_{PV} (right) for $Z \to \mu\mu$ events, showing an overall good agreement between data and MC simulation.

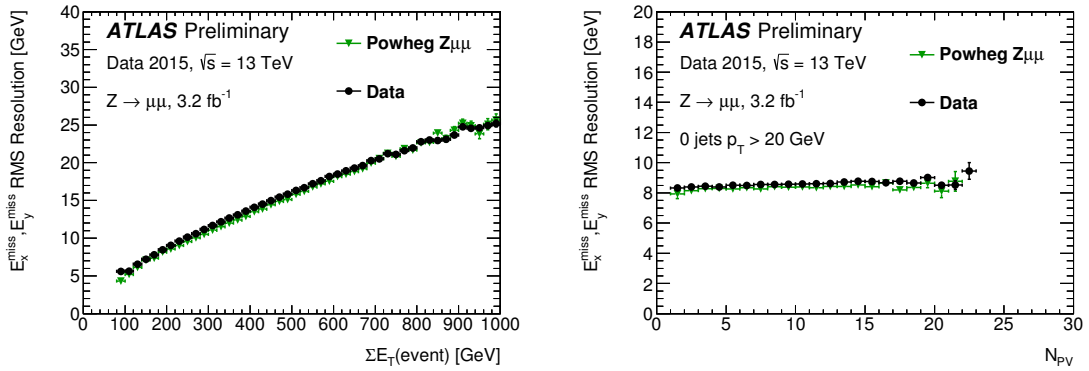

Figure 4.10: E_T^{miss} resolution for simulated $Z \to \mu\mu$ events overlaid with 2015 data as a function of the $\sum E_T$ in the event (left) and of the number of primary vertexes (right) for events with 0 jets [81].

The E_T^{miss} scale can also be estimated in $Z \to \ell\ell$ events, by taking the mean value of the component of the $\vec{p}_{\mathrm{T}}^{\,\mathrm{miss}}$ along the $\mathbf{p_T^Z}$ axis in the transverse plane. The unit vector of $\mathbf{p_T^Z}$ is called $\mathbf{A_Z}$ and is defined as:

$$\mathbf{A_Z} = \frac{\mathbf{p_T}^{\ell^+} + \mathbf{p_T}^{\ell^-}}{|\ \mathbf{p_T}^{\ell^+} + \mathbf{p_T}^{\ell^-}\ |}, \tag{4.7}$$

where $\mathbf{p_T}^{\ell^+}$ and $\mathbf{p_T}^{\ell^-}$ are the transverse momenta of the leptons from the Z boson decay. $\mathbf{A_Z}$ is sensitive to the balance between the hard objects (the leptons) and the soft hadronic recoil. If the balance is perfect, then $\langle E_T^{miss} \cdot A_Z \rangle$ =0 is expected. The E_T^{miss} scale for data and MC is shown in Figure 4.11 for $Z \to ee$ events. The agreement between data and MC is good, the negative bias of about 5 GeV at low p_T^Z most probably indicates an underestimation of the E_T^{miss} due to soft neutral particles not included in the computation and to the limited acceptance of the ID.

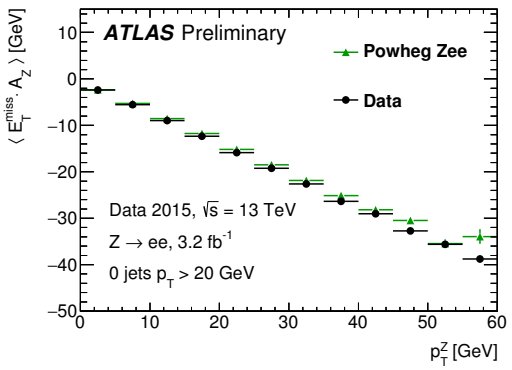

Figure 4.11: E_T^{miss} scale for simulated $Z \to ee$ events overlaid with 2015 data as a function of the p_T^Z for events with 0 jets [81].

Chapter 5

Sensitivity studies for sbottom quark searches at $\sqrt{s}$ =13 TeV

As it was already mentioned in Chapter 2, searches for the Supersymmetric partners of the quarks of the third generation constitute one of the pillars of the ATLAS and CMS physics programs at the LHC.

Run-1 searches for the top and the bottom squarks with pp collisions at center-of-mass energies of 7 and 8 TeV have set stringent limits on these particles. In particular, Figure 5.1 shows the diagram corresponding to the pair production of the bottom squark ($\tilde{b}$), decaying exclusively as $\tilde{b} \rightarrow b\tilde{\chi}_1^0$.

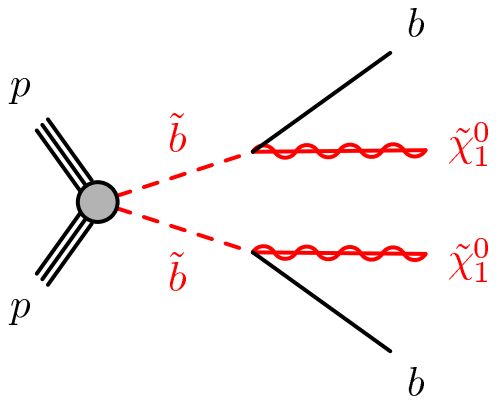

Figure 5.1: Diagram illustrating the pair production and decay of a bottom squark ($\tilde{b}$) decaying as $\tilde{b} \rightarrow b\tilde{\chi}_1^0$ with 100% branching ratio.

The Run-1 results for this channel are collected in Ref. [82] and presented in Figure 5.2. The search was performed in final states with two b-tagged jets and missing transverse momentum. A 95% confidence level limit of the mass of the lightest bottom squark, $m_{\tilde{b}_1}$, above 640 GeV was set for neutralino masses $m_{\tilde{\chi}_1^0} < 150$ GeV.

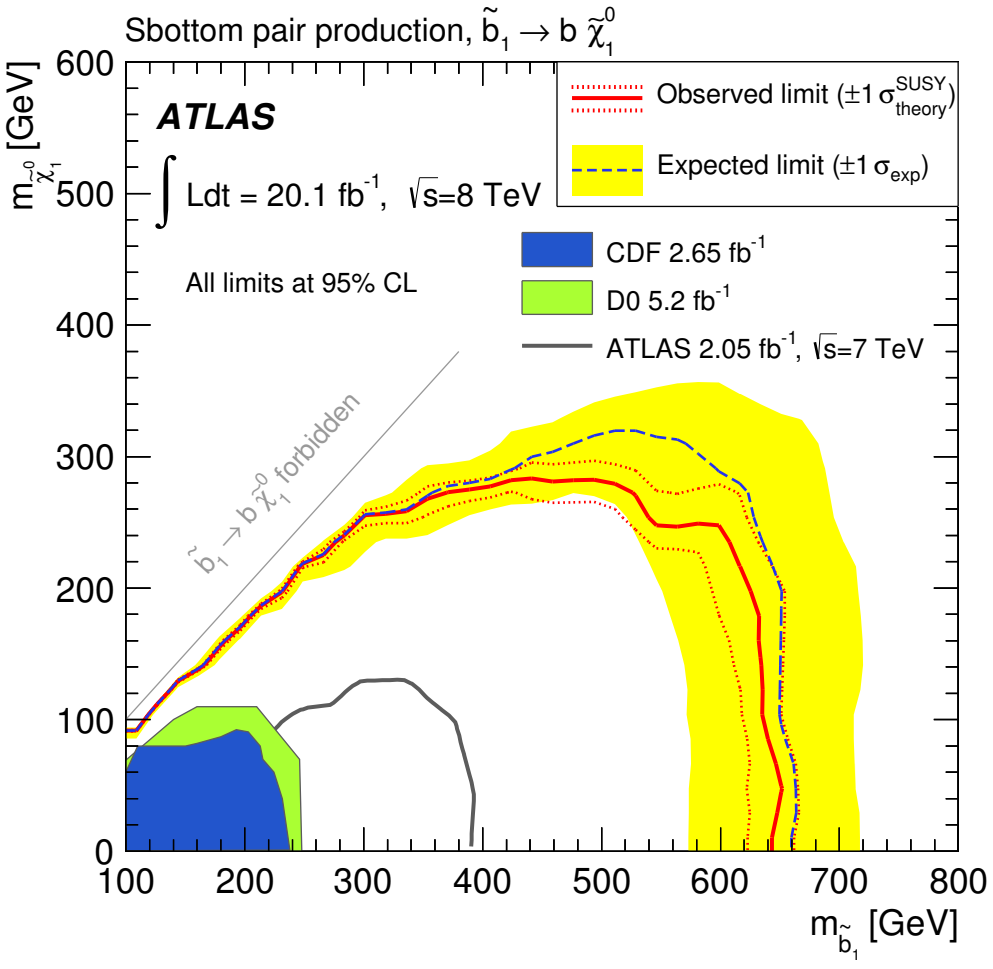

Figure 5.2: Expected and observed exclusion limits at 95% CL in the ($m_{\tilde{b}_1}$, $m_{\tilde{\chi}_1^0}$) mass plane for the direct sbottom pair production with the sbottom decaying exclusively as $\tilde{b}_1 \rightarrow b\tilde{\chi}_1^0$ at $\sqrt{s} = 8$ TeV as presented in Ref. [82].

In this chapter, a new study of the sensitivity of the search for bottom squarks in the same final state is presented. The study was performed before the start of Run-2, and in view of the increase of the center-of-mass energy of pp collisions at the LHC from 8 to 13 TeV. The aim of this study was that of providing a reference for the expected discovery reach for different integrated luminosities and several assumptions on the total systematic uncertainty on the SM predictions.

It was already anticipated that the increase of the center-of-mass energy of the pp collisions would have resulted in a large increase in the sensitivity for those searches targeting heavy stops and sbottoms. For a stop/sbottom with a mass of 800 GeV, the production cross section increases of almost a factor 10 (increasing from 2.9 fb at $\sqrt{s} = 8$ TeV to 28 fb at $\sqrt{s} = 13$ TeV).

The sensitivity study is performed using the first available simulated samples at $\sqrt{s} = 13$ TeV for the SM background estimation. These samples, produced in 2014, were only aimed for optimization studies and sensitivity projections. The Monte Carlo statistics in these preliminary samples at $\sqrt{s} = 13$ TeV was significantly lower than that of the MC samples used later for the actual Run-2 analysis. This constituted an important limitation for the sensitivity studies presented here.

The signal regions used in the 8 TeV analysis are used as a starting point for this study and re-optimized for bottom squarks above the Run-1 mass limit ($\gtrsim 700$ GeV).

Different benchmark luminosity scenarios, ranging from 1 fb^{-1} to 10 fb^{-1}, are considered, as potential references for the luminosity to be collected in 2015.

The sensitivity study is documented in the ATLAS public note *Sensitivity studies for squarks and gluinos with 1-10 fb^{-1} of 13 TeV data* (ATL-PHYS-PUB-2015-005, March 2015), together with similar studies for gluino pair production.

5.1 Simulated event samples

Monte Carlo simulated samples are used to estimate background and signal contributions in the signal region as well as for the signal region optimization. The signal samples of sbottom pair production with subsequent sbottom decay as $\tilde{b}_1 \to b\tilde{\chi}_1^0$ with 100% branching ratio are produced using the MADGRAPH v5 generator [44] and leading-order matrix elements with up to two additional partons. The CTEQ6L1 [31] PDF set is used in the generation. PYTHIA 6.425 [40] with the AUET2B tune [83] is used for parton shower and hadronization, and to model the underlying event. The signal samples are normalized to the NLO+NLL cross sections, as detailed in Ref. [84]. The list of signal samples considered is shown in Table 5.1.

Sample	Dataset ID	Generated events	σ [pb] (NLO+NLL)
$(m_{\tilde{b}_1}, m_{\tilde{\chi}_1^0}) = (700, 1)$ GeV	202260	20000	0.067
$(m_{\tilde{b}_1}, m_{\tilde{\chi}_1^0}) = (800, 1)$ GeV	202266	50000	0.028
$(m_{\tilde{b}_1}, m_{\tilde{\chi}_1^0}) = (900, 1)$ GeV	202270	10000	0.013
$(m_{\tilde{b}_1}, m_{\tilde{\chi}_1^0}) = (1000, 1)$ GeV	202277	10000	0.006

Table 5.1: Signal samples for sbottom pair production used in the analysis.

Simulated $t\bar{t}$ events are generated using the POWHEG generator [45], which implements the NLO matrix element for inclusive $t\bar{t}$ production, with the CT10 PDF set [32]. POWHEG is interfaced to PYTHIA 6.425 with the CTEQ6L1 set of PDFs using the Perugia2012 tune [85]. Samples of single top quark backgrounds corresponding to the t-, s- and Wt production mechanisms are generated with POWHEG using the CT10 PDF set. All samples are interfaced to PYTHIA 6.425 with the CTEQ6L1 set of parton distribution functions using the Perugia2012 tune. Overlaps between the $t\bar{t}$ and Wt final states are removed using the diagram removal scheme in Ref. [86].

Simulated W/Z+jets samples are produced using Sherpa [43] with massive b, c-quarks with up to four additional partons in the matrix element and parton shower and are normalized to NLO QCD theoretical cross sections [87]. Other small background contributions from diboson (WW, ZZ, and WZ) processes are not included in this study due to the lack of simulated samples. The impact of these backgrounds can be considered negligible for the purpose of the sensitivity studies.

A summary of the MC generation parameters for the different SM background processes is collected in Table 5.2.

Sample	Generator	PDF	Shower	Normalization
$t\bar{t}$	POWHEG	CT10	PYTHIA 6.425	NNLO+NNLL
W+jets	SHERPA	CT10	SHERPA	NLO
Z+jets	SHERPA	CT10	SHERPA	NLO
Single top	POWHEG	CT10	PYTHIA 6.425	**From generator**
$t\bar{t}V$ $(V = W, Z)$	MADGRAPH	CTEQ6L1	PYTHIA 6.427	**From generator**

Table 5.2: A summary of generators, PDF sets and cross section calculations used for the various MC samples to simulate SM background processes.

5.2 Objects definition and selection

In this section some information about the definition of the objects used in the study, specifically (b-)jets, electrons, muons and the missing transverse momentum, is provided.

Jet definition. Jets are reconstructed using the anti-k_t algorithm with a distance parameter R=0.4 and are seeded by topological calorimeter clusters, as described in Section 4.4. They are calibrated with the local cluster weighting (LCW) calibration

method and the jet energy scale calibration, corresponding to the LCW+JES calibration scheme [69]. All selected jets are required to be in the central region of the detector ($|\eta|<2.8$) with $p_T > 30$ GeV.

Jets originating from b-quarks are identified using the MV1 algorithm using the 70% efficiency working point. This corresponds to a MV1 weight larger than 0.7892, as described in Section 4.5. The b-jets are initially selected with $p_T > 30$ GeV and $|\eta|<2.5$.

Electrons. Electrons are reconstructed as described in Section 4.2 and are selected using the medium identification criteria, with $p_T > 15$ GeV and $|\eta^{cluster}| < 2.47$. These initially selected electrons are used to perform the overlap removal between leptons and jets, as described below. In order to reproduce the electron energy scale resolution as measured in the 8 TeV data, smearing factors are applied to MC for the reconstructed electrons. No isolation requirement is applied in these studies.

Muons. Muons are reconstructed combining information from the inner detector and the muon spectrometer (combined muons), as described in Section 4.3. Only muons with $p_T > 10$ GeV and $|\eta| < 2.4$ are selected and required to pass the loose quality requirements. A smearing is applied to the muon p_T in order to correct the imperfect muon momentum resolution as simulated by the MC to that measured in the 8 TeV data. Muons with features consistent with those of a cosmic ray are rejected. As for electrons, no isolation requirement is applied on the muon candidates.

Removing overlapping objects. In order to avoid double counting of final state objects, which may fall into more than one category, a procedure is followed to remove overlaps. A typical case is that when an isolated electron is reconstructed both as an electron and as a jet. To avoid this situation, firstly jets with $\Delta R < 0.2$ from an electron are removed from the jet list in the event. Secondly electrons (muons) are removed from the electron (muon) list if their distance to the closest jet is $\Delta R < 0.4$.

$E_{\mathrm{T}}^{\mathrm{miss}}$ **definition.** The $E_{\mathrm{T}}^{\mathrm{miss}}$ is calculated as described in Section 4.6. The muon term is not included, as muons are considered as invisible particles in this study. The soft term is built from topoclusters not associated to any reconstructed object. The use of a track-based estimation of this soft activity was studied and no significant improvement was observed at that time compared to the calorimeter based definition adopted here. Nevertheless, this aspect was further reviewed for the final Run-2 analysis.

Event preselection. A minimum set of preselection criteria is applied, despite of the fact that this is a MC based study.

- *Vertex selection*: events are selected to have at least a reconstructed primary vertex with two tracks of $p_T > 400$ MeV associated to it.

- *Jet cleaning*: fake jets can arise from non-collision background or cosmic events with a catastrophic muon energy deposit in the calorimeters or fake signals in the calorimeter (either from noise bursts or from the presence of coherent noise). A set of requirements which have high rejection against fake jets and preserves essentially the 100% of the signal jets is applied. These requirements are based on the timing of the calorimeter signal with respect to that of the bunch crossing, on the quality of the fit to the calorimeter pulse shapes, on the fraction of jet energy belonging to specific calorimeter samples, and on the amount of jet charged fraction [1] (as measured in the Inner Detector).

5.3 Signal region definition

The signal region is designed to target large mass splittings Δm between the sbottom and the neutralino mass (Δm = $m_{\tilde{b}_1} - m_{\tilde{\chi}_1^0}$ >250 GeV), identifying two b-tagged high-p_{T} leading jets as products of the two bottom squarks decays. The optimization of the selection for this region is similar to the one adopted for the 8 TeV analysis [82] and is based on a set of variables which have been proven to be useful to reject the SM background effectively:

- min[$\Delta\phi(jet_{1,2,3}, E_{\mathrm{T}}^{\mathrm{miss}})$]: defined as the minimum $\Delta\phi$ between any of the three leading jets and the $E_{\mathrm{T}}^{\mathrm{miss}}$. The background from QCD multijet is characterized by small values of this variable, since for these events the $E_{\mathrm{T}}^{\mathrm{miss}}$ is likely to be aligned with a jet in the transverse plane.

- m_{eff}: This is defined as the scalar sum of the p_{T} of the two leading jets with p_{T} >30 GeV and $|\eta|$ <2.5 and the $E_{\mathrm{T}}^{\mathrm{miss}}$.

$$m_{eff} = \sum_{i \leq 2} (p_{\mathrm{T}}^{\mathrm{jet}})_i + E_{\mathrm{T}}^{\mathrm{miss}} \tag{5.1}$$

  This variable is used in association with the $E_{\mathrm{T}}^{\mathrm{miss}}$in order to further reject the QCD multijet background.

- m_{BB}: this is defined as the invariant mass of the two b-jets. A selection on this variable helps reducing the contamination from $t\bar{t}$ events.

- m_{CT}: the contransverse mass ([82, 88]) is a kinematic variable defined to measure the masses of pair-produced semi-invisibly decaying heavy particles. For two identical decays of heavy particles (the bottom squarks, in this analysis) into two visible

[1] The charged fraction is defined as $f_{\mathrm{ch}} = \sum p_{\mathrm{T}}^{\mathrm{track,jet}} / p_{\mathrm{T}}^{\mathrm{jet}}$, where $\sum p_{\mathrm{T}}^{\mathrm{track,jet}}$ is the scalar sum of the transverse momenta of the tracks associated to the primary vertex within a cone of radius 0.4 around the jet axis, and $p_{\mathrm{T}}^{\mathrm{jet}}$ is the transverse momentum as determined from the calorimetric measurements.

particles v_1 and v_2 (the b-quarks), and two invisible particles ($\tilde{\chi}_1^0$), m_{CT} is defined as:

$$m_{CT}^2(v1,\ v2) = [E_T(v1) + E_T(v2)]^2 - [\mathbf{p}_{\mathrm{T}}(v1) - \mathbf{p}_{\mathrm{T}}(v2)]^2, \tag{5.2}$$

with $E_T = \sqrt{p_{\mathrm{T}}^2 + m^2}$. It has a kinematical endpoint at

$$m_{CT}^{max} = \frac{m_i^2 - m_X^2}{m_i^2}, \tag{5.3}$$

where i is the initially pair produced particle. This variable is extremely effective in suppressing the top production background ($i = t$, $X = W$), for which the endpoint is at about 135 GeV.

The signal region selection, referred to as SRA in the 8 TeV analysis [82], is outlined in Table 5.3.

SRA selection	
Event cleaning	No bad jets, vertex requirements
Lepton veto	No e (μ) with $p_{\mathrm{T}}>$ 15(10) GeV
$E_{\mathrm{T}}^{\mathrm{miss}}$	$>$ 250 GeV
jet 1	$p_{\mathrm{T}}>$ 130 GeV , $\lvert\eta\rvert<$ 2.8
jet 2	$p_{\mathrm{T}}>$ 50 GeV , $\lvert\eta\rvert<$ 2.8
jet multiplicity	Veto on 4^{th} jet with $p_{\mathrm{T}}>$ 30 GeV
b-tagging	2 b-jets (jet 1 and jet 2) with $\mid \eta \mid$<2.5
$\min[\Delta\phi(jet_{1,2,3}, E_{\mathrm{T}}^{\mathrm{miss}}]$	>0.4
$E_{\mathrm{T}}^{\mathrm{miss}}/m_{eff}$	>0.25
m_{BB}	>200 GeV
m_{CT}	>400 GeV

Table 5.3: The event selection in SRA.

In the 8 TeV analysis, several signal regions were defined by varying the cut on m_{CT} (150 GeV to 350 GeV), targeting different regions of the $m_{\tilde{b}_1} - m_{\tilde{\chi}_1^0}$ phase space.

The discovery significance is optimized as a function of the m_{CT} cut for the signal points corresponding to $m_{\tilde{b}_1}$ =700 GeV, $m_{\tilde{\chi}_1^0}$ = 1 GeV and $m_{\tilde{b}_1}$ =800 GeV, $m_{\tilde{\chi}_1^0}$ =1 GeV (see Figure 5.3).

The m_{CT} requirement, m_{CT} >400 GeV, is found to be optimal for the signal with $m_{\tilde{b}_1}$ =700 GeV, $m_{\tilde{\chi}_1^0}$ = 1 GeV. This threshold is close to the maximum of the significance for the signal with $m_{\tilde{b}_1}$ =800 GeV, $m_{\tilde{\chi}_1^0}$ = 1 GeV, but safely distant from the sudden drop in significance which occurs at ∼600 GeV, the latter due to lack of statistics in the background simulation (affecting, for example, the Wt-channel single top background). As discussed in the next chapter, a tighter requirement in SRA-like signal regions will be adopted in the Run-2 analysis, since the MC statistics will not be a limiting factor anymore.

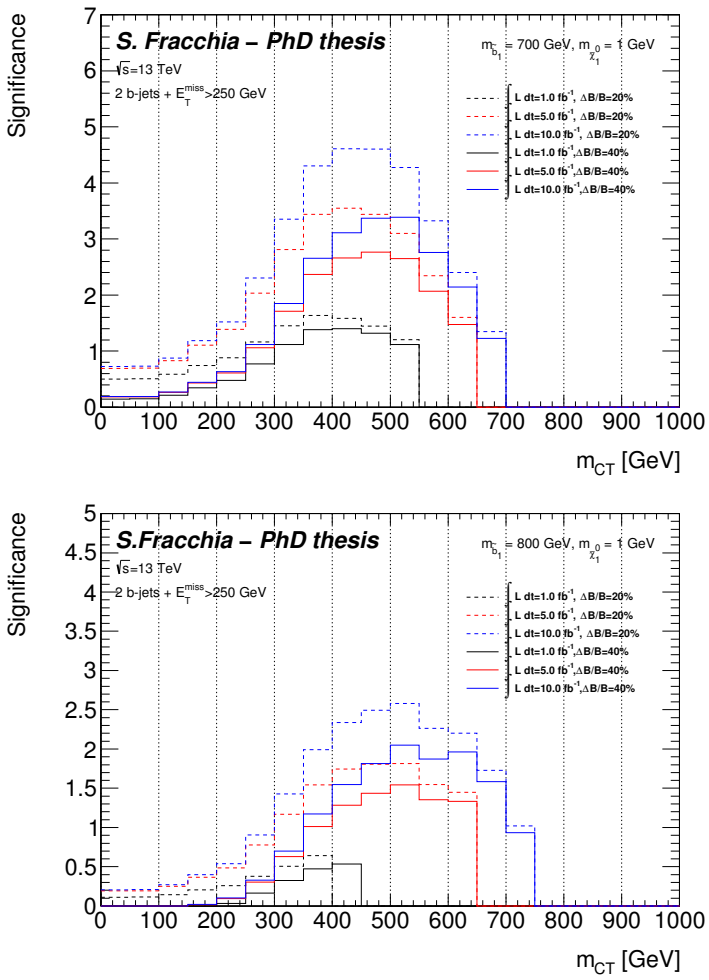

Figure 5.3: The significance, computed using the BINOMIALOBSZ function from ROOSTATS [89], with an uncertainty of 20 or 40% on the SM background expectation, as a function of the m_{CT} threshold for the SRA selection for different values of integrated luminosity. The signal points used correspond to $m_{\tilde{b}_1}$ =700 GeV, $m_{\tilde{\chi}_1^0} = 1$ GeV (top) and $m_{\tilde{b}_1}$ =800 GeV, $m_{\tilde{\chi}_1^0} = 1$ GeV (bottom). The significance has been computed only in the presence of at least one signal event, for each luminosity.

In the course of the studies, a small difference is introduced in the event selection with respect to the 8 TeV analysis, which concerns the jet multiplicity requirement. In the 8 TeV strategy, jets with p_{T} >30 GeV were selected in the signal region and a veto on any third jet with p_{T} >50 GeV was applied. Here, in order to adopt a uniform p_{T} requirement on the jet selection, events with a fourth jet with p_{T} above 30 GeV are vetoed in the signal region, thus keeping the jet definition consistent across the different variables used in the selection.

The other difference with respect to the 8 TeV strategy is the tighter requirement on the $E_{\mathrm{T}}^{\mathrm{miss}}$, raised from 150 GeV to 250 GeV, in order to take into account the foreseen $E_{\mathrm{T}}^{\mathrm{miss}}$ trigger-threshold in Run-2, and to maintain the analysis at the plateau of the trigger

efficiency.

Studies were performed indicating that this new approach does not affect the relative background composition in the signal region, while it increases the signal selection efficiency by about 10%.

5.4 Results

Table 5.4 shows the expected background yields for the analysis, corresponding to a total integrated luminosity of 1 fb^{-1}. As expected, the SM background is dominated by the irreducible Z($\rightarrow \nu\bar{\nu}$) + heavy flavour jets contribution, followed by single top and W($\rightarrow l\nu$) + heavy flavour jets processes. In addition, the signal yields for several sbottom masses, in the range between 700 GeV and 1 TeV, and a neutralino mass of 1 GeV are included.

	SRA ($m_{CT} > 400$ GeV)
Background prediction (events in 1 fb^{-1})	0.85 ± 0.11
$W(\rightarrow e\nu)$+jets	0.06 ± 0.02
$W(\rightarrow \mu\nu)$+jets	0.07 ± 0.00
$W(\rightarrow \tau\nu)$+jets	0.08 ± 0.02
Z/γ^* ($\rightarrow$ e^+ e^-)+jets	0.00 ± 0.00
Z/γ^* ($\rightarrow$ μ^+ μ^-)+jets	0.01 ± 0.00
$Z/\gamma^*(\rightarrow \tau^+\tau^-)$+jets	0.00 ± 0.00
$Z(\rightarrow \nu\bar{\nu})$+jets	0.50 ± 0.02
$t\bar{t}$	0.00 ± 0.00
single top	0.14 ± 0.10
$t\bar{t}$+W/Z	0.00 ± 0.00
SUSY signal ($m_{\tilde{b}_1}$ =700 GeV, $m_{\tilde{\chi}_1^0} = 1$ GeV)	2.24 ± 0.09
SUSY signal ($m_{\tilde{b}_1}$ =800 GeV, $m_{\tilde{\chi}_1^0} = 1$ GeV)	1.01 ± 0.02
SUSY signal ($m_{\tilde{b}_1}$ =900 GeV, $m_{\tilde{\chi}_1^0} = 1$ GeV)	0.49 ± 0.03
SUSY signal ($m_{\tilde{b}_1}$ =1000 GeV, $m_{\tilde{\chi}_1^0} = 1$ GeV)	0.24 ± 0.01

Table 5.4: The event yields in SRA for the considered background and signal samples, corresponding to an integrated luminosity of 1 fb^{-1}.

Figure 5.4 presents several of the relevant distributions in the signal region. In this case, a total integrated luminosity of 5 fb^{-1} is considered.

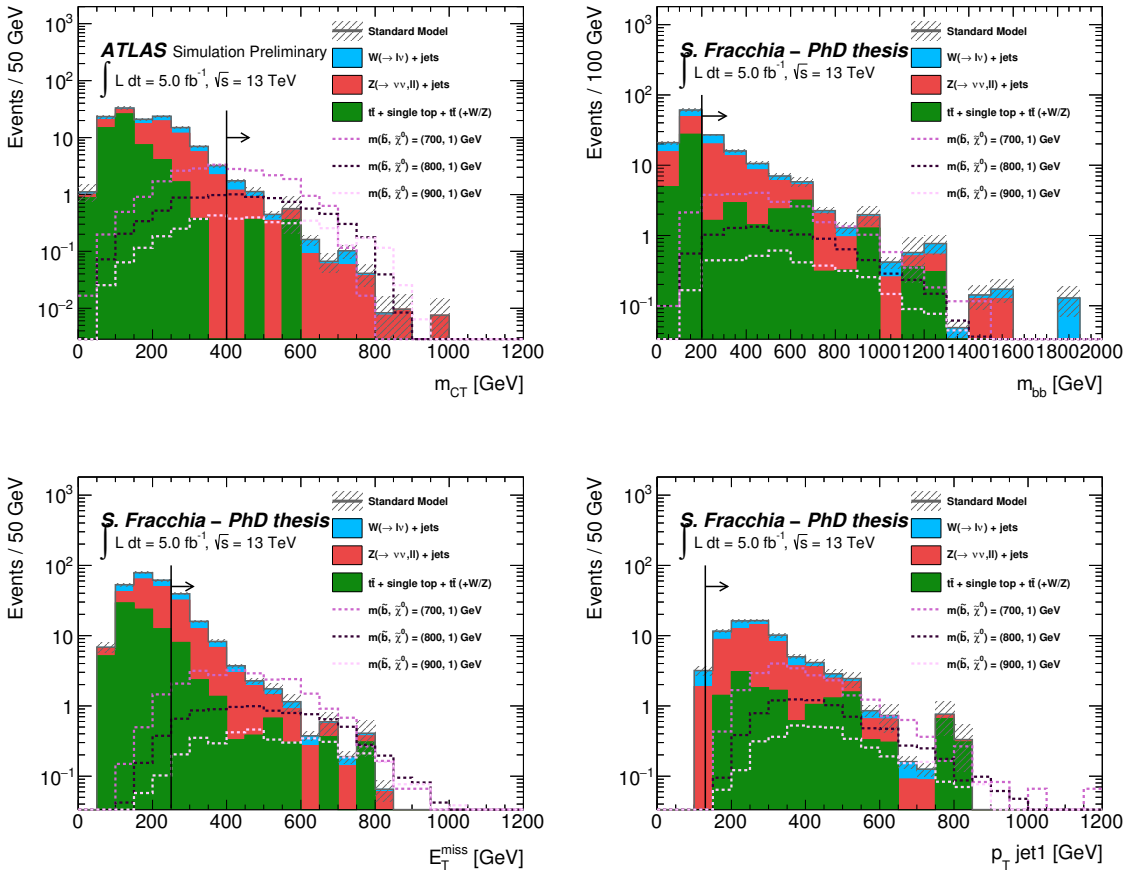

Figure 5.4: Distributions of the invariant mass of the two b-tagged jets, m_{CT}, $E_{\mathrm{T}}^{\mathrm{miss}}$, and the leading jet p_{T} in the signal region corresponding to a total integrated luminosity of 5 fb^{-1}. Each figure includes all the selection requirements except the one on the variable displayed. For illustration purposes, the distribution of several scenarios for sbottom pair production with different sbottom masses are included. The shaded bands show the size of the Monte Carlo statistical uncertainty. The final bin in all figures contains the overflows.

The results are translated into discovery prospects for a sbottom pair production signal. This study is limited to a light neutralino and a sbottom mass in the range between 700 GeV and 1 TeV. The statistical treatment is based on the BINOMIALOBSZ function from ROOSTATS [89] and was validated using the full HistFitter [90] machinery and the 8 TeV background estimation strategy. This requires as input the number of observed events (here defined as SUSY signal plus SM background), the SM background expectation, and the uncertainty on the SM background expectation.

Scenarios assuming 10% and 20% systematic uncertainties on the background estimate are considered, similarly to what was measured in the Run-1 analysis, as well as more pessimistic scenarios of 30% and 40% uncertainties.

Figures 5.5- 5.8 present the p-values obtained for the background-only hypothesis as a function of the sbottom mass. Four values of the total integrated luminosity in the range between 1 fb^{-1} and 10 fb^{-1} were used, corresponding to the initial expectation for the first year of the LHC Run-2 phase.
The study indicated that, provided nature was gentle, in a data sample of 5 fb^{-1}, a 3σ-level observation would be possible for sbottom masses below 750 GeV, assuming that the total systematic uncertainty on the background was contained within 10%. After the integration of 10 fb^{-1} of data, a 5σ discovery could be claimed for sbottom masses below 720 GeV, while a 3σ-level observation could be feasible in the data for a mass of 800 GeV.

As expected, the sensitivity is rapidly affected by the inflation of systematic uncertainties. For sbottom masses above 800 GeV, the signal selection does not have enough sensitivity anymore and a further optimization with tighter m_{CT} requirements is necessary.

As it was mentioned above, the signal region selection was influenced by the limited Monte Carlo statistics for the simulated samples used for these studies. Nevertheless, they constituted a good reference and starting point for the work developed subsequently towards and during Run-2. A tighter selection was ultimately used in the Run-2 analysis for the region targeting large Δm . The further optimizations adopted after these studies make the discovery prospects presented here quite pessimistic with respect to what was eventually achieved in the Run-2 analysis.

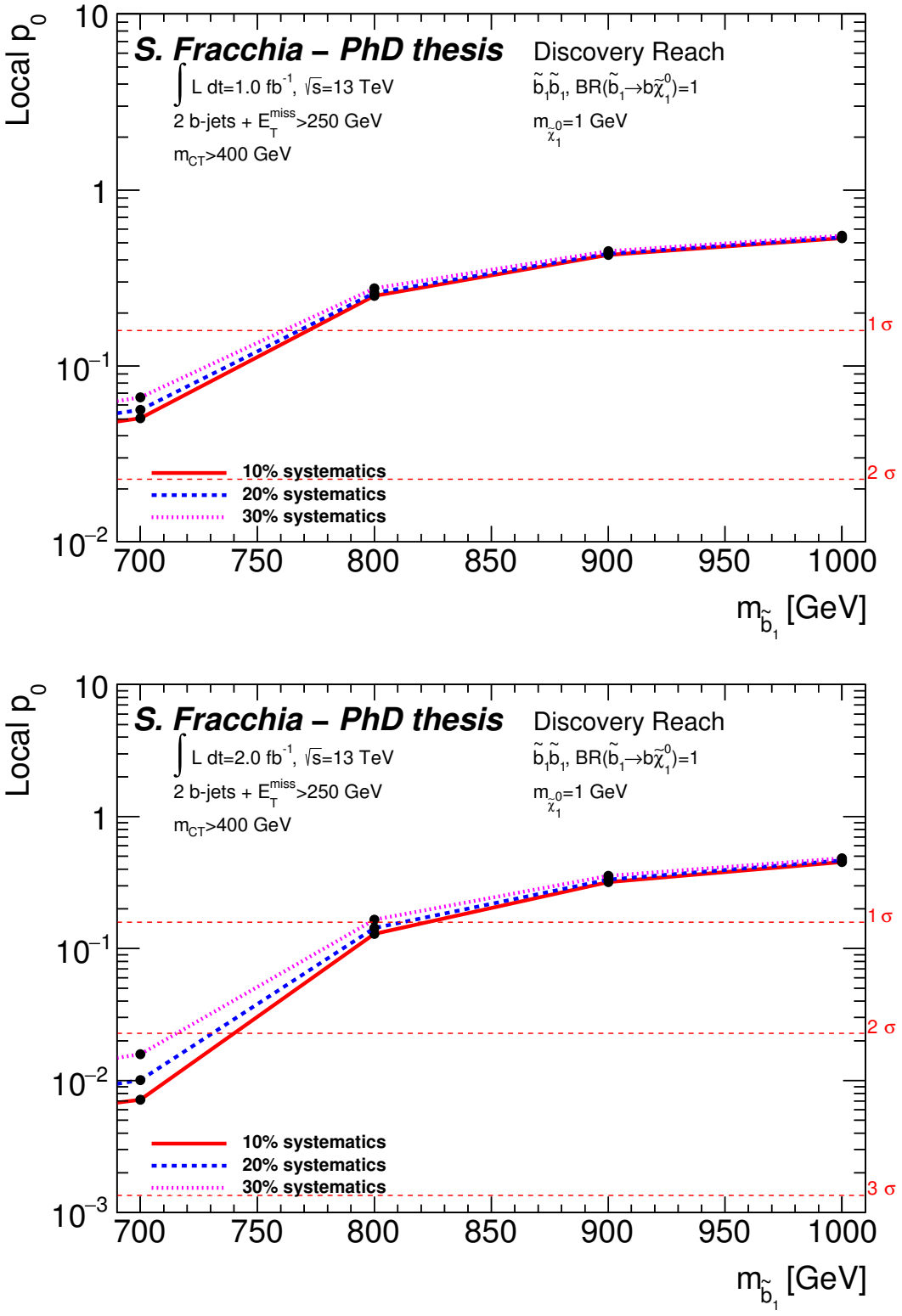

Figure 5.5: The p-values for a SM background only hypothesis as a function of the sbottom mass for different scenarios for the uncertainty on the total SM background, each plot corresponding to a fixed value of total integrated luminosity (1 and 2 fb^{-1}, respectively).

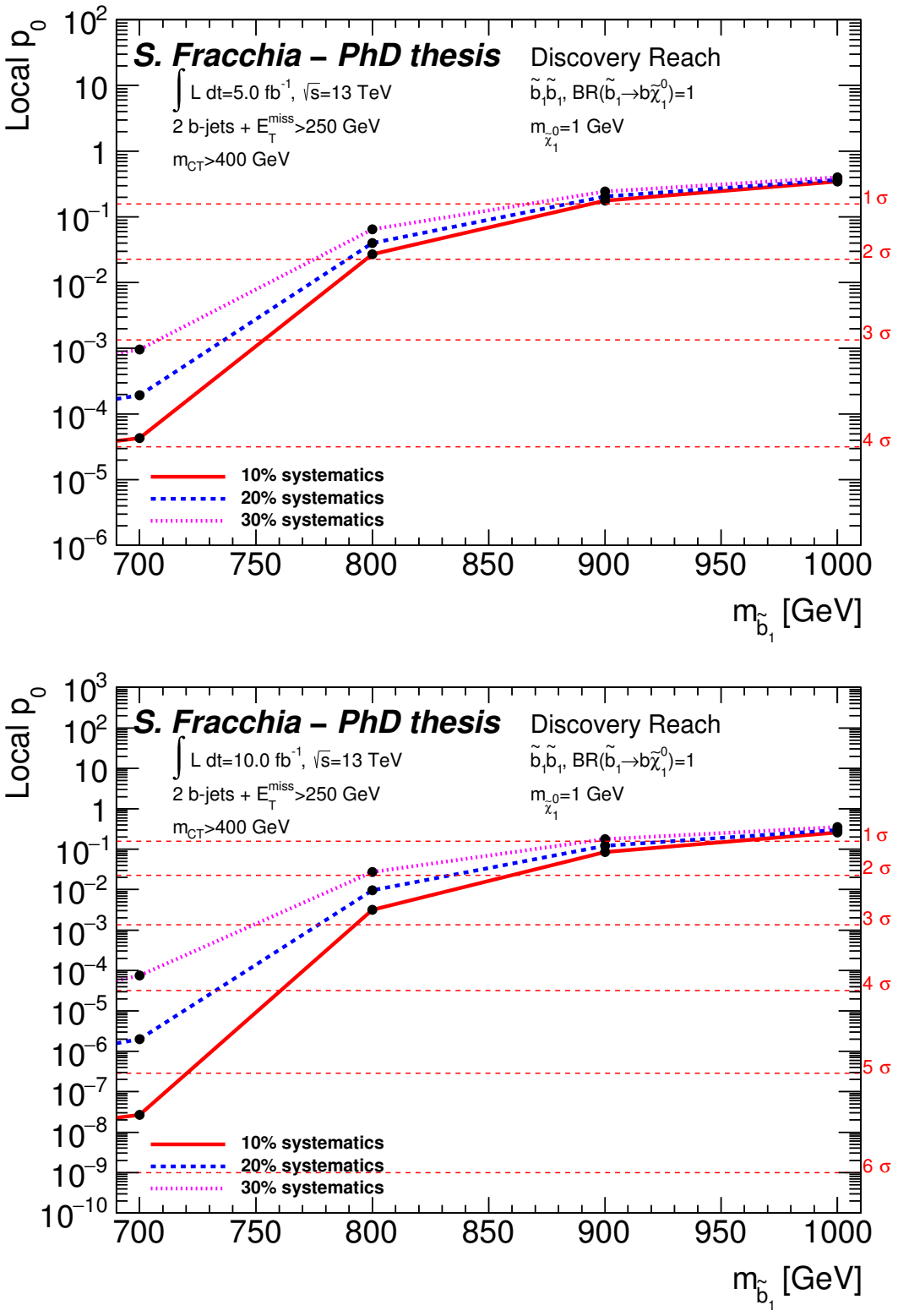

Figure 5.6: The p-values for a SM background only hypothesis as a function of the sbottom mass for different scenarios for the uncertainty on the total SM background, each plot corresponding to a fixed value of total integrated luminosity (5 and 10 fb^{-1}, respectively).

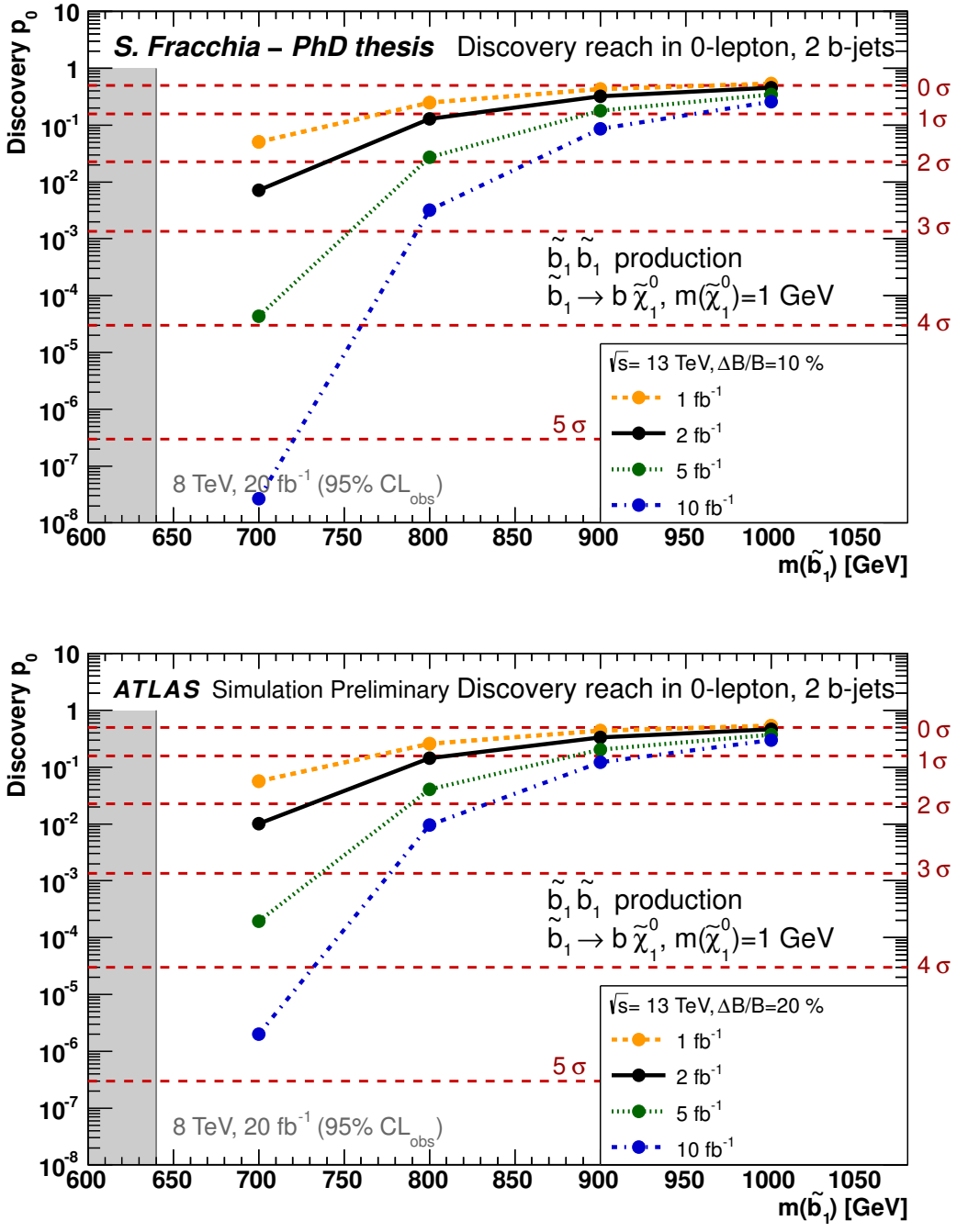

Figure 5.7: The p-values for a SM background only hypothesis as a function of the sbottom mass for different scenarios for the total integrated luminosity, each plot corresponding to a fixed uncertainty on the total SM background (10% and 20%, respectively).

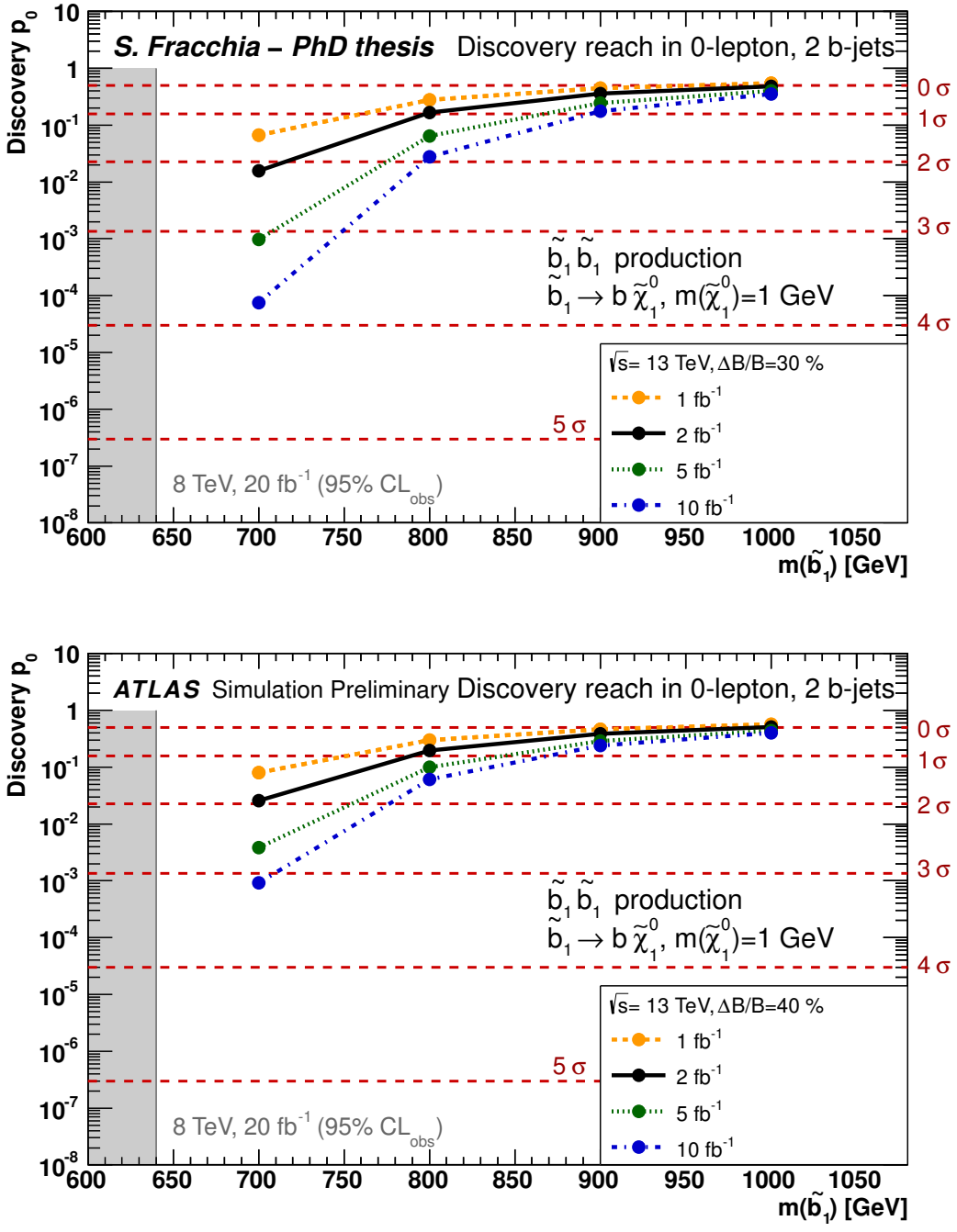

Figure 5.8: The p-values for a SM background only hypothesis as a function of the sbottom mass for different scenarios for the total integrated luminosity, each plot corresponding to a fixed uncertainty on the total SM background (30% and 40%, respectively).

Chapter 6

Search for the sbottom quark at $\sqrt{s}$ =13 TeV

This chapter is devoted to the description of the search for the direct pair production of sbottom quarks, in final states with b-jets and missing transverse momentum. The search is performed using the $\sqrt{s}$=13 TeV collision data delivered in 2015 by the LHC. This analysis led to the following publications:

- *Search for bottom squark pair production in proton-proton collisions at $\sqrt{s}$ =13 TeV with the ATLAS detector* (Eur. Phys. J. C, (2016) 76:547).
- *Search for Bottom Squark Pair Production with the ATLAS Detector in proton-proton Collisions at $\sqrt{s}$ =13 TeV* (ATLAS-CONF-2015-066, December 2015).

6.1 Data and Monte Carlo samples

The analysis uses the data sample collected in proton-proton collisions with the ATLAS detector during 2015, at a center-of-mass energy of 13 TeV. The total integrated luminosity available after requiring that tracking detectors, calorimeters, muon chambers and magnets were fully operational during the data taking corresponds to 3.20±0.16 fb^{-1}.

6.1.1 Monte Carlo simulated samples

The main SM background processes, as well as the SUSY signals, are estimated using MC samples, which will be briefly described in the following. MC generated events are required to pass through a detailed simulation of the ATLAS detector based either fully on GEANT4 [91] or on a faster parameterization [92] for the calorimeter response and on GEANT4 for all the rest.

Simulated minimum-bias events generated with Pythia 8 [93] and `MSTW2008LO` [33, 94]

are superimposed to the hard scattering events, in order to take into account the in-time and out-of-time pileup conditions. The bunch spacing for the bunch crossings is 25 ns and corresponds to the LHC configuration during the 2015 data taking period.

The heavy flavor decays are relevant for this analysis and are modeled using the `EvtGen` [95, 96] program. The main SM background processes and the signal samples are described below.

6.1.2 W+jets and Z+jets

The W+jets and Z+jets processes are simulated using Sherpa 2.1.1 [43] with up to four additional partons in the matrix element (0,1,2 jets at NLO plus 3 and 4 jets at LO) and using massive b/c-quarks, CT10 [32] parton distribution functions and its own model of hadronization. The MC samples are normalized to the next-to-next-to-leading order (NNLO) QCD theoretical cross sections, as described in Ref. [97].

6.1.3 Top

The production of top quark pairs ($t\bar{t}$) is simulated using the Powheg-Box generator [45, 98, 99], interfaced to Pythia 6 [40] and using the Perugia2012 tune [85]. The $t\bar{t}$ samples are normalized to the NNLO cross section including the resummation of soft gluon emission at next-to-next-to-leading logarithmic accuracy using `Top++2.0` [100].

Single top samples corresponding to the t-, s- and Wt production mechanisms are generated with Powheg-Box interfaced to Pythia 6. The NLO cross sections obtained from the generator are used for these samples.

6.1.4 Other SM backgrounds

The associated production of a top pair with a vector boson, $t\bar{t}+W/Z$ is generated at LO with Madgraph 5 [44] interfaced to Pythia 8, with up to two ($t\bar{t}+W$), one ($t\bar{t}+Z$) or no ($t\bar{t}+WW$) extra parton included in the matrix elements. The samples are normalized to the corresponding NLO cross sections.

6.1.5 Signal samples

The signal samples simulate the pair production of sbottoms, decaying according to $\tilde{b}_1 \to b\tilde{\chi}_1^0$ with a branching ratio of 100%. Samples for several different assumptions on the $\tilde{b}_1$ and $\tilde{\chi}_1^0$ masses are generated. Events are generated by Madgraph 5 interfaced to Pythia 8 with the ATLAS 14 tune [101] for the modeling of the sbottom decay, of the parton showering (PS), hadronization and underlying event. The matrix element calculation is performed at tree level, and includes the emission of up to two additional partons.

The parton density functions used for the generation are the NNPDF23LO [102]. The parton shower matching is done using the CKKW-L [103] prescription, with a matching scale set to one quarter of the pair-produced superpartner mass. The signal cross sections are calculated to NLO accuracy in the strong coupling constant, adding the resummation of soft gluon emission at next-to-leading-logarithmic accuracy [104].

6.2 Objects definition

In this section, the physics objects used in the analysis will be briefly described.

Jets (and b-jets) and $E_{\mathrm{T}}^{\mathrm{miss}}$ represent the key ingredients of this search, whereas leptons are used both to veto the electroweak backgrounds in the signal regions and to define the different control samples.

The objects definitions are very similar to the ones illustrated in Chapter 5, with some changes due to improvements in the reconstruction and further optimization studies.

A detailed description of the reconstruction of physics objects is given in Chapter 4.

Jets. Jets are reconstructed using the anti-k_t algorithm with a distance parameter $R = 0.4$ (in $\eta - \phi$ space) and are seeded by topological calorimeter clusters calibrated at the EM energy scale. Only jets with $p_{\mathrm{T}} > 20$ GeV and $|\eta| < 2.8$ are selected. For the jets used in the signal regions selection the p_{T} requirement is increased to 35 GeV and a requirement on the JVT is applied, which allows to reject events with jets arising from pileup collisions as described in Section 4.4.3. The JVT is required to be larger than 0.59 for jets with $p_{\mathrm{T}} < 60$ GeV and $|\eta| < 2.4$.

The b-jets are identified using the MV2c20 algorithm, as described in Section 4.5, using the 77% nominal efficiency working point.

Electrons. Electrons are preselected using the loose identification criteria with $p_{\mathrm{T}} > 10$ GeV and $|\eta^{cluster}| < 2.47$. These preselected electrons are used to perform the lepton-jet overlap removal, as it will be described later in this section, and for vetoing events with leptons in the signal regions. The electrons used to select events in the control regions are required, in addition, to have $p_{\mathrm{T}} > 26$ GeV in order to satisfy the lepton trigger requirements (see below). They are also required to be isolated, to pass the tight selection criteria and to satisfy the recommended impact parameter (IP) requirements ($d_0/\sigma(d_0) < 5$, $z_0 sin(\theta) < 0.5$)[1].

Muons. Muons are reconstructed combining the information from the inner detector and the muon spectrometer (combined muons). Muons are preselected with $p_{\mathrm{T}} > 10$ GeV

[1] The impact parameters z_0 and d_0 are respectively the longitudinal and transverse impact parameters calculated with respect to the primary vertex

and $|\eta| < 2.4$ and required to pass the medium track quality requirements. Similarly to the electrons, preselected muons are used for the overlap removal and for the lepton veto in the signal regions, while the muons used for the control region selections are required, in addition, to have $p_{\mathrm{T}} > 26$ GeV, to be isolated and to pass the recommended IP requirements ($d_0/\sigma(d_0) < 3$, $z_0 sin(\theta) < 0.5$).

Missing transverse momentum. As described in Section 4.6, the missing transverse momentum vector $\vec{p}_{\mathrm{T}}^{\mathrm{miss}}$, whose magnitude is indicated by $E_{\mathrm{T}}^{\mathrm{miss}}$, is obtained from the vectorial sum of the transverse momenta of preselected electrons, muons and jets, as defined above. Identified photons are also included in the computation. In this analysis, the soft term $(E_{\mathrm{T}}^{\mathrm{miss}})^{\mathrm{SoftTerm}}$ is built from tracks not associated to any reconstructed object.

As it will be described in Section 6.5, a control region with two leptons is used to extract the normalization of the Z+jets background. In this control region, the missing transverse momentum is recomputed by subtracting the total lepton 3-vector, in order to model the expected $E_{\mathrm{T}}^{\mathrm{miss}}$ distribution for the dominant decay mode in the signal regions ($Z \to \nu\nu$). This corrected $E_{\mathrm{T}}^{\mathrm{miss}}$ will be referred as $\tilde{E}_{\mathrm{T}}^{\mathrm{miss}}$.

Removing overlapping objects. As already mentioned in Section 5.2, single final state objects may fall into more than one category, such as an electron being reconstructed both as an electron and as a jet. The following procedure is followed to remove overlaps between final state objects:

- If an electron and a muon share a reconstructed track: if the muon is calo-tagged then it is removed, otherwise the electron is dropped.
- If the distance in $\Delta\mathrm{R} = \sqrt{\Delta\eta^2 + \Delta\phi^2}$ between a jet and a preselected electron is $\Delta\mathrm{R} < 0.2$, then the jet is dropped, unless the jet is b-tagged, in which case the electron is dropped. b-jets are here selected using a looser efficiency working point (80%), as described in Section 4.5.
- If the distance in $\Delta\mathrm{R}$ between a jet and a preselected electron is $0.2 < \Delta\mathrm{R} < 0.4$, then the electron is dropped.
- Finally, if the distance in $\Delta\mathrm{R}$ between a jet and a preselected muon is < 0.4, then the muon is dropped.

Trigger strategy. Different trigger logics are used because of the different selections in the analysis regions.

In the signal and validation regions, where a lepton veto is applied, events are selected using the lowest unprescaled $E_{\mathrm{T}}^{\mathrm{miss}}$ trigger logic, called `HLT_xe70`, which reaches its 95% efficiency for offline values of the missing transverse momentum of about 200 GeV.

In the control regions used to estimated the dominant backgrounds in the signal regions, events containing one or two leptons are selected making use of the first unprescaled single lepton triggers, which are listed below:

- `HLT_e24_lhmedium_L1EM20VH` || `HLT_e60_lhmedium` || `HLT_e120_lhloose` for electrons
- `HLT_mu20_iloose_L1MU5` || `HLT_mu50` for muons

In both the electron and the muon cases, the lowest p_T triggers require the lepton to be isolated. In order to recovery the trigger efficiency at high p_T, these triggers are combined with the lowest unprescaled triggers which do not require lepton isolation.

Both data and MC events are required to pass the trigger selection, and efficiency scale factors are applied to the MC events in order to correct for the differences with respect to data.

6.3 Event selection

In this section, the basic selection criteria applied to all the analysis regions will be described. These common preselection criteria allow to suppress large contribution of multijet and non-collision background contributions. A summary of the common preselection criteria is given in Table 6.1.

- Events are required to have at least one reconstructed primary vertex, consistent with the beam spot envelope, and to have at least two isolated tracks with p_{T} >400 MeV. If two or more vertexes fulfill these requirements, the one with the largest $\sum p_T^2$ is chosen as primary vertex. This requirement helps removing beam-related backgrounds and cosmic rays.
- Similar jet cleaning requirements to the ones described in Section 5.2 are applied to reject fake jets. These requirements are applied on preselected jets after the overlap removal. Events with one or more preselected jet failing these cleaning requirements are rejected.
- Events containing a preselected muon satisfying $\sigma(q/p)/|q/p| > 0.2$ before the overlap removal are rejected.
- Events containing a candidate cosmic muon after the overlap removal are rejected. Candidate cosmic muons are defined as preselected muons having $|z_0| > 1$ mm or $|d_0| > 0.2$ mm.

- The $E_{\mathrm{T}}^{\mathrm{miss}}$ is required to be above 100 GeV. In the control region targeting Z+jets events (CRzA) this selection is inverted, in order to remove the contamination from $t\bar{t}$ events (see Section 6.5.1).
- The two leading jets, ordered in p_{T}, are required to have $p_{\mathrm{T}} > 50$ GeV and $|\eta| < 2.8$.
- A jet veto is applied on the number of selected jets in the event, in order to suppress the contamination from backgrounds with large jet multiplicity. Events are allowed to have up to three jets with $p_{\mathrm{T}} > 20$ GeV and $\eta < 2.8$. A fourth p_{T} ordered jet is allowed, provided its p_{T} is lower than 50 GeV.
- Exactly two b-tagged jets are required. This selection is dropped in the control region for W+jets (see CRwA in Table 6.6), in which events with only one b-tagged jet are required.
- $\min[\Delta\phi(\mathrm{jet}_{1-4}, E_{\mathrm{T}}^{\mathrm{miss}})] > 0.4$, where $\min[\Delta\phi(\mathrm{jet}_{1-4}, E_{\mathrm{T}}^{\mathrm{miss}})]$ is defined as the minimum $\Delta\phi$ between any of the (at most) four leading jets and the missing transverse momentum vector. As already mentioned in Section 5.3, the background from QCD multi-jet is characterized by small values of this variable.
- $E_{\mathrm{T}}^{\mathrm{miss}}/m_{eff} > 0.25$, where m_{eff} is defined as in Equation 5.1.

No bad jets + vertex requirements
Leading two jets with $p_{\mathrm{T}} > 50$ GeV, $\|\eta\| < 2.8$
Veto on 4^{th} jet with $p_{\mathrm{T}} > 50$ GeV, $\|\eta\| < 2.8$
Exactly two b-tagged jets, 77% working point (1 b-tagged jet for CRw only)
$\min[\Delta\phi(\mathrm{jet}_{1-4}, E_{\mathrm{T}}^{\mathrm{miss}})] > 0.4$
$E_{\mathrm{T}}^{\mathrm{miss}}/m_{eff} > 0.25$
$E_{\mathrm{T}}^{\mathrm{miss}} > 100$ GeV

Table 6.1: Preselection requirements, common to all control, validation and signal regions definitions.

6.4 Signal regions definition

Two types of signal regions are defined in this analysis, designed for targeting different values of the mass splitting Δm between the sbottom and the neutralino masses.

The so-called A-type signal regions are designed to target large mass splittings (indicatively $\Delta\mathrm{m}(\tilde{b}_1, \tilde{\chi}_1^0) = m_{\tilde{b}_1} - m_{\tilde{\chi}_1^0} > 250$ GeV), identifying two b-tagged high-p_{T} leading jets as products of the two bottom squarks decays. Another signal region, SRB, is designed to provide sensitivity for the signal points for the compressed scenario with low $\Delta\mathrm{m}(\tilde{b}_1, \tilde{\chi}_1^0)$ splittings .

For both scenarios, the analysis strategy is similar to that of the 8 TeV search [82].

The A-type signal regions include further reoptimizations with respect to the benchmark signal region presented in Chapter 5. Details are provided in the following subsections.

6.4.1 SRA

A series of requirements on variables which have been proven to be effective in rejecting the SM background is applied, as listed below. In particular, the contransverse mass m_{CT}, already defined in Equation 5.3, is the key discriminating variable for this type of signal region. All the requirements are applied on top of the common preselection criteria described previously.

- Events with preselected electrons or muons are vetoed.
- The two b-tagged jets are required to be the two leading-p_{T} jets.
- The p_{T} requirement on the leading jet is increased to 130 GeV.
- The requirement on $E_{\mathrm{T}}^{\mathrm{miss}}$ is increased to 250 GeV, in order to guarantee the full efficiency of the $E_{\mathrm{T}}^{\mathrm{miss}}$ trigger.
- A selection on the invariant mass of the two b-jets (m_{bb}) is introduced. This cut is extremely useful to reduce the contamination from $t\bar{t}$ events as well to distinguish between these and single top events in the two control regions defined to constrain their normalization (see Section 6.5).
- Three overlapping signal regions are finally defined, SRA250, SRA350 and SRA450, with increasing requirements on the m_{CT} variable: 250, 350 and 450 GeV, respectively. Each of these signal regions provides better sensitivity in a given area of the sbottom-neutralino mass plane, going towards higher sbottom masses.

The SRA definition is summarized in Table 6.2. Table 6.3 shows the background yields in SRA for an integrated luminosity of 3.2 fb^{-1} .

SRA250	SRA350	SRA450
No preselected electron or muon		
Leading (in p_{T}) two jets b-tagged		
$p_{\mathrm{T}} > 130$ GeV for the leading jet		
$m_{\mathrm{bb}} > 200$ GeV		
$E_{\mathrm{T}}^{\mathrm{miss}} > 250$ GeV		
Veto on 4^{th} jet with $p_{\mathrm{T}} > 50$ GeV		
$m_{\mathrm{CT}} > 250$ GeV	$m_{\mathrm{CT}} > 350$ GeV	$m_{\mathrm{CT}} > 450$ GeV

Table 6.2: Summary of SRA definitions.

	SRA250	SRA350	SRA450
Total bkg	23.413 ± 0.463	5.626 ± 0.173	1.482 ± 0.057
W+jets	3.603 ± 0.210	0.982 ± 0.090	0.246 ± 0.024
Z+jets	16.090 ± 0.371	3.698 ± 0.124	1.001 ± 0.040
$t\bar{t}$	1.096 ± 0.115	0.177 ± 0.038	0.044 ± 0.020
Single top	2.178 ± 0.115	0.642 ± 0.057	0.152 ± 0.020
Diboson	0.210 ± 0.080	0.065 ± 0.042	0.016 ± 0.016
$t\bar{t}$+Z	0.133 ± 0.007	0.028 ± 0.003	0.008 ± 0.002
$t\bar{t}$+W	0.019 ± 0.003	0.006 ± 0.002	0.002 ± 0.001

Table 6.3: Expected background yields in SRA for 3.2 fb^{-1}. Only statistical uncertainties are shown.

The dominant SM background process in SRA consists in the production of a Z boson in association with jets coming from the fragmentation of heavy flavor (HF) quarks (mostly b, but also c), followed by the decay of the Z boson into neutrinos. Other relevant backgrounds are single top production (dominated by the Wt production channel), W+ HF jets and $t\bar{t}$ production. For these last three processes, the dominant contribution arises from 1-lepton events, where the lepton is either lost or out of acceptance, or it is a τ lepton that decayed into hadrons.

6.4.2 SRB

An additional signal region (SRB) is introduced to target signal models in which the mass splitting between sbottom and neutralino is of the order of 100 GeV. In this case, a boosted bottom squark pair is needed to satisfy the trigger requirements. Similarly to the strategy used in the Run-1 search, SRB selects events where a bottom squark pair is produced in association with a jet from initial-state radiation (ISR).
The SRB requirements are listed below and summarized in Table 6.4.

- As for SRA, events with preselected electrons or muons are vetoed.
- The requirement on $E_{\mathrm{T}}^{\mathrm{miss}}$ is tightened to 400 GeV.
- The two b-tagged jets are required to be the second and the third leading-p_{T} jets.
- The p_{T} requirement on the leading jet (from ISR) is increased to 300 GeV.
- The leading jet is required to be pointing in the direction opposite to the $E_{\mathrm{T}}^{\mathrm{miss}}$ by requiring the azimuthal angle between the leading jet and the $E_{\mathrm{T}}^{\mathrm{miss}}$, $\Delta\phi(1^{\mathrm{st}}\text{ jet},\ \mathrm{E}_{\mathrm{T}}^{\mathrm{miss}})$, to be higher than 2.5.

SRB selection
No preselected electron or muon
>2 jets , =2 b-jets
Leading-p_{T} jet anti-b-tagged, $p_{\mathrm{T}} > 300$ GeV
Sub-leading-p_{T} jet b-tagged, $p_{\mathrm{T}} > 50$ GeV
4th jet p_{T}(jet) < 50 GeV (if any)
$\Delta\phi(1^{\mathrm{st}}$ jet, $\mathrm{E}_{\mathrm{T}}^{\mathrm{miss}}) > 2.5$
$E_{\mathrm{T}}^{\mathrm{miss}} > 400$ GeV

Table 6.4: SRB definition.

Table 6.5 shows the background yields in SRB corresponding to an integrated luminosity of 3.2 fb^{-1}. From this table it can be seen that the main expected SM background process in SRB is $t\bar{t}$ production, followed by Z+jets production.

	SRB
Total background	10.787 ± 0.305
W+jets	1.113 ± 0.081
Z+jets	2.810 ± 0.101
$t\bar{t}$	5.568 ± 0.205
Single top	0.987 ± 0.135
Diboson	0.191 ± 0.070
$t\bar{t}$+Z	0.063 ± 0.006
$t\bar{t}$+W	0.014 ± 0.003

Table 6.5: Expected background yields in SRB for 3.2 fb^{-1}. Only statistical uncertainties are shown.

6.5 Background estimation

The dominant background processes are constrained using MC samples normalized with data in selected control regions, which are designed in order to achieve a high purity for the process to constrain and low signal contamination. The optimal control region is defined with a topology as close as possible to that of the signal region, thus allowing a partial cancellation of the systematic uncertainties. However, in some cases, it is necessary to relax some of the selection requirements in order to allow the control region having a sufficient number of events to avoid a too large statistical uncertainty.

Just to make a simple illustration, the contribution from a given background process to a given signal region SR, N_{bkg}^{SR}, would be determined from the correspondent control

region CR with a semi data-driven estimate, according to:

$$N_{bkg}^{SR} = N_{bkg,\,MC}^{SR} \times \frac{\left(N_{data}^{CR} - N_{bkg-others,\,MC}^{CR}\right)}{N_{bkg,\,MC}^{CR}}, \tag{6.1}$$

where $N_{bkg,\,MC}^{SR}$ is number of events of the given background process predicted by the MC simulation in the signal region, N_{data}^{CR} and $N_{bkg,\,MC}^{CR}$ denote the number of events for the data and the given background process in the control region, respectively and $N_{bkg-others,\,MC}^{CR}$ is the number of events of the other background processes subtracted by the background of interest in the control region. The ratio:

$$NF_{bkg}^{CR} = \frac{\left(N_{data}^{CR} - N_{bkg-others,\,MC}^{CR}\right)}{N_{bkg,\,MC}^{CR}}, \tag{6.2}$$

is the normalization factor of the background of interest extracted from the control region. In this analysis, the normalization factors are extracted with a simultaneous fit of all the control regions, as it will be described in Section 6.6, to take into account cross-talks of different background sources. Experimental and theoretical systematic uncertainties are included in the fit, to properly take into account correlations. The distributions in the signal and control regions used in the global fit consist of one single bin, meaning that the shape of the control region distributions is taken from MC. It is therefore fundamental in this analysis to verify that the MC simulation represents well the shape of the distributions in data.

In addition, validation regions are defined in order to verify the solidity of the background estimation. This type of regions are not used in the global fit, but the normalization factors, extracted from the control regions, are checked against data in the validation regions.

Separate and independent background estimation strategies are developed for SRA and SRB, respectively. Four orthogonal control regions are defined for the normalization of the four most relevant backgrounds in SRA. A $Z(\rightarrow \ell\ell)$+HF jets sample is used to define normalization factors for the dominant $Z(\rightarrow \nu\nu)$+ HF jets background. The other three control regions are defined in order to enhance the $t\bar{t}$, single top (Wt) and W+HF jets processes. A similar strategy is adopted for SRB, where two control regions are used for extracting the normalization of the $Z(\rightarrow \nu\nu)$+ HF jets and the $t\bar{t}$ backgrounds.

The remaining SM backgrounds from diboson and $t\bar{t}+W/Z$ production in SRA and from single top, W+ jets, diboson and $t\bar{t}+W/Z$ production in SRB are determined using MC simulated samples, while the multijet background contribution is estimated with a data-driven technique in both cases.

In the following subsections, details of the definition of the different control regions and of the data-driven determination of the multijet background will be given.

6.5.1 Control regions for SRA

The four different control regions used for the background estimation in SRA are described below. Table 6.6 summarizes the selection criteria of the different control regions for SRA.

Z+jets control region. The control region for the normalization of the Z+jets background (CRzA) is defined by selecting a relatively pure sample of Z+HF jets with $Z \to \ell\ell$ (where $\ell = e$ or μ), with the two leptons required to have the same flavor and opposite sign. This can be achieved by applying a selection on the invariant mass of the di-lepton system corresponding to a window around the value of the Z mass. An upper cut on the $E_{\mathrm{T}}^{\mathrm{miss}}$ is applied to remove events with real $E_{\mathrm{T}}^{\mathrm{miss}}$, in particular $t\bar{t}$ production. Further $t\bar{t}$ suppression is achieved by increasing the requirement on the p_{T} of the leading lepton. Finally, a selection on $\tilde{E}_{\mathrm{T}}^{\mathrm{miss}}$ is applied. As mentioned in Section 6.2, this variable is obtained by subtracting the lepton momenta from $\vec{p}_{\mathrm{T}}^{\mathrm{miss}}$, in order to model the missing neutrinos from the Z decay.

$t\bar{t}$ and single top control regions. Two control regions with exactly one lepton ($\ell = e, \mu$) and two b-jets in the final state are used to estimate the $t\bar{t}$ and the single top contributions. The two processes can be separated by applying a requirement on the invariant mass of the $b\bar{b}$ pair and on the minimum invariant mass between the lepton and one of the two b-jets, defined as:

$$\mathrm{m}_{b\ell}^{\mathrm{min}} = \mathrm{min}_{i=1,2}\left(m_{\ell b_i}\right). \tag{6.3}$$

This variable is bound from above to $\sqrt{m_t^2 - m_W^2}$ for $t\bar{t}$ production.

W+jets control region. Finally, a control region dominated by W+HF jets production can be constructed only requiring one b-tagged jet instead of two, as for the other control regions. In this way the W+jets and the $t\bar{t}$ control regions are different enough to be adequate in extracting simultaneously both the W+jets and the $t\bar{t}$ normalization factors. The two leading jets, rather than the two b-jets, are used to compute m_{CT} and m_{bb}.

6.5.2 Control regions for SRB

The two control regions used in the global fit for SRB are described below. The selection criteria for both control regions are given in Table 6.7.

Variable	Units	CRzA	CRttA	CRstA	CRwA
Preselection		✓	✓	✓	✓ (1 b-jet)
Lepton selection ($\ell = e, \mu$)		2 SF	1	1	1
Lepton $p_{\mathrm{T}}(\ell_1, \ell_2)$	GeV	$(> 90, > 20)$	$(> 26, -)$	$(> 26, -)$	$(> 26, -)$
$\mathrm{m}_{\ell\ell}$	GeV	$[76 - 106]$	-	-	-
m_{T}	GeV	-	-	-	> 30
Leading jet p_{T}	GeV	-	> 130	-	> 130
$E_{\mathrm{T}}^{\mathrm{miss}}$	GeV	< 100	> 100	> 100	> 100
$\tilde{E}_{\mathrm{T}}^{\mathrm{miss}}$	GeV	> 100	-	-	-
m_{bb}	GeV	> 200	< 200	> 200	$(m_{bj}) > 200$
m_{CT}	GeV	-	> 150	> 150	> 150
$\mathrm{m}_{b\ell}^{\mathrm{min}}$	GeV	-	-	> 170	-

Table 6.6: Definition of the control regions associated to SRA.

$t\bar{t}$ control region A dedicated control region for the $t\bar{t}$ background (CRtopB) is constructed, close to the SRB definition, by selecting events with exactly one lepton ($\ell = e, \mu$). The cuts on $E_{\mathrm{T}}^{\mathrm{miss}}$ and the leading jet p_{T} have been relaxed to enhance the statistics. Additionally, the requirement on m_{bb} is inverted to remove contributions from single top and W+jets events.

Z+jets control region Similarly to CRzA, the selection in the CRzB region is based on the invariant mass requirement for the two same-flavor lepton system and the cuts on $E_{\mathrm{T}}^{\mathrm{miss}}$ and $\tilde{E}_{\mathrm{T}}^{\mathrm{miss}}$.

Variable	Units	CRzB	CRtopB
Preselection		✓	✓
Lepton selection ($\ell = e, \mu$)		2 SF	1
Lepton p_{T} (ℓ_1, ℓ_2)	GeV	$(> 26, > 20)$	$(> 26, -)$
Leading-p_{T} jet p_{T}	GeV	> 50	> 130
Leading-p_{T} jet		not b-tagged	not b-tagged
Sub-leading-p_{T} jet		b-tagged	b-tagged
$\Delta\phi(1^{\mathrm{st}}$ jet, $\tilde{\mathrm{E}}_{\mathrm{T}}^{\mathrm{miss}})$		> 2.0	> 2.5
$\mathrm{m}_{\ell\ell}$	GeV	$[76 - 106]$	-
$\tilde{E}_{\mathrm{T}}^{\mathrm{miss}}$	GeV	> 100	-
$E_{\mathrm{T}}^{\mathrm{miss}}$	GeV	< 100	> 200

Table 6.7: Definition of the control regions associated to SRB.

6.5.3 Alternative methods for Z+jets background estimation

Two alternative methods have been developed for further validation of the Z+jets background estimation, given the importance of this background in both the SRA and SRB regions.

The first method relies on the similarity of the kinematics of the Z+jets and γ+jets processes [105]. This is particularly true when the p_{T} of the photon is significantly larger than the mass of the Z boson. In this alternate method, the event yields are measured in control regions with a selection identical to that of SRA and SRB, but replacing the $E_{\mathrm{T}}^{\mathrm{miss}}$ with the p_{T} of the photon vectorially added to the $\vec{p}_{\mathrm{T}}^{\mathrm{miss}}$. The yields obtained in these control regions are then propagated to SRA and SRB. This is done using a reweighing factor derived from MC simulation, which takes into account the differences in the kinematics between the two processes as well as residual effects arising from the acceptance and reconstruction efficiency for photons.

The second method, only applied to SRA, relies on MC simulation to verify that the shape of the m_{CT} distribution is compatible in the case of events with no b-tagged jets and events with two b-tagged jets. This prove allows to build a control region similar to the nominal Z+jets control region, but selecting events without b-tagged jets requirements and, therefore, with higher statistics. The m_{CT} in this case is computed using the two leading jets, which are required to be anti-b-tagged. The shape of the m_{CT} distribution is then taken from that of this control region, and the normalization is re-scaled with the ratio of Z$\rightarrow \ell\ell$ events without b-tagged jets to events with two b-tagged jets in data, after corrections are applied to take into account the difference in the two-lepton selection used to define this new control region.

The results obtained from the new methods are compared to the nominal prediction obtained after the global fit. The results are found to be in agreement within uncertainties with the estimates obtained from the global fit to the control regions, which will be described in Section 6.6. The difference between these new methods and the nominal prediction is taken into account as an extra systematic in the Z+jets background yield, as discussed in Section 6.7.

6.5.4 Multijet background

The background from *multijet production* with large $E_{\mathrm{T}}^{\mathrm{miss}}$ mostly originates from a jet in the calorimeter whose energy was misreconstructed and, to a lesser extent, from the presence of neutrinos in the final state from heavy-flavor hadron decays.

In this analysis, the multijet background is estimated from data using the so-called jet smearing method, described in Ref. [105], which relies on the assumption that the fake $E_{\mathrm{T}}^{\mathrm{miss}}$ from this background is dominated by fluctuations in the jet response in the detector. The latter can be measured in data by smearing the jet response in seed events with well-measured $E_{\mathrm{T}}^{\mathrm{miss}}$. MC dijet events are used to obtain the jet response function, which is then cross-checked in data events where the $E_{\mathrm{T}}^{\mathrm{miss}}$ can be un-ambiguously attributed to the mismeasurement of one of the jets. This data-driven estimation predicts a negligible contribution of the multijet background in all the analysis regions.

6.5.5 Validation regions

As it was already mentioned, it is useful to define validation regions to be used as a cross check of the extracted normalization factors, as determined in the control regions.

Two validation regions are defined for SRA, with the same selection criteria as the signal regions, but inverting the requirement either on the m_{CT} (VRAmct) or on the m_{bb} (VRAmbb). Their selections are summarized in Table 6.8. In both cases the selected samples are background-dominated, with a potential signal contamination of $\lesssim 1\%$ for the non-excluded signal models considered.

	Units	VRAmbb	VRAmct
No baseline electron or muon		✓	✓
Leading (in p_{T}) two jets b-tagged		✓	✓
$p_{\mathrm{T}} > 130$ GeV for the leading jet		✓	✓
m_{bb}	GeV	< 200	> 200
$E_{\mathrm{T}}^{\mathrm{miss}}$	GeV	> 250	> 250
Veto on 4^{th} jet with $p_{\mathrm{T}} > 50$ GeV		✓	✓
m_{CT}	GeV	> 150	< 150

Table 6.8: Definition of the validation regions associated to SRA.

As seen in Table 6.9, the selection of the validation region VRB for the SRB is similar to the SRB selection but with lower $E_{\mathrm{T}}^{\mathrm{miss}}$ and leading jet p_{T}. In this case, the signal contamination is at most 20% for the non-excluded signal models considered.

Variable	Units	VRB
Preselection		✓
Lepton selection ($\ell = e, \mu$)		0
Lepton p_{T} (ℓ_1, ℓ_2)	GeV	-
Leading-p_{T} jet p_{T}	GeV	$[100, 300]$
Leading-p_{T} jet		not b-tagged
Sub-leading-p_{T} jet		b-tagged
$\Delta\phi(1^{\mathrm{st}}$ jet, $\tilde{\mathrm{E}}_{\mathrm{T}}^{\mathrm{miss}})$		> 2.5
$\mathrm{m}_{\ell\ell}$	GeV	-
$\tilde{E}_{\mathrm{T}}^{\mathrm{miss}}$	GeV	-
$E_{\mathrm{T}}^{\mathrm{miss}}$	GeV	$[250, 300]$

Table 6.9: Definition of the validation region associated to SRB.

6.6 The fit strategy

The global fit strategy is based on the profile likelihood method. It determines the normalization factors applied to the different MC expectations of the background processes, for which systematic uncertainties and potential correlations are taken into account. The global fit is used to test whether the data are compatible with background-only predictions.

The test statistics which is used for the hypothesis testing in this analysis is the log-likelihood ratio [106]. This is based on the likelihood function, which is defined as a product of the Poissonian probabilities of the different bins corresponding to each control regions and to the signal region:

$$L(\vec{\mu},\vec{\theta}) = \prod_{c\in\text{regions}} \frac{\nu_c(\vec{\mu},\vec{\theta})^{n_c}}{n_c!} e^{-\nu_c(\vec{\mu},\vec{\theta})} \prod_{p\in\text{params}} P_p(\theta_p), \tag{6.4}$$

where

$$\nu_c(\vec{\mu},\vec{\theta}) = [\mu(\vec{\theta})S_c + \sum_{j}^{\text{bkg}} \mu_{b,j}(\vec{\theta})B_{c,j}]^{n_c} \tag{6.5}$$

In Eqs. 6.4- 6.5 n_c represents the number of events measured in each region, S_c and $B_{c,j}$ are the expected nominal number of events for the signal and each of the background processes considered, μ is the strength of the signal process, with $\mu = 0$ for the background-only hypothesis and $\mu = 1$ for the signal plus background hypothesis and $\mu_{b,j}$ are the floating normalizations of the background processes, which are determined in the control regions. The parameters μ and $\mu_{b,j}$ are indicated collectively with $\vec{\mu}$. The vector $\vec{\theta}$ is a set of nuisance parameters that parametrize the different systematic uncertainties. The value of the single nuisance parameters can float around the measured central uncertainty value according to a Gaussian probability distribution, in order to find the configuration which maximizes the likelihood. Finally, P_p is a constraining term, which describes an auxiliary measurement used to constrain the nuisance parameter θ_p. In this analysis, the constraining term is assumed to be Gaussian distributed, except for the nuisance parameters dedicated to the statistical uncertainties, which are Poissonian distributed.

By maximizing this function, it is possible to calculate the normalization factors and nuisance parameters used to estimate the yield of each process and the level of systematic uncertainties in the different regions.

To test an hypothesized value of μ, the log-likelihood test statistic can be defined as:

$$q_\mu = -2\ln\frac{L(\mu,\hat{\hat{\vec{\theta}}})}{L(\hat{\mu},\hat{\vec{\theta}})}, \tag{6.6}$$

where $\hat{\mu}$ and $\vec{\hat{\theta}}$ are the values of μ and θ which maximize the likelihood and $\vec{\hat{\hat{\theta}}}$ is the value of θ which maximizes the likelihood for the chosen value of μ.

Higher values of q_μ correspond to increasing compatibility between the data and μ. In an analysis whose purpose is to discover a new signal process, the background-only hypothesis has to be tested against the background plus signal hypothesis. If, instead, the purpose of the analysis is to set limits on a signal process, the background plus signal hypothesis has to be tested against the background-only hypothesis. The level of agreement of the observed data with a given hypothesis, H, is quantified by computing the probability, under the assumption of H, of finding data of equal or greater incompatibility with the predictions of H. This probability is called p-value and it is defined, given the test statistic q_μ, by integrating the probability density function between the observed q_μ value and infinity as:

$$p_\mu = \int_{q_{\mu,\,\mathrm{obs}}}^{\infty} f(q_\mu|\mu)\, dq_\mu. \tag{6.7}$$

The estimations of $f(q_\mu|\mu)$ can be done with pseudo-experiments using Monte Carlo methods. However, these methods are computationally heavy and, for this reason, an approximation valid in the large sample limit is normally used to describe the log-likelihood ratio (asymptotic approximation).

6.6.1 The *CLs* method

The CL_s method [107] is introduced motivated by the need to protect the results for cases in which the analysis has very low sensitivity and, via statistical fluctuations, both the background-only and the signal plus background hypotheses could be rejected at the same time. The CL_s is defined as the p-value of the signal plus background hypothesis divided by one minus the p-value of the background-only hypothesis:

$$\begin{aligned} CL_{s+b} &= p_{s+b}, \\ CL_b &= 1 - p_b, \\ CL_s &= \frac{CL_{s+b}}{CL_b} \end{aligned} \tag{6.8}$$

With the CLs method, in the cases where the analysis is sensitive to the signal process under study, then $CL_s \approx CL_{s+b}$. In the cases where the analysis is not sensitive, instead, CL_b is small, thus increasing the value of CL_s and avoiding the exclusion of the signal model. In this analysis, the CL_s is calculated for each signal model under evaluation. A given signal model is excluded at 95% CL if its CL_s is below 0.05.

6.6.2 Fit configurations

In this analysis, the statistical treatment is performed using the HistFitter package [90] and three fit configurations are used for different purposes.

Background-only fit: Only the control regions are used to constrain the fit parameters and any potential signal contribution is neglected everywhere ($\mu = 0$). This type of fit is used to extract the normalization factors of the background processes and their systematic uncertainties. The signal regions are treated as validation regions in this type of fit.

Model-independent signal fit: Both control and signal regions are used simultaneously in the fit and the signal contamination is neglected in the control regions. However, in this analysis this contribution is negligible due to the requirement of leptons in the control regions. This fit configuration is used to extract the 95% CL model-independent upper limits on the visible cross section, and for this the signal strength parameter is fixed to $\mu_{\mathrm{s}} = 1$.

Model-dependent signal fit (exclusion fit): Both control and signal regions are used simultaneously in the fit. The signal contribution is taken into account as predicted by the tested model in all the control and signal regions. The model-dependent signal fit configuration is used in the scenario of no excess of data with respect to the SM background prediction is observed. The results of the fit are translated into exclusion limits in the parameter space of the model under consideration. The exclusion limits are computed with the CLs method, as it was described in the previous subsection.

6.7 Systematic uncertainties

As it was discussed in the previous section, the systematic uncertainties on the expected background values are included in the likelihood function as nuisance parameters (NPs). The systematic uncertainties need to be considered for both the background and the signal processes and can be divided into experimental and theoretical uncertainties. As it was already mentioned in Section 6.5, the use of the control regions in the global fit, to normalize the dominant background processes in the signal region, allows to take into account the correlations of the systematic uncertainties between them. Provided that the topology of the control and signal region is very similar, this also reduces the impact of the uncertainties in the signal region, via the use of the data to constrain the MC predictions.

6.7.0.1 Experimental systematics

Several experimental uncertainties are considered. All the values of the systematic uncertainties quoted in the following refer to the final results after the global fit.

Jet energy scale (JES): The uncertainty on the absolute jet energy scale (JES) is one of the dominant experimental uncertainties. In this analysis, the JES uncertainty is parametrized by a set of three single nuisance parameters, which are the result of combining several systematic sources, from the different steps of the jet energy scale calibration [70]. The impact of the JES uncertainties to the total background uncertainty in the signal regions is found to vary between 15% and 30% in SRA and ∼25% in SRB.

Jet energy resolution (JER). Variations of the jet energy resolution (JER) might affect the jet multiplicity in the event and, therefore, also the jet veto applied in the signal region selections. A single JER systematic variation is considered, which is obtained by smearing the p_{T} of the simulated jets. The impact of the JER uncertainties varies between 20% and 35% in SRA and is below <10% in SRB.

***b*-tagging.** The b-tagging uncertainty is one of the most important systematic uncertainties for this analysis. It is evaluated by varying the $\eta-$, $p_{\mathrm{T}}-$ and flavor-dependent scale factors applied to each jet in the MC simulation, within ranges that reflect the systematic uncertainty on the measured tagging efficiency and mistag rates. The b-tagging variations are applied separately to b-jets, c-jets and light jets, leading to three uncorrelated nuisance parameters. A fourth nuisance parameter, related to the uncertainty on the efficiency extrapolation at high p_{T}, is considered. The b-tagging uncertainties translate into a total background uncertainty in the range between 25% and 45% for SRA and are about 15% in SRB.

Jet Vertex Tagger (JVT). In order to match the observed efficiency of the JVT in data, JVT scale factors are applied to the MC. These scale factors are varied within uncertainties which take into account the limited statistics of the Sherpa $Z+$jets reference sample used as nominal, the residual contamination of pileup jets and the use of different MC generators. The impact of this uncertainty is found to be below 3% in all the signal regions.

$E_{\mathrm{T}}^{\mathrm{miss}}$ soft term. The systematic uncertainty on each individual term of the $E_{\mathrm{T}}^{\mathrm{miss}}$ can be evaluated by propagating the uncertainties of the reconstructed objects that are used to reconstruct it, with the exception of the contributions to the scale and resolution uncertainties coming from the soft term. These uncertainties arise from both the MC modeling and the effects of pileup, and are estimated from $Z \to \mu\mu$ events with two different methods, as described in Ref. [108]. One method determines the soft term uncertainties by comparing observables in data with the MC prediction for events without jets. The second method uses inclusive events and makes use of the balance between the $E_{\mathrm{T}}^{\mathrm{miss}}$ soft term and the total transverse momentum of the hard objects in the events. Four uncorrelated nuisance parameters are used in the fit to parametrize these uncertainties. The $E_{\mathrm{T}}^{\mathrm{miss}}$ soft term uncertainties contribute to the total background uncertainty less than 15% in SRA and are about 4% in SRB.

Lepton energy scale and resolution. Uncertainties on the calibration of electron and muon energy scale and resolution are taken into account, similarly to the jets. These uncertainties are parametrized using five nuisance parameters in total and they are found to be very small in all the signal regions, contributing at most 2% to the total background uncertainty.

Lepton efficiency. The uncertainty on the scale factors applied to MC to match the corresponding reconstruction, identification, isolation and trigger efficiencies are parametrized with ten nuisance parameters (four separate parameters for reconstruction, identification, isolation and trigger efficiency for electrons, respectively, and six separate parameters for reconstruction, identification and trigger efficiency for muons, separately for the statistical and the systematical error on the scale factors). The contribution from these uncertainties to the total background is found to be <10% for all the signal regions.

Luminosity. The uncertainty on the integrated luminosity is ±5% and was derived from a preliminary calibration of the luminosity scale using a pair of x-y beam-separation scans performed in August 2015, following a methodology similar to the one described in [109]. This uncertainty affects the purely MC-driven background predictions.

6.7.0.2 Theory systematics on backgrounds

As discussed below, in most of the cases, the theoretical uncertainties are evaluated using MC samples produced using different generators or simulation parameters.

Z+jets and W+jets. The Z+jets and W+jets modeling uncertainties are evaluated using alternative samples generated with different renormalization and factorization scales, merging and resummation scales. The uncertainties are derived from the difference between the predictions from the nominal samples and the variation samples in each signal region. Each variation is evaluated independently and added in quadrature. Combined, these uncertainties contribute to the total background uncertainty in a range between 25% and 35% (20% and 22%) in SRA and is about 12% (27%) in SRB, for the Z+jets (W+jets) process.

W+jets heavy flavor fraction. The uncertainty related to the flavor composition of the jets produced in association with the W bosons is accounted for by varying the heavy flavor fraction in W+jets by 40%, following the measurement in Ref. [110]. For SRA, the uncertainty also accounts for the different requirements on b-jets between CRwA and the signal region. The impact of this uncertainty on the total background uncertainty is in a range between 15% and 20%.

Uncertainty on Z+jets from alternative methods: An additional uncertainty in the Z+jets estimate is taken as the largest deviation between the nominal background-only fit result and each of the alternative data-driven estimates described in Section 6.5.3. This results in an additional 25%, 25% and 40% uncertainty in SRA250, SRA350 and SRA450, respectively.

$t\bar{t}$ and single top. Uncertainties in the modeling of the $t\bar{t}$ and single top processes are dominant in the SRB ans sizable in SRA. Several sources of uncertainties affecting the nominal configuration (POWHEG+PYTHIA) were considered. This includes uncertainties on the MC generators and the modeling of parton showers employed, uncertainties related to initial and final state soft gluon radiation modeling, variations in the set of parameters that govern the parton showering, and uncertainties due to the choice of renormalization and factorization scales and PDFs. Altogether, they contribute to the total background uncertainty in a range between 15% and 20% for SRA and are about 70% in SRB.

Other small backgrounds. Uncertainties on other backgrounds such as diboson and $t\bar{t}$+V are also estimated by comparisons of the nominal sample with alternative samples differing in generator or parameter settings and their impact on the total background estimation is found to be negligible. The cross sections used to normalize the MC yields

to the highest order available are varied according to the scale uncertainty of the theoretical calculation, i.e. 5% for 6% for diboson, 13% and 12% for $t\bar{t}$+W and $t\bar{t}$+Z, respectively.

A summary of the systematic uncertainties considered in this analysis, related to their corresponding nuisance parameters, is given in Table 6.10.

Before performing the global fit, it is important to check the shape agreement between data and MC simulation for the relevant distributions in the control and validation regions.

An illustration of the background composition in each of the control and validation regions, as defined in Table 6.6- 6.9, can be seen in Figure 6.1. As anticipated, the background composition (pre-fit) is dominated by Z+jets production in CRzA and CRzB, by $t\bar{t}$ production in CRtopA and CRtopB, by W+jets in CRwA and by single top in CRstA.

Some relevant pre-fit distributions for the control and validation regions associated to SRA and SRB are shown in Figure 6.3-6.9 and Figure 6.10-6.12, respectively. The uncertainty bands in these distributions include the statistical and systematical uncertainties. The agreement in the shapes of the distributions between MC and the data is generally good.

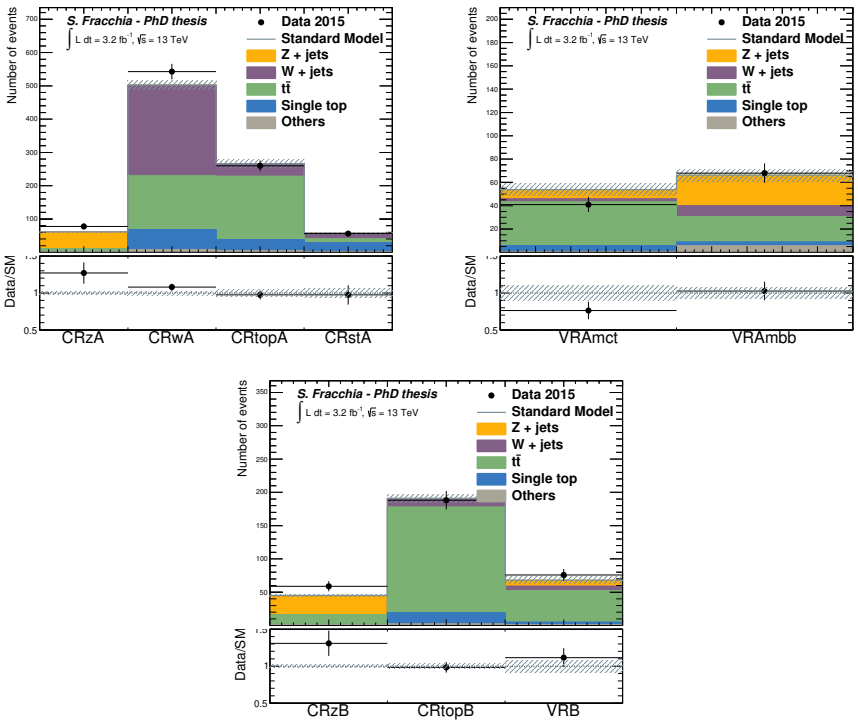

Figure 6.1: Expected background yields in the control and validation regions for SRA and SRB for 3.2 fb^{-1}, before the global fit is performed. Statistical and systematic uncertainties are shown.

Parameter definition	
Free parameters	**Definition**
mu_Z	Normalization factor
mu_W	Normalization factor (only for SRA)
mu_Top	Normalization factor
mu_ST	Normalization factor (only for SRA)
Nuisance parameters	**Definition**
alpha_JET_GroupedNP_1	Uncertainty on the jet energy scale.
alpha_JET_GroupedNP_2	Uncertainty on the jet energy scale.
alpha_JET_GroupedNP_3	Uncertainty on the jet energy scale.
alpha_JET_JER_SINGLE_NP	Uncertainty on the jet energy resolution.
alpha_JvtEfficiency	Uncertainty due to the jet vertex tagger requirement.
alpha_FT_EFF_B_systematics	Uncertainty due to the b-tagging (for b-jets).
alpha_FT_EFF_C_systematics	Uncertainty due to the b-tagging (for c-jets).
alpha_FT_EFF_Light_systematics	Uncertainty due to the b-tagging (for $light$-jets).
alpha_FT_EFF_extrapolation	Uncertainty due to the b-tagging (efficiency extrapolation at high p_{T}).
alpha_MET_SoftTrk_Scale	Uncertainty on the soft term energy scale of the missing transverse energy.
alpha_MET_SoftTrk_ResoPara	Uncertainty on the soft term energy resolution of the missing transverse energy (along ptHard axis).
alpha_MET_SoftTrk_ResoPerp	Uncertainty on the soft term energy resolution of the missing transverse energy (perpendicular to ptHard axis).
alpha_MET_SoftTrk_ResoCorr	Uncertainty on the soft term energy resolution of the missing transverse energy (simultaneous application of previous two).
alpha_EG_RESOLUTION_ALL	Uncertainty on the energy resolution of electrons.
alpha_EG_SCALE_ALL	Uncertainty on the energy scale of electrons.
alpha_EL_EFF_Reco_TotalCorrUncertainty	Uncertainty on the reconstruction efficiency of electrons.
alpha_EL_EFF_ID_TotalCorrUncertainty	Uncertainty on the identification efficiency of electrons.
alpha_EL_EFF_Iso_TotalCorrUncertainty	Uncertainty on the isolation efficiency of electrons.
alpha_EL_EFF_Trigger_TotalCorrUncertainty	Uncertainty on the trigger efficiency of electrons.
alpha_MUONS_ID	Uncertainty on the energy scale of muons (ID tracks).
alpha_MUONS_MS	Uncertainty on the energy scale of muons (MS tracks).
alpha_MUONS_SCALE	Uncertainty on the energy scale of muons.
alpha_MUON_EFF_STAT	Uncertainty on the reconstruction efficiency of muons (stat. error on the SF).
alpha_MUON_EFF_SYS	Uncertainty on the reconstruction efficiency of muons (sys. error on the SF).
alpha_MUON_ISO_STAT	Uncertainty on the isolation efficiency of muons (stat. error on the SF).
alpha_MUON_ISO_SYS	Uncertainty on the isolation efficiency of muons (sys. error on the SF).
alpha_MUON_EFF_TrigStatUncertainty	Uncertainty on the trigger efficiency of muons(stat. error on the SF).
alpha_MUON_EFF_TrigSystUncertainty	Uncertainty on the trigger efficiency of muons(sys. error on the SF).
alpha_Lumi	Uncertainty on the measurement of the luminosity in ATLAS.
alpha_ZjetsTH	Theory uncertainty on Z+jets background.
alpha_WjetsTH	Theory uncertainty on W+jets background.
alpha_WbFrac	Theory uncertainty on W+jets heavy flavor fraction.
alpha_WcFrac	Theory uncertainty on W+jets heavy flavor fraction.
alpha_DD_syst	Uncertainty on Z+jets background from alternate methods.
alpha_ttbarTH	Theory uncertainty on $t\bar{t}$ background.
alpha_singleTTH	Theory uncertainty on single top background.

Table 6.10: List of all nuisance parameters used in the analysis and their definition in terms of normalization factors and sources of systematic uncertainty.

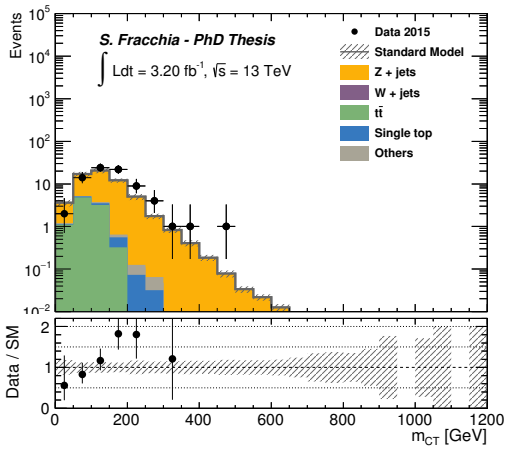

(a)

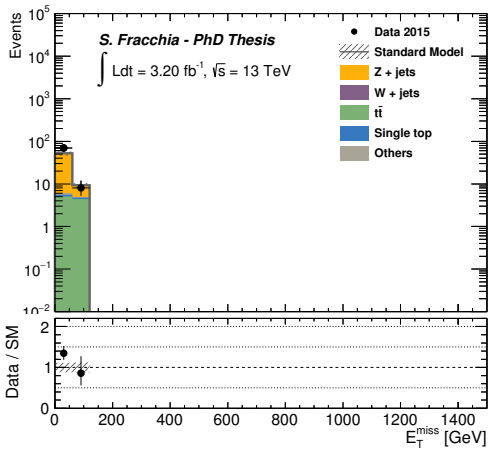

(b)

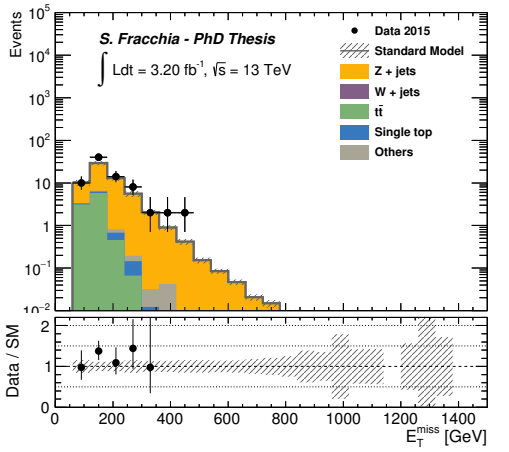

(c)

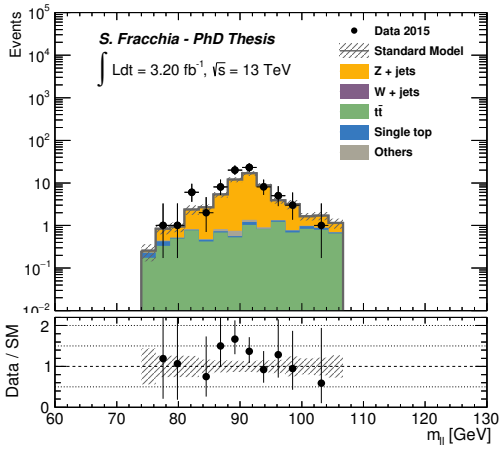

(d)

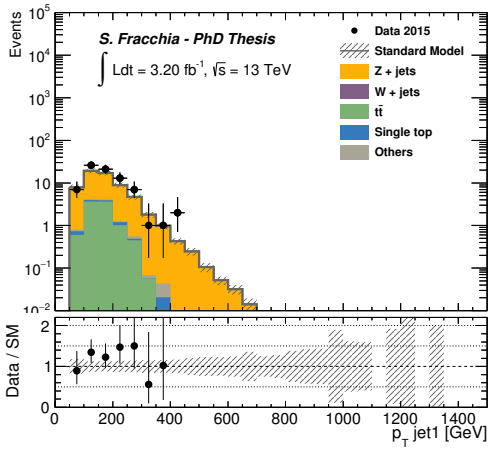

(e)

Figure 6.2: Pre-fit distributions of (a) m_{CT}, (b) $E_{\mathrm{T}}^{\mathrm{miss}}$, (c) $\tilde{E}_{\mathrm{T}}^{\mathrm{miss}}$, (d) $\mathrm{m}_{\ell\ell}$ and (e) leading jet p_{T} in the Z+jets control region for SRA. The grey band shows the total statistical and detector systematic uncertainty on the background expectation.

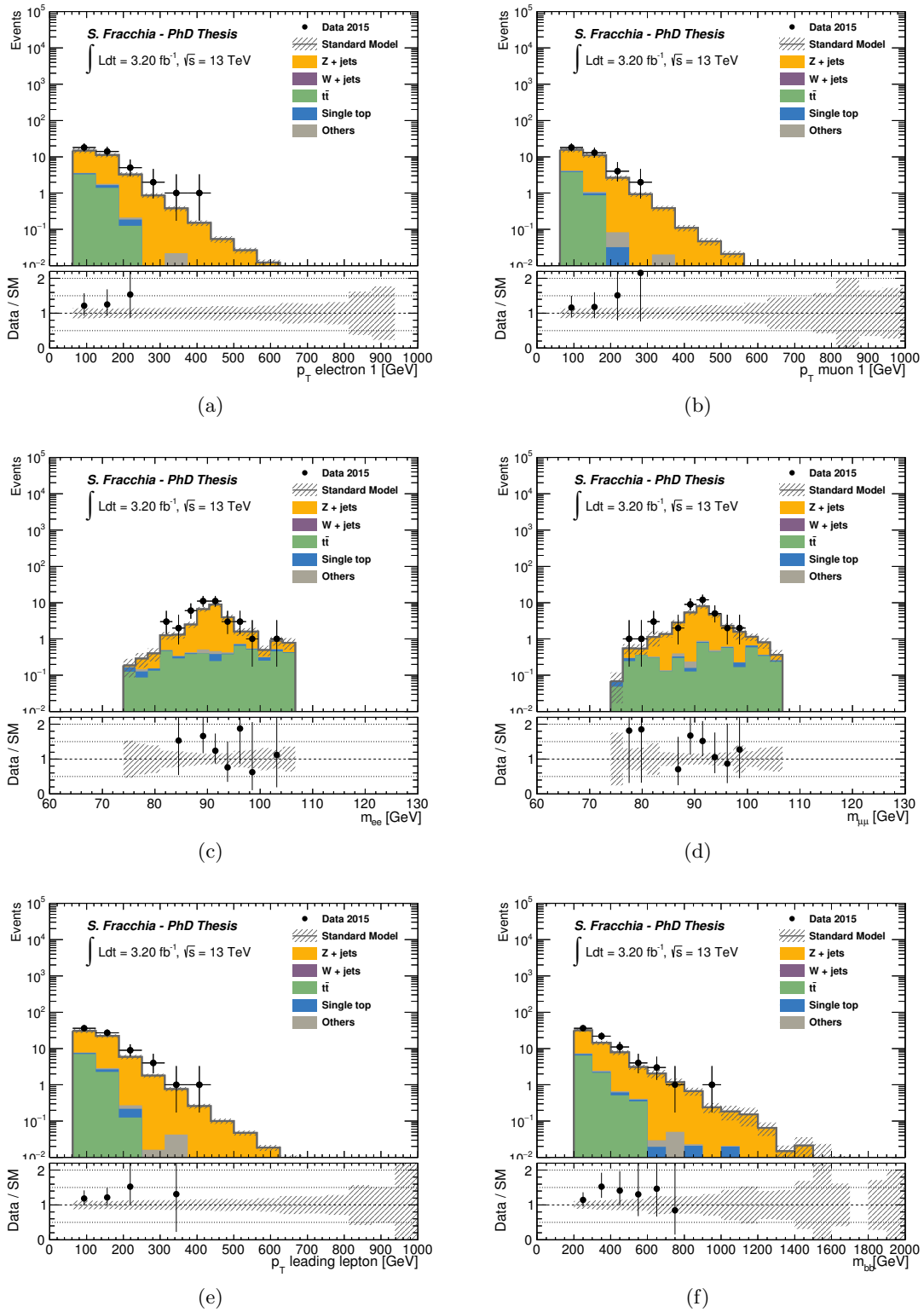

(a) (b) (c) (d) (e) (f)

Figure 6.3: Pre-fit distributions of (a) p_{T} of the leading lepton in the ee channel, (b) p_{T} of the leading lepton in the $\mu\mu$ channel, (c) $m_{\ell\ell}$ in the e channel, (d) $m_{\ell\ell}$ in the $\mu\mu$ channel (e) p_{T} of the leading lepton and (f) m_{bb} in the Z+jets control region for SRA. The grey band shows the total statistical and detector systematic uncertainty on the background expectation.

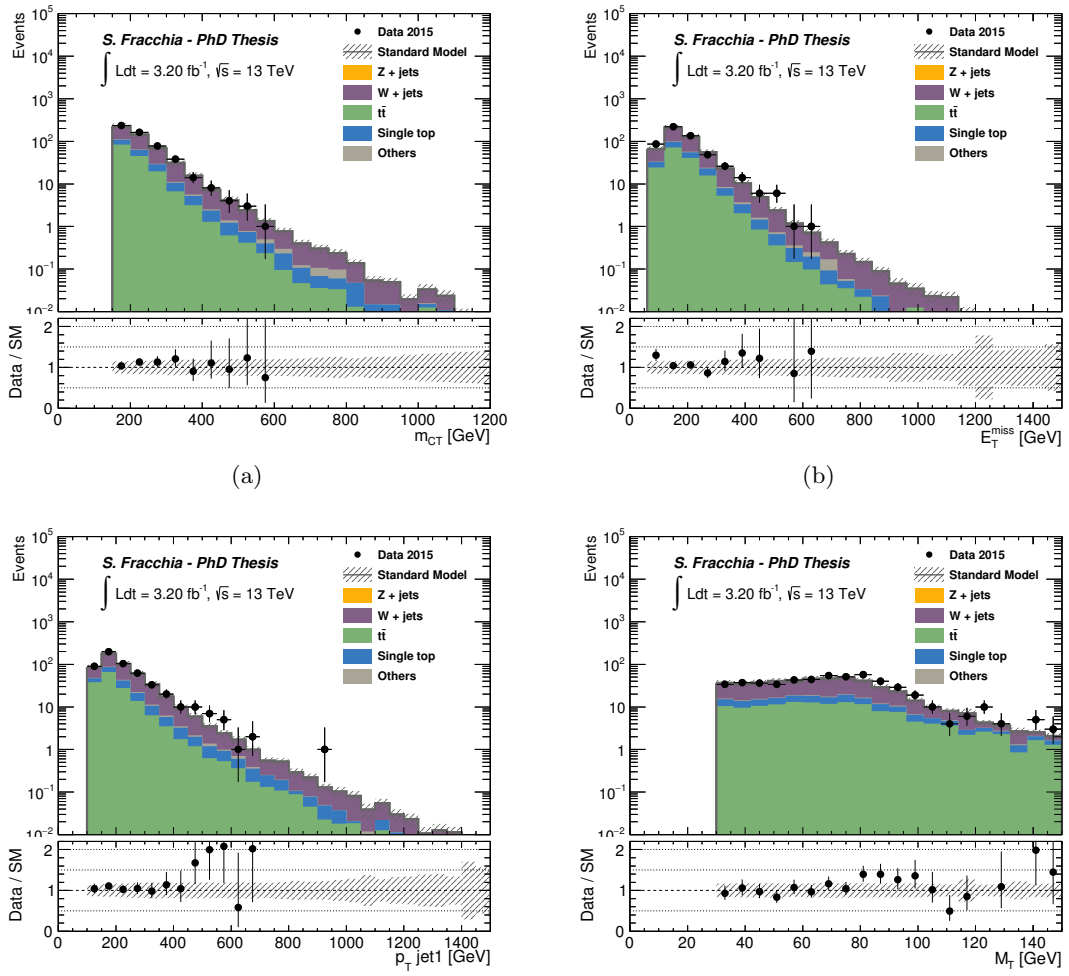

(a) (b)

(c) (d)

Figure 6.4: Pre-fit distributions of (a) m_{CT}, (b) $E_{\mathrm{T}}^{\mathrm{miss}}$, (c) leading jet p_{T} and (d) m_{T} in the W+jets control region for SRA. The grey band shows the total statistical and detector systematic uncertainty on the background expectation.

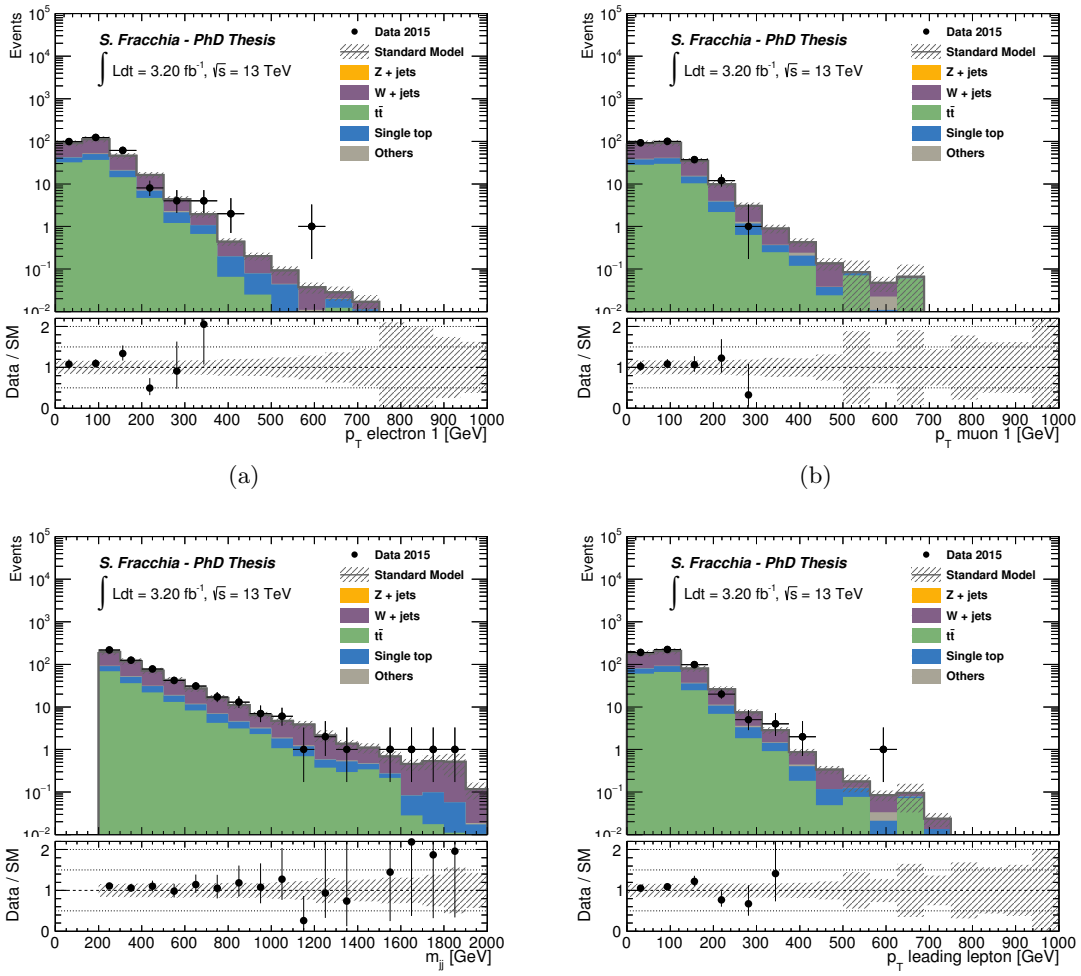

(a) (b)

(c) (d)

Figure 6.5: Pre-fit distributions of (a) p_{T} of the lepton in the e channel, (b) p_{T} of the lepton in the μ channel, (c) m_{jj} and (d) leading lepton p_{T} in the W+jets control region for SRA. The grey band shows the total statistical and detector systematic uncertainty on the background expectation.

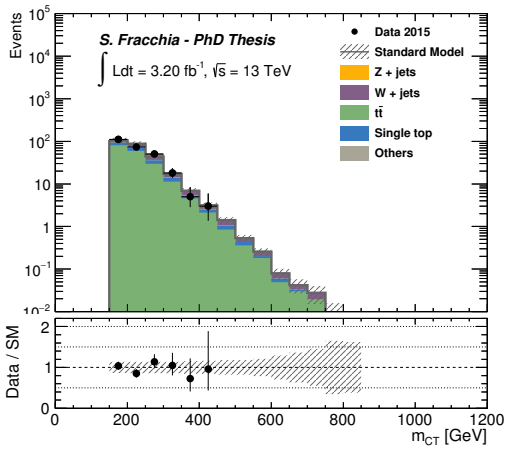

(a)

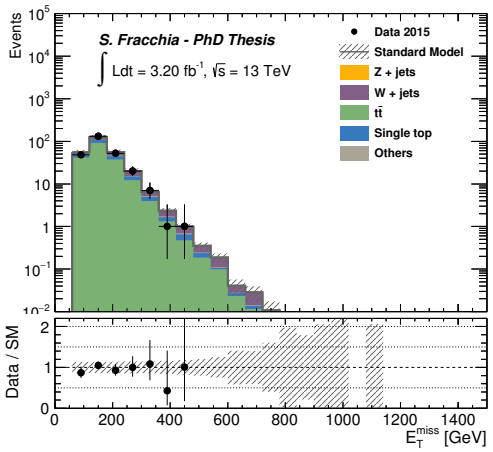

(b)

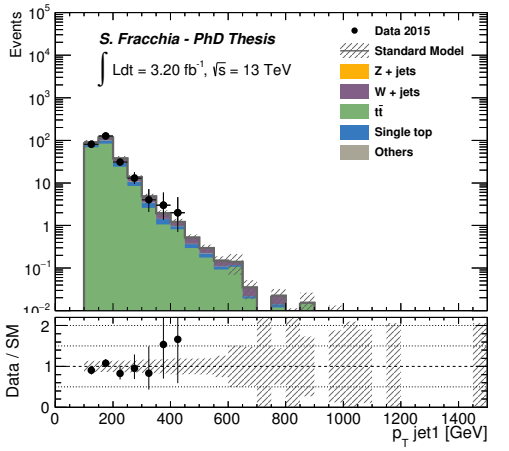

(c)

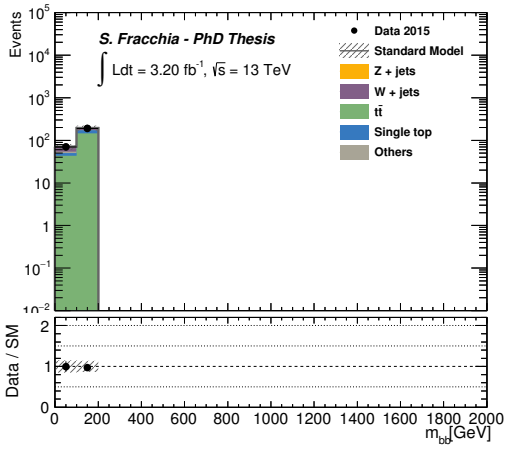

(d)

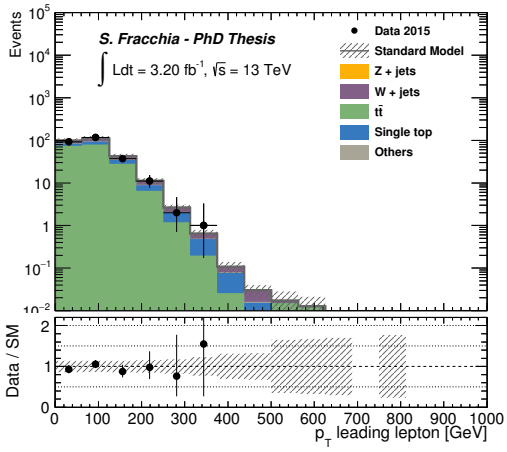

(e)

Figure 6.6: Pre-fit distributions of (a) m_{CT}, (b) $E_{\mathrm{T}}^{\mathrm{miss}}$, (c) leading jet p_{T}, (d) m_{bb} and (e) the p_{T} of the leading lepton in the $t\bar{t}$ control region for SRA. The grey band shows the total statistical and detector systematic uncertainty on the background expectation.

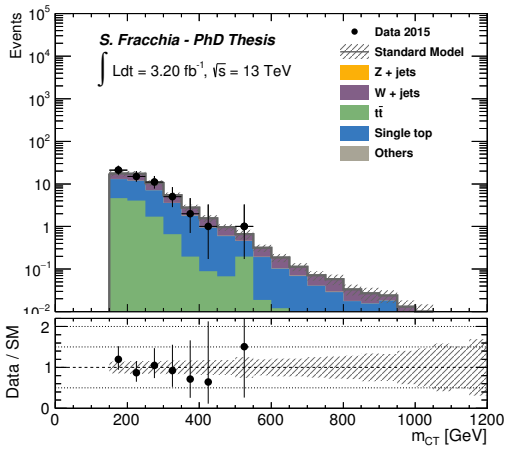

(a)

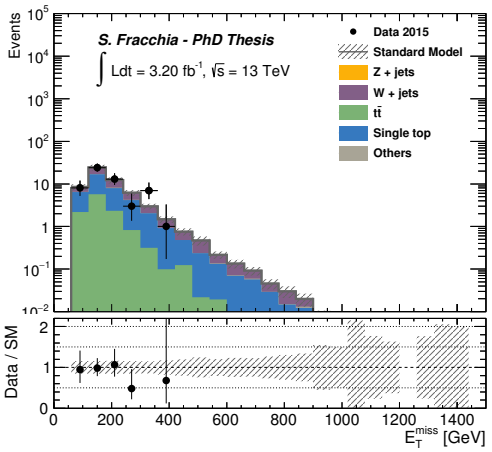

(b)

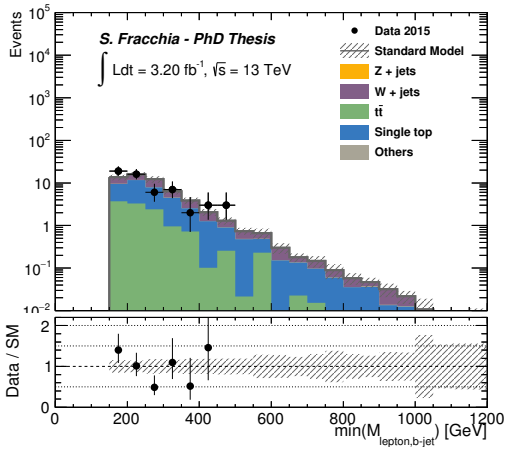

(c)

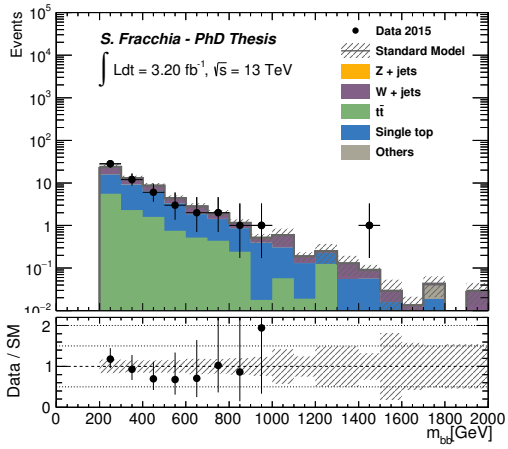

(d)

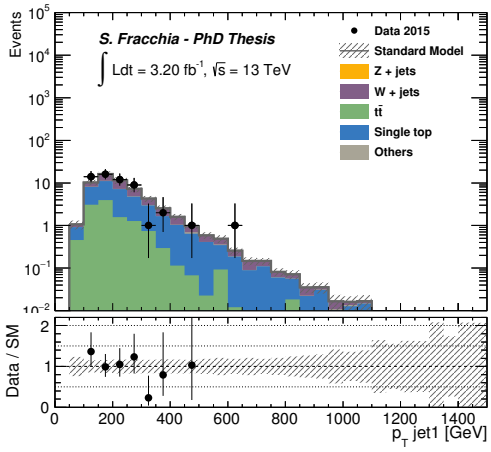

(e)

Figure 6.7: Pre-fit distributions of (a) m_{CT}, (b) $E_{\mathrm{T}}^{\mathrm{miss}}$, (c) $\mathrm{m}_{b\ell}^{\mathrm{min}}$, (d) m_{bb} and (e) leading jet p_{T} in the single top control region for SRA. The grey band shows the total statistical and detector systematic uncertainty on the background expectation.

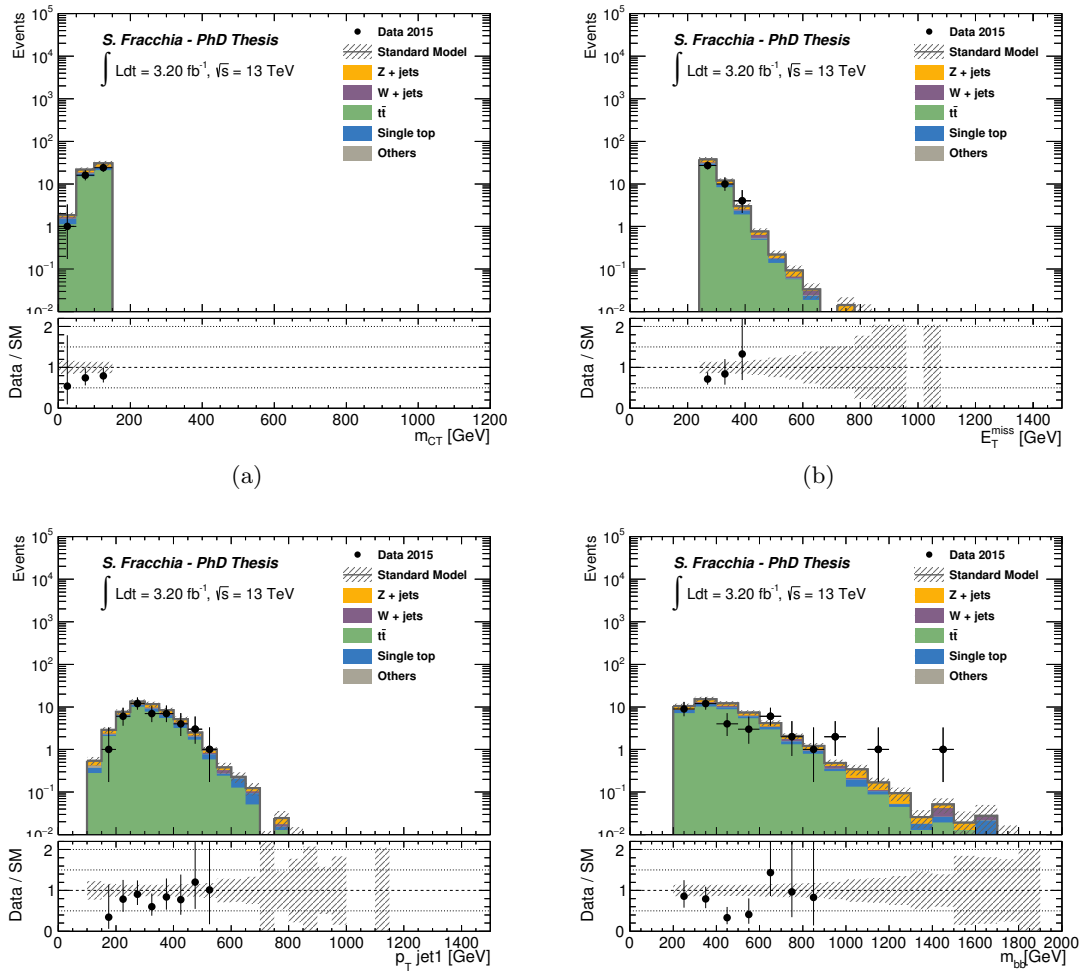

(a) (b)

(c) (d)

Figure 6.8: Pre-fit distributions of (a) m_{CT}, (b) $E_{\mathrm{T}}^{\mathrm{miss}}$, (c) leading jet p_{T} and (d) m_{bb} in VRAmct. The grey band shows the total statistical and detector systematic uncertainty on the background expectation.

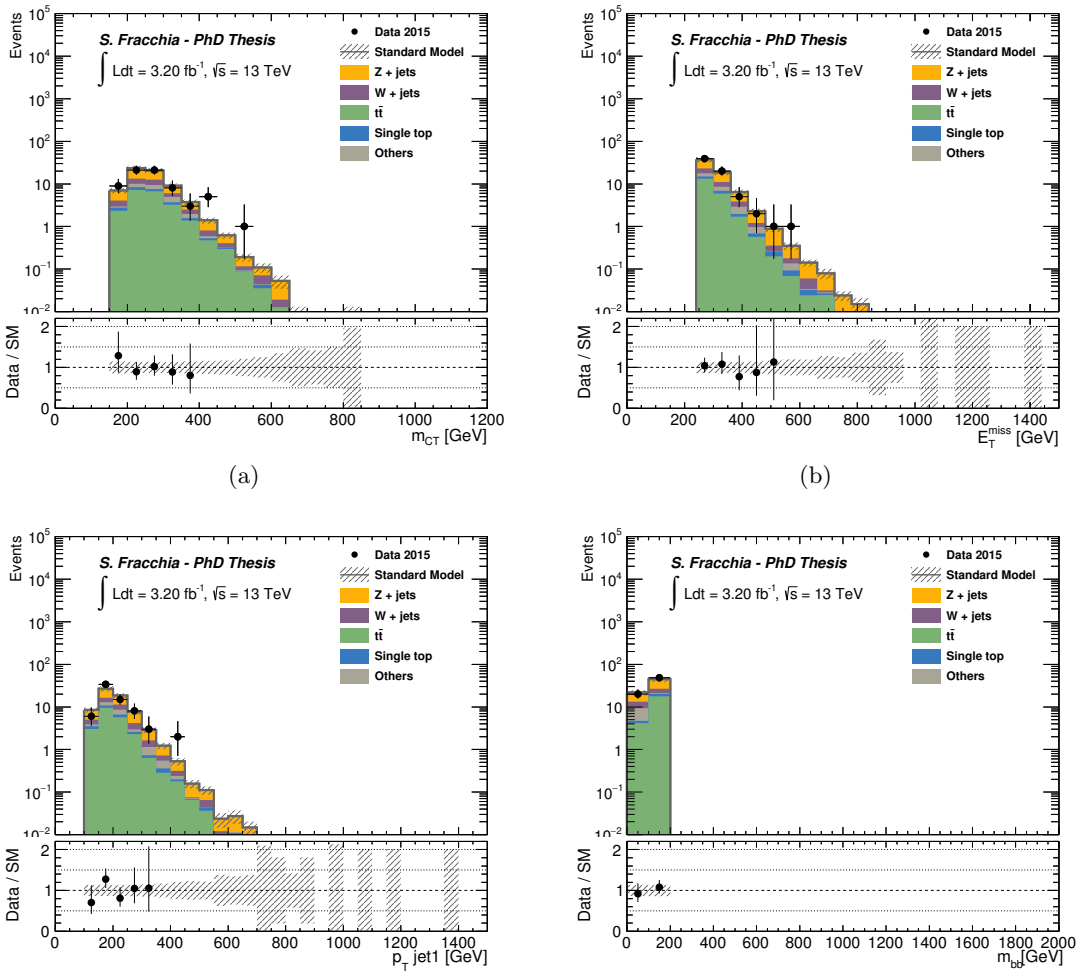

(a) (b)

(c) (d)

Figure 6.9: Pre-fit distributions of (a) m_{CT}, (b) $E_{\mathrm{T}}^{\mathrm{miss}}$, (c) leading jet p_{T} and (d) m_{bb} in VRAmbb. The grey band shows the total statistical and detector systematic uncertainty on the background expectation.

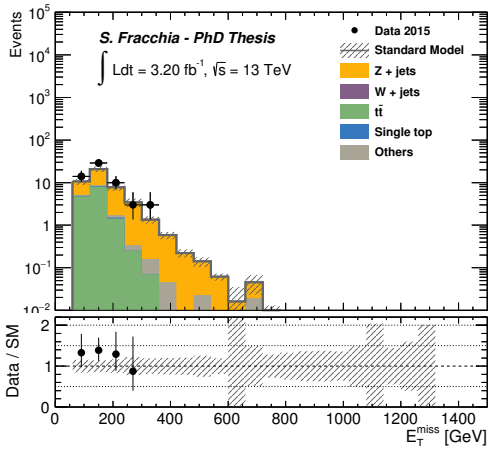

(a)

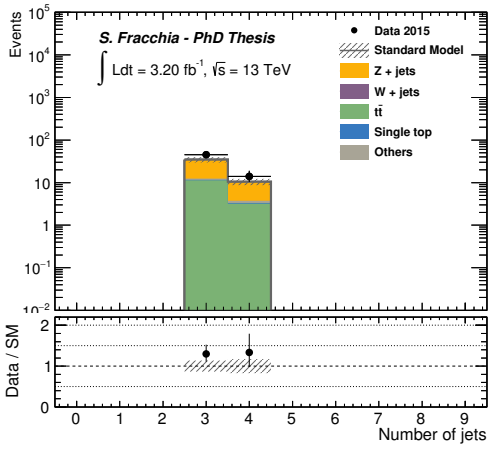

(b)

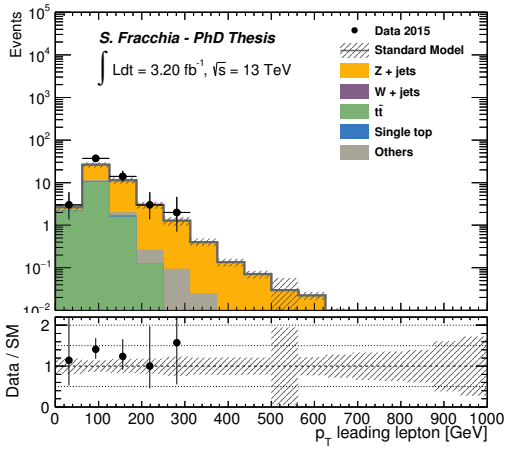

(c)

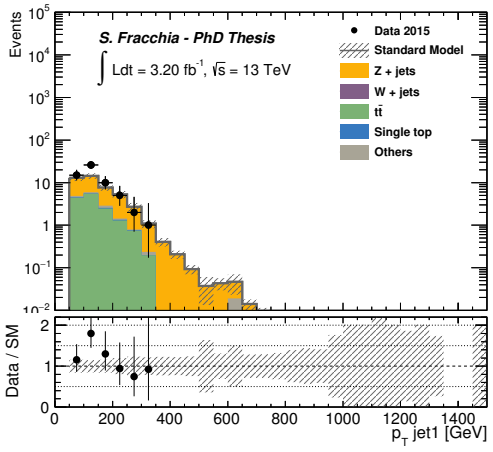

(d)

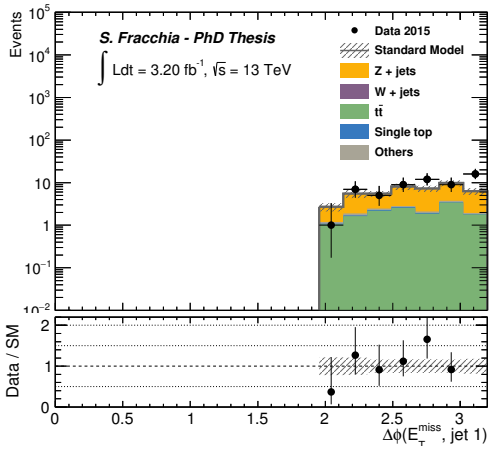

(e)

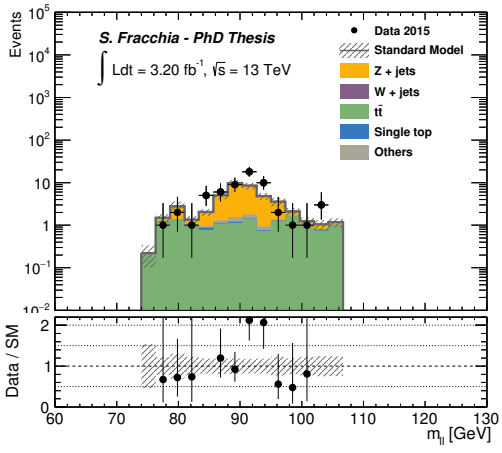

(f)

Figure 6.10: Pre-fit distributions of (a) $\tilde{E}_{\mathrm{T}}^{\mathrm{miss}}$, (b) jet multiplicity, (c) leading lepton p_{T}, (d) leading jet p_{T}, (e) $\Delta\phi(1^{\mathrm{st}}$ jet, $\mathrm{E}_{\mathrm{T}}^{\mathrm{miss}})$ and (f) $\mathrm{m}_{\ell\ell}$ in the Z+jets control region for SRB. The grey band shows the total statistical and detector systematic uncertainty on the background expectation.

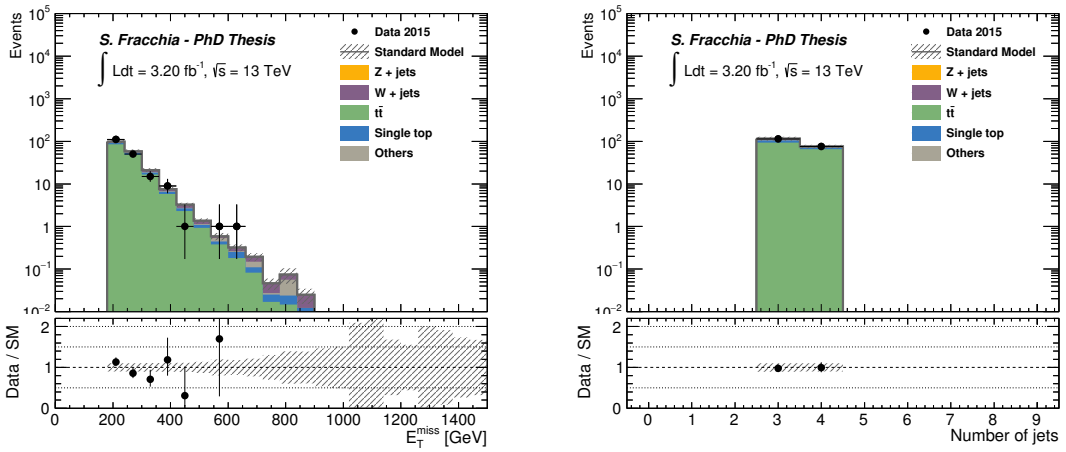

(a)

(b)

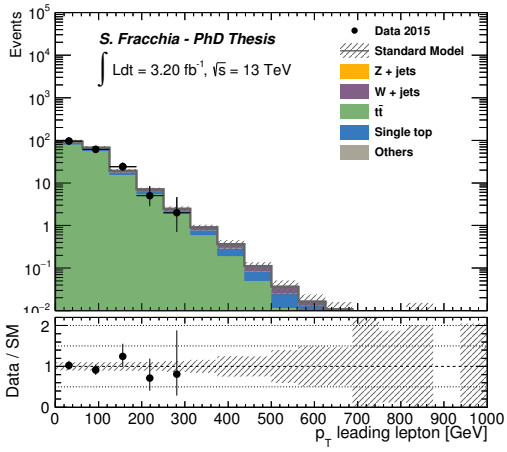

(c)

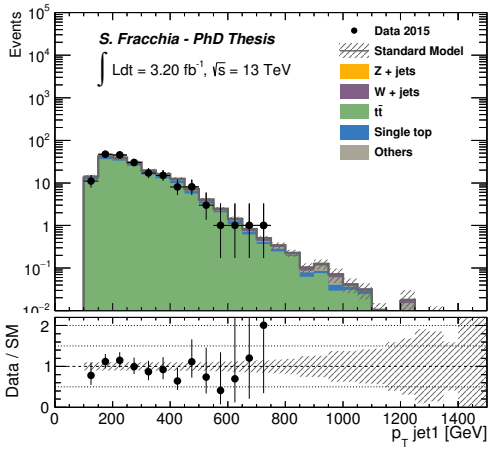

(d)

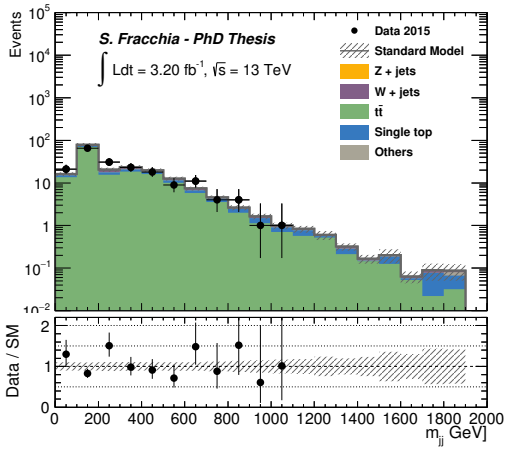

(e)

Figure 6.11: Pre-fit distributions of (a) $E_{\mathrm{T}}^{\mathrm{miss}}$, (b) jet multiplicity, (c) leading lepton p_{T}, (d) leading jet p_{T} and (e) m_{jj} in the $t\bar{t}$ control region for SRB. The grey band shows the total statistical and detector systematic uncertainty on the background expectation.

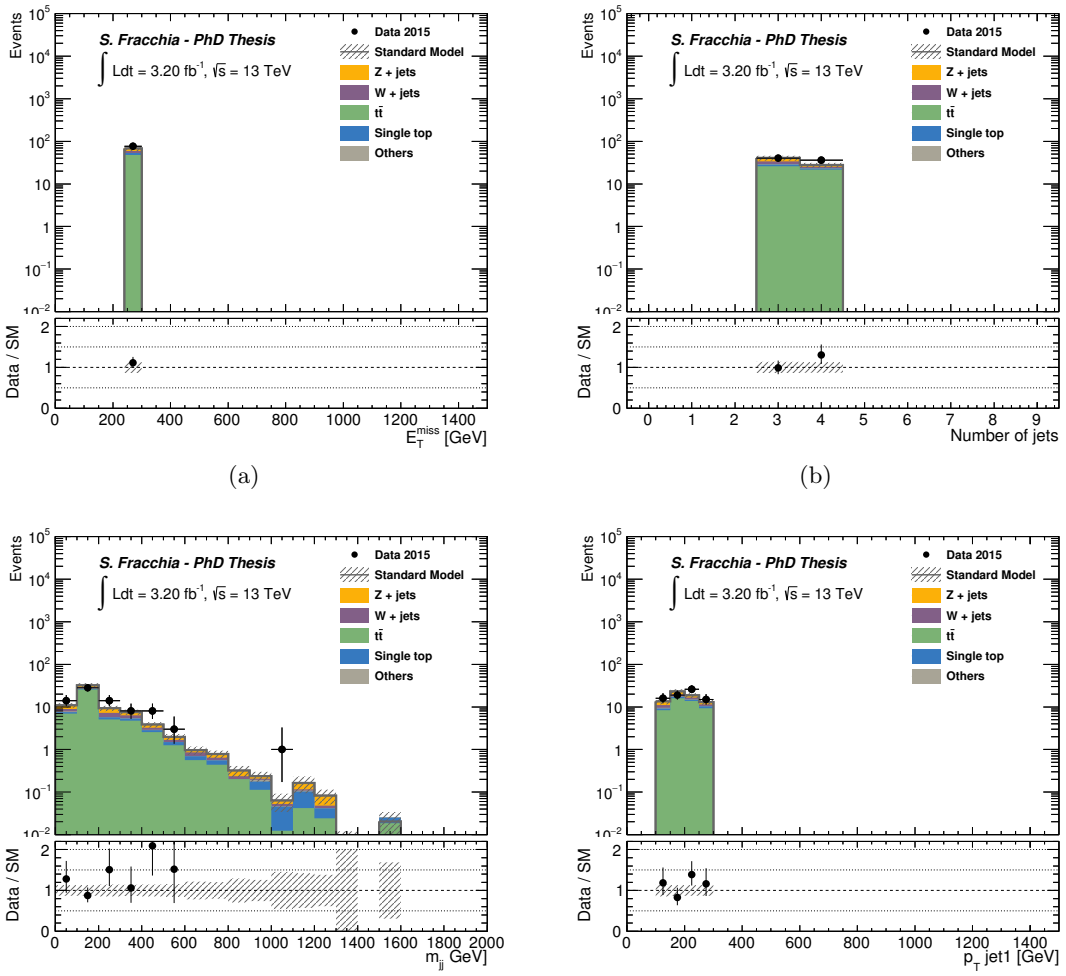

(a) (b) (c) (d)

Figure 6.12: Pre-fit distributions of (a) $E_{\mathrm{T}}^{\mathrm{miss}}$, (b) jet multiplicity, (c) m_{jj} and (d) leading jet p_{T} in VRB. The grey band shows the total statistical and detector systematic uncertainty on the background expectation.

6.8 Background contributions after the global fit

The normalization factors for the different backgrounds are extracted from the control regions by means of the background-only fit, as described in Section 6.6.

The data and background event yields for the control and validation regions associated to SRA and SRB are shown in Table 6.11 and Table 6.12, respectively. For each control region, the MC predicted yields before and after the background-only fit are shown. The data and total background predictions in the control region are in agreement by construction after the background-only fit is performed. The two validation regions for SRA show a slight over-prediction of background events compared to the data, but compatible within the statistical and systematic uncertainties.

The normalization factors for the background processes in the different selections are shown in Table 6.13 and Table 6.14 for SRA and SRB, respectively. The uncertainties on the normalization factors include both the statistical and systematic components. Within the uncertainties, the normalization factors for $t\bar{t}$ and single top are compatible with unity. A small deviation from unity is observed for the W+jets and, more significantly, for the Z+jets normalization factors. The latter was extensively studied in the course of the analysis, leading to the development of the alternative methods for the Z+jets estimation, which were described in Section 6.5.3.

The distribution of the pulls of the nuisance parameters, representing their deviation from the central value according to a normal Gaussian distribution with mean 0 and sigma 1, as well as the correlations among the normalization factors and the nuisance parameters in the global fit, are presented in Figures 6.13- 6.14 for SRA and SRB, respectively. A strong deviation from unity for the sigma values of the nuisance parameters would mean that a mismodeling is being adjusted by an artificial variation of the systematic parameters. Similarly, such a behavior would translate into large (anti-)correlations between the different nuisance parameters. The correlation matrices of the fit parameters are shown in Figures 6.15- 6.16, for SRA and SRB, respectively. From the pulls distributions it can be seen that none of the nuisance parameters is strongly adjusted in the fit. From the correlation matrices, it can be seen that the normalization factors are correlated among each other, as a consequence of the cross contamination between the background processes in the different control regions. Moreover, correlations between the normalization factors and some systematic uncertainties are also significant like, for example, in the case of the `alpha_WbFrac` nuisance parameter. In this case their systematic effects are compensated by the normalization factors, computed in the control regions. The nuisance parameters for the systematic uncertainties are almost uncorrelated among themselves.

The region compositions for the control and validation regions after the background-only fit are shown in Figures 6.17. As a consequence of applying the normalization factors obtained after the fit, the background composition in each region is slightly different with

respect to the composition pre-fit, shown in Figure 6.1.

Finally, the distributions of some relevant variables for each control and validation region after the background-only fit are shown in Figures 6.18-6.28. All the distributions show a reasonable agreement between data and simulation in the control and validation regions, indicating a good modeling of the SM background processes.

CR/VR channels	CRzA	CRwA	CRttA	CRstA	VRmctA	VRmbbA
Observed events	78	543	260	56	41	68
Fitted bkg events	78.01 ± 8.82	543.00 ± 23.29	260.11 ± 16.12	55.88 ± 7.42	54.25 ± 7.44	75.61 ± 7.50
Fitted Zjets events	67.65 ± 8.98	3.76 ± 0.64	1.38 ± 0.23	0.94 ± 0.17	10.78 ± 3.35	35.34 ± 6.30
Fitted Wjets events	0.00 ± 0.00	327.54 ± 43.47	45.04 ± 14.19	20.24 ± 5.71	2.94 ± 0.84	11.36 ± 4.05
Fitted TTbar events	9.01 ± 1.63	153.71 ± 26.17	180.97 ± 22.66	11.15 ± 2.09	35.60 ± 6.88	20.76 ± 3.82
Fitted SingleTop events	0.75 ± 0.36	50.01 ± 22.42	27.19 ± 12.19	23.03 ± 10.22	4.65 ± 2.12	2.60 ± 1.20
Fitted DiBosons events	0.27 ± 0.06	7.02 ± 1.11	4.84 ± 0.62	0.37 ± 0.08	0.18 ± 0.06	5.29 ± 0.59
Fitted ttbarZ events	0.32 ± 0.03	0.56 ± 0.14	0.41 ± 0.04	0.06 ± 0.01	0.08 ± 0.01	0.22 ± 0.07
Fitted ttbarW events	0.01 ± 0.00	0.39 ± 0.03	0.26 ± 0.03	0.10 ± 0.01	0.03 ± 0.00	0.03 ± 0.01
MC exp. SM events	61.41	502.99	266.58	57.47	53.71	66.21
MC exp. Zjets events	50.45	2.81	1.03	0.70	8.04	26.35
MC exp. Wjets events	0.00	270.54	37.20	16.72	2.43	9.38
MC exp. TTbar events	9.45	161.22	189.94	11.69	37.34	21.78
MC exp. SingleTop events	0.91	60.45	32.88	27.83	5.62	3.15
MC exp. DiBosons events	0.27	7.03	4.85	0.37	0.18	5.29
MC exp. ttbarZ events	0.32	0.56	0.41	0.06	0.08	0.22
MC exp. ttbarW events	0.01	0.39	0.26	0.10	0.03	0.03

Table 6.11: Background-only fit results in the control and validation regions associated to the SRA selection for an integrated luminosity of 3.2 fb^{-1}. The uncertainties shown include the statistical and the systematic uncertainties.

CR/VR channels	CRzB	CRtopB	VRB
Observed events	59	188	76
Fitted bkg events	59.00 ± 7.66	188.01 ± 13.71	71.81 ± 6.71
Fitted Zjets events	43.10 ± 7.86	0.30 ± 0.12	13.96 ± 3.17
Fitted Wjets events	0.00 ± 0.00	12.91 ± 4.74	6.42 ± 3.42
Fitted TTbar events	14.24 ± 1.95	155.98 ± 14.97	46.64 ± 5.95
Fitted SingleTop events	0.42 ± 0.07	16.62 ± 2.13	3.95 ± 0.61
Fitted DiBosons events	0.83 ± 0.36	1.31 ± 0.20	0.50 ± 0.16
Fitted ttbarZ events	0.38 ± 0.04	0.57 ± 0.09	0.28 ± 0.06
Fitted ttbarW events	0.03 ± 0.01	0.31 ± 0.03	0.05 ± 0.01
MC exp. SM events	45.05	190.92	68.10
MC exp. Zjets events	28.88	0.20	9.36
MC exp. Wjets events	0.00	12.92	6.43
MC exp. TTbar events	14.52	158.97	47.53
MC exp. SingleTop events	0.42	16.63	3.95
MC exp. DiBosons events	0.83	1.31	0.50
MC exp. ttbarZ events	0.38	0.57	0.28
MC exp. ttbarW events	0.03	0.31	0.05

Table 6.12: Background-only fit results in the control and validation regions associated to the SRB selection for an integrated luminosity of 3.2 fb^{-1}. The uncertainties shown include the statistical and the systematic uncertainties.

μ_{st}	0.83 ± 0.37
μ_{top}	0.95 ± 0.13
μ_W	1.21 ± 0.18
μ_Z	1.34 ± 0.18

Table 6.13: Normalization multiplicative factors obtained from the background-only fit with 3.2 fb^{-1}, for each of the main backgrounds in SRA. The uncertainties include both statistical and systematic sources.

μ_{top}	0.98 ± 0.10
μ_Z	1.49 ± 0.27

Table 6.14: Normalization multiplicative factors obtained from the background-only fit with 3.2 fb^{-1}, for each of the main backgrounds in SRB. The uncertainties include both statistical and systematic sources.

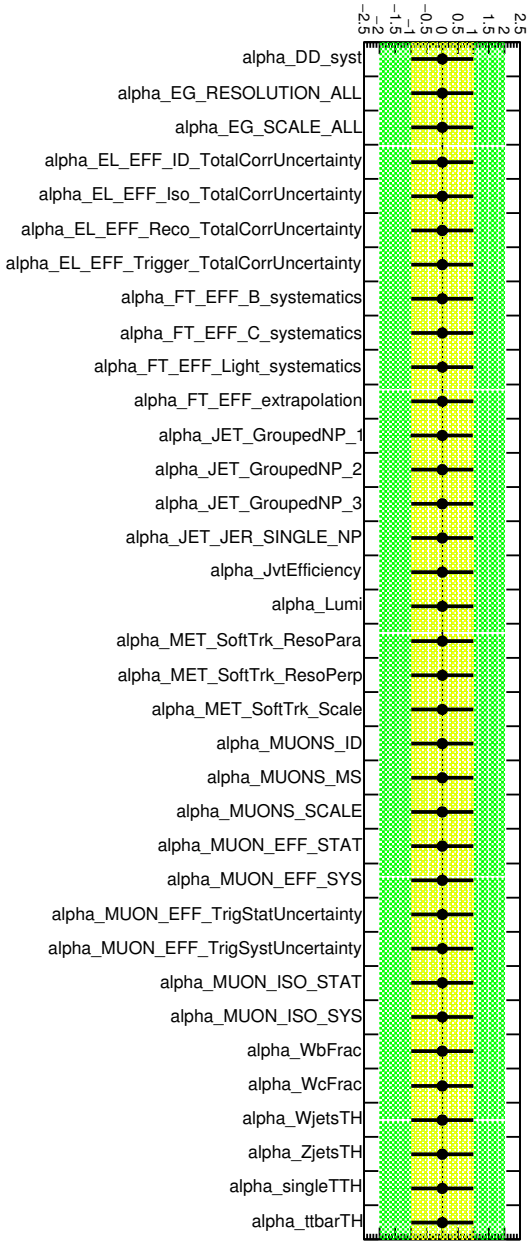

Figure 6.13: Pulls of nuisance parameters obtained from the background-only fit for SRA channels with 3.2 fb^{-1} of data.

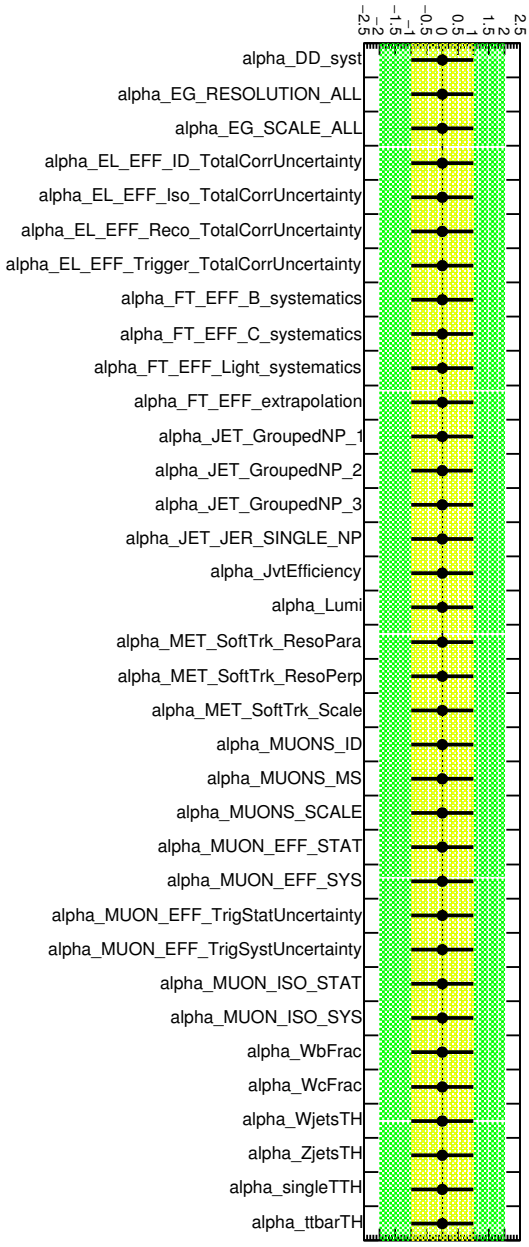

Figure 6.14: Pulls of nuisance parameters obtained from the background-only fit for SRB channels with 3.2 fb^{-1} of data.

Figure 6.15: Correlation matrix of fit parameters, obtained from the background-only fit for SRA with 3.2 fb^{-1} of data. Only the nuisance parameters with any correlation factor above 0.1 are shown.

Figure 6.16: Correlation matrix of fit parameters, obtained from the background-only fit for SRB with 3.2 fb^{-1} of data. Only the nuisance parameters with any correlation factor above 0.1 are shown.

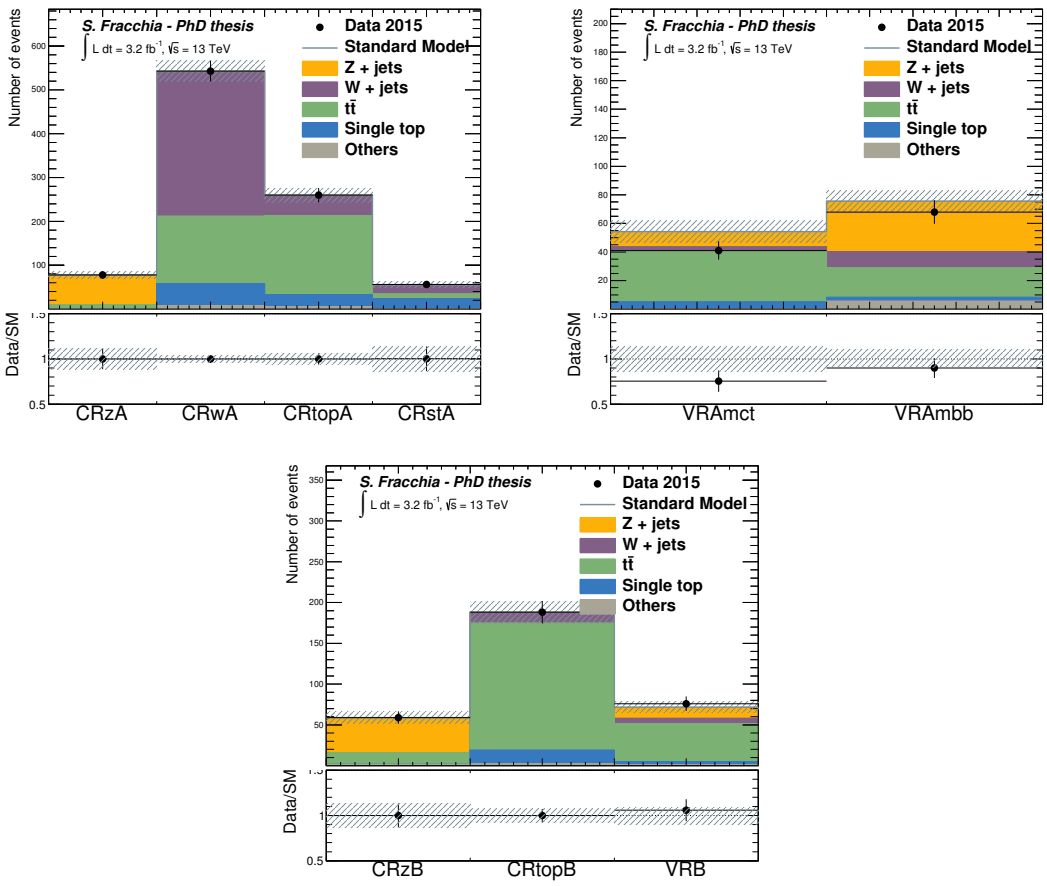

Figure 6.17: Post-fit background yields in the control and validation regions for SRA and SRB for 3.2 fb^{-1}. Statistical and systematical uncertainties are shown.

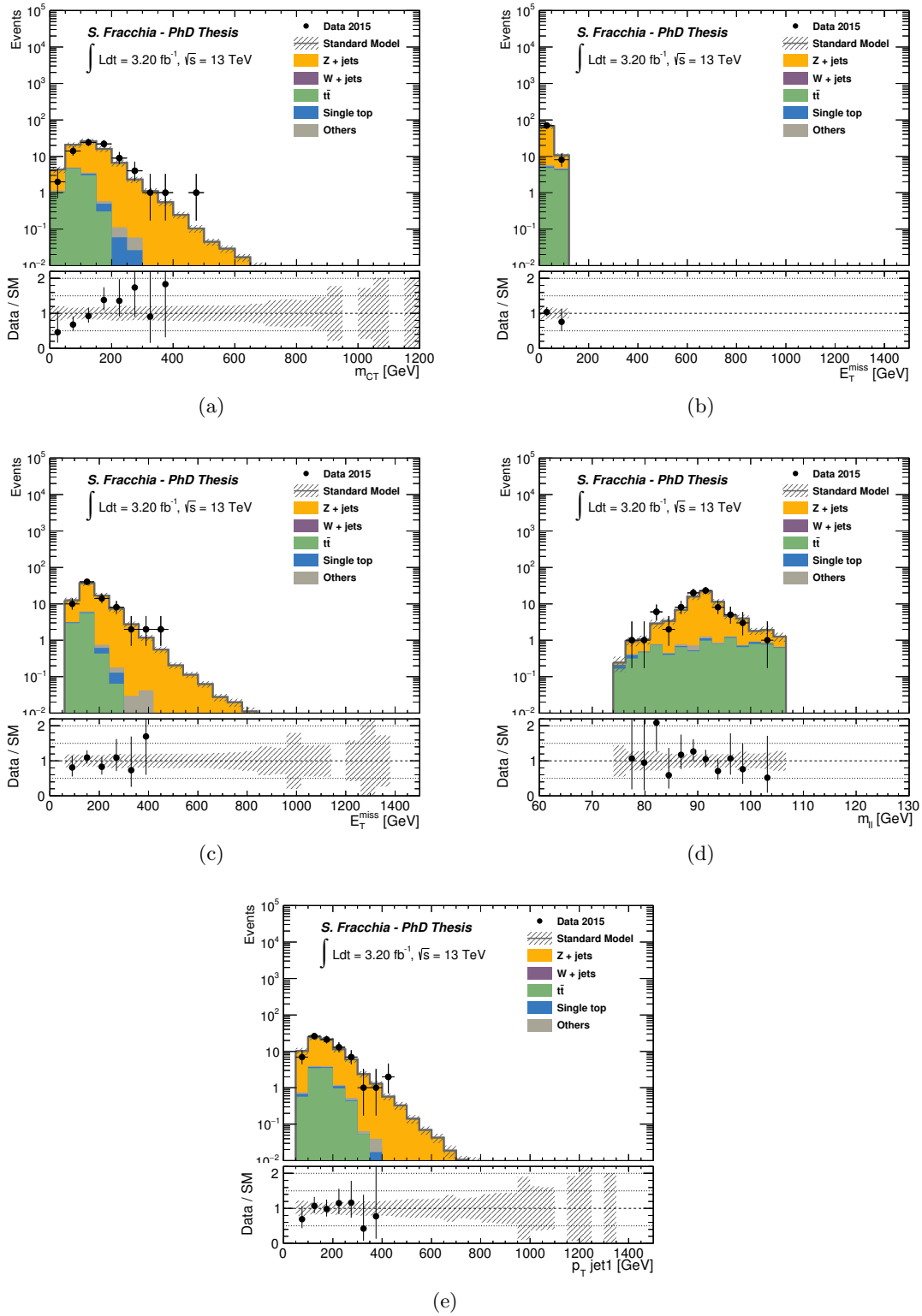

(a) (b) (c) (d) (e)

Figure 6.18: Post-fit distributions of (a) m_{CT}, (b) $E_{\mathrm{T}}^{\mathrm{miss}}$, (c) $\tilde{E}_{\mathrm{T}}^{\mathrm{miss}}$, (d) $\mathrm{m}_{\ell\ell}$ and (e) leading jet p_{T} in the Z+jets control region for SRA. The grey band shows the total statistical and detector systematic uncertainty on the background expectation.

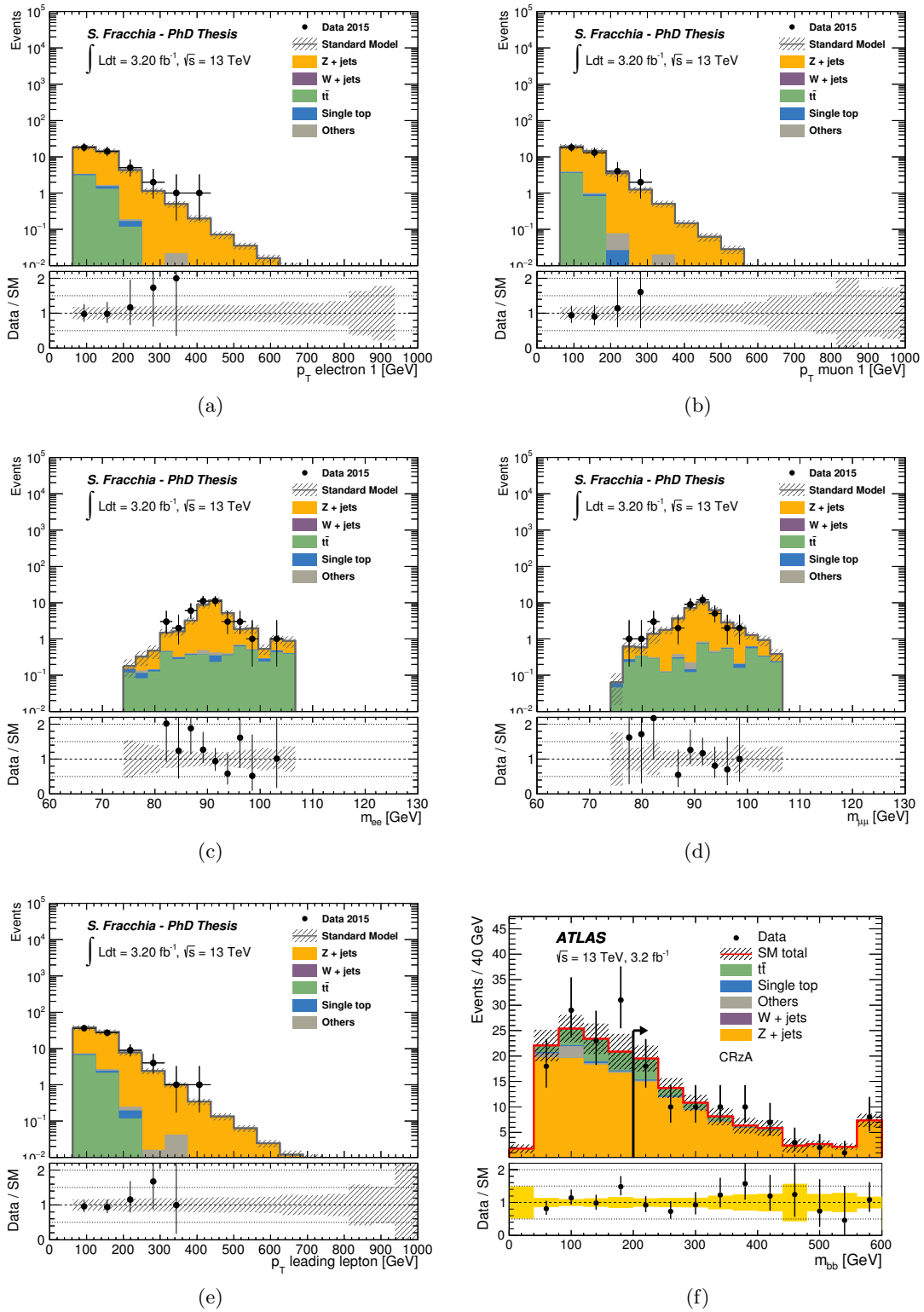

Figure 6.19: Post-fit distributions of (a) p_{T} of the leading lepton in the ee channel, (b) p_{T} of the leading lepton in the $\mu\mu$ channel, (c) $\mathrm{m}_{\ell\ell}$ in the e channel, (d) $\mathrm{m}_{\ell\ell}$ in the $\mu\mu$ channel (e) p_{T} of the leading lepton and (f) m_{bb} in the Z+jets control region for SRA. The grey band shows the total statistical and detector systematic uncertainty on the background expectation.

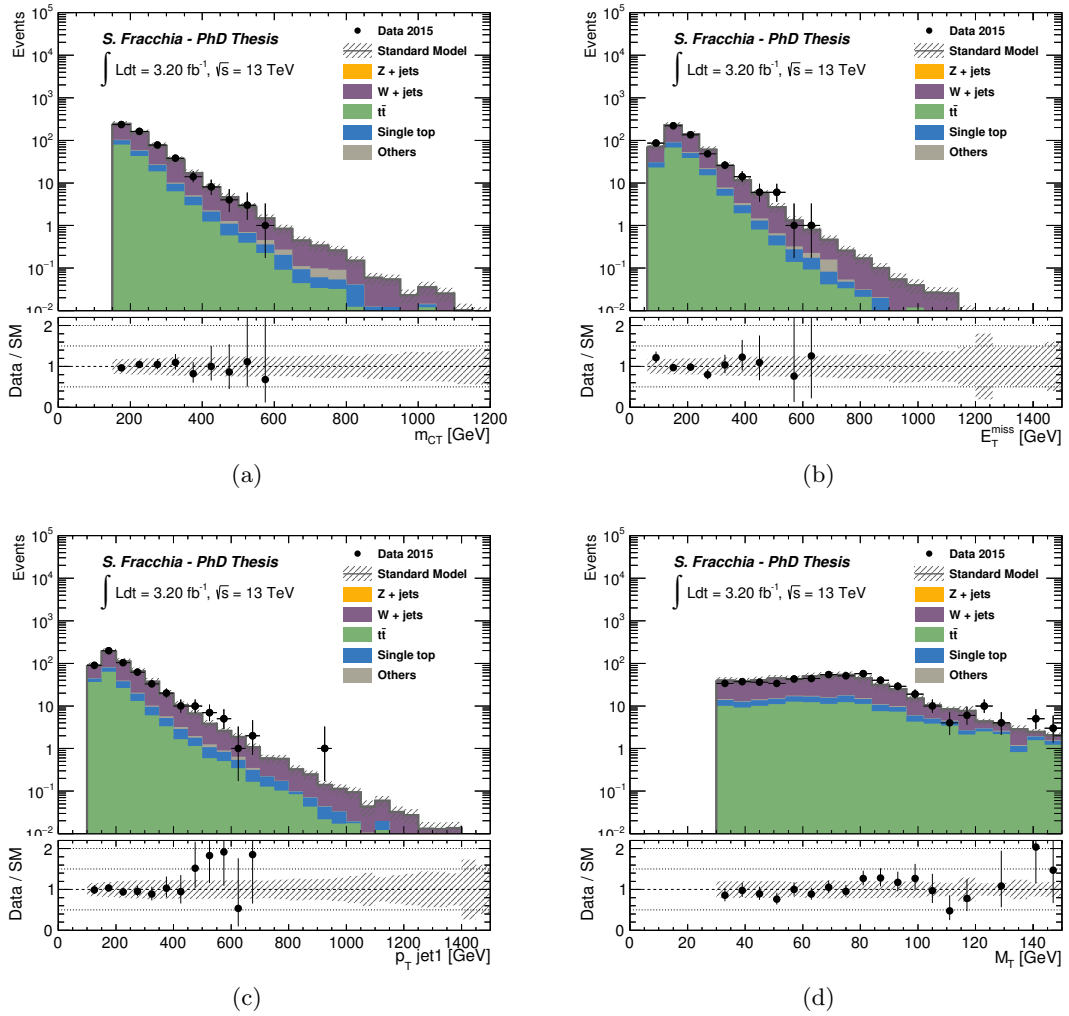

Figure 6.20: Post-fit distributions of (a) m_{CT}, (b) $E_{\mathrm{T}}^{\mathrm{miss}}$, (c) leading jet p_{T} and (d) m_{T} in the W+jets control region for SRA. The grey band shows the total statistical and detector systematic uncertainty on the background expectation.

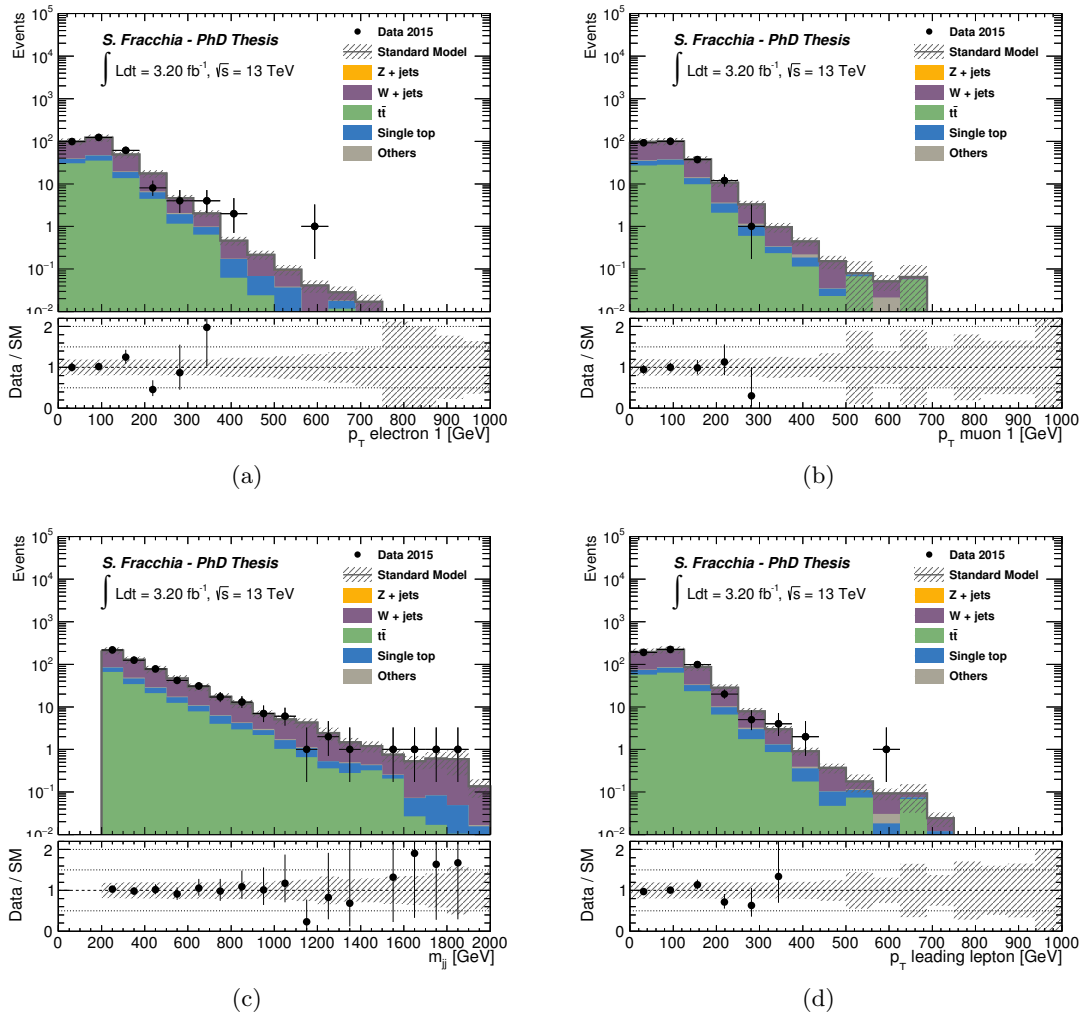

Figure 6.21: Post-fit distributions of (a) p_{T} of the lepton in the e channel, (b) p_{T} of the lepton in the μ channel, (c) m_{jj} and (d) leading lepton p_{T} in the W+jets control region for SRA. The grey band shows the total statistical and detector systematic uncertainty on the background expectation.

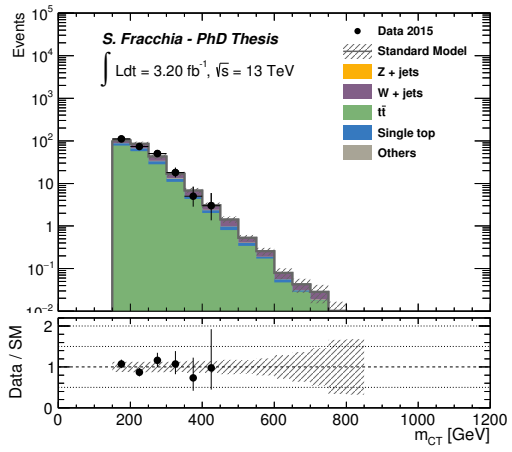

(a)

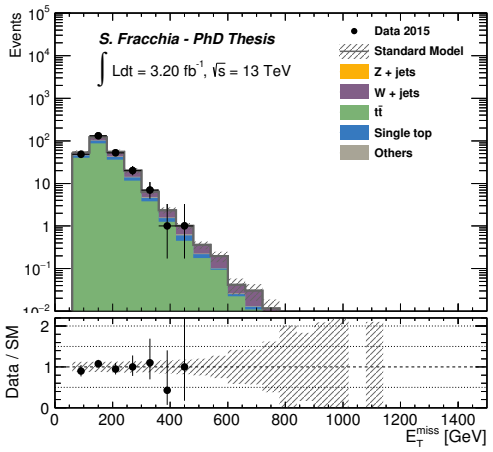

(b)

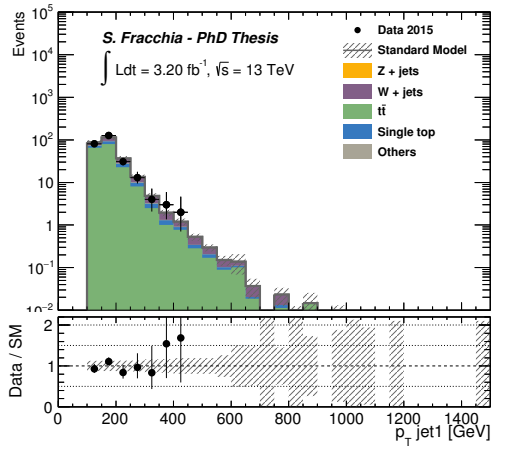

(c)

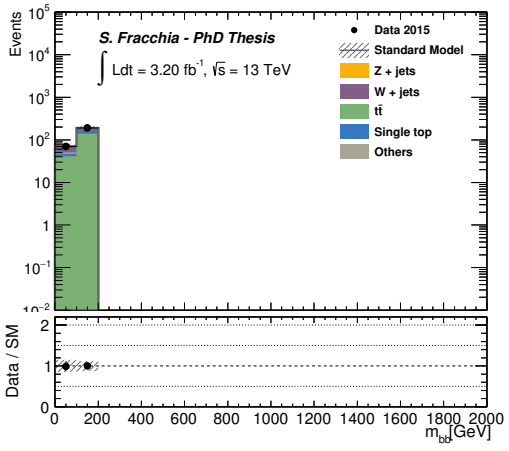

(d)

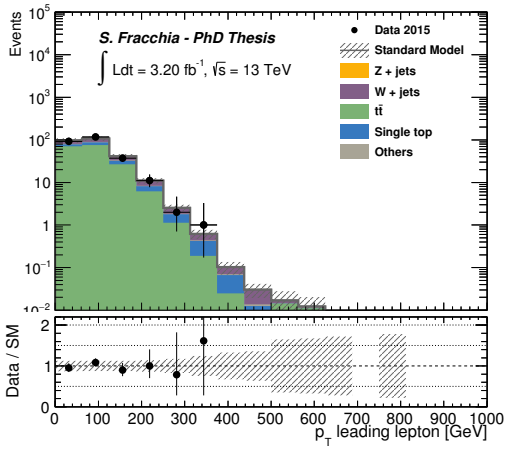

(e)

Figure 6.22: Post-fit distributions of (a) m_{CT}, (b) $E_{\mathrm{T}}^{\mathrm{miss}}$, (c) leading jet p_{T}, (d) m_{bb} and (e) the p_{T} of the leading lepton in the $t\bar{t}$ control region for SRA. The grey band shows the total statistical and detector systematic uncertainty on the background expectation.

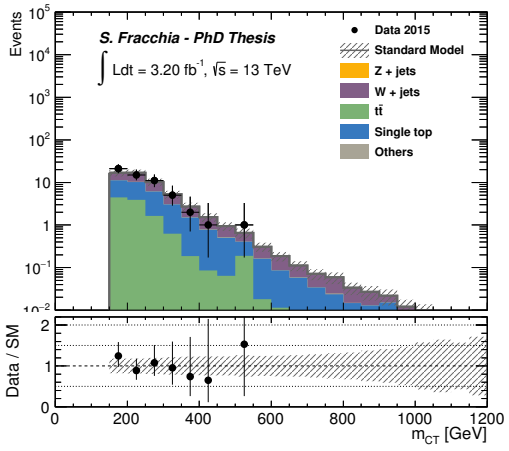

(a)

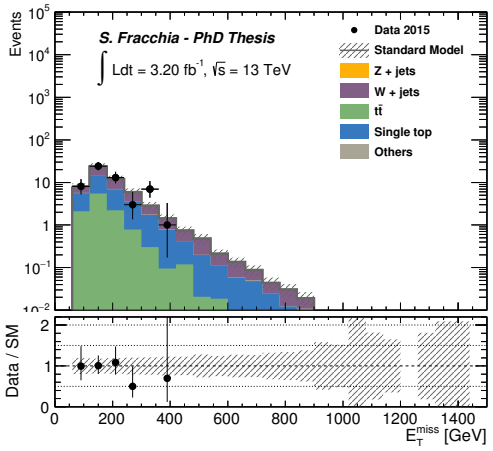

(b)

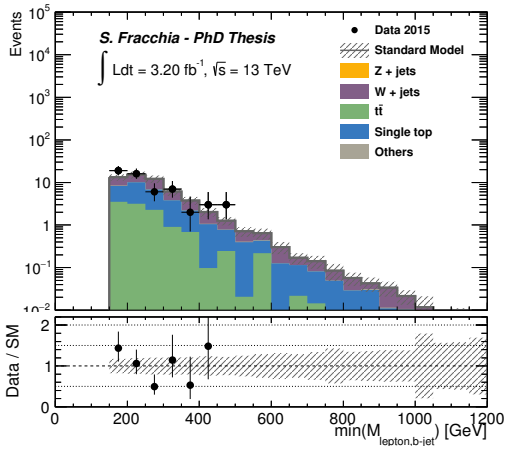

(c)

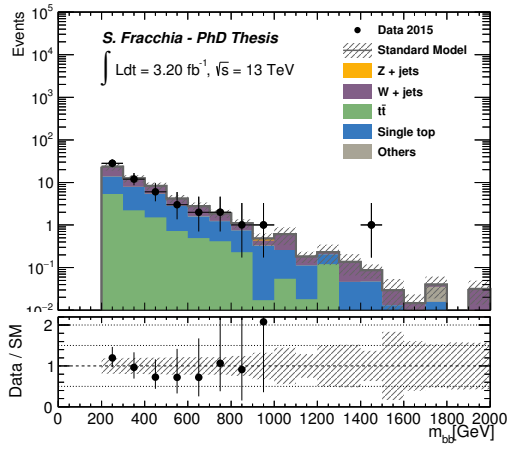

(d)

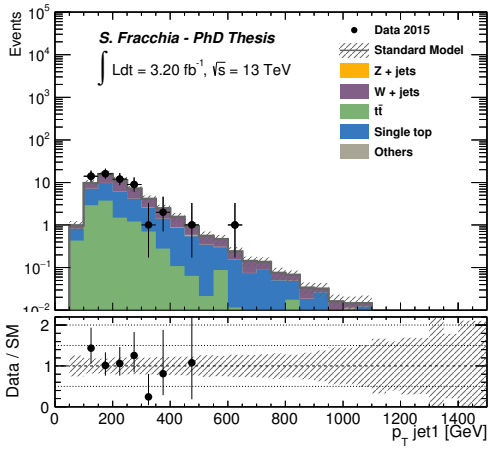

(e)

Figure 6.23: Post-fit distributions of (a) m_{CT}, (b) $E_{\mathrm{T}}^{\mathrm{miss}}$, (c) $\mathrm{m}_{b\ell}^{\mathrm{min}}$, (d) m_{bb} and (e) leading jet p_{T} in the single top control region for SRA. The grey band shows the total statistical and detector systematic uncertainty on the background expectation.

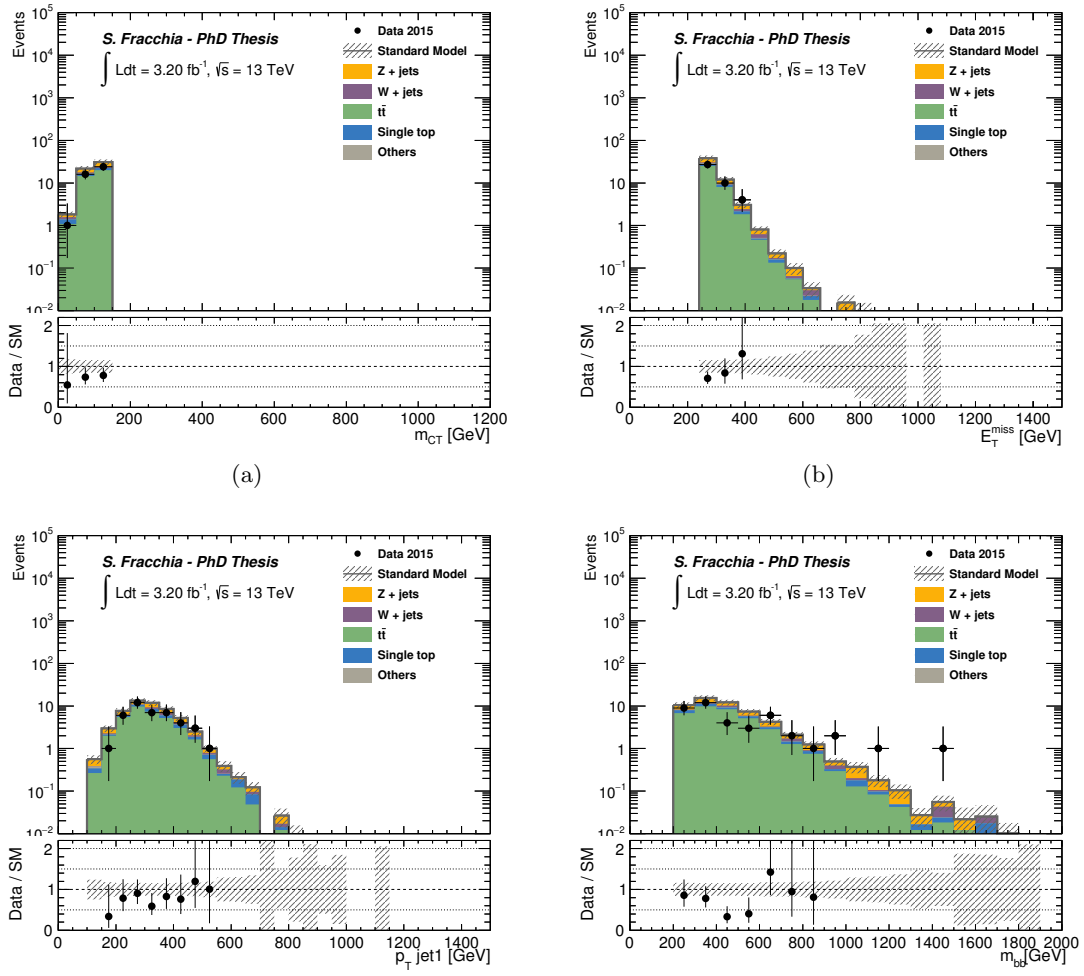

(a) (b)

(c) (d)

Figure 6.24: Post-fit distributions of (a) m_{CT}, (b) $E_{\mathrm{T}}^{\mathrm{miss}}$, (c) leading jet p_{T} and (d) m_{bb} in VRAmct. The grey band shows the total statistical and detector systematic uncertainty on the background expectation.

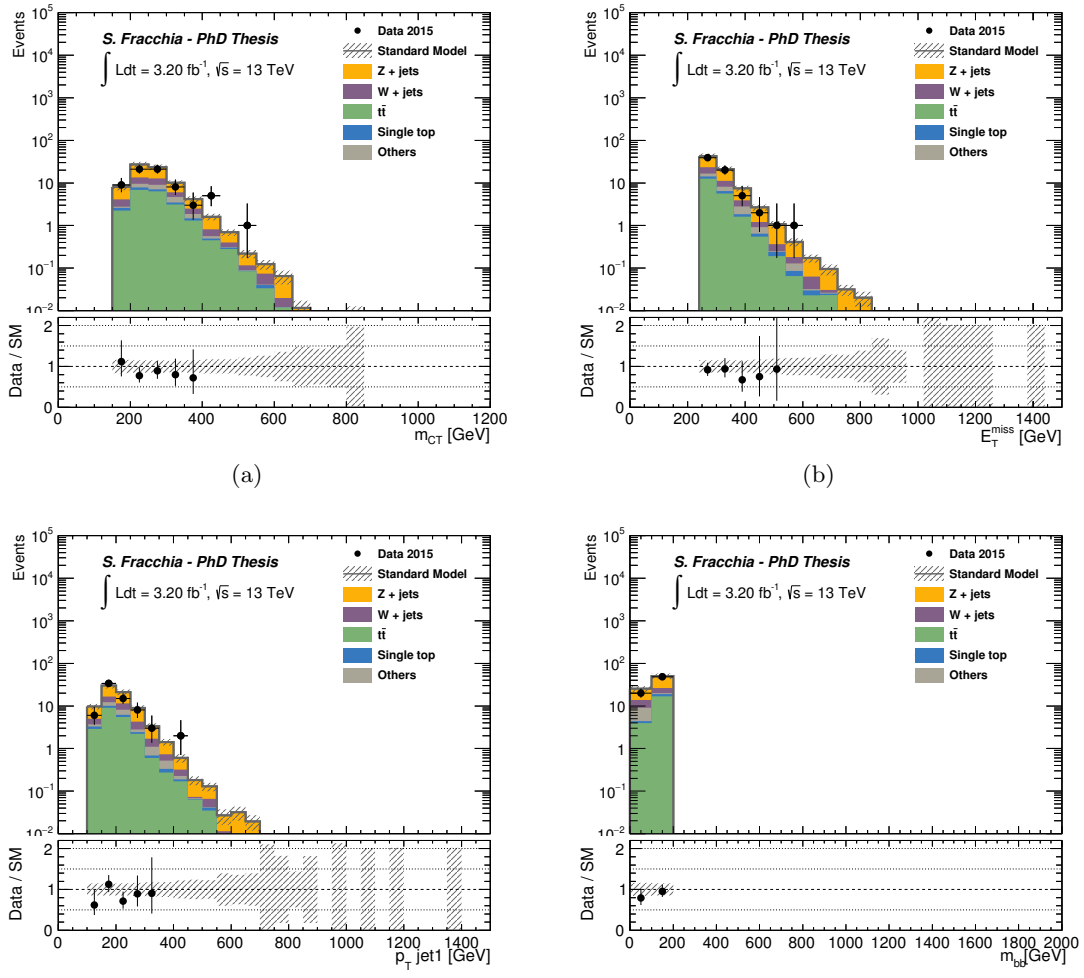

(a) (b)

(c) (d)

Figure 6.25: Post-fit distributions of (a) m_{CT}, (b) $E_{\mathrm{T}}^{\mathrm{miss}}$, (c) leading jet p_{T} and (d) m_{bb} in VRAmbb. The grey band shows the total statistical and detector systematic uncertainty on the background expectation.

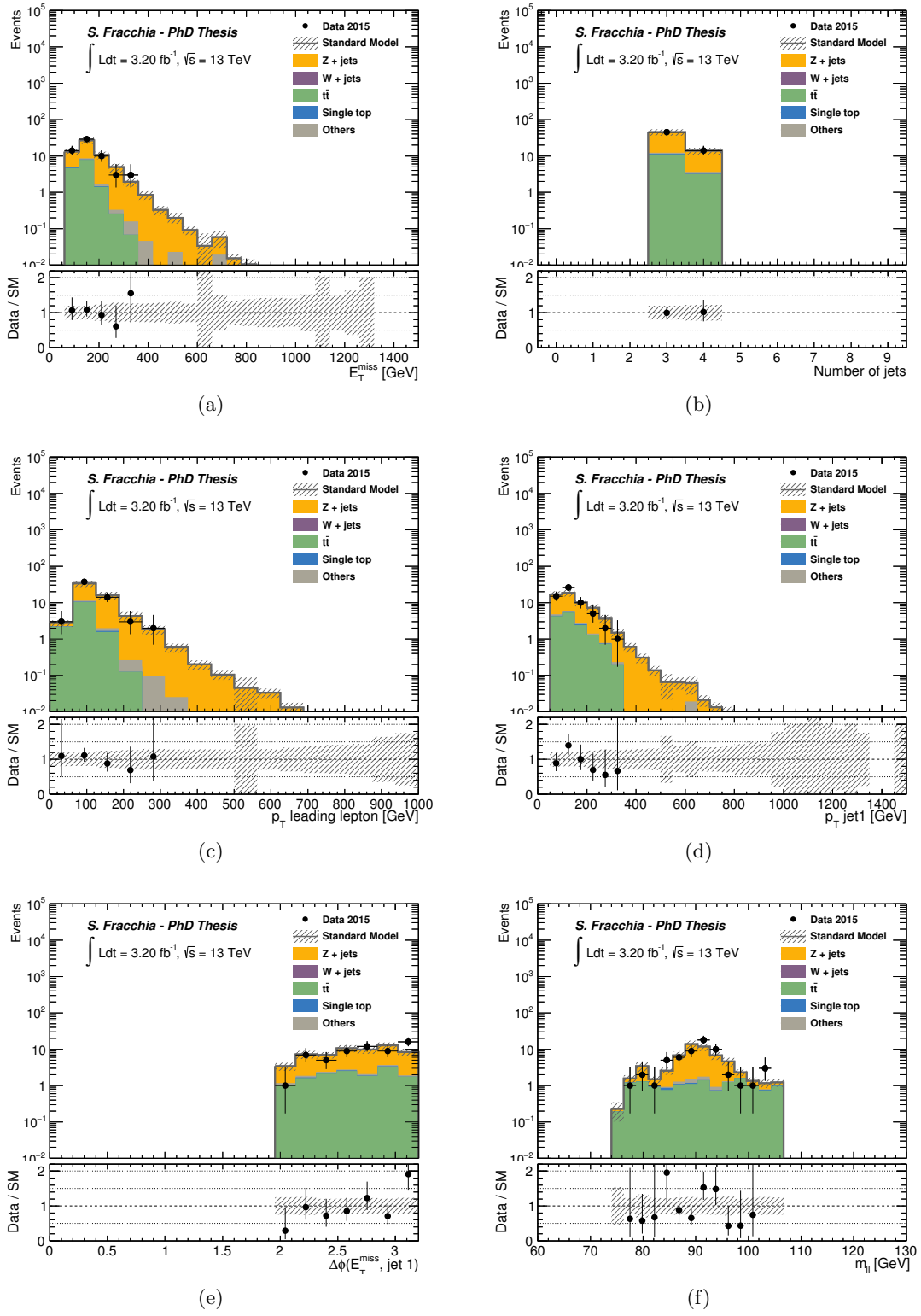

(a) (b) (c) (d) (e) (f)

Figure 6.26: Post-fit distributions of (a) $\tilde{E}_{\mathrm{T}}^{\mathrm{miss}}$, (b) jet multiplicity, (c) leading lepton p_{T}, (d) leading jet p_{T}, (e) $\Delta\phi(1^{\mathrm{st}}$ jet, $\mathrm{E}_{\mathrm{T}}^{\mathrm{miss}})$ and (f) $\mathrm{m}_{\ell\ell}$ in the Z+jets control region for SRB. The grey band shows the total statistical and detector systematic uncertainty on the background expectation.

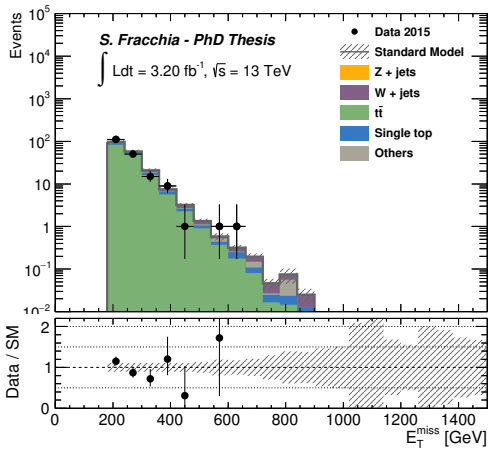

(a)

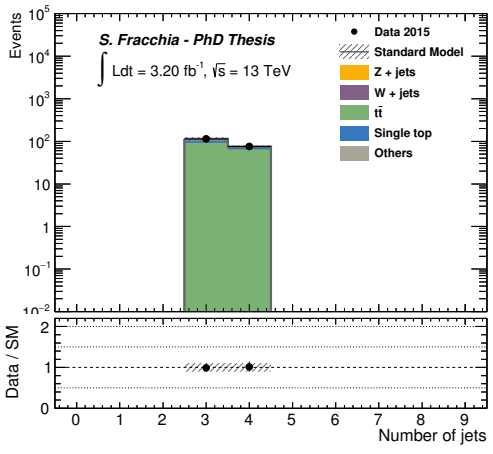

(b)

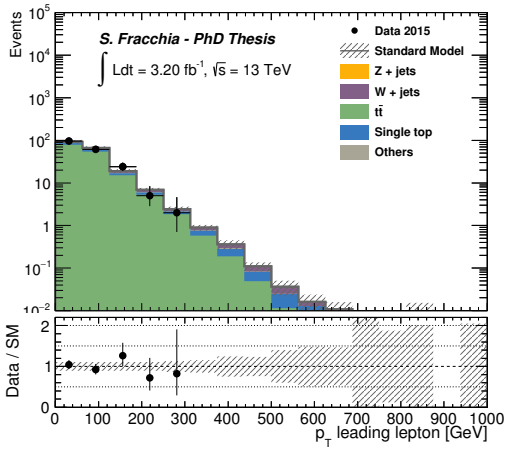

(c)

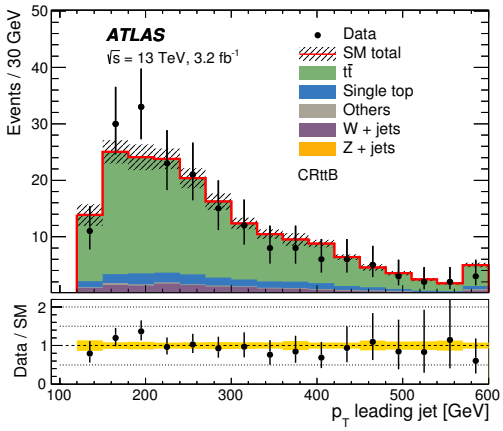

(d)

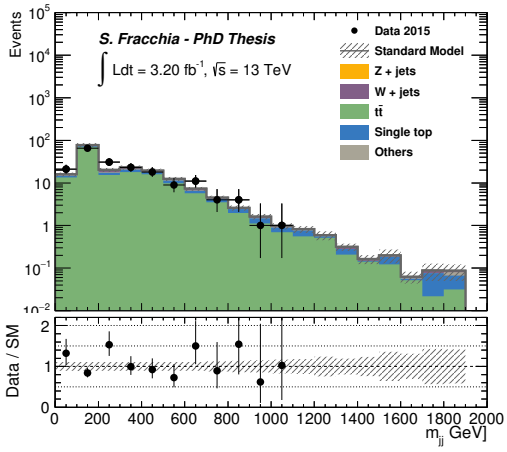

(e)

Figure 6.27: Post-fit distributions of (a) $E_{\mathrm{T}}^{\mathrm{miss}}$, (b) jet multiplicity, (c) leading lepton p_{T}, (d) leading jet p_{T} and (e) m_{jj} in the $t\bar{t}$ control region for SRB. The grey band shows the total statistical and detector systematic uncertainty on the background expectation.

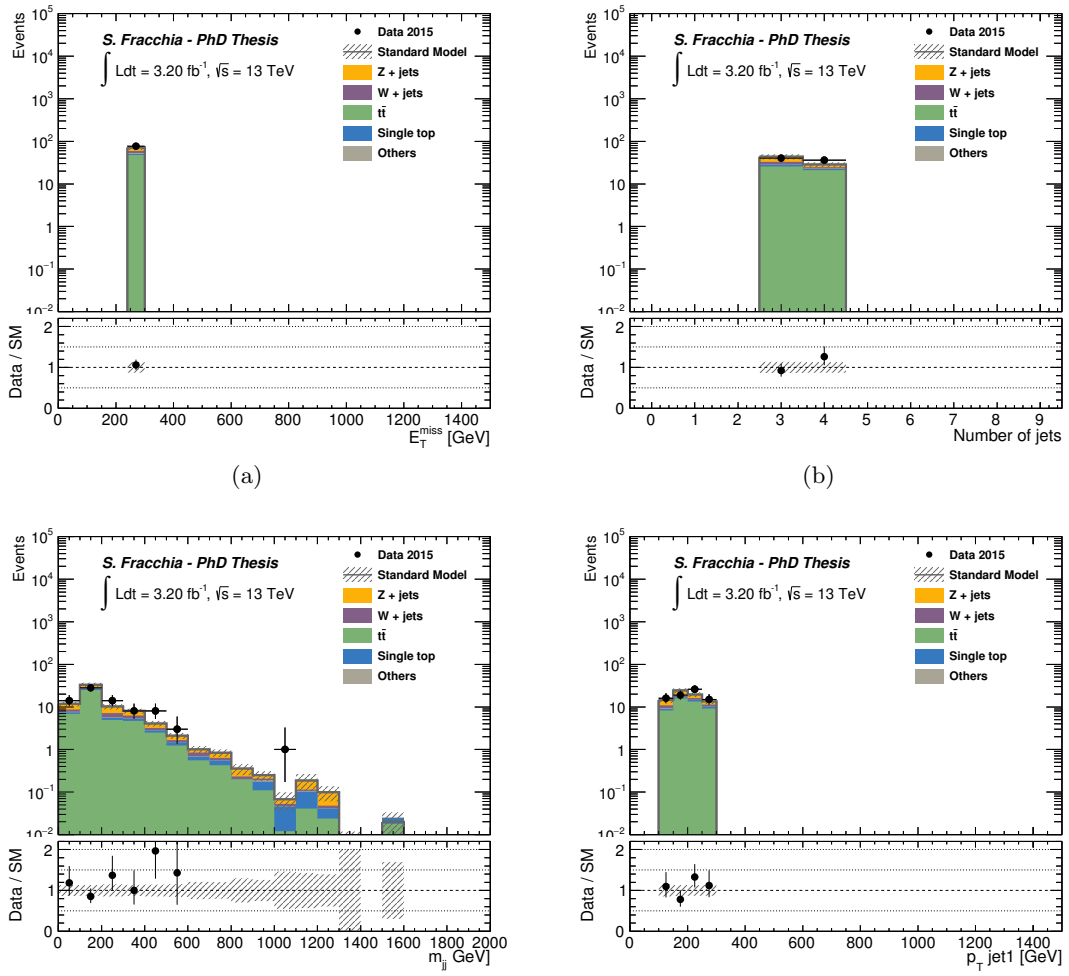

(a) (b)

(c) (d)

Figure 6.28: Post-fit distributions of (a) $E_{\mathrm{T}}^{\mathrm{miss}}$, (b) jet multiplicity, (c) m_{jj} and (d) leading jet p_{T} in VRB. The grey band shows the total statistical and detector systematic uncertainty on the background expectation.

6.9 Results

The data and the background predictions in the signal regions are shown in Table 6.15. A good agreement is observed in all the signal regions, except for a small over-prediction of the background in SRB.

The background predictions carry an uncertainty that varies between 16% and 22%. The full breakdown of the different sources of uncertainty are presented in Tables 6.16-6.19. In all the SRA regions, the total background uncertainty is dominated by the systematic uncertainty related to the normalization factor for the SM Z+jets background and to the one associated to the alternate data-driven methods for the Z+jets background estimation, while the theoretical uncertainty on the $t\bar{t}$ background dominates in SRB.

The distributions of some relevant variable in the signal regions are shown in Figures 6.29-6.30. In these distributions, the normalization factors as determined in the global fit are applied to the MC predictions. The m_{CT} distributions in SRA, with the Z+jets background estimated using the alternative methods described in Section 6.5.3 are also shown in Figure 6.31. The shape agreement between data and MC in the distributions is generally good.

Signal region channels	SRA250	SRA350	SRA450	SRB
Observed events	23	6	1	6
Fitted bkg events	29.15 ± 4.71	6.95 ± 1.23	1.84 ± 0.39	12.02 ± 2.50
Fitted Zjets events	21.58 ± 4.30	4.96 ± 1.08	1.34 ± 0.36	4.19 ± 1.30
Fitted Wjets events	4.36 ± 1.33	1.19 ± 0.41	0.30 ± 0.12	1.11 ± 0.57
Fitted TTbar events	1.05 ± 0.45	0.17 ± 0.08	0.04 ± 0.02	5.46 ± 2.03
Fitted SingleTop events	1.80 ± 1.01	0.53 ± 0.30	0.13 ± 0.07	0.99 ± 0.36
Fitted DiBosons events	0.21 ± 0.05	0.07 ± 0.04	$0.02^{+0.02}_{-0.02}$	0.19 ± 0.05
Fitted ttbarZ events	0.13 ± 0.02	0.03 ± 0.00	0.01 ± 0.00	0.06 ± 0.01
Fitted ttbarW events	0.02 ± 0.00	0.01 ± 0.00	0.00 ± 0.00	0.01 ± 0.00
MC exp. SM events	23.33	5.60	1.47	10.75
MC exp. Zjets events	16.09	3.70	1.00	2.81
MC exp. Wjets events	3.60	0.98	0.25	1.11
MC exp. TTbar events	1.10	0.18	0.04	5.57
MC exp. SingleTop events	2.18	0.64	0.15	0.99
MC exp. DiBosons events	0.21	0.07	0.02	0.19
MC exp. ttbarZ events	0.13	0.03	0.01	0.06
MC exp. ttbarW events	0.02	0.01	0.00	0.01

Table 6.15: Fit results for SRA250, SRA350, SRA450 and SRB for an integrated luminosity of 3.2 fb^{-1}. The results are obtained from the control regions using the background-only fit (see text for details). The uncertainties include the statistical and the systematic uncertainties.

Uncertainty of channel	SRA250
Total background expectation	29.15
Total statistical ($\sqrt{N_{\text{exp}}}$)	±5.40
Total background systematic	±4.71 [16.16%]
mu_Z	±2.86 [9.8%]
alpha_DD_syst	±1.98 [6.8%]
alpha_ZjetsTH	±1.75 [6.0%]
alpha_JET_JER_SINGLE_NP	±1.64 [5.6%]
alpha_FT_EFF_extrapolation	±0.99 [3.4%]
mu_ST	±0.80 [2.8%]
mu_W	±0.66 [2.2%]
alpha_singleTTH	±0.63 [2.2%]
alpha_MET_SoftTrk_ResoPara	±0.63 [2.1%]
alpha_WbFrac	±0.60 [2.1%]
alpha_FT_EFF_B_systematics	±0.55 [1.9%]
alpha_FT_EFF_Light_systematics	±0.53 [1.8%]
alpha_JET_GroupedNP_1	±0.49 [1.7%]
alpha_ttbarTH	±0.37 [1.3%]
alpha_WjetsTH	±0.35 [1.2%]
alpha_WcFrac	±0.34 [1.2%]
alpha_MET_SoftTrk_ResoPerp	±0.33 [1.1%]
alpha_EL_EFF_ID_TotalCorrUncertainty	±0.32 [1.1%]
alpha_JET_GroupedNP_2	±0.18 [0.61%]
alpha_MUON_EFF_TrigStatUncertainty	±0.16 [0.55%]
mu_Top	±0.14 [0.50%]
alpha_MUON_EFF_SYS	±0.13 [0.45%]
alpha_EL_EFF_Reco_TotalCorrUncertainty	±0.12 [0.40%]
alpha_EL_EFF_Iso_TotalCorrUncertainty	±0.11 [0.36%]
alpha_JvtEfficiency	±0.10 [0.33%]
alpha_EL_EFF_Trigger_TotalCorrUncertainty	±0.09 [0.30%]
alpha_FT_EFF_C_systematics	±0.08 [0.26%]
alpha_MUON_EFF_TrigSystUncertainty	±0.07 [0.24%]
alpha_MUONS_MS	±0.06 [0.21%]
alpha_MET_SoftTrk_Scale	±0.06 [0.20%]
alpha_JET_GroupedNP_3	±0.06 [0.19%]
alpha_MUONS_ID	±0.06 [0.19%]
alpha_MUON_ISO_SYS	±0.05 [0.18%]
alpha_EG_RESOLUTION_ALL	±0.04 [0.15%]
alpha_MUONS_SCALE	±0.04 [0.14%]
alpha_MUON_EFF_STAT	±0.04 [0.13%]
alpha_EG_SCALE_ALL	±0.03 [0.11%]
alpha_Lumi	±0.02 [0.06%]
alpha_MUON_ISO_STAT	±0.02 [0.05%]

Table 6.16: Breakdown of the dominant systematic uncertainties on background estimates in SRA250, for an integrated luminosity of 3.2 fb^{-1}. The percentages show the size of the uncertainty relative to the total expected background.

Uncertainty of channel	SRA350
Total background expectation	6.95
Total statistical ($\sqrt{N_{\text{exp}}}$)	±2.64
Total background systematic	±1.23 [17.75%]
mu_Z	±0.66 [9.5%]
alpha_DD_syst	±0.63 [9.0%]
alpha_FT_EFF_extrapolation	±0.42 [6.1%]
alpha_JET_JER_SINGLE_NP	±0.39 [5.6%]
alpha_ZjetsTH	±0.35 [5.0%]
mu_ST	±0.24 [3.4%]
alpha_WbFrac	±0.20 [2.9%]
alpha_FT_EFF_B_systematics	±0.20 [2.8%]
alpha_singleTTH	±0.19 [2.7%]
mu_W	±0.18 [2.6%]
alpha_JET_GroupedNP_1	±0.16 [2.4%]
alpha_FT_EFF_Light_systematics	±0.13 [1.9%]
alpha_WcFrac	±0.13 [1.8%]
alpha_MET_SoftTrk_ResoPara	±0.10 [1.4%]
alpha_WjetsTH	±0.08 [1.2%]
alpha_EL_EFF_ID_TotalCorrUncertainty	±0.07 [1.1%]
alpha_ttbarTH	±0.06 [0.85%]
alpha_JET_GroupedNP_2	±0.05 [0.71%]
alpha_MUON_EFF_TrigStatUncertainty	±0.04 [0.54%]
alpha_MUON_EFF_SYS	±0.03 [0.44%]
alpha_EL_EFF_Reco_TotalCorrUncertainty	±0.03 [0.40%]
alpha_EL_EFF_Iso_TotalCorrUncertainty	±0.02 [0.36%]
mu_Top	±0.02 [0.34%]
alpha_JvtEfficiency	±0.02 [0.30%]
alpha_EL_EFF_Trigger_TotalCorrUncertainty	±0.02 [0.30%]
alpha_MET_SoftTrk_ResoPerp	±0.02 [0.28%]
alpha_EG_SCALE_ALL	±0.02 [0.27%]
alpha_MUON_EFF_TrigSystUncertainty	±0.02 [0.24%]
alpha_MUONS_ID	±0.01 [0.22%]
alpha_MUONS_MS	±0.01 [0.20%]
alpha_FT_EFF_C_systematics	±0.01 [0.17%]
alpha_MUON_ISO_SYS	±0.01 [0.17%]
alpha_MUON_EFF_STAT	±0.01 [0.13%]
alpha_MUONS_SCALE	±0.01 [0.13%]
alpha_Lumi	±0.00 [0.07%]
alpha_MUON_ISO_STAT	±0.00 [0.05%]
alpha_EG_RESOLUTION_ALL	±0.00 [0.04%]
alpha_JET_GroupedNP_3	±0.00 [0.04%]
alpha_MET_SoftTrk_Scale	±0.00 [0.01%]

Table 6.17: Breakdown of the dominant systematic uncertainties on background estimates in SRA350, for an integrated luminosity of 3.2 fb^{-1}. The percentages show the size of the uncertainty relative to the total expected background.

Uncertainty of channel	SRA450
Total background expectation	1.84
Total statistical ($\sqrt{N_{\text{exp}}}$)	±1.35
Total background systematic	±0.39 [21.41%]
alpha_DD_syst	±0.25 [13.4%]
mu_Z	±0.18 [9.7%]
alpha_FT_EFF_extrapolation	±0.16 [8.8%]
alpha_ZjetsTH	±0.10 [5.4%]
alpha_JET_JER_SINGLE_NP	±0.08 [4.5%]
alpha_FT_EFF_B_systematics	±0.06 [3.2%]
mu_ST	±0.06 [3.1%]
alpha_WbFrac	±0.05 [2.9%]
alpha_MET_SoftTrk_ResoPerp	±0.05 [2.9%]
mu_W	±0.04 [2.4%]
alpha_singleTTH	±0.04 [2.4%]
alpha_JET_GroupedNP_2	±0.04 [2.1%]
alpha_WcFrac	±0.03 [1.5%]
alpha_JET_GroupedNP_1	±0.03 [1.4%]
alpha_MET_SoftTrk_ResoPara	±0.02 [1.3%]
alpha_FT_EFF_Light_systematics	±0.02 [1.2%]
alpha_WjetsTH	±0.02 [1.2%]
alpha_EL_EFF_ID_TotalCorrUncertainty	±0.02 [1.1%]
alpha_JET_GroupedNP_3	±0.02 [1.0%]
alpha_ttbarTH	±0.01 [0.80%]
alpha_MUON_EFF_TrigStatUncertainty	±0.01 [0.54%]
alpha_MUON_EFF_SYS	±0.01 [0.44%]
alpha_EL_EFF_Reco_TotalCorrUncertainty	±0.01 [0.40%]
alpha_FT_EFF_C_systematics	±0.01 [0.40%]
alpha_EL_EFF_Iso_TotalCorrUncertainty	±0.01 [0.36%]
alpha_JvtEfficiency	±0.01 [0.36%]
mu_Top	±0.01 [0.31%]
alpha_EL_EFF_Trigger_TotalCorrUncertainty	±0.01 [0.30%]
alpha_MUON_EFF_TrigSystUncertainty	±0.00 [0.24%]
alpha_MUONS_MS	±0.00 [0.23%]
alpha_EG_RESOLUTION_ALL	±0.00 [0.21%]
alpha_MUON_ISO_SYS	±0.00 [0.18%]
alpha_MUONS_ID	±0.00 [0.16%]
alpha_MUON_EFF_STAT	±0.00 [0.13%]
alpha_MUONS_SCALE	±0.00 [0.12%]
alpha_MET_SoftTrk_Scale	±0.00 [0.08%]
alpha_Lumi	±0.00 [0.07%]
alpha_MUON_ISO_STAT	±0.00 [0.05%]
alpha_EG_SCALE_ALL	±0.00 [0.04%]

Table 6.18: Breakdown of the dominant systematic uncertainties on background estimates in SRA450, for an integrated luminosity of 3.2 fb^{-1}. The percentages show the size of the uncertainty relative to the total expected background.

Uncertainty of channel	SRB
Total background expectation	12.02
Total statistical ($\sqrt{N_{\text{exp}}}$)	±3.47
Total background systematic	±2.50 [20.77%]
alpha_ttbarTH	±1.91 [15.9%]
alpha_DD_syst	±0.96 [8.0%]
mu_Z	±0.77 [6.4%]
alpha_JET_GroupedNP_1	±0.64 [5.3%]
mu_Top	±0.53 [4.4%]
alpha_WjetsTH	±0.40 [3.4%]
alpha_WbFrac	±0.36 [3.0%]
alpha_singleTTH	±0.35 [2.9%]
alpha_ZjetsTH	±0.28 [2.3%]
alpha_FT_EFF_Light_systematics	±0.19 [1.6%]
alpha_FT_EFF_B_systematics	±0.14 [1.2%]
alpha_Lumi	±0.12 [0.98%]
Lumi	±0.09 [0.76%]
alpha_FT_EFF_C_systematics	±0.08 [0.69%]
alpha_EL_EFF_ID_TotalCorrUncertainty	±0.08 [0.65%]
alpha_WcFrac	±0.07 [0.61%]
alpha_JET_JER_SINGLE_NP	±0.07 [0.58%]
alpha_MET_SoftTrk_ResoPara	±0.07 [0.57%]
alpha_MET_SoftTrk_ResoPerp	±0.06 [0.54%]
alpha_MUON_EFF_TrigStatUncertainty	±0.05 [0.45%]
alpha_JET_GroupedNP_2	±0.05 [0.45%]
alpha_MUON_EFF_SYS	±0.03 [0.28%]
alpha_EL_EFF_Reco_TotalCorrUncertainty	±0.03 [0.25%]
alpha_EL_EFF_Iso_TotalCorrUncertainty	±0.03 [0.22%]
alpha_JvtEfficiency	±0.02 [0.20%]
alpha_EL_EFF_Trigger_TotalCorrUncertainty	±0.02 [0.19%]
alpha_MUON_EFF_TrigSystUncertainty	±0.02 [0.19%]
alpha_MUONS_SCALE	±0.02 [0.16%]
alpha_MUONS_ID	±0.02 [0.15%]
alpha_MUON_ISO_SYS	±0.01 [0.12%]
alpha_FT_EFF_extrapolation	±0.01 [0.12%]
alpha_JET_GroupedNP_3	±0.01 [0.11%]
alpha_EG_SCALE_ALL	±0.01 [0.11%]
alpha_MUON_EFF_STAT	±0.01 [0.10%]
alpha_MET_SoftTrk_Scale	±0.01 [0.09%]
alpha_MUONS_MS	±0.01 [0.05%]
alpha_EG_RESOLUTION_ALL	±0.01 [0.04%]
alpha_MUON_ISO_STAT	±0.00 [0.03%]

Table 6.19: Breakdown of the dominant systematic uncertainties on background estimates in SRB, for an integrated luminosity of 3.2 fb^{-1}. The percentages show the size of the uncertainty relative to the total expected background.

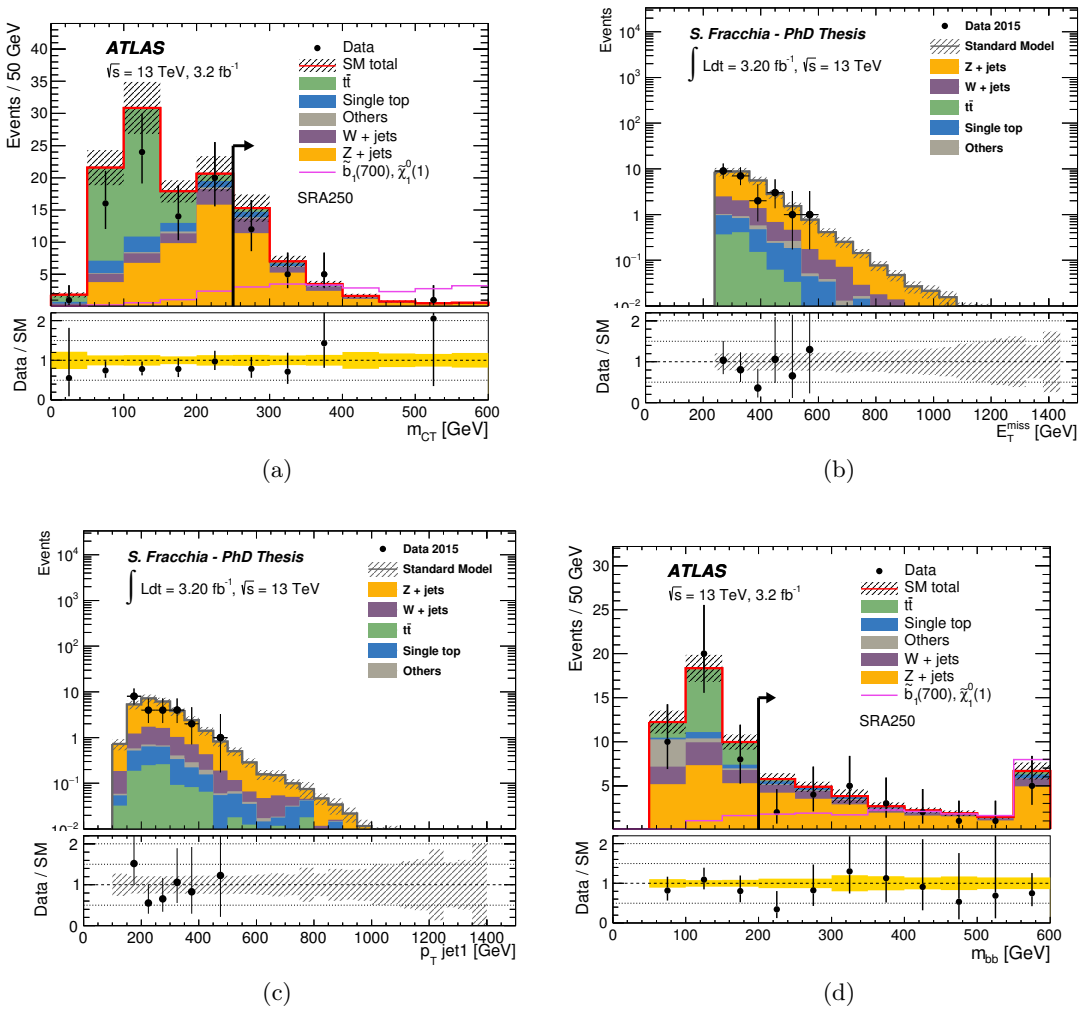

Figure 6.29: Post-fit distributions for (a) m_{CT} before the m_{CT} cut, (b) $E_{\mathrm{T}}^{\mathrm{miss}}$, (c) leading jet p_{T} and m_{bb} before the m_{bb} cut in SRA250. The arrows in the plots indicate the bins corresponding to SRA250. The shaded band include the statistical and the systematic uncertainties on the background expectation.

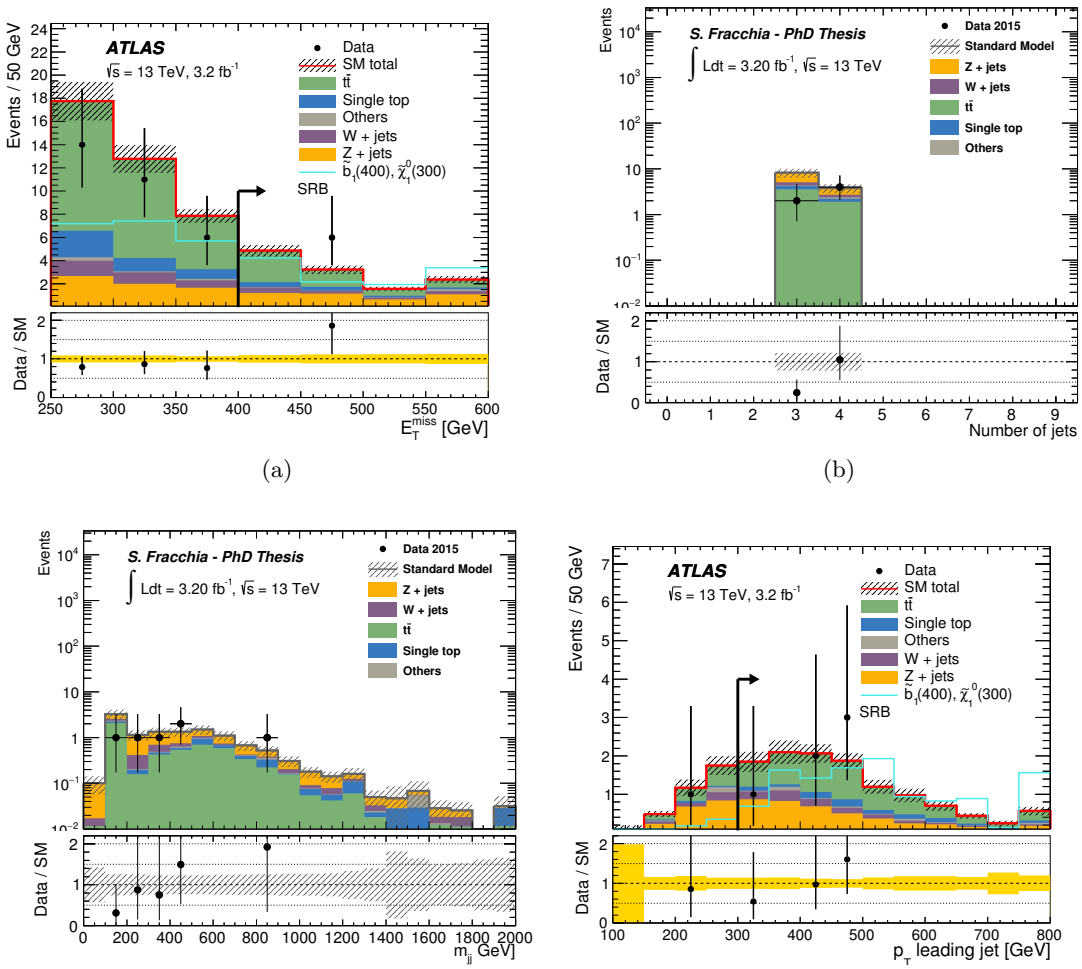

(a) (b)

(c) (d)

Figure 6.30: Post-fit distributions for (a) $E_{\mathrm{T}}^{\mathrm{miss}}$ before the $E_{\mathrm{T}}^{\mathrm{miss}}$ cut, (b) jet multiplicity, (c) m_{jj} and (d) leading jet p_{T} before the leading jet p_{T} cut in SRB. The arrows in the plots indicate the bins corresponding to SRB. The shaded band include the statistical and the systematic uncertainties on the background expectation.

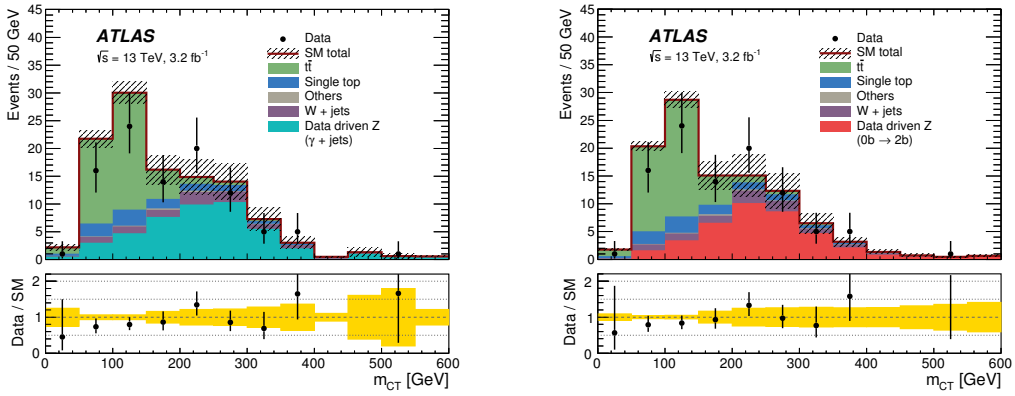

(a) (b)

Figure 6.31: Comparison between data and SM predictions for the m_{CT} distribution in SRA, with the Z+jets background evaluated using the data-driven prediction derived from γ+jets (a) or the data-driven prediction derived from Z+light jets processes (b).

6.9.1 Model-independent limits

The level of agreement between the data and the SM predictions for the total number of events in the different inclusive signal regions SRA250, SRA350, SRA450 and SRB is translated into upper limits for the presence of new phenomena. The model-independent fit, as described in Section 6.6, is performed in both the control and signal regions, for each of the inclusive signal regions. As a result, model-independent 95% CL upper limits on the visible cross section, defined as the production cross section times acceptance times efficiency $\sigma \times A \times \varepsilon$, are extracted, considering the systematic uncertainties in the SM backgrounds and the uncertainty in the integrated luminosity.

The results from the model-independent fit are presented in Table 6.20. Values of $\sigma \times A \times \varepsilon$ above 3.38 fb, 1.93 fb, 1.23 fb and 1.90 fb are excluded at 95% CL for SRA250, SRA350, SRA450 and SRB, respectively. Upper limits on the number of signal events (and on the number of signal events given the expected number of background events) are also estimated and presented in the table.

Signal Channel	$(\langle\epsilon\sigma\rangle^{95}_{\text{obs}})$ [fb]	(S^{95}_{obs})	(S^{95}_{exp})	CL_B	$p(s=0)$
SRA250	3.38	10.8	$13.7^{+6.0}_{-3.3}$	0.21	0.86
SRA350	1.93	6.2	$6.5^{+3.2}_{-1.0}$	0.38	0.94
SRA450	1.23	3.9	$4.1^{+1.9}_{-0.5}$	0.29	0.69
SRB	1.90	6.1	$8.8^{+3.0}_{-2.4}$	0.08	0.49

Table 6.20: Left to right: 95% CL upper limits on the visible cross section ($\langle\epsilon\sigma\rangle^{95}_{\text{obs}}$) and on the number of signal events (S^{95}_{obs}). The third column (S^{95}_{exp}) shows the 95% CL upper limit on the number of signal events, given the expected number (and $\pm1\sigma$ excursions on the expectation) of background events. The last two columns indicate the CL_B value, i.e. the confidence level observed for the background-only hypothesis, and the discovery p-value ($p(s=0)$).

6.10 Interpretation

The model-dependent fit as described in Section 6.6 is performed and exclusion limits are derived for the simplified models described in Section 6.1.1, which correspond to the production of pairs of bottom squarks in the final state. In this case, the experimental and theoretical systematic uncertainties on the signal model are included in the fit. The experimental uncertainties are assumed to be fully correlated with those for the SM background.

The experimental uncertainties are dominated by the b-tagging and JES/JER variations. The total experimental uncertainty varies between 20% and 25% across the sbottom-neutralino mass plane. The theoretical uncertainties in the NLO+NLL cross section are calculated for each SUSY signal model and vary between 15% and 20% for bottom squark masses in the range between 400 GeV and 900 GeV. They are dominated by the uncertainties in the renormalization and factorization scales, followed by the uncertainty in the PDF and uncertainties in the modeling of initial-state parton showers.

The fit is performed separately for each SUSY model and each selection criteria and the one with the best expected 95% CL limit is adopted as nominal. The expected and observed combined exclusion limits at 95% CL in the $(m_{\tilde{b}_1}, m_{\tilde{\chi}^0_1})$ plane are shown in Figure 6.32. The expected limits are obtained from MC pseudo experiments. In this Figure, the dashed black and solid bold red lines show the 95% CL expected and observed limits respectively. The shaded (yellow) bands around the expected limits illustrate the impact of the experimental uncertainties while the dotted red lines show the impact on the observed limit of the variation of the nominal signal cross section by 1σ theoretical uncertainty. Also shown for reference are the observed limits from the 8 TeV analysis [82, 111] and the limits from the Run-2 monojet analysis [112]. The latter is devoted to very compressed scenarios with $m_{\tilde{b}_1} \approx m_{\tilde{\chi}^0_1}$.

As expected, SRA450 is the signal region providing the best sensitivity for the large sbottom-neutralino mass splittings, while SRB extends the exclusion for the more com-

pressed scenarios, although the monojet analysis has the highest sensitivity in the extreme case of very small mass splittings, as anticipated. Bottom squarks masses up to 800 (840) GeV are excluded for $\tilde{\chi}_1^0$ below 360 (300) GeV. Differences between the $\tilde{b}_1$ and the $\tilde{\chi}_1^0$ masses above 100 GeV are excluded up to $\tilde{b}_1$ masses of 500 GeV.

Additional material on the model-dependent fits and their combination is collected in Appendix A.

The results extend significantly the previous Run-1 exclusion, despite of the smaller integrated luminosity. This must be mostly attributed to the increased center-of-mass energy in Run-2 but also reflects the significant improvements in b-tagging and analysis strategy, leading to reduced background uncertainties.

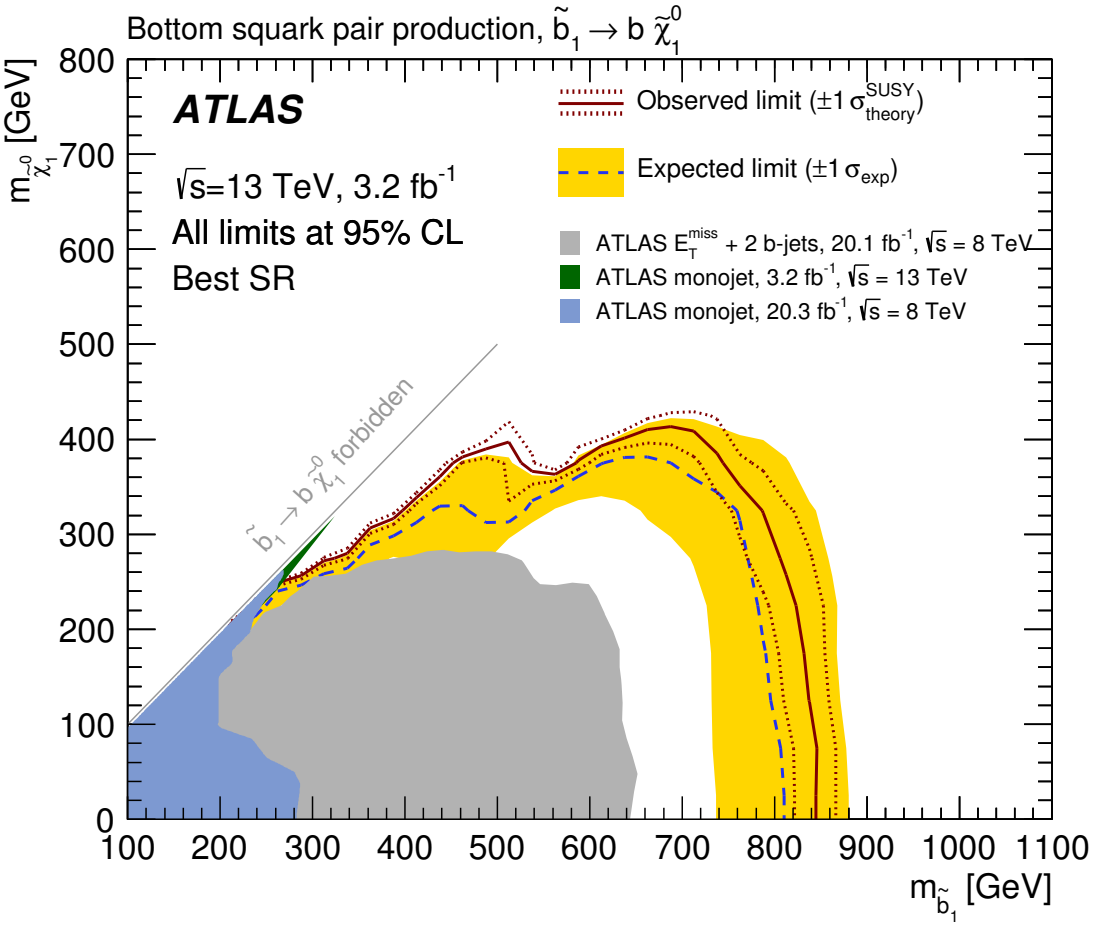

(a)

Figure 6.32: Observed and expected exclusion limits at 95% CL, as well as $\pm 1\ \sigma$ variation of the expected limit, in the $\tilde{b}_1 - \tilde{\chi}_1^0$ mass plane. The signal region with the best expected sensitivity is adopted for each point of the parameter space. The yellow band around the expected limit (dashed line) shows the impact of the experimental and SM background theoretical uncertainties. The dotted lines show the impact on the observed limit of the variation of the nominal signal cross section by $\pm 1\ \sigma$ of its theoretical uncertainties. The exclusion limits from the Run-1 ATLAS searches [82, 111] and from the 13 TeV monojet search [112] are also superimposed. The latter limit is only published for values of $m_{\tilde{b}_1} - m_{\tilde{\chi}_1^0} = 5$ and 20 GeV.

6.10.1 Sensitivity prospects

As a final study, future discovery and exclusion prospects have been derived for the sbottom search, based on the analysis strategy described in this chapter.

The prospects are fully based on the MC expectations, which have been re-scaled to 15 and 30 fb^{-1} of integrated luminosity, roughly the dataset collected in 2016 for summer and winter conferences, respectively. The significance for each signal point has been computed using the BINOMIALOBSZ function from ROOSTATS [89], already used for the projections presented in Chapter 5, and assuming a fixed uncertainty on the total SM background of 20%.

These projections are shown in Figure 6.33. For large $\Delta m(\tilde{b}_1, \tilde{\chi}_1^0)$, with 30 fb^{-1}, one could discover the sbottom quark up to masses of ∼900 GeV, while a sbottom quark with mass of 1 TeV would be excluded.

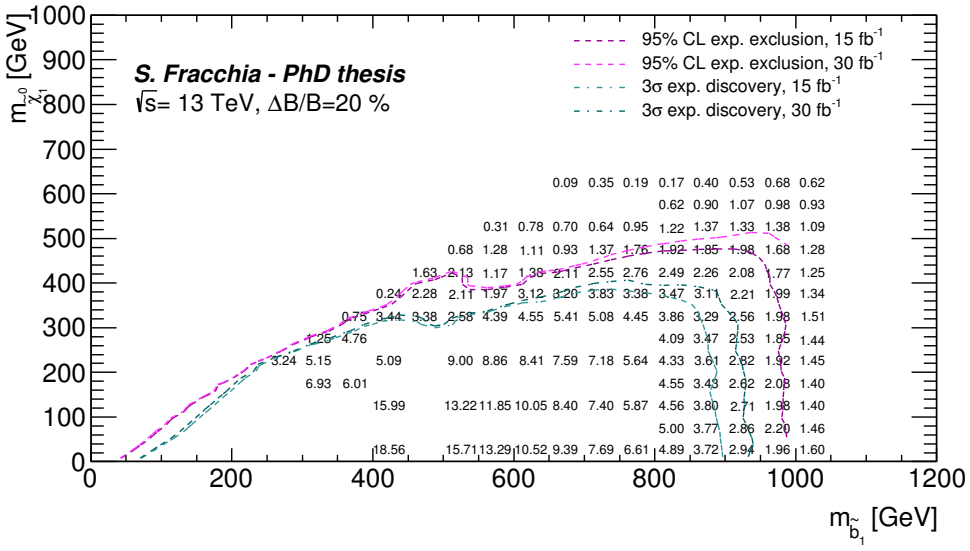

Figure 6.33: Discovery and exclusion projections for 15 and 30 fb^{-1}, for a fixed uncertainty on the total SM background of 20%. Numbers correspond to the significance for each signal point computed with the BINOMIALOBSZ function from ROOSTATS [89].

To conclude, it is worth to mention that a study of the expected exclusion and discovery reach at the high luminosity LHC (HL-LHC) was performed in 2014, including projections for the sbottom analysis. The study is documented in Ref. [113]. The integrated luminosity scenarios considered are 300 fb^{-1} and 3000 fb^{-1}, which should correspond to the integrated luminosity collected by the end of the LHC phase (∼2022) and at the end of HL-LHC phase (∼2030). Increased pileup conditions have been taken into account in the study, corresponding to $\langle\mu\rangle$ ∼60 for the 300 fb^{-1} and $\langle\mu\rangle$ ∼140 for the 3000 fb^{-1}. The study was based on the Run-1 analysis strategy and systematics uncertainties. The projection of the m_{CT} distribution for 300 fb^{-1}, including three signal models, is shown in Figure 6.34 (a). Figure 6.34 (b) shows the expected 95% exclusion limits and discov-

ery reach for bottom squark pair production with 300 fb^{-1} and 3000 fb^{-1} of integrated luminosity.

Although these projections are likely pessimistic, they clearly state that, in the next phases of the LHC, it will be possible to verify or exclude the existence of the sbottom quark up to very large masses well above the TeV-scale and probably say a final word on the naturalness of SUSY.

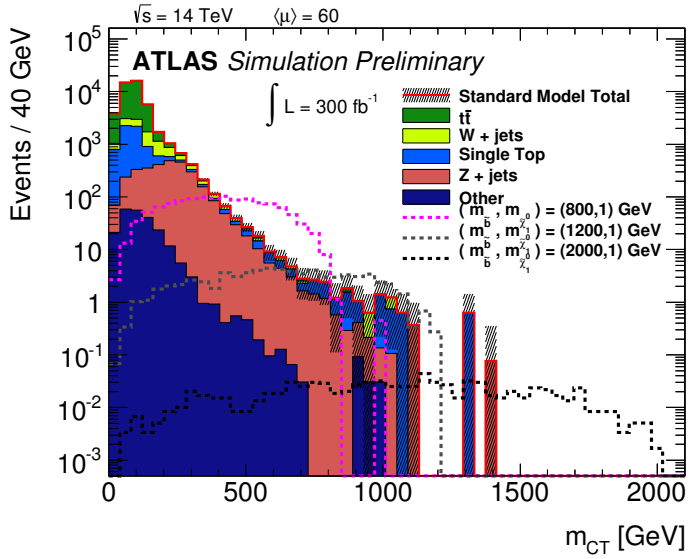

(a)

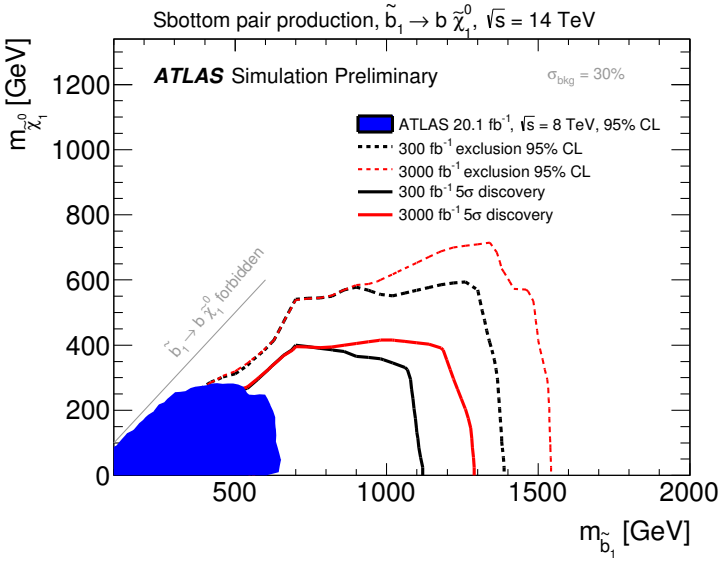

(b)

Figure 6.34: Distribution of the m_{CT} variable for 300 fb^{-1} for three signal models and the SM backgrounds (a). Expected 95% CL exclusion limits and discovery reach for bottom squark pair production with 300 fb^{-1} and 3000 fb^{-1} of integrated luminosity (b). [113]

Chapter 7

Conclusions

This thesis is mainly devoted to the search for the lightest bottom squark, performed in final states with large missing transverse momentum and two b-jets. In the assumption of R-parity conservation, a simplified signal model is considered consisting in the direct production of a pair of bottom squarks, each decaying exclusively into a b-quark and the lightest neutralino. The search for the bottom squark in Run-2 is presented, using the data from pp collisions collected by the ATLAS Experiment in 2015 at $\sqrt{s}$ =13 TeV, corresponding to an integrated luminosity of 3.2 fb^{-1}.

Different signal regions are defined in this search, optimized in order to have sensitivity to a broad range of signal models with different sbottom and neutralino masses. The Standard Model background processes contributing to the targeted final states are considered, for which the dominant backgrounds are constrained in dedicated control regions by means of a profile likelihood fit.

The observed data are found to be in agreement with the SM predictions. The results are interpreted in terms of model independent 95% confidence level upper limits on the visible cross section. Values in the range between 3.38 fb and 1.23 fb are found to be excluded for the different selections.

Exclusion limits at 95% confidence level are finally placed on the sbottom-neutralino mass plane. Sbottom masses up to 800 GeV are excluded for neutralino masses below 360 GeV (840 GeV for neutralino masses below 100 GeV). Differences in mass above 100 GeV between the sbottom and the neutralino are excluded up to sbottom masses of 500 GeV. The exclusion limits obtained in this thesis extend significantly the results obtained from the Run-1 search. The results were published by the ATLAS Collaboration, leading to one article in a journal and two public notes for conferences.

Prospects for future searches are also given, showing that in the next years, with more data delivered by the LHC, it will be possible to verify or exclude the existence of the bottom squark beyond the TeV-scale. Similar considerations hold for the searches for the top squark. Altogether, the next years of the LHC will be crucial for saying a final word on natural SUSY.

Appendix A

Additional material from the model-dependent fit

The expected and observed combined exclusion limits at 95% CL in the $(m_{\tilde{b}_1}, m_{\tilde{\chi}_1^0})$ plane are shown in Figure A.1, with the indication of the signal region providing the best expected limit for each signal point superimposed to the exclusion limits. As expected, SRA regions provided the best sensitivity for the large sbottom-neutralino mass splittings and the increased m_{CT} requirements allow to extend the exclusion towards larger sbottom masses. The region SRB, instead, dominates in the scenarios with small mass splittings.

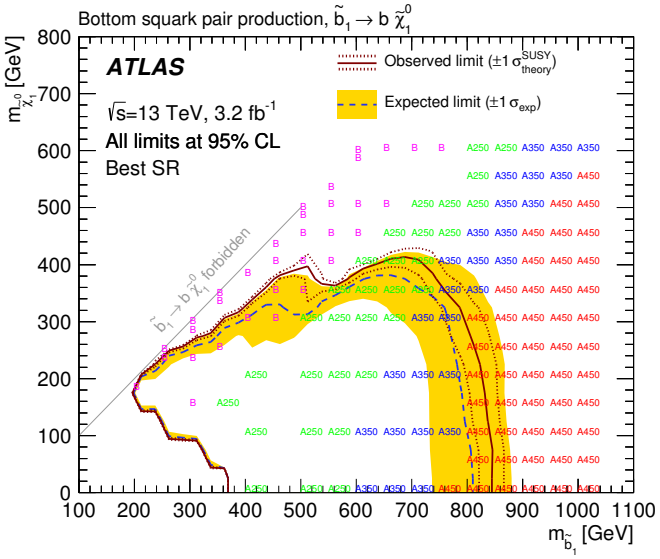

(a)

Figure A.1: Combined expected and observed exclusion limits at 95% CL in the $(m_{\tilde{b}_1}, m_{\tilde{\chi}_1^0})$ plane. For each signal point, the signal region which leads to the best expected limit is indicated.

The values of the expected, observed CLs and of the 95% CL excluded model cross sections for the combined limits are shown in Figure A.2.

Figure A.3-A.5 show the exclusion limits separately for each signal region with the correspondent values of the expected and observed CLs and of the 95% CL excluded model cross sections. As an example, assuming a χ_1^0 mass of 200 GeV, 95% CL exclusions on the visible cross section in the range between 0.59 and 0.02 are obtained, as a function of the sbottom mass. The data has the sensitivity to exclude signal cross sections for sbottom mass below about 830 GeV.

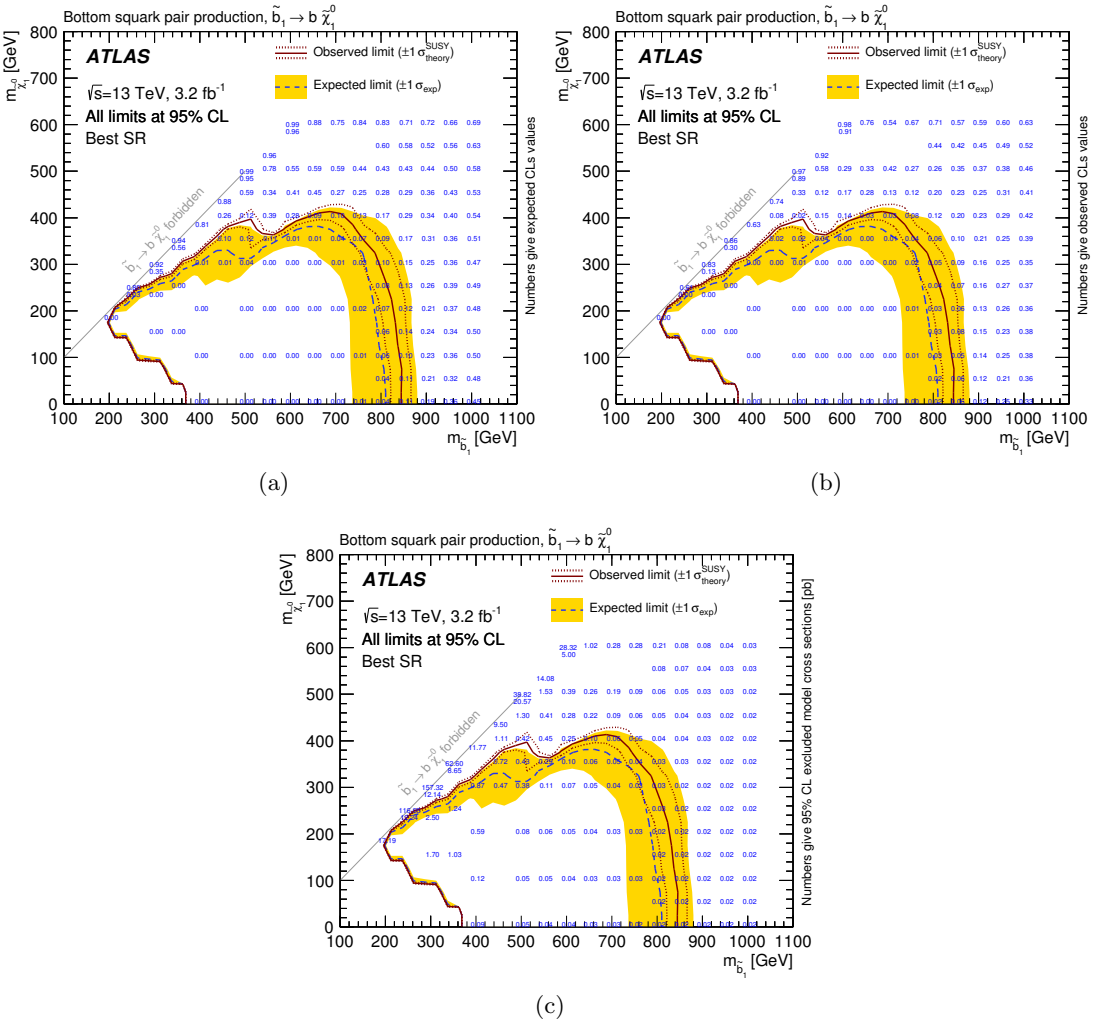

Figure A.2: Combined expected and observed exclusion limits at 95% CL in the $(m_{\tilde{b}_1}, m_{\tilde{\chi}_1^0})$ with the expected (a) and observed (b) CLs values superimposed. The 95% CL excluded model cross sections are shown in (c). The dashed black and solid bold red lines show the 95% CL expected and observed limits respectively, including all uncertainties. The shaded (yellow) bands around the expected limits show the impact of the experimental uncertainties while the dotted red lines show the impact on the observed limit of the variation of the nominal signal cross section by 1σ theoretical uncertainty.

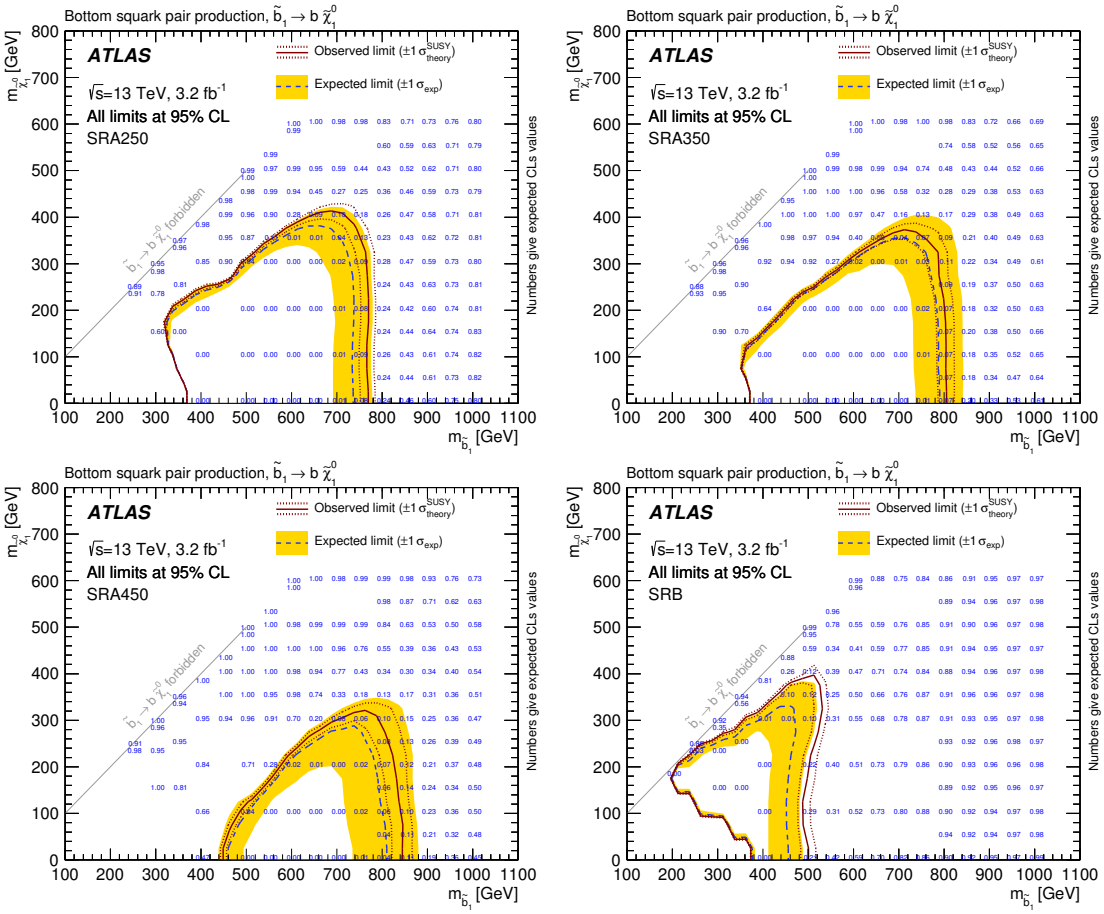

Figure A.3: Expected and observed exclusion limits at 95% CL in the $(m_{\tilde{b}_1}, m_{\tilde{\chi}_1^0})$ plane for the four signal regions defined in this analysis. Numbers show the expected CLs values. The dashed black and solid bold red lines show the 95% CL expected and observed limits respectively, including all uncertainties. The shaded (yellow) bands around the expected limits show the impact of the experimental uncertainties while the dotted red lines show the impact on the observed limit of the variation of the nominal signal cross section by 1σ theoretical uncertainty.

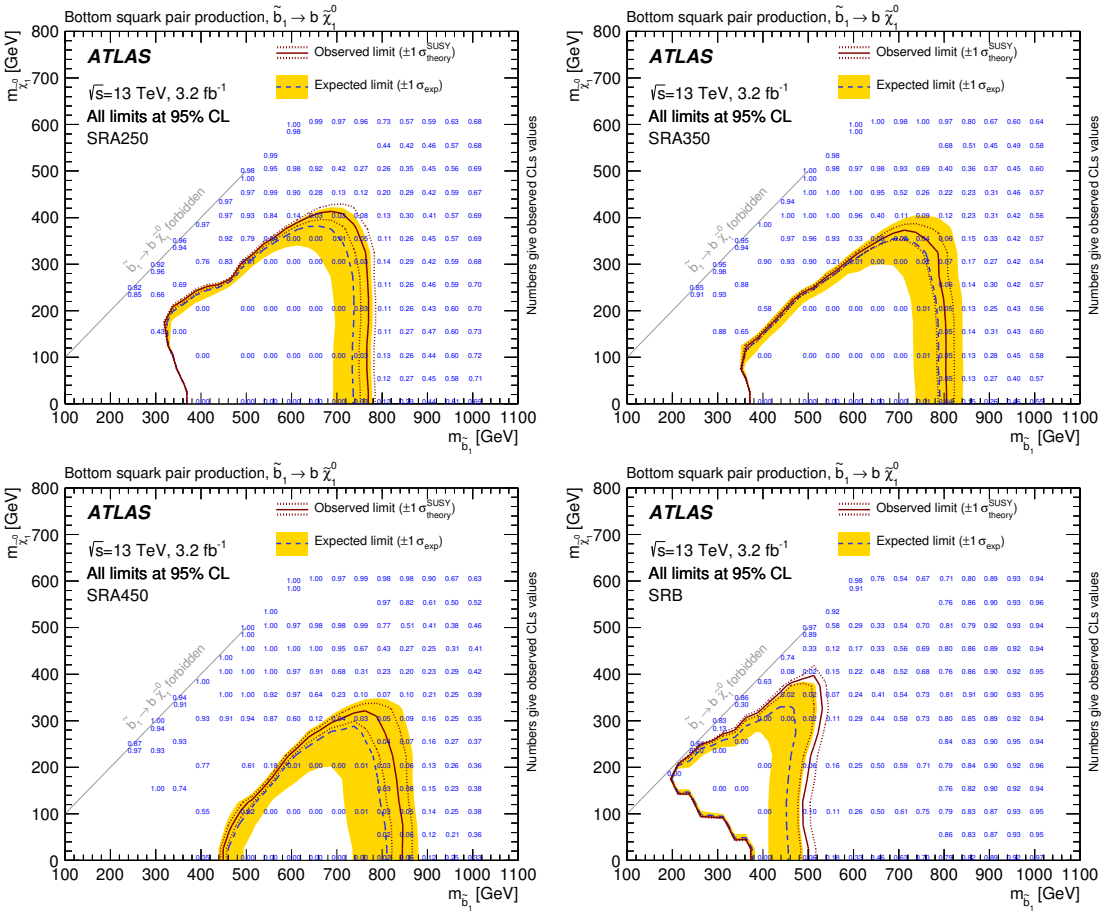

Figure A.4: Same as in previous figure, numbers show the observed CLs values.

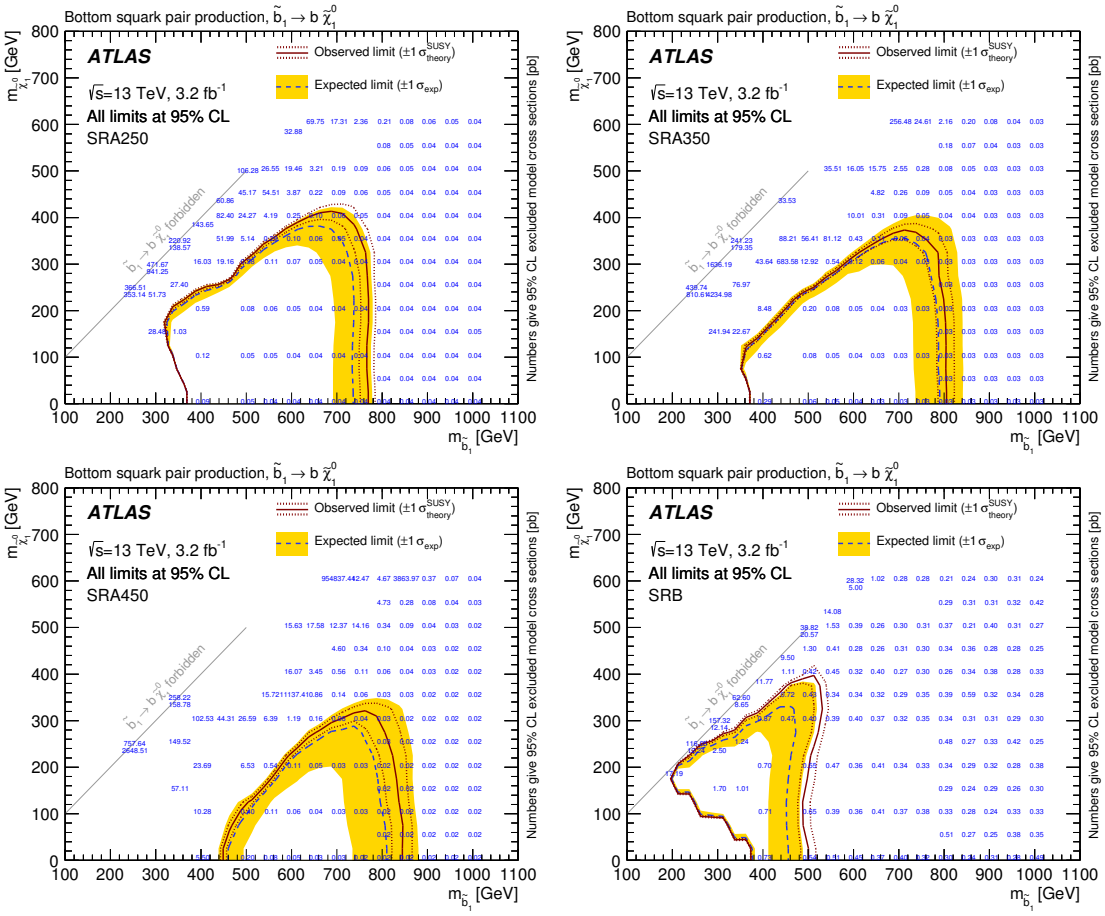

Figure A.5: Same as in previous figure, numbers show the 95% CL excluded model cross sections.

Appendix B

TileCal work

The Tile Calorimeter (TileCal) is the central hadronic calorimeter of the ATLAS experiment at the LHC and it was described in Section 3.2.3. Part of the work towards this PhD thesis was devoted to the calibration and the operation activities of TileCal.

The work included the contribution to the activities of calibration of TileCal using an integrator-based readout system, which provides the signal coming from inelastic proton-proton collisions at low momentum transfer during ATLAS collisions. These minimum bias signals can be used to monitor the ATLAS instantaneous luminosity, as well as to study radiation effects on the TileCal scintillators. In particular, the integrator signals coming from minimum bias interactions collected during 2012 were used to detect and quantify the effect of the irradiation of the TileCal scintillators at the end of the LHC Run-1, by studying the average response of calorimeter cells in the Extended Barrel as a function of the time and of the integrated charge.

The calibration work also included responsibilities in the framework recording the minimum bias data and in making the data available for the luminosity and the irradiation studies.

Besides the work related to the TileCal calibration, a significant amount of time was devoted to ensure the correct operations of TileCal, by taking the role of TileCal Run Coordinator for a four-months term in May-August 2016 (and previously of Deputy Run Coordinator for other four months).

B.1 Irradiation effect on the response of the scintillators in the ATLAS Tile Calorimeter

B.1.1 Introduction

TileCal consists of four partitions, two Long Barrels (LB) and two External Barrels (EB), and it is divided in two sides, A ($\eta > 0$) and C ($\eta < 0$). Each partition is segmented in 64 wedges, or modules, which correspond to a granularity of ~ 0.1 rad in the

ϕ coordinate. Each module is radially segmented in three layers, called A, B(C) and D, with a segmentation of 0.1 in η for layers A, B(C) and of 0.2 for layer D. A scheme of the TileCal cells is shown in Figure B.1.

The energy loss of the particles produced in the collisions, while passing through the calorimeter, gives rise to scintillating light which is proportional to the energy deposition in the tiles. Wavelength shifting fibers conduct the light from the scintillating tiles to the photomultiplier tubes (PMTs).

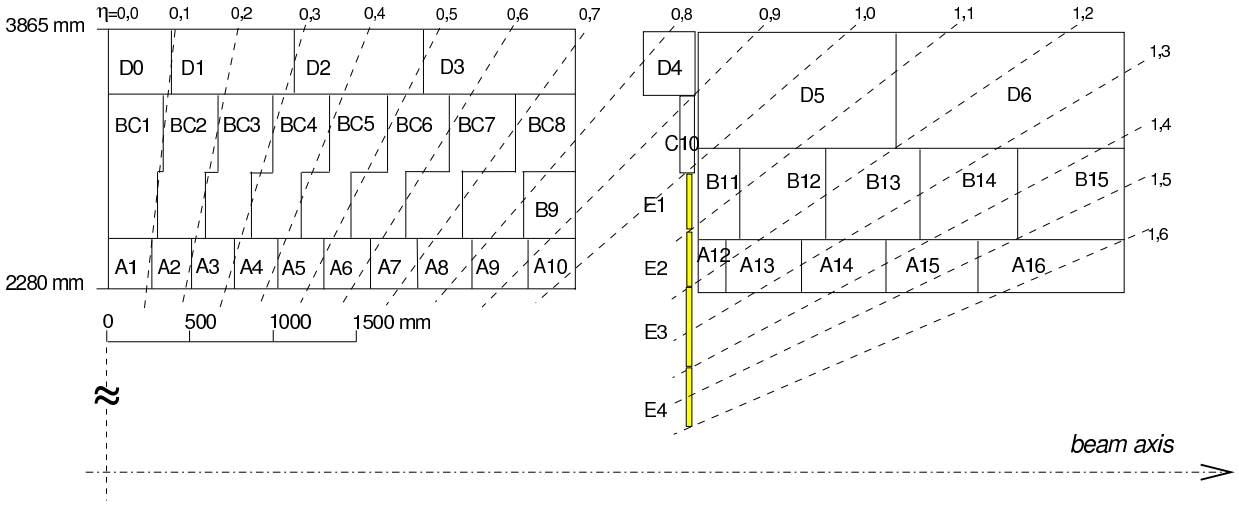

Figure B.1: Schematic representation of the TileCal cells.

The monitoring and equalization of the calorimeter response at each stage of the signal development is allowed by a movable ^{137}Cs radioactive source, a laser calibration system and a charge injection system. The ^{137}Cs calibration system is inclusive and emulates the full readout chain, while the Laser system allows to monitor only the PMTs response and the readout electronics. Moreover, during the LHC data taking, an integrator based readout provides signals coming from inelastic proton-proton collisions at low momentum transfer and allows monitoring the instantaneous ATLAS luminosity as well as the response of calorimeter cells. Minimum bias currents have been used to detect and quantify the irradiation effect of TileCal scintillators using the data taken during 2012 which corresponds to about 22 fb^{-1} of integrated luminosity. The response variation for an irradiated cell has been studied combining the information from three calibration systems (cesium, laser and minimum bias). The results on the effect of irradiation on the calorimeter response are reported.

B.1.2 TileCal calibration systems

As pointed out, the monitoring and calibration of the calorimeter response at each stage of the signal treatment are allowed by different calibration systems. A scheme of the TileCal calibration systems and the corresponding readout signal paths is shown in

Figure B.2. In the following, the three calibration systems used in this study are briefly described.

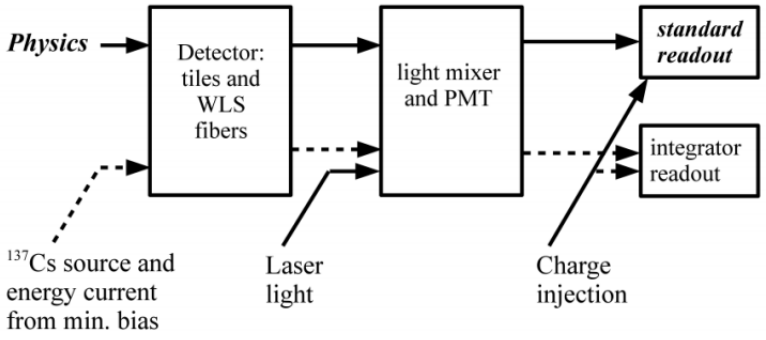

Figure B.2: A scheme of the TileCal calibration systems and the corresponding readout signal paths. The first box stands for the optical components such as the scintillating tiles and the wavelength shifting fibers, which are monitored using the Cesium and the Minimum Bias systems. The second box represents the PMTs which are monitored by illuminating them with a Laser system. Finally, a Charge Injection System (CIS) is implemented for the calibration of the front-end electronic gains.

B.1.2.1 The cesium system

A ^{137}Cs radioactive source, which emits γ's of 662 keV, is driven through the calorimeter using hydraulic control during dedicated Cesium (Cs) scans [114]. The current originating from the energy deposited in the scintillating tiles is read out from the integrator circuits of each channel and normalised to the cell size along the beam axis (see Figure B.1). The Cesium scans, which are performed with a periodicity of one or two months, are used to equalize the response of the calorimeter at the electromagnetic scale [55] and to monitor the stability of the optical components. The precision of the calibration using the Cesium source is better than 0.3%.

B.1.2.2 The laser system

The laser calibration system [115] makes use of light from a 532 nm laser and is used to monitor and calibrate each of the TileCal PMTs. The light is emitted in short pulses ($\sim$15 ns) similar to physics signals. The laser signal is sent to each PMT by means of optical fibers. Laser measurements are performed on a weekly timescale and are used for monitoring the PMTs response stability and linearity between two Cesium scans and for timing adjustment of the electronics. The laser allows determining the PMT gain variation with a precision better than 0.5%.

B.1.2.3 The minimum bias system

Soft parton interactions, or the so-called Minimum Bias (MB) events, are dominating processes in the proton-proton collisions at the LHC. The integrator system [116] of each PMT integrates the response to the MB signals over time and allows monitoring the response of all calorimeter cells during data-taking as well as the ATLAS instantaneous luminosity [117].

The integrator is printed on a circuit board plugged to the so-called 3-in-1 card [116]. A 12-bit ADC card digitizes the integrator output which ranges up to 5 V before saturating the ADC. The integrator gain can be varied by selecting one among six predefined resistors that also define the integration time, which ranges between 10-20 ms. The integrator gains are configured depending on the instantaneous luminosity. The average gain stability has been better than 0.1% during the first run of the LHC [117].

B.1.3 Study of the cells response variation

A method for estimating the effect of irradiation on the TileCal scintillators has been developed, exploiting the Minimum Bias (MB) and the Laser systems for the direct evaluation of the effect and the cesium system as a cross check. The study considered only the cells in the Extended Barrel, since those are the most exposed to irradiation.

The combination of the calibration systems has also allowed studying the evolution of the response of a very irradiated cell as a function of the time and the integrated luminosity.

The main idea underlying these studies is (as already pointed out) the fact that the MB and Cs currents are sensitive to both PMT gain variation and scintillator irradiation, while the Laser currents are sensitive to the PMT gain variation only. One can therefore subtract the gain variation measured by Laser from the total response variation seen by Cs or MB. MB currents are chosen because there are more MB runs than the Cs scans.

In the following subsections, the method used to treat the data will be illustrated.

B.1.3.1 The method

Since MB currents depend on the instantaneous luminosity and cannot provide an absolute measurement of the cell response variation, one needs to consider the variation of the ratio between a probe cell and a reference cell.

The criteria adopted in the choice of the reference cell include the requirement that the cell is rather protected from irradiation but at the same time it has enough signal to be usable. The cell in the outer layer of the Extended Barrel with $0.9 <| \eta |< 1.0$, called D5 (see Figure B.1), has been chosen for this purpose. The ratio between the currents measured by the PMTs reading the probe cell and the reference cell, indicated as $Cell_{probe}/Cell_{ref}$, does not depend on the variation of luminosity and should be flat in

time. Any deviation from the flat behaviour is an indication that the probe cell response is evolving in a different way with respect to the reference cell. By varying the probe cell position from a low to a high irradiation zone, it should be possible to see a correlation between the decrease of response and the radiation amount.

The variation of the cells response does not depend only on irradiation of the active material (scintillators). The gain of the PMTs reading the cells fluctuates as well, depending on the current they integrate (the gain decreases during data taking and recovers during technical stops). This effect reflects on the cell response variation, though it has nothing to do with the radiation damage, and can be subtracted using the Laser system (which is only sensitive to the PMT gain variation).

The study has been performed using data from MB collisions collected between the end of April and the end of November 2012. The total integrated luminosity delivered in this period corresponds to about 22 fb^{-1}.

The integrator current evolves as a function of the LumiBlock number [1] for each minimum bias data taking period (run). For each channel, the average of the integrator current over all the measurements in a single LumiBlock is computed. The ratios $Cell_{probe}/Cell_{ref}$ between the average currents per LumiBlock are used to build a distribution which is fitted with a Gaussian function in order to estimate its parameters μ (mean) and σ (RMS) for a given run.

The μ values of the fitted functions are then used to compute the response variation of the probe cell relatively to the reference cell D5, using the formula

$$\text{Relative response variation} = \frac{[\text{channel/D5}]}{[\text{channel/D5}]_{ref}} - 1, \tag{B.1}$$

where *ref* refers to the first data taking period in chronological order, taken as a reference.

It is interesting to plot the distribution of the difference between the values of the cell response variations as measured by the MB and the Cs systems, which are supposed to be very similar. This distribution is shown in Figure B.3. The difference between Cs and MB variation is required to be less than 1% in order to discard measurements potentially affected by occasional readout errors. This removes less than 2% of the data sample.

B.1.4 Results

The combined use of the three calibration systems has allowed estimating the response variation of all the cells in the inner and middle layer of the Extended Barrels and to detect and evaluate the effect of the radiation damage on their scintillators. The results of this study will be presented in the following paragraphs, starting from the case of a very exposed cell.

[1] The atomic unit of ATLAS data is the Luminosity Block (LumiBlock). One LumiBlock contains 2 minutes of data taking, but this can vary due to run conditions and other operational issues.

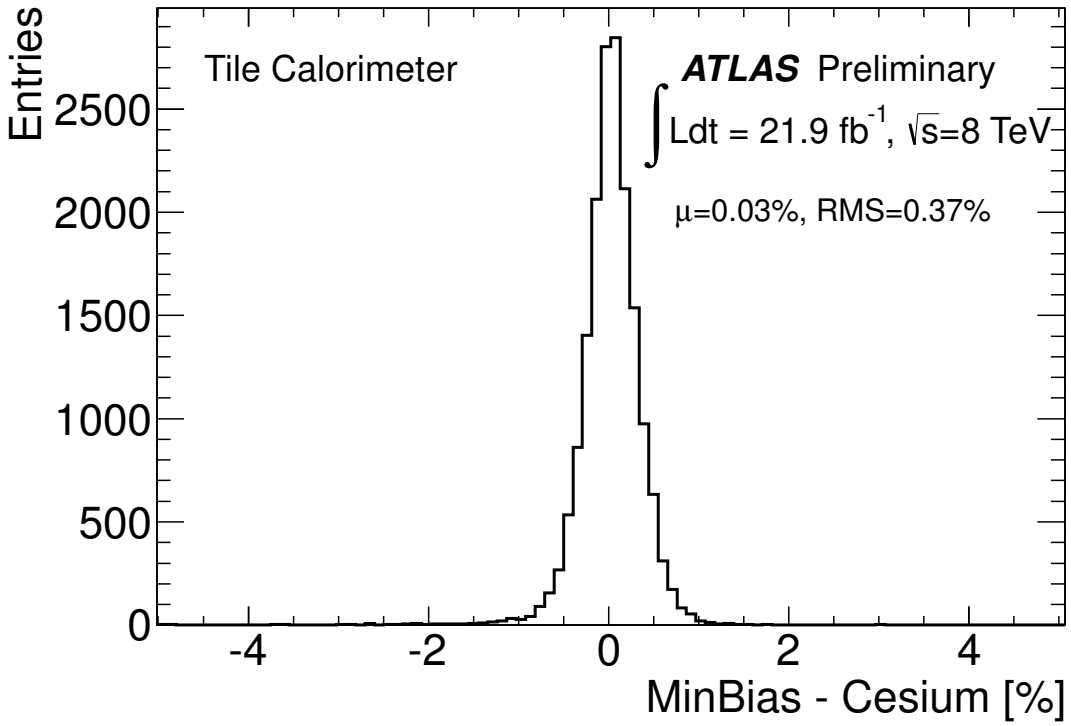

Figure B.3: The distribution of the difference between the relative variation of the response to Minimum Bias and Cesium currents. The points correspond to all inner and middle layer cells in the Extended Barrel, covering the region $1.0 <| \eta |< 1.7$ [118].

B.1.4.1 Response variation of a very exposed cell

The variation of the response as measured by MB, Cesium and Laser systems for cells in the inner layer of the Extended Barrel, covering the region $1.2 <| \eta |< 1.3$, as a function of the time is showed in Figure B.4. MB data cover the period from the beginning of April to the end of November 2012. The Cesium and Laser data cover the period from mid-March to mid-December. The integrated luminosity quoted in the plot is the total delivered in this period.

As already observed in 2011 data, the down-drifts of the PMT gains (seen by Laser) coincide with the collision periods while up-drifts are observed during machine development periods and at the end of the proton data-taking (beginning of December).

In the case of MB and Laser, the absolute response variation for cell A13 has been obtained by multiplying the variation of the ratio of currents A13/D5 by the absolute response variation of cell D5 seen by the Cesium system. The variation versus time for the response of the three systems is normalized to the first Cs scan (taken in March, before the start of collisions data taking).

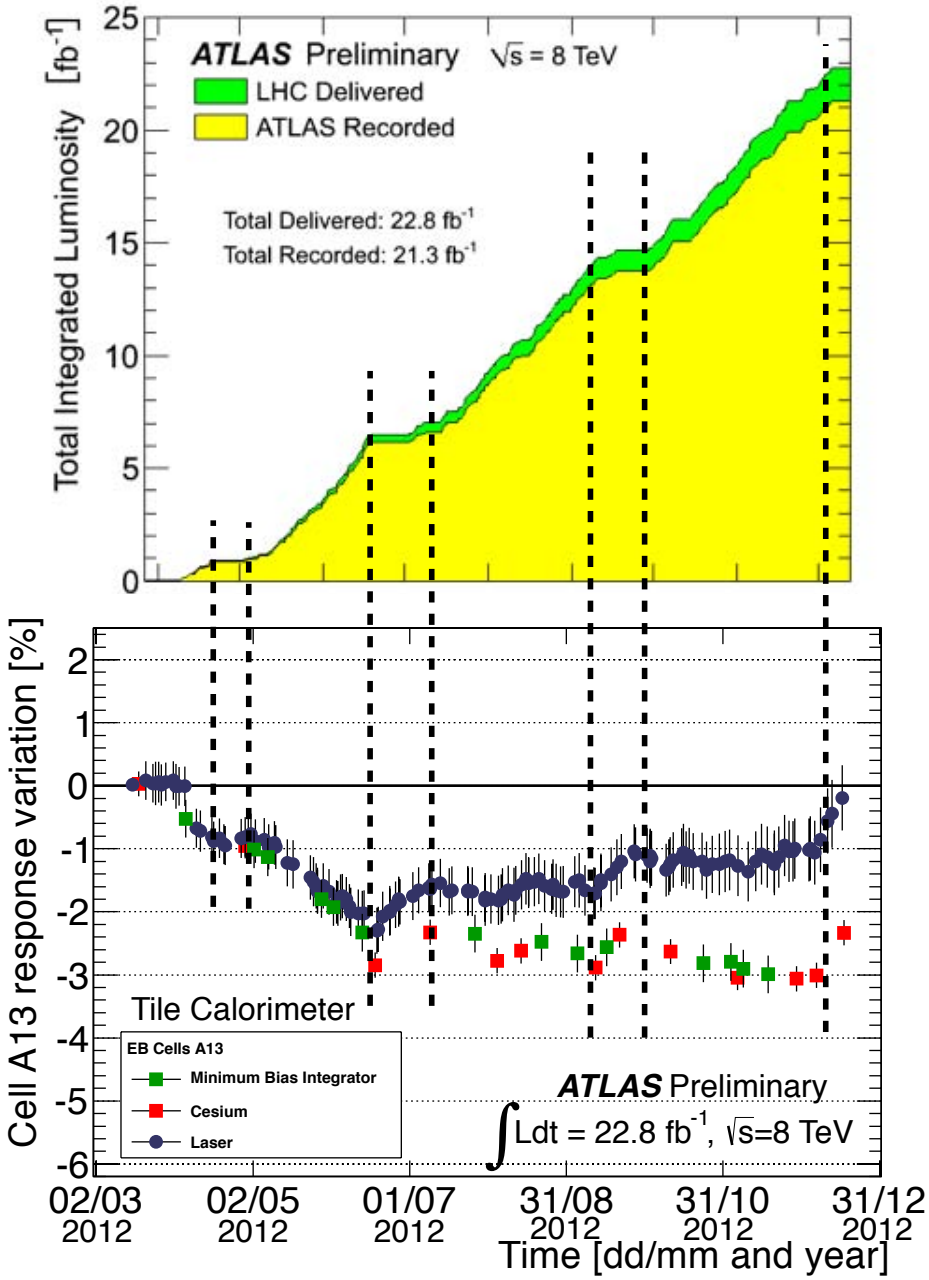

Figure B.4: The variation of the response to Minimum Bias, Cesium and Laser for cells in the inner layer of the Extended Barrel, covering the region $1.2 <| \eta |< 1.3$, as a function of the time, compared to the time evolution of the total integrated luminosity collected by ATLAS. [118]. More details in the text.

B.1.4.2 Effect of radiation damage on the scintillators

Under the assumption that the radiation impact comes from the integrated energy flux, the integrated charge is an appropriate observable which would allow comparing the irradiation effect on the same scale for all cells independently from their position in the

calorimeter. One of the goals of this study is to show that all cell responses follow the same pattern vs the collected integrated charge.

In order to compute the integrated charge collected in each of the cells considered in this analysis, one has to consider the linear dependence between MB signal and the instantaneous luminosity [117]. For each channel i one can compute the constant factors $\alpha_i = I_i(t)/L(t)$, where $I_i(t)$ is the anode current and $L(t)$ the instantaneous luminosity. The factors α_i depend on the cell size and position. The constant factors are computed using a single minimum bias data taking period, averaging over 10 successive LumiBlocks.

The total integrated charge up to a given time is therefore given by

$$Q_i(t) = \alpha_i \int_{t_0}^{t} L(t)dt, \tag{B.2}$$

where t_0 is the starting time of the reference run. The ATLAS integrated luminosity, which is provided by the ATLAS Luminosity Task Force, is the total delivered one, and not the one corresponding to stable beam periods only.

The relative variation of the response to MB currents, after the subtraction of the Laser component, has been plotted in Figure B.5 as a function of the integrated charge for all the cells in the A (a) and B (b) layers of the Extended Barrels. Cells in the A layer collected more integrated charge (maximum charge ∼1400 mC) with respect to those in the B layer (maximum charge ∼500 mC). Figure B.5 (c) shows the profiles of the plots in the Figures B.5 (a) and (b). It can be seen that, as expected, the two sets of cells show the same behaviour as a function of the collected integrated charge.

B.1.5 Conclusions

After a brief overview of the ATLAS Tile Calorimeter and of the three calibration systems: Cs, Laser and MB, a method for estimating the effect of the irradiation on the calorimeter scintillators, based on the combined use of the three systems, has been described.

The combination of the Cesium, Laser and Minimum Bias calibration systems allowed determining the evolution of the response of very irradiated cells as a function of the ATLAS integrated luminosity in 2012. A loss of ∼2% in the channel response has been detected as the maximum irradiation effect.

The effect of the irradiation damage on the scintillators of the TileCal cells in the Extended Barrels has also been detected and quantified.

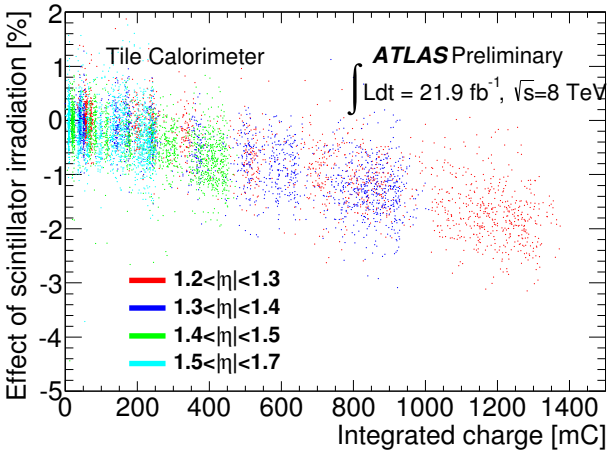

(a)

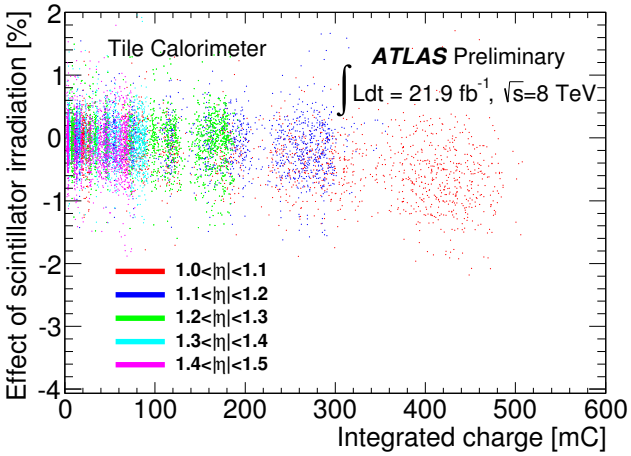

(b)

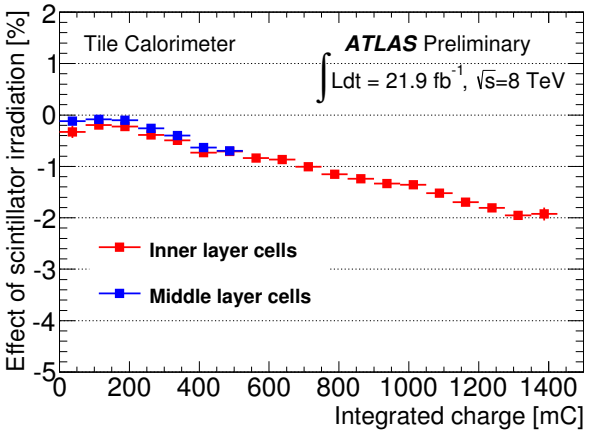

(c)

Figure B.5: The relative variation of the MB response, after the subtraction of the Laser component, as a function of the integrated charge for the cells in the A (a) and B (b) layers of the EB and the average variation for the two sets of cells superimposed (c) [118]. The cells considered are A13, A14, A15, A16, B11, B12, B13, B14, B15 and B16 (see Figure B.1).

Appendix C

Search for the Standard Model Higgs boson in associated $(W/Z)H(\rightarrow b\bar{b})$ production at $\sqrt{s}$ =7,8 TeV

In the early stages of the work towards this thesis, effort was devoted to the search for the SM Higgs boson (H) in associated production with a vector boson (W/Z), with the Higgs boson decaying into a $b\bar{b}$ pair. The $H \rightarrow b\bar{b}$ decay mode is predicted by the SM to have a branching ratio of 58% for $m_H = 125$ GeV [119]. An inclusive search for the Higgs boson in this particular decay mode is not possible at the LHC, because this signature would be overwhelmed by the QCD multijet background. For this reason, the Higgs is required to be produced in association with something else, such as a $t\bar{t}$ pair or, as in this case, a vector boson. By selecting the leptonic decay products of the vector boson it is possible to reduce the background contamination and increase the signal-to-background ratio to affordable values.

The work was performed considering the channel where the Higgs boson is produced in association with a Z boson and the latter decays to neutrinos. This channel gives a final state which is essentially the same as the one studied in the search for the bottom squark (see Chapters 5 and 6), characterized by two b-jets and missing transverse momentum.

The search is documented in the ATLAS conference note: *Search for the $b\bar{b}$ decay of the Standard Model Higgs boson in associated (W/Z)H production with the ATLAS detector* (ATLAS-CONF-2013-079, July 2013). It is performed using the full data recorded in pp collisions during the LHC Run-1, corresponding to integrated luminosities of 4.7 fb^{-1} at $\sqrt{s}$ =7 TeV and 20.3 fb^{-1} at $\sqrt{s}$ =8 TeV. The processes considered are the associate $(W/Z)H$ production, with $W \rightarrow \ell\nu$, $Z \rightarrow \ell\ell$ ($\ell = e,\ \mu$) and $Z \rightarrow \nu\nu$. The search strategy considers the simultaneous analysis of all the three different channels at once.

The optimization of the analysis is performed for a Higgs boson mass of 125 GeV. The signal regions are divided into three categories, with 0, 1 or 2 leptons respectively, depending on the decay mode of the vector boson. The event selection in the signal regions requires exactly two b-jets, which are used to form the dijet system. At most one additional jet is allowed. Additional requirements on the angular separation between the jets and the $E_{\mathrm{T}}^{\mathrm{miss}}$ are applied in the 0-lepton channel to reject the multijet background. In the 1-lepton (2-lepton) channel, requirements are imposed on $E_{\mathrm{T}}^{\mathrm{miss}}$ and on the transverse mass m_T^W (invariant mass $m_{\ell\ell}$) to select events consistent with the presence of a W (Z) boson. The transverse momentum of the vector boson (p_T^V) is reconstructed as the $E_{\mathrm{T}}^{\mathrm{miss}}$ in the 0-lepton channel, as the magnitude of the vector sum of the lepton and the $\vec{p}_{\mathrm{T}}^{\mathrm{miss}}$ in the 1-lepton channel and as the magnitude of the vector sum of the two leptons in the 2-lepton channel.

For each lepton category, a further categorization, based on five p_T^V intervals, is applied, with boundaries at 0, 90, 120, 160 and 200 GeV. Only the last three intervals are used for the 0-lepton channel, in order to guarantee the efficiency of the $\vec{E}_{\mathrm{T}}^{\mathrm{miss}}$ trigger. Further requirements on the angular separation between the two jets of the dijet system are applied depending on the p_T^V interval. An extra categorization on the number of jets (2 or 3) is defined.

The SM background composition in the signal regions varies from channel to channel and with the p_T^V and jet selections. Overall, $Z + bb$, $t\bar{t}$ and $W + bb$ production represent the most important SM process contributing to the total background. Dedicated control regions are used to constrain the background contamination. Their definition is very similar to the signal regions one, although the regions are required to have only 1 or no b-tagged jets.

A combined likelihood fit is performed, similarly to what was described in Section 6.6. In this case, though, the shape of the m_{bb} variable is used in the fit. The m_{bb} distributions in all the signal channels are used as inputs to the global fit, together with the event yields in all the control regions. Similarly to the case of the sbottom analysis, several experimental and theoretical systematic uncertainties are considered and used as nuisance parameters in the global fit.

The expected SM Higgs boson cross section is multiplied by the signal strength parameter μ. This parameter is allowed to freely float in the global fit.

After performing the global fit, no significant excess is found in data with respect to the background-only predictions. The fitted value of the signal strength parameter, after combining all lepton channels and data-taking periods, is found to be $\mu = 0.2 \pm 0.5(\mathrm{stat.}) \pm 0.4(\mathrm{syst.})$ for $m_H = 125$ GeV. The fitted μ values can be seen in Figure C.1 for the 7 TeV, 8 TeV and combined datasets, as well as separately for the three lepton channels and combined. Figure C.2 shows the m_{bb} distribution in data after subtracting all the backgrounds except that of the diboson processes. In the course of the search, the diboson signal has been

used to validate the rather complex analysis procedure and fitting strategy. In the figure, the Higgs boson signal contribution is also shown, both with its fitted signal strength and with the expected SM cross section.

The upper limits at 95% CL on the Higgs boson production cross section can be seen in Figure C.3, in the mass range 100-150 GeV. The observed limit for $m_H = 125$ GeV is 1.4 times the SM Higgs boson production cross section (1.3 for the expected limit).

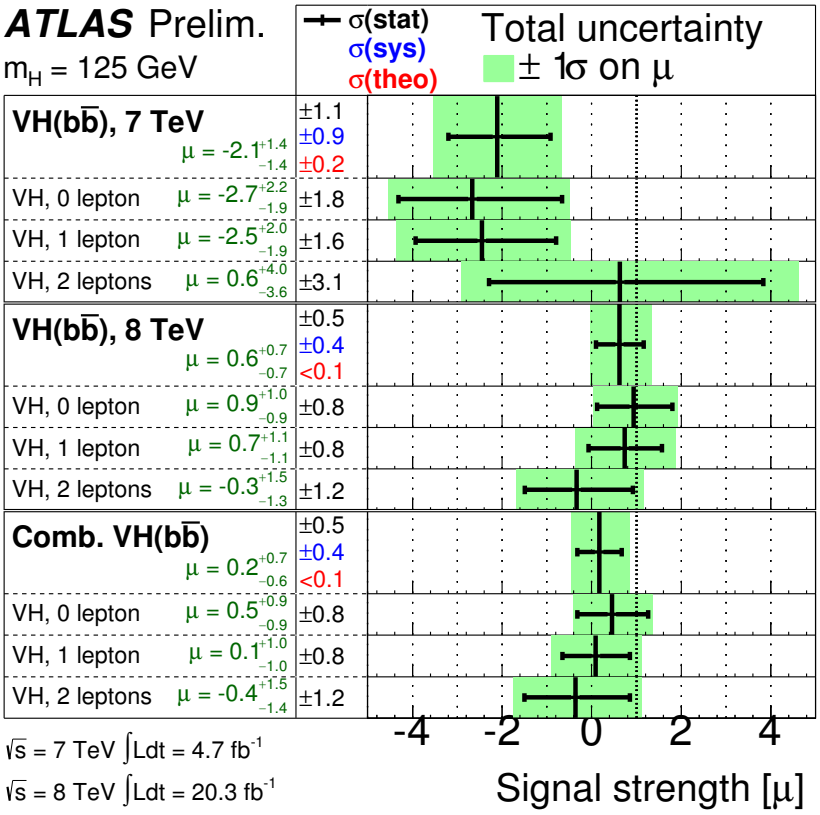

Figure C.1: The fitted values of the Higgs boson signal strength parameter μ for the 7 TeV, 8 TeV, and combined datasets, and for the three channels separately and combined, all for m_H=125 GeV [120].

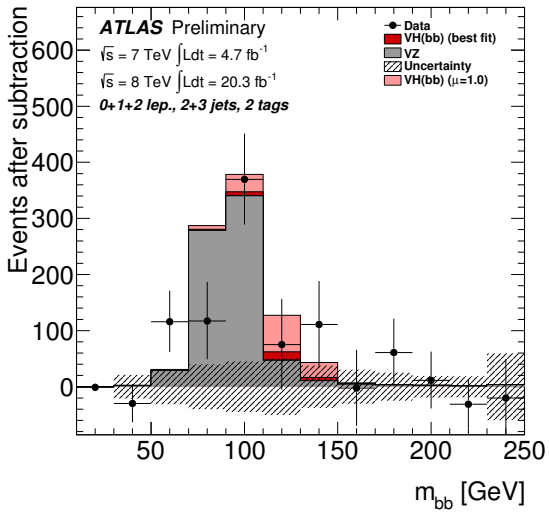

Figure C.2: The post-fit m_{bb} distribution in data after subtraction of all backgrounds except for the diboson processes and for the associated WH and ZH production of a SM Higgs boson with m_H=125 GeV. The Higgs boson signal contribution is shown both with its fitted signal strength (indicated as best fit) and as expected for the SM cross section (indicated as $= 1.0$). The error bands include both statistical and systematic uncertainties [120].

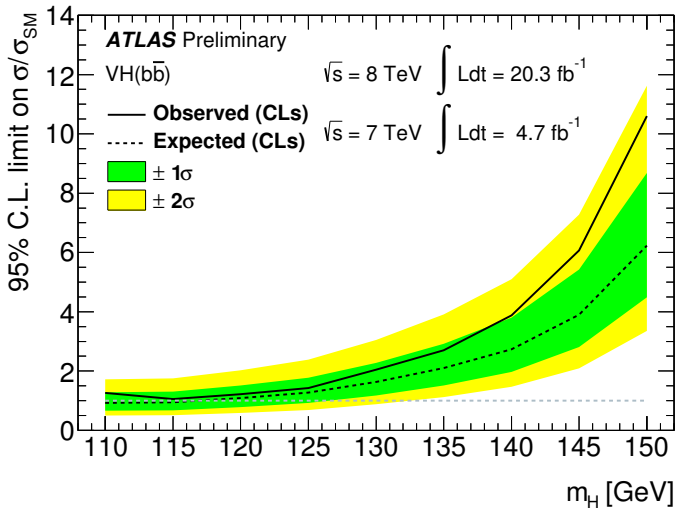

Figure C.3: Expected (dashed) and observed (solid) 95% CL cross section upper limits, normalized to the SM Higgs boson production cross section, as a function of m_H for all channels and data taking periods combined. The expected upper limit is given for the background-only hypothesis. The green and yellow bands represent the 1σ and 2σ ranges of the expectation in the absence of a signal [120].

These results represent an improvement in the analysis sensitivity with respect to the previous ATLAS search in this channel [121]. An update of the analysis was performed subsequently, with a similar strategy but also including multivariate techniques for better discrimination of the signal and background. The final results from the Run-1 analysis are documented in Ref. [122]. The combined signal strength parameter was found to be $\mu = 0.51 \pm 0.31(\text{stat.}) \pm 0.24(\text{syst.})$. The updated values for the signal strength parameter can be seen in Figure C.4, while the updated cross section upper limits are shown in Figure C.5.

These results show that the analysis did not have enough sensitivity to discover the Higgs boson in this particular production and decay channel at $\sqrt{s}$ =7 and 8 TeV. A reduction of the sensitivity is observed at $\sqrt{s}$ =13 TeV, due to the decrease of the signal-to-background ratio. The preliminary results of this search with the $\sqrt{s}$ =13 TeV data collected in the first part of 2016, corresponding to an integrated luminosity of 13.2 fb^{-1}, are documented in Ref. [123]. The combined signal strength parameter is found to be $\mu = 0.21^{+0.36}_{-0.35}(\text{stat.}) \pm 0.36(\text{syst.})$ in this case.

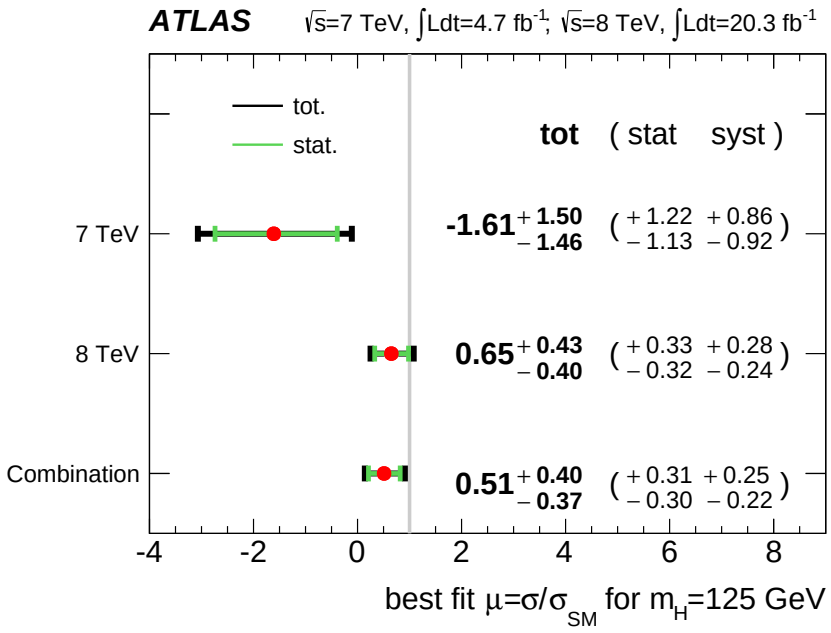

Figure C.4: The fitted values of the Higgs boson signal strength parameter μ for the 7 TeV, 8 TeV, and combined datasets, and for the three channels separately and combined, all for m_H=125 GeV [122].

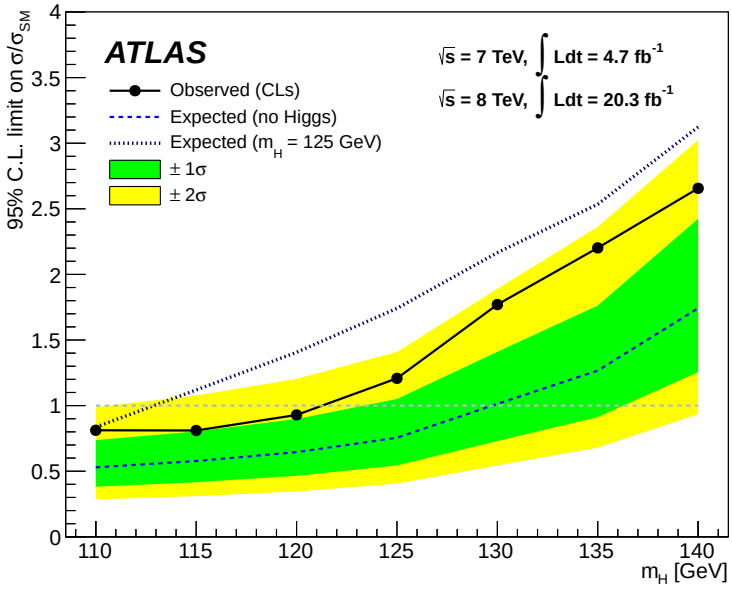

Figure C.5: Expected (dashed) and observed (solid) 95% CL cross section upper limits, normalized to the SM Higgs boson production cross section, as a function of m_H for all channels and data taking periods combined. The expected upper limit is given for the background-only hypothesis. The green and yellow bands represent the 1σ and 2σ ranges of the expectation in the absence of a signal [122].

Bibliography

[1] M. E. Peskin and D. V. Schroeder, "*An Introduction to quantum field theory*", (1995).

[2] S. Glashow, "*Partial Symmetries of Weak Interactions*", Nucl. Phys. **22**, 579 (1961).

[3] S. Weinberg, "*A Model of Leptons*", Phys. Rev. Lett. **19**, 1264 (1967).

[4] A. Salam, "*Gauge Unification of Fundamental Forces*", Rev. Mod. Phys. **52**, 525 (1980).

[5] D. Griffiths, "*Introduction to elementary particles*", (2010).

[6] G. 't Hooft, "*Dimensional regularization and the renormalization group*", Nucl. Phys. **B61**, 455 (1973).

[7] W. A. Bardeen, A. J. Buras, D. W. Duke, and T. Muta, "*Deep-inelastic scattering beyond the leading order in asymptotically free gauge theories*", Phys. Rev. D **18**, 3998 (1978).

[8] M. C. Gonzalez-Garcia and Y. Nir, "*Neutrino masses and mixing: Evidence and implications*", Rev. Mod. Phys. **75**, 345 (2003).

[9] Particle Data Group, "*The Review of Particle Physics*", Chin. Phys. **C40**, 100001 (2016).

[10] H. Goldstein, "*Classical Mechanics*", (1980).

[11] E. Fermi, "*Tentativo di una Teoria Dei Raggi β*", Il Nuovo Cimento (1924-1942) (1934).

[12] ATLAS Collaboration, "*Observation of a new particle in the search for the Standard Model Higgs boson with the ATLAS detector at the LHC*", Phys. Lett. **B716**, 1 (2012).

[13] CMS Collaboration, "*Observation of a new boson at a mass of 125 GeV with the CMS experiment at the LHC*", Phys. Lett. **B716**, 30 (2012).

[14] ATLAS, CMS, "*Combined Measurement of the Higgs Boson Mass in pp Collisions at $\sqrt{s} = 7$ and 8 TeV with the ATLAS and CMS Experiments*", Phys. Rev. Lett. **114**, 191803 (2015).

[15] S. Bethke, "*The 2009 World Average of alpha(s)*", Eur. Phys. J. **C64**, 689 (2009).

[16] S. P. Martin, "*A Supersymmetry primer*", Adv. Ser. Direct. High Energy Phys. **21**, 1 (2010).

[17] I. J. R. Aitchison, "*Supersymmetry and the MSSM: An Elementary introduction*", (2005).

[18] M. Drees, "*An Introduction to supersymmetry*", (1996).

[19] G. Ross, "*Grand Unified Theories*", (2003).

[20] M. E. Peskin, "*Beyond the standard model*", p. 49 (1997).

[21] K. Garrett and G. Duda, "*Dark Matter: A Primer*", Adv. Astron. **2011**, 968283 (2011).

[22] S. Dimopoulos, "*Softly broken supersymmetry and SU(5)*", Nucl. Phys. **B193**, 150 (1981).

[23] R. A. Flores and M. Sher, "*Higgs Masses in the Standard, Multi-Higgs and Supersymmetric Models*", Annals Phys. **148**, 95 (1983).

[24] S. Kraml, "*Stop and sbottom phenomenology in the MSSM*", (1999).

[25] LHC New Physics Working Group, D. Alves, "*Simplified Models for LHC New Physics Searches*", J. Phys. **G39**, 105005 (2012).

[26] E. Witten, "*Dynamical Breaking of Supersymmetry*", Nucl. Phys. **B188**, 513 (1981).

[27] R. Ellis, W. Stirling, and B. Webber, *QCD and Collider Physics*Cambridge Monographs on Particle Physics, Nuclear Physics and Cosmology (Cambridge University Press, 2003).

[28] J. M. Campbell, J. W. Huston, and W. J. Stirling, "*Hard Interactions of Quarks and Gluons: A Primer for LHC Physics*", Rept. Prog. Phys. **70**, 89 (2007).

[29] J. C. Collins, D. E. Soper, and G. F. Sterman, "*Factorization of Hard Processes in QCD*", Adv. Ser. Direct. High Energy Phys. **5**, 1 (1989).

[30] G. Altarelli and G. Parisi, "*Asymptotic Freedom in Parton Language*", Nucl. Phys. **B126**, 298 (1977).

[31] H.-L. Lai *et al.*, "*Global QCD analysis and the CTEQ parton distributions*", Phys. Rev. **D51**, 4763 (1995).

[32] H.-L. Lai *et al.*, "*New parton distributions for collider physics*", Phys. Rev. **D82**, 074024 (2010).

[33] A. Martin, W. Stirling, R. Thorne, and G. Watt, "*Parton distributions for the LHC*", Eur. Phys. J. **C63**, 189 (2009).

[34] R. D. Ball *et al.*, "*Parton distributions for the LHC Run II*", JHEP **04**, 040 (2015).

[35] Particle Data Group, J. Beringer *et al.*, "*The Review of Particle Physics*", Phys. Rev. **D86**, 010001 (2012).

[36] M. A. Dobbs *et al.*, "*Les Houches guidebook to Monte Carlo generators for hadron collider physics*", p. 411 (2004).

[37] M. Mangano and T. Stelzer, "*Tools for the simulation of hard hadronic collisions*", Ann. Rev. Nucl. Part. Sci. **55**, 555 (2005).

[38] S. Catani, F. Krauss, R. Kuhn, and B. Webber, "*QCD matrix elements + parton showers*", JHEP **0111**, 063 (2001).

[39] M. L. Mangano, M. Moretti, F. Piccinini, and M. Treccani, "*Matching matrix elements and shower evolution for top-quark production in hadronic collisions*", JHEP **0701**, 013 (2007).

[40] T. Sjostrand, S. Mrenna, and P. Z. Skands, "*PYTHIA 6.4 Physics and Manual*", JHEP **0605**, 026 (2006).

[41] G. Corcella *et al.*, "*HERWIG 6: An Event generator for hadron emission reactions with interfering gluons (including supersymmetric processes)*", JHEP **0101**, 010 (2001).

[42] M. Bahr, S. Gieseke, and M. H. Seymour, "*Simulation of multiple partonic interactions in Herwig++*", JHEP **0807**, 076 (2008).

[43] T. Gleisberg *et al.*, "*Event generation with SHERPA 1.1*", JHEP **02**, 007 (2009).

[44] J. Alwall, M. Herquet, F. Maltoni, O. Mattelaer, and T. Stelzer, "*MadGraph 5 : Going Beyond*", JHEP **1106**, 128 (2011).

[45] S. Frixione, P. Nason, and C. Oleari, "*Matching NLO QCD computations with Parton Shower simulations: the POWHEG method*", JHEP **0711**, 070 (2007).

[46] L. Evans and P. Bryant, "*LHC Machine*", JINST **3**, S08001 (2008).

[47] O. S. Brning *et al.*, "*LHC Design Report Vol III*", (2004).

[48] ALICE Collaboration, K. Aamodt *et al.*, "*The ALICE experiment at the CERN LHC*", JINST **3**, S08002 (2008).

[49] ATLAS Collaboration, "*The ATLAS Experiment at the CERN Large Hadron Collider*", JINST **3**, S08003 (2008).

[50] CMS Collaboration, "*The CMS experiment at the CERN LHC*", JINST **3**, S08004 (2008).

[51] LHCb Collaboration, J. Alves, A. Augusto *et al.*, "*The LHCb Detector at the LHC*", JINST **3**, S08005 (2008).

[52] C. De Melis, "*The CERN accelerator complex. Complexe des acclrateurs du CERN*", (2016), General Photo.

[53] M. Capeans *et al.*, "*ATLAS Insertable B-Layer Technical Design Report*", (2010).

[54] ATLAS Collaboration, "*Readiness of the ATLAS Liquid Argon Calorimeter for LHC Collisions*", Eur. Phys. J. **C70**, 723 (2010).

[55] ATLAS Collaboration, "*Readiness of the ATLAS Tile Calorimeter for LHC collisions*", Eur. Phys. J. **C70**, 1193 (2010).

[56] ATLAS Collaboration, "*Technical Design Report for the Phase-I Upgrade of the ATLAS TDAQ System*", CERN-LHCC-2013-018 (2013).

[57] ATLAS Collaboration, "*Improved luminosity determination in pp collisions at* $\sqrt{s}$ *= 7 TeV using the ATLAS detector at the LHC*", Eur. Phys. J. **C73**, 2518 (2013).

[58] A. B. Poy *et al.*, "*The detector control system of the ATLAS experiment*", Journal of Instrumentation **3**, P05006 (2008).

[59] S. Kolos, A. Corso-Radu, H. Hadavand, M. Hauschild, and R. Kehoe, "*A software framework for Data Quality Monitoring in ATLAS*", Journal of Physics: Conference Series **119**, 022033 (2008).

[60] T. Golling, H. S. Hayward, P. U. E. Onyisi, H. J. Stelzer, and P. Waller, "*The ATLAS Data Quality Defect Database System*", Eur. Phys. J. **C72**, 1960 (2012).

[61] ATLAS Collaboration, "*Performance of the ATLAS Inner Detector Track and Vertex Reconstruction in the High Pile-Up LHC Environment*", ATLAS-CONF-2012-042 (2012).

[62] ATLAS Collaboration, "*Electron reconstruction and identification efficiency measurements with the ATLAS detector using the 2011 LHC proton-proton collision data*", Eur. Phys. J. **C74**, 2941 (2014).

[63] W. Lampl *et al.*, "*Calorimeter clustering algorithms: Description and performance*", (2008).

[64] ATLAS Collaboration, "*Electron efficiency measurements with the ATLAS detector using the 2015 LHC proton-proton collision data*", ATLAS-CONF-2016-024 (2016).

[65] ATLAS Collaboration, "*Electron and photon energy calibration with the ATLAS detector using data collected in 2015 at* $\sqrt{s}$ *=13 TeV*", ATL-PHYS-PUB-2016-015 (2016).

[66] ATLAS Collaboration, "*Electron and photon energy calibration with the ATLAS detector using LHC Run 1 data*", (2014).

[67] ATLAS Collaboration, "*Muon reconstruction performance of the ATLAS detector in proton–proton collision data at* $\sqrt{s}$*=13 TeV*", Eur. Phys. J. **C76**, 1 (2016).

[68] M. Cacciari, G. P. Salam, and G. Soyez, "*The Anti-k(t) jet clustering algorithm*", JHEP **0804**, 063 (2008).

[69] ATLAS Collaboration, "*Jet energy measurement and its systematic uncertainty in proton-proton collisions at* $\sqrt{s}$ *= 7 TeV with the ATLAS detector*", Eur. Phys. J. **C75**, 17 (2015).

[70] ATLAS Collaboration, "*Jet Calibration and Systematic Uncertainties for Jets Reconstructed in the ATLAS Detector at* $\sqrt{s}$ *= 13 TeV*", ATLAS-PHYS-PUB-2015-015 (2015).

[71] ATLAS Collaboration, "*Pile-up subtraction and suppression for jets in ATLAS*", ATLAS-CONF-2013-083 (2013).

[72] ATLAS Collaboration, "*Performance of pile-up mitigation techniques for jets in pp collisions at* $\sqrt{s}$*=8 TeV using the ATLAS detector*", (2015).

[73] ATLAS Collaboration, "*Jet global sequential corrections with the ATLAS detector in proton-proton collisions at sqrt(s) = 8 TeV*", ATLAS-CONF-2015-002 (2015).

[74] ATLAS Collaboration, "*Determination of the jet energy scale and resolution at ATLAS using Z/*γ*-jet events in data at* $\sqrt{s)}$ *=8 TeV*", ATLAS-CONF-2015-057 (2015).

[75] ATLAS Collaboration, "*Public plots: In situ JES performance plots using full 13 TeV 2015 dataset*", (2015), "http://atlas.web.cern.ch/Atlas/GROUPS/PHYSICS/PLOTS/JETM-2015-003/".

[76] ATLAS Collaboration, "*Public plots: Jet energy scale uncertainties using full 13 TeV 2015 dataset*", (2016), "http://atlas.web.cern.ch/Atlas/GROUPS/PHYSICS/PLOTS/JETM-2016-002/".

[77] ATLAS Collaboration, "*Commissioning of the ATLAS high-performance b-tagging algorithms in the 7 TeV collision data*", ATLAS-CONF-2011-102 (2011).

[78] ATLAS Collaboration, G. Aad *et al.*, "*Expected Performance of the ATLAS Experiment - Detector, Trigger and Physics*", (2009).

[79] ATLAS Collaboration, "*Expected performance of the ATLAS b-tagging algorithms in Run-2.*", (2015).

[80] ATLAS Collaboration, "*Performance of missing transverse momentum reconstruction with the ATLAS detector in the first proton-proton collisions at* $\sqrt{s}$ *=13 TeV*", ATL-PHYS-PUB-2015-027 (2015).

[81] ATLAS Collaboration, "*Public plots: Missing transverse energy* (E_T^{miss}) *performance and systematic uncertainties using the full 2015 dataset*", (2016), "http://atlas.web.cern.ch/Atlas/GROUPS/PHYSICS/PLOTS/JETM-2016-003/".

[82] ATLAS Collaboration, "*Search for direct third-generation squark pair production in final states with missing transverse momentum and two b-jets in* $\sqrt{s}$*=8 TeV pp collisions with the ATLAS detector*", JHEP **10**, 189 (2013).

[83] ATLAS Collaboration, "*ATLAS tunes of PYTHIA6 and Pythia8 for MC11*", ATL-PHYS-PUB-2011-009 (2011).

[84] C. Borschensky *et al.*, "*Squark and gluino production cross sections in pp collisions at* $\sqrt{s}$ *= 13, 14, 33 and 100 TeV*", Eur.Phys.J. **C74**, 3174 (2014).

[85] P. Z. Skands, "*Tuning Monte Carlo Generators: The Perugia Tunes*", Phys. Rev. **D82**, 074018 (2010).

[86] S. Frixione, E. Laenen, P. Motylinski, and B. R. Webber, "*Single-top production in MC@NLO*", JHEP **03**, 092 (2006).

[87] ATLAS Collaboration, "*Single Boson and Diboson Production Cross Sections in pp Collisions at* $\sqrt{s} = 7$ *TeV*", ATL-COM-PHYS-2010-695 (2010).

[88] Tovey, D. R., "*On measuring the masses of pair-produced semi-invisibly decaying particles at hadron colliders*", JHEP **04**, 034 (2008).

[89] L. Moneta *et al.*, "*The RooStats Project*", (2011).

[90] M. Baak *et al.*, "*HistFitter software framework for statistical data analysis*", Eur. Phys. J. **C75**, 153 (2015).

[91] GEANT4, S. Agostinelli *et al.*, "*GEANT4: A Simulation toolkit*", Nucl. Instrum. Meth. **A506**, 250 (2003).

[92] ATLAS Collaboration, W. Lukas, "*Fast Simulation for ATLAS: Atlfast-II and ISF*", J. Phys. Conf. Ser. **396**, 022031 (2012).

[93] T. Sjöstrand, S. Mrenna, and P. Z. Skands, "*A Brief Introduction to PYTHIA 8.1*", Comput. Phys. Commun. **178**, 852 (2008).

[94] A. Martin, W. Stirling, R. Thorne, and G. Watt, "*Update of parton distributions at NNLO*", Phys. Lett. **B 652**, 292 (2007).

[95] D. J. Lange, "*The EvtGen particle decay simulation package*", Nucl. Instrum. Meth. **A462**, 152 (2001).

[96] M. Smizanska and J. Catmore, "*EvtGen in ATLAS*", ATL-COM-PHYS-2004-041 (2004).

[97] S. Catani *et al.*, "*Vector boson production at hadron colliders: A Fully exclusive QCD calculation at NNLO*", Phys. Rev. Lett. **103**, 082001 (2009).

[98] P. Nason, "*A new method for combining NLO QCD with shower Monte Carlo algorithms*", JHEP **11**, 040 (2004).

[99] S. Alioli, P. Nason, C. Oleari, and E. Re, "*A general framework for implementing NLO calculations in shower Monte Carlo programs: the POWHEG BOX*", JHEP **06**, 043 (2010).

[100] M. Czakon and A. Mitov, "*Top++: A Program for the Calculation of the Top-Pair Cross-Section at Hadron Colliders*", Comput. Phys. Commun. **185**, 2930 (2014), 1112.5675.

[101] ATLAS Collaboration, "*ATLAS Run 1 Pythia8 tunes*", ATL-PHYS-PUB-2014-021 (2014).

[102] S. Carrazza, S. Forte, and J. Rojo, "*Parton Distributions and Event Generators*", p. 89 (2013).

[103] L. Lonnblad and S. Prestel, "*Matching Tree-Level Matrix Elements with Interleaved Showers*", JHEP **03**, 019 (2012).

[104] W. Beenakker *et al.*, "*Squark and gluino hadroproduction*", Int. J. Mod. Phys. **A 26**, 2637 (2011).

[105] ATLAS Collaboration, "*Search for squarks and gluinos with the ATLAS detector in final states with jets and missing transverse momentum using* 4.7 fb^{-1} *of* $\sqrt{s}$=7 TeV *proton-proton collision data*", Phys. Rev. D **87**, 012008 (2013).

[106] ROOT Collaboration, K. Cranmer, G. Lewis, L. Moneta, A. Shibata, and W. Verkerke, "*HistFactory: A tool for creating statistical models for use with RooFit and RooStats*", (2012).

[107] A. L. Read, "*Presentation of search results: the CLs technique*", J. Phys. **G28**, 2693 (2002).

[108] ATLAS Collaboration, "*Performance of Missing Transverse Momentum Reconstruction in ATLAS studied in Proton-Proton Collisions recorded in 2012 at 8 TeV*", ATLAS-CONF-2013-082 (2013).

[109] ATLAS Collaboration, "*Improved luminosity determination in pp collisions at* $\sqrt{s}$ *=7 TeV using the ATLAS detector at the LHC*", Eur. Phys. J. **C73**, 2518 (2013).

[110] ATLAS Collaboration, "*Measurement of the cross-section for W boson production in association with b-jets in pp collisions at* $\sqrt{s}$ *= 7 TeV with the ATLAS detector*", J. High Energy Phys. **06**, 084. 53 p (2013).

[111] ATLAS Collaboration, "*Search for pair-produced third-generation squarks decaying via charm quarks or in compressed supersymmetric scenarios in pp collisions at* $\sqrt{s} = 8$ *TeV with the ATLAS detector*", Phys. Rev. **D90**, 052008 (2014).

[112] ATLAS Collaboration, "*Search for new phenomena in final states with an energetic jet and large missing transverse momentum in pp collisions at* $\sqrt{s} = 13 TeV$ *using the ATLAS detector*", Phys. Rev. **D94**, 032005 (2016).

[113] ATLAS Collaboration, "*Search for Supersymmetry at the high luminosity LHC with the ATLAS experiment*", ATL-PHYS-PUB-2014-010 (2014).

[114] E. Starchenko *et al.*, "*Cesium monitoring system for ATLAS Tile Hadron Calorimeter*", Nucl. Instrum. Meth. **A494**, 381 (2002).

[115] S. Viret, "*LASER monitoring system for the ATLAS Tile Calorimeter*", Nucl. Instrum. Meth. **A617**, 120 (2010).

[116] K. Anderson *et al.*, "*Design of the front-end analog electronics for the ATLAS tile calorimeter*", Nucl. Instrum. Meth. **A551**, 469 (2005).

[117] G. Gonzalez Parra, "*Integrator based readout in Tile Calorimeter of the ATLAS experiment*", ATL-TILECAL-PROC-2011-010 (2011).

[118] S. Fracchia, "*Irradiation effect on the response of the scintillators in the ATLAS Tile Calorimeter*", PoS(TIPP2014)024 (2014).

[119] A. Djouadi, J. Kalinowski, and M. Spira, "*HDECAY: A Program for Higgs boson decays in the standard model and its supersymmetric extension*", Comput. Phys. Commun. **108**, 56 (1998).

[120] ATLAS Collaboration, "*Search for the $b\bar{b}$ decay of the Standard Model Higgs boson in associated (W/Z)H production with the ATLAS detector* ", ATLAS-CONF-2013-079 (2013).

[121] ATLAS Collaboration, "*Search for the Standard Model Higgs boson produced in association with vector boson and decaying to bottom quarks with the ATLAS detector*", ATLAS-CONF-2012-161 (2012).

[122] ATLAS Collaboration, "*Search for the $b\bar{b}$ decay of the Standard Model Higgs boson in associated (W/Z)H production with the ATLAS detector*", J. High Energy Phys. **2015**, 69 (2015).

[123] ATLAS Collaboration, "*Search for the Standard Model Higgs boson produced in association with a vector boson and decaying to a $b\bar{b}$ pair in pp collisions at 13 TeV using the ATLAS detector*", ATLAS-CONF-2016-091 (2016).

Acknowledgments

First of all, I could never be grateful enough to Mario Martínez. He was the most supportive and careful supervisor I could have asked for. He guided me during these years with extreme attention and patience, and he taught me how to become an experimental physicist (or at least he tried hard). He took care of every single detail of my work and of this thesis. I will never finish to thank him for all of this, as well as for all the great opportunities he gave me during my PhD.

During my years at IFAE, I had the pleasure to work together with some very talented and helpful researchers. Very special thanks go to Martín Tripiana and Arely Cortés for having been a real point of reference for me. Their passion and enthusiasm were extremely inspiring. I am also thankful to Paolo Francavilla, Vincent Giangiobbe and Veronica Sorín, who helped me to move my very first steps in ATLAS.

A very exciting part of my PhD years was related to the activities in the Tile Calorimeter group. Thanks to Ilya Korolkov for his guidance in my qualification task and thanks to the whole TileCal community, and especially to Oleg Solovyanov, for their help and support during my months as TileCal run coordinator.

Part of my thesis was funded by the ATLAS PhD grant, a special grant scheme from a donation from the Fundamental Physics Prize winners, Fabiola Gianotti and Peter Jenni, and from the Winton Charitable Foundation. I am very grateful to all of them for this extraordinary opportunity.

These years would have not been so pleasant without the other IFAE (ex-)PhD students, with whom I spent long hours in the office (and sometimes also outside). I shared with them a lot of things, such as the excitement (and sometimes the frustration) of our research, as well as liters of coffee. Thanks to Valerio, Garoe, Roger and Cora. And thanks to Andrea, for being a real friend and a very special person.

To my parents goes all my deepest gratitude. Se sono arrivata qui è in buona parte grazie a voi e ai vostri insegnamenti. Grazie per essere sempre stati presenti, benché lontani, e per non avermi mai fatto mancare il vostro supporto e il vostro incoraggiamento.

Finally, I need to thank Daniele. He is the person who had to deal with all the hysteria, which was an integral part of my PhD education, and with all the "I cannot. I have to work". Despite of this, he decided to stay along. Grazie per avermi supportato e, soprattutto, sopportato in questi anni, e spero che continuerai a farlo in futuro.

These were four very challenging years, rich of great satisfactions but also of very difficult moments. For once, I would dare to say that I am proud of myself and of what I have achieved (but I will not say it too loud).